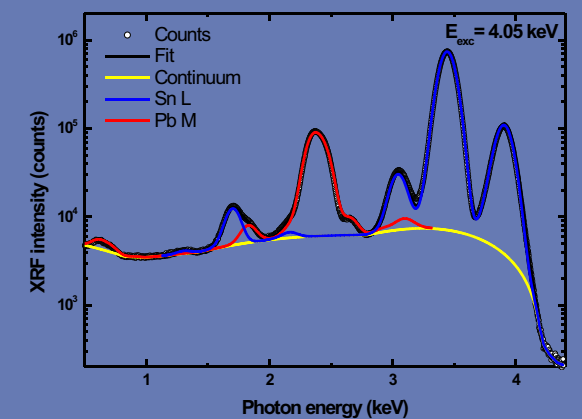


# Physico-Chemical Research of Cultural Heritage Materials Using Microanalytical Methods

L.K. Herrera Quintero



Instituto de Ciencia de Materiales de Sevilla  
 Consejo Superior de Investigaciones Científicas  
 Universidad de Sevilla  
 2009

L.K. Herrera Quintero Physico-Chemical Research of Cultural Heritage Materials Using Microanalytical Methods

# Physico-Chemical Research of Cultural Heritage Materials Using Microanalytical Methods

Liz Karen Herrera Quintero

The work described in this thesis was performed at Material Science Institute of Seville – Spanish Scientific Council (ICMSE –CISC), Seville, Spain. It is part of the research program of Marie Curie Action (Advanced Research Training on the Conservation of Cultural Heritage)

© L.K Herrera

ISBN

cover:





**MATERIAL SCIENCE  
INSTITUTE OF SEVILLE**



**SPANISH SCIENTIFIC COUNCIL  
SEVILLE UNIVERSITY**

**DOCTORAL THESIS**

**Physico-Chemical Research of  
Cultural Heritage Materials Using Microanalytical  
Methods**

**Liz Karen Herrera Quintero  
Seville, February de 2009**





**INSTITUTO DE CIENCIA  
DE MATERIALES DE SEVILLA**



**CONSEJO SUPERIOR DE INVESTIGACIONES  
CIENTÍFICAS  
UNIVERSIDAD DE SEVILLA**

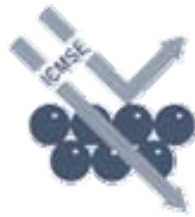
**TESIS DOCTORAL**

**Physico-Chemical Research of  
Cultural Heritage Materials Using Microanalytical  
Methods**

**Liz Karen Herrera Quintero**

**Sevilla, Febrero de 2009**





**Physico-Chemical Research of  
Cultural Heritage Materials Using Microanalytical Methods**

**Liz Karen Herrera Quintero**

**Memoria presentada para optar al grado de  
Doctor por la Universidad de Sevilla  
Sevilla, Febrero de 2009**

**Fdo. Liz Karen Herrera Quintero**

**Los directores de la Tesis Doctoral:**

**Fdo.Dr. Ángel Javier  
Justo Erbez**

**Fdo. Dr. Jose Luis  
Pérez Rodríguez**

**Tutor de la Tesis  
Fdo. Juan Poyato Ferrera**



## Publications

*The work presented in this thesis report has been resulted in the following publications:*

### Chapter I

**L.K. Herrera**, M. Cotte, M.C. Jimenez de Haro, A. Duran, A. Justo, J.L. Perez Rodriguez: Characterisation of iron oxide-based pigments by synchrotron-based micro X-ray diffraction. *Applied Clay Science* 42 (2008) 57-62.

**L.K. Herrera**, S. Montalbani, G. Chiavari, M. Cotte, A.V Solé, A. Duran, A. Justo, J.L. Perez-Rodriguez: Identification of pictorial materials from Bocanegra paintings. *Talanta* (2008) *submitted*.

**L.K. Herrera**, M. Cotte, S. Montalbani, G. Chiavari, A. Duran, A. Justo, J.L. Perez-Rodriguez: Characterisation of azurite and malachite pigments by combined application of  $\mu$ -X-ray diffraction/ $\mu$ -X-ray fluorescence in the cross sections from Spanish baroque paintings. *Applied Physics A* (2009) *submitted*.

### Chapter II

**L.K. Herrera**, A. Duran, M.L. Franquelo, A. Justo, J.L. Perez-Rodriguez: Amalgam degradation (Hg/Sn) of ancient glass mirrors. *Journal of Non-Crystalline Solids* (2009) *in press*.

**L.K. Herrera**, A. Duran, M.L. Franquelo, M.C. Jimenez de Haro, A. Justo, J.L. Perez-Rodriguez: Studies of tin-mercury alloy of ancient Spanish mirrors. *Journal of Cultural Heritage* 10 (2008) 1-5.

**L.K. Herrera**, A. Duran, M.L. Franquelo, A.R. González-Elipe, J.P. Espinós, J. Rubio-Zuazo, A. Justo, J.L. Perez-Rodriguez: Study by grazing incident diffraction and surface spectroscopy of amalgam from Cultural Heritage ancient mirrors in *European Journal of Chemistry* 7 (2009) 47-53

**L.K. Herrera**, A. Justo, J.L. Perez-Rodriguez: Study of nanocrystalline SnO<sub>2</sub> particles formed during the corrosion processes of ancient amalgam mirrors. *Journal of Nano research* (2009) *in press*.

### Chapter III

**L.K. Herrera**, A. Justo, J. A. Sans, G. Martínez-Criado, A. Muñoz-Paez: Chemical composition of the metal pipe of a Spanish baroque organ as determined by  $\mu$ XRF. *Trac Trend Anal Chem.* (2009) *submitted*.

### Chapter IV

**L.K. Herrera**, A. Duran, M.C. Jimenez de Haro, M.L. Franquelo, A. Justo, J.L. Perez Rodríguez: Identification of cellulose fibres belonging to Spanish Cultural Heritage using

synchrotron high resolution x-ray diffraction and complementary techniques. Applied Physics A (2009) *submitted*.

## Chapter V

A. Duran, **L.K. Herrera**, M.C. Jimenez de Haro, A. Justo, J.L. Perez-Rodriguez: Non-destructive analysis of Cultural Heritage artefacts from Andalusia, Spain, by X-ray diffraction with Göbel mirrors. *Talanta* 76 (2008) 183-188.

A. Duran, **L.K. Herrera**, M.C. Jimenez de Haro, J.L. Perez-Rodriguez, A. Justo: Degradation of metals used in the baroque period in Andalusia, Spain *Revista de Metalurgia* (2009) *in press*.

A. Duran, J.L. Perez-Rodriguez, **L.K. Herrera**, M.C. Jiménez de Haro, M.D. Robador, A. Justo: "Copper alloys deterioration due to anthropogenic action." *Revista de Metalurgia* 44 (2008) 85-91.

### *Other publications:*

**L.K. Herrera**, S. Le Borgne, H. A. Videla: Modern methods for materials characterisation and surface analysis to study the effects of biodeterioration and weathering on buildings of Cultural Heritage. *Journal on Architectural Heritage: Conservation, Analysis and Restoration* 3 (2009) 1-18.

**L.K. Herrera**, H. A. Videla: Surface analysis and materials characterisation for the study of biodeterioration and weathering effects on cultural property. *International biodeterioration and biodegradation*. (2009) *in press*.

A. Duran, J.L. Perez-Rodriguez, M.C. Jimenez de Haro, **L.K. Herrera**, A. Justo: Degradation of Metals Used in the Cultural Heritage Andalusia, Spain. *Journal of Cultural Heritage* 9 (2008) 184-188.

A. Duran, **L.K. Herrera**, M<sup>a</sup>.D. Robador, J.L. Pérez-Rodríguez "Color Study of Mudejar Paintings of the Pond at the Palace of "Reales. *Color Research and Application* 32 (2007) 489-495.

A. Justo-Esteban, **L. K. Herrera**, A. Durán, B. Sigüenza, M.C. Jiménez de Haro, O. Laguna, A. Justo: Análisis del proceso de restauración del órgano Cavaillé-Coll de la Iglesia de la Merced de Burgos. Ed. Junta de Castilla y León artes graficas San Miguel S.L. Spain. (2009) *in press*

J.L. Perez-Rodriguez, A. Justo, J. Poyato, A. Duran, M.C. Jiménez de Haro, B. Sigüenza, **L.K. Herrera**, M.L. Franquelo: Estudio de materiales y técnicas de realización, utilizadas en obras de arte y procesos de alteración in *La investigación sobre patrimonio cultural*. Ed Cesareo Sáiz Jimenez, Miguel Ángel Candelero. Red Temática del Consejo Superior de Investigaciones Científicas (2008) 15-34. ISBN 978-84-691-0049-3.

## Acknowledgements

At the outset, I wish to express my deepest thanks to my supervisors, Dr. Ángel Justo Erbéz and Dr. Jose Luis Pérez Rodríguez, for their advice and fruitful cooperation during the course of this work. Special thanks to Prof. Dr. Juan Poyato for his made usefully suggestions.

I am particularly grateful to Prof. Dra. Adela Muñoz Paéz for her wonderful scientific supports.

I am also thankful for the financial support of the European Commission, Marie Curie Action MEST-CT2004-513915.

I want to acknowledge the Material Science Institute of Seville – Spanish Scientific Council (ICMSE –US) of Seville for the facilities and instrumentation used in the majority of the experimental work carried out in this thesis report. Additionally, I wish to thank all of the members and colleagues of the Institute for their assistance and help, as well as for creating a friendly atmosphere for my work.

Financial support from the Spanish Government MAT2004-04498, MAT2005-04838 and MAT2007-63234 is gratefully acknowledged.

I would also like to thank the European Synchrotron Radiation Facility for the ID21, ID18F (a microfocusing beamline for x-ray fluorescence and micro-diffraction), BM25 (the Spanish CRG beamline for absorption and diffraction), and BM02 (the D2AM French CRG beamline), as well as for their assistance during the experiments.

I would like to thank “*Dirección general de Bienes Culturales*” from the Andalusia Government and Fine Arts Museum of Seville for supplying the samples studied in this work.

Thanks to Maria del Carmen Jimenez de Haro for her assistance with the electron microscope.

I want to express my deepest appreciation to Professor Héctor Videla for his continued support and advice through the years.

I would like to thank Professor Guisepe Chiavari and Simona Montalbani for their help in the analytical pyrolysis and GC/Mass Spectrometry completed during my research training at the Chemistry School of the University of Bologna.

I would like to thank Dr. Marine Cotte for her assistance and help during the discussion and analysis of the x-ray synchrotron radiation data collected from the ID18F beamline.

I would like to thank Dr. Eric Dooryhee for his assistance and support of the work carried out in the synchrotron beamline ESRF-CRG/BM02.

I would like to thank Dr. Cesareo Saiz Jimenez for the coordination of the project and advanced research training on the conservation of Cultural Heritage.

Finally, I am indebted to my parents, brother and beloved Xabier for their constant support, advice, and encouragement.



---

**Contents**

<b>Introduction</b> .....	<b>3</b>
<hr/>	
<b>CHAPTER I. STUDIES AND RESEARCH OF PAINTINGS</b>	<b>7</b>
<hr/>	
Introduction-----	9
I.1. Advanced Combined Application of $\mu$ -X-ray Diffraction/ $\mu$ -X-ray Fluorescence with Conventional Techniques for the Identification of Pictorial Materials from Baroque Andalusia Paintings .....	11
I.1.1. Research aims .....	11
I.1.2. Historical context .....	12
I.1.3. Experimental .....	12
I.1.3.1. Sampling-----	12
I.1.3.2 Analytical techniques: instruments and methods-----	14
I.1.4. Results and discussion .....	18
I.1.4.1. Textile identification .....	18
I.1.4.2. Identification of preparation layers .....	19
I.1.4.3. Identification of pictorial layers .....	23
I.1.4.4. Organic binding medium .....	30
I.1.5 Conclusions .....	31
I.1.6 References .....	32
I. 2. Characterisation of iron oxide-based pigments by micro X-Ray diffraction	35
I.2.1 Research aims .....	36
I.2.2. Experimental .....	36
I.2.2.1 Materials-----	36
I.2.2.2 Sample preparation-----	36
I.2.3. Analytical methods .....	37
I.2.3.1 Conventional laboratory techniques .....	37

I.2.3.2 Synchrotron-based micro X-ray diffraction and micro X-ray fluorescence techniques -----	37
I.2.4 .Results and discussion -----	37
I.2.5. Conclusions -----	43
I.2.6.References -----	44
I. 3. Synchrotron-based X-ray experiments used for the study of an iron oxide micrometric pigment in 18th century paintings -----	46
I.3.1. Research aims-----	46
I.3.2. Experimental -----	46
I.3.3. Results and discussion -----	47
I.3.4. Conclusions -----	50
I.3.5. References-----	50
I. 4. Characterisation of azurite and malachite pigments by combined application of $\mu$ -X-ray diffraction/ $\mu$ -X-ray fluorescence in cross sections from Spanish Baroque paintings -----	51
I.4.1. Research aims-----	53
I.4.2. Experimental -----	53
I.4.2.1. Sample preparation -----	55
I.4.3. Results and discussion -----	55
I.4.3.1. Analysis of the blue-green layer in the samples-----	55
I.4.3.2. Identification of organic components in the blue layers of the samples -----	61
I.4.3.3. $\mu$ XRF/ $\mu$ XRD analysis of a thin cross section -----	61
I.4.4. Conclusions -----	65
I.4.5. References-----	65
<b>CAPTER II. STUDIES ON ANCIENT MIRRORS</b> -----	<b>67</b>
II. Hg/Sn amalgam degradation of ancient glass mirrors -----	69
II.1. Research aims -----	70

II.2. Samples studied -----	70
II.3. Experimental method -----	71
II.4. Results -----	74
II.4.1. General Microanalysis of the glasses-----	74
II.4.2. Conventional studies of the amalgam surfaces-----	74
II.4.2.1. Sample 1 -----	75
II.4.2.2. Sample 2 -----	78
II.4.2.3. Sample 3 -----	79
II.4.2.4. Sample 4 -----	81
II.4.3. XPS studies of the amalgams surfaces -----	83
II.4.4. Spectroscopic studies of tin in the amalgams surfaces -----	85
II.5. Synchrotron experiments -----	87
II.5.1. Grazing incident diffraction using synchrotron radiation -----	87
II.5.2. Composition by semi-quantitative X-Ray diffraction -----	90
II.6. Discussion -----	92
II.7. Conclusions -----	94
II.8. References -----	97
II.1. Study of nanocrystalline SnO <sub>2</sub> particles formed during the corrosion processes of ancient amalgam mirrors -----	101
II.1.1. Research aims -----	102
II.1.2. Materials -----	102
II.1.3. Experimental method -----	102
II.1.4. Results and discussion -----	102
II.1.4.1. Corroded amalgams -----	102
II.1.4.2. Characterisation of tin dioxide nanoparticles -----	105
II.5. Conclusions -----	106
II.6. References -----	106

---

**CHAPTER III. STUDIES ON BAROQUE METALLIC ORGAN PIPES** **111**

---

III.1. Chemical composition of the metal pipes of Spanish baroque organs as determined by laboratory and synchrotron techniques -----	112
--	-----

III.1.2. Organ description-----	112
III. 1.3. Spanish baroque organ-----	113
III.1.4. Research aims -----	113
III.1.5. Materials -----	113
III.1.6. Experimental -----	114
III.1.6.1. Sample preparation -----	114
III.1.6.2. SEM/EDX investigation -----	115
III.1.6.3. XRD analysis -----	115
III.1.6.4. $\mu$ XRF measurements -----	115
III.1.6.4.1. $\mu$ XRF elemental mappings at high excitation energy -----	115
III.1.6.4.2. $\mu$ XRF elemental mappings at low excitation energy-----	116
III. I.7. Data treatments-----	117
III.1.8. Results and discussion-----	117
III.1.8.1. Characterisation and analysis of untreated samples using laboratory techniques -----	117
III.1.8.2. Characterisation and analysis of metallographic cross-sections using laboratory techniques-----	117
III.1.8.3. Synchrotron Radiation Studies -----	119
III.1.8.3.1. $\mu$ XRF elemental mapping at high excitation energy -----	121
III.1.8.3.2. $\mu$ XRF elemental mappings at low excitation energy-----	123
III.1.9. Conclusions -----	126
III.1.10. References -----	126
 III.2. Chemical composition of the red pipes of a Spanish baroque organ -----	 128
III.2.1. Research aims -----	129
III.2.2. Experimental -----	129
III.2.2.1. Analytical technique -----	129
III.2.2.2. Samples-----	129
III.2.3. Results and discussion -----	129
III.2.3.1. Microstructural Observations-----	129
III.2.4. References -----	134

---

**CAPITULO IV. STUDIES OF ANCIENT FIBRES** **135**


---

IV. Identification of cellulose fibres belonging to Spanish cultural heritage using synchrotron x-ray diffraction and laboratory techniques -----	137
IV.1. Research aim -----	137
IV.2. Structure of fibres -----	137
IV.2.1. Hierarchical description of natural fibres -----	138
IV.2.2. Flax description -----	139
IV.2.3. Cotton description-----	139
IV.2.4. Cellulose degradation-----	139
IV.2.5. Crystalline index -----	141
IV.3. Experimental -----	142
IV.3.1. Samples Selection-----	142
IV.3.2. Samples preparation -----	143
IV.3.3. Analytical techniques-----	144
IV.4. Results and discussions-----	145
IV.4.1. Optical and Scanning electron microscopes investigations -----	145
IV.4.2. FTIR Spectroscopy -----	148
IV.4.3. X-ray diffraction studies by synchrotron radiation -----	150
IV.5. Conclusions -----	153
IV.6. References -----	154

---

**CAPITULO V. STUDIES OF METALLIC ARTEFACTS** **159**


---

V. Analysis of cultural heritage metallic artefacts from Andalusia -----	161
V.1. Introduction -----	161
V.2. Graded Multilayer Optics -----	161
V.3. Research aims -----	162
V.4. Materials -----	162
V.4.1. Bronze samples -----	162
V.4.2. Iron samples -----	163

V.4.3. Lead samples -----	164
V.4.3.1. Lead seals -----	164
V.4.3.2. Lead-rich organ pipes -----	165
V.5. Results and discussion -----	165
V.6. Conclusions-----	178
V.7. References -----	179

---

<b>CAPITULO VI CONCLUSIONS</b>	<b>183</b>
--------------------------------	------------

---

VI Conclusions -----	185
----------------------	-----

---

<b>CAPITULO VII Resumen</b>	<b>191</b>
-----------------------------	------------

---

VI Resumen -----	193
------------------	-----

**List of abbreviations**

CI Crystalline Index

EDX Energy Dispersive X-ray Spectroscopy

ESRF European Synchrotron Radiation Facility

GID Grazing Incident Diffraction

FTIR Fourier Transform Infrared

OM Optical Microscope

PY-GC-MS Pyrolysis-Gas Chromatography-Mass Spectrometry

GC-MS Gas Chromatography-Mass Spectrometry

REELS Reflection Electron Energy-Loss Spectroscopy

SEM Scanning Electron Microscopy

SR Synchrotron Radiation

SR-XRD Synchrotron Radiation X-ray Diffraction

SR-XRF Synchrotron Radiation X-ray Fluorescence

XPS X-Ray Photoelectron Spectroscopy

XRD X-Ray Diffraction

XRF X-Ray Fluorescence

$\mu$ FTIR Micro Fourier Transform Infrared

$\mu$ Raman Micro Raman Spectroscopy

$\mu$ XRD Micro X-Ray Diffraction

$\mu$ XRF Micro X-Ray Fluorescence

The term “Cultural Heritage Materials” includes canvas paintings, mural paintings, metals, ceramics, woods, fibres, rocks, mortars, and others. All are affected by weathering, air pollution and human activities, leading in some cases to the total destruction of the cultural assets.

Over the past decade, intensive and multi-disciplinary research has been carried out in the interface between art, archaeology and solid state science. Early work used routine analytical techniques. However, new procedures and instruments are now being developed and adapted to analyse ancient materials. The increasing development of technologies based on X-ray microbeam experiments has been crucial for successful analysis at the submicron and nano levels.

The Cultural Heritage Group at the Materials Science Institute of Seville has strong expertise in the advancement of conservation science and the characterisation of materials and alteration processes. In particular, a strong effort has been made in the last few years to develop innovative methodologies and techniques. These advancements have contributed to the knowledge of cultural heritage and conservation science.

The field of Cultural Heritage has been actively cultivated by several research groups in different parts of the world. However, in Spain (particularly in Andalusia), less attention has been paid to this area of research. Recently, the Andalusian Government has become involved; they recently promoted the program “Andalusian Baroque period of Art” in an effort to promote new advances in this area. The Fine Arts Museum of Seville, the Fine Arts Schools of the University of Seville and the University of Malaga are also involved in the promotion knowledge of Andalusian Cultural Heritage.

The research work included in this thesis is focused on the characterisation of five different materials: paintings, baroque mirrors, natural fibres, organ pipes and several metallic artefacts, which are representative of Spanish Cultural Heritage. All of these ornamental elements are characteristic of the Andalusian Baroque period of art.

One of the main contributions of this work is the application of synchrotron radiation-based techniques at the European Synchrotron Radiation Facility (ESRF) within the Cultural Heritage Group. These synchrotron x-ray techniques were carried out in combination with other analytical laboratory techniques such as x-ray diffraction, micro-infrared, micro-Raman spectroscopy, optical and electron microscopy, and mass spectrometry.

Synchrotron radiation was very powerful and useful in the detection, analysis and distribution of different elements and crystal phases. These findings are critical to the different aspects of the artwork.

The main points developed in this work can be highlighted as follows:

- i)* To provide chemical descriptions of the organic and inorganic components of the different materials present in multi-layered paintings.
- ii)* To characterise different pigments coexisting in the same layers of paintings using  $\mu$ XRF/ $\mu$ XRD on thin cross sections.
- iii)* To demonstrate that synchrotron radiation micro-imaging techniques have the ability to analyse pictorial layers. This analysis includes grains at the micrometer scale, which are difficult to analyse with other laboratory techniques.
- iv)* To contribute to a better understanding of the degradation of amalgam mirrors present in historical buildings. Specific emphasis was placed on the study of corrosion products and the alloying element. Knowledge of these mechanisms will help to preserve these art objects.
- v)* The combined use of GID and XPS provided insight into surface chemical structures and the degradation of different amalgam mirrors. They served as useful non-destructive research tools for the study of cultural heritage artefacts.
- vi)* The SRXRD experimental setup used on the amalgam surfaces offers a unique opportunity to obtain a depth profile analysis of samples under identical conditions. This analysis allows for correlation of information between the surface and bulk properties of the mirrors.
- vii)* To prove that the surface layers of amalgam mirrors were mainly composed of nanometre-sized particles of cassiterite.
- viii)* To find the distribution and correlation of trace elements present in the tin and lead phases of the Spanish pipe baroque organ.
- ix)* To obtain a correlation between the XRD patterns of the old and new tongues of the Spanish reed pipes of the baroque organs. The advantage of synchrotron-based  $\mu$ XRF is that it allows for determination of the elemental and chemical distributions of the main phases and trace elements.
- x)* To identify the morphologies and structures of the textile fibres found in important Spanish artwork and to identify any possible degradation of these fibres.

This thesis is organised into five different chapters. Each chapter focuses on a different material.

Chapter 1 illustrates the chemical description of the organic and inorganic components of baroque paintings from Andalusia. In particular, it describes the stratigraphy sequence used in parallel with the information supplied by laboratory techniques. It also describes recent applications of microanalytical synchrotron radiation using the ID18F beam line at the European Synchrotron Radiation Facility (ESRF). This is exemplified by the identification of pigments and binders in canvases painted by Bocanegra at the beginning of the XVIth century. Another interesting example of the synchrotron technique is the characterisation of iron pigments in wall paintings of the San Agustin Church of Monastery in Cordoba, Spain. This study revealed the presence of monazite (a reddish-brown cerium) and lanthanum phosphate  $[(\text{Ce},\text{La})\text{PO}_4]$  in the iron oxide pigments. Finally, the presence of azurite and malachite pigments in important Andalusia baroque paintings was investigated.

Chapter 2 presents an analytical approach. It combines scanning electron microscopy (SEM), x-ray analysis (EDX), Raman spectroscopy, Fourier Transform Infrared Spectroscopy (FTIR), Grazing Incidence Diffraction (GID), surface-spectroscopic methods (XPS and REELS), Transmission Electron Microscopy (TEM), and synchrotron radiation-based x-ray diffraction (SR-XRD) to characterise amalgam surfaces with different degrees of alteration. The surfaces were historical mirrors in Andalusia dated between the XVII and XVIII centuries.

Chapter 3 describes the distributions and correlations of trace elements present in the tin and lead phases of a Spanish pipe baroque organ. The compositions and microstructures of historic and modern tongues of reed pipes from baroque organs were studied using a combination of laboratory techniques. These techniques included new microanalytical methods at the ID 18F and ID21 beam lines at the ESRF. These methods allowed for elemental and chemical imaging of the main phases and the trace elements at a sub-micrometer scale.

Chapter 4 focused on cellulose-based plant fibres. In the field of cultural heritage, historical textiles require the best preservation possible to ensure longevity. Cellulose fibres are present in important historical artefacts, including canvas, documents, and filling materials. In this chapter, several cellulose fibres were investigated by synchrotron radiation x-ray diffraction (SR-XRD). The information obtained by SR-XRD was

confirmed by other laboratory techniques, including scanning electron microscopy (SEM) and Fourier transform infrared spectroscopy (FTIR).

Chapter 5 focused on the non-destructive analytical method of x-ray diffraction with Göbel mirrors. This chapter included a study of the superficial alteration of some metallic artefacts (bent and flat) from important artworks. In most cases, these artefacts cannot be studied by the conventional method of powder diffraction. Göbel mirrors and low fixed incidence angles were used to study superficial and underlying layers of metallic samples.

## Introduction

Analytical methods and techniques are an essential requirement in the cultural heritage field, as they provide the means to understand the objects under investigation. By identifying materials (such as pigments, binders, mixtures, and processes), we can reach back through time and develop a deeper understanding of the craftsmanship and technology used. Analytical methods allow us to contribute to the blooming activity at the interface between art and science. Contributing to the development of diagnostic techniques is necessary for practical applied art conservation.

The techniques concerned include: Scanning electron microscopy (SEM), X-ray energy dispersive spectrometry (EDX), micro X-ray analyses (including synchrotron radiation  $\mu$ -X-ray diffraction ( $\mu$ XRD) and  $\mu$ -X-ray fluorescence ( $\mu$ XRF), Fourier transform infrared spectroscopy (FTIR), and analytical pyrolysis in-line with GC and mass spectrometry (PY-GC/MS), [1–3].

Synchrotron radiation has become an increasingly important tool for research in the fields of art, archaeometry, and the conservation of objects of cultural heritage significance. Synchrotron is a source of intense, bright light of variable wavelength; the principal properties of synchrotron radiation are as follows: high flux and brilliance, ability to produce a fast data collection and the possibility to use small sample size, small beam footprint: it enables area mapping at millimetre to micron length-scale. The wavelength tunability and the energy region can be selected to suit the problem at hand [4-7]. Synchrotron techniques are particularly suited to non destructive or to the micro characterisation of different materials including organic and inorganic materials, either amorphous or crystalline. New developments in synchrotron radiation techniques result in a significant advance to study the samples at micrometer length scale through the combination of different non-destructive techniques. The most employed till now have been synchrotron X-ray fluorescence and diffraction and, to a lesser extent, small angle scattering (on wood, bone and hair) and infrared microscopy. The synchrotron beam can be focused in sub micrometric spots, allowing the examination of very small samples. The list of artwork studied by using SR is made up of a large variety of materials [4].

The analytical methods used in this field of research are identical to those used at the cutting edge of modern materials science. Methods developed for advanced physics and chemistry can be applied to ancient and modern materials, as the problems

encountered in the areas of advanced technology and cultural heritage are surprisingly similar. Depending on the information required, one might use a combination of non-invasive techniques; however, one should aim at the maximization of information and the minimization of the consumed volume [8, 9]. The use of non-invasive techniques is increasing due to the improved development of instruments (e.g. able to determine the elemental and mineral composition of the micrometric multilayers of micro-samples) [10]. Analytical studies of paintings performed on the microscopic and molecular level are the focus of this chapter. Microscopic and molecular studies are carried out on paint samples derived from the painting itself. These samples are unique and in limited supply. Assuming that such samples are representative of an area under study, valuable general information about the painting can be deduced. The information can be maximized by sequential analyses using different complimentary techniques.

This chapter illustrates the chemical description of the different work of art, using, the information supplied by laboratory techniques and recent applications of microanalytical methods using synchrotron radiation at the ID18F beam line at the European Synchrotron Radiation Facility (ESRF).

## **I.1. Advanced combined application of $\mu$ -X-ray diffraction / $\mu$ -X-ray fluorescence with conventional techniques for the identification of pictorial materials from Baroque Andalusia paintings**

### **Introduction**

There have been major advances in pictorial techniques in the course of the history, in terms of both the materials used and the superimposition of layers to produce a polychromic image. The in-depth study of these two aspects can produce particularly useful information for the characterisation and dating of work of arts, as well as information of the state of preservation of a work.

The process of investigating paintings includes the identification of materials to solve technical and historical art questions, and to aid in the deduction of the original appearance and in the establishment of the chemical and physical conditions for adequate restoration and conservation. In particular, we have focused on the identification of several samples taken from six famous canvases painted by Pedro Atanasio Bocanegra, who created a very special collection depicting the life of San Ignacio, which is located in the church of *San Justo y Pastor* of Granada, Spain.

The characterisation of the inorganic and organic compounds of the textiles, preparation layers, and pictorial layers have been carried out using an XRD diffractometer, SEM observations, EDX spectrometry, FTIR spectroscopy (both in reflection and transmission mode), pyrolysis/gas chromatography/mass-spectrometry and synchrotron-based micro X-ray techniques. In this work, the advantages over conventional X-ray diffraction of using combined Synchrotron-based  $\mu$ X-ray diffraction and  $\mu$  X-ray fluorescence in the identification of multi-layer paintings is demonstrated.

#### **I.1. 1. Research aims**

The main objective of this work is:

- i) Carried out the completely identification of inorganic pigments, binding medium and support in six famous canvases painted by Bocanegra using laboratory techniques.
- ii) Apply the synchrotron micro-imaging techniques in micrometer multilayer paintings for reveal the atomic, molecular and structural composition of the paintings.

### **I.1.2. Historical context**

The first reports of Pedro Atanasio Bocanegra as a painter are from 1661 [11]. He included in his paintings many elements of his master, Alonso Cano. The archbishops of Granada nominated him to be the painter of the cathedral church in 1674. Later, Bocanegra worked in Seville and Madrid, being nominated the court painter in 1676. The most important work realized in Granada was in the Jesuitical convent. The name of the church convent was San Pablo, which was changed to San Justo y Pastor after the Jesuitical expulsion. The building that occupied the convent is actually located in the square of the University in Granada.

According to Gomez Moreno [11], the Bocanegra paintings of the *San Justo y Pastor* of the church that represents the passages of the *S. Ignacio of Loyola life* (1491-1540) were carried out in two steps. In the first, Bocanegra painted three canvases: “*San Ignacio herido a las puertas de Pamplona*”, “*La Aparición de San Pedro*” and “*San Ignacio azotado por un armenio*”. In the second step, he created the other three paintings between 1670 and 1671, where these are considered the most important works of oriental Andalusia painting [12]. These canvas paintings are “*La Visión de la Storta*”, “*La Aparición de la Trinidad a San Ignacio*” and “*S. Ignacio enviando a predicar a S. Fco. Javier and S. Fco. de Borja*”. In these paintings, the author shows technical advances and a greater intensity of color that is reminiscent of the art of Valdes Leal [13]. The painting details are described in Fig. 1.

### **I.1.3. Experimental**

#### **I.1.3.1. Sampling**

The samples were collected by taking small samples close to areas that were already damaged. Twenty samples extracted from different representative zones of the paintings were analyzed.

In Conventional cross-section, the samples were prepared as cylinder moulds and were embedded in epoxy resin as follows: The paint piece was placed on top of the hardened block and carefully covered with resin, and then cast and left to cure for 24h at room temperature. Next, the sample was cut to expose a face showing the cross-section of the paint layer. Finally, the surface was carefully polished on a rotating disc covered with abrasive SiC paper which spanned a grain size from 800 to 1200 mesh, and then finished

with a cloth [14, 15]. This method is useful for observation with an optical microscope, SEM/EDX, or FTIR spectrometer that requires a more careful preparation in terms of surface polish.



Fig.1. Bocanegra paintings. (a) "San Ignacio herido en las puertas de Pamplona" (b) "Aparición de San Pedro a San Ignacio para curarle" (c) "San Ignacio azotado por un armenio a su vuelta del Monte de los Olivos, consolado por Cristo" (d) "San Ignacio envía a predicar a San Francisco Javier a las Indias y a San Francisco de Borja a Occidente" (e) "Visión de La Storta, camino de Roma, en que se aparece la Trinidad a San Ignacio" (f) "Aparición de la Trinidad a San Ignacio."

Microtomy is a technique for cutting cross-sections of material, which was originally used by biologists for soft tissue specimen preparation [16]. It has been used to cut harder materials [17] and adapted for cross-sections of hard ceramic, semiconductor, and metal coatings, as well as composites and multilayers. The microtome cutting method (Fig.2a) can be used to prepare TEM samples of biological tissue, polymer, and crystalline materials. Using this particular method, a sample can be made in the form of

uniform thin films without affecting the chemical composition or structure. In this process a diamond knife is used to slice uniformly thin sections of material for cross-sectional.

Samples were embedded in a resin (Leica HistoResin) to prepare thin sections and then were cut into slides. Several thicknesses were tested using a Leica EM UC6rt microtome (Fig.2b), and 20-30 $\mu\text{m}$  was chosen as the most appropriate thickness [18] for SR  $\mu\text{XRF}/\mu\text{XRD}$  analyses.

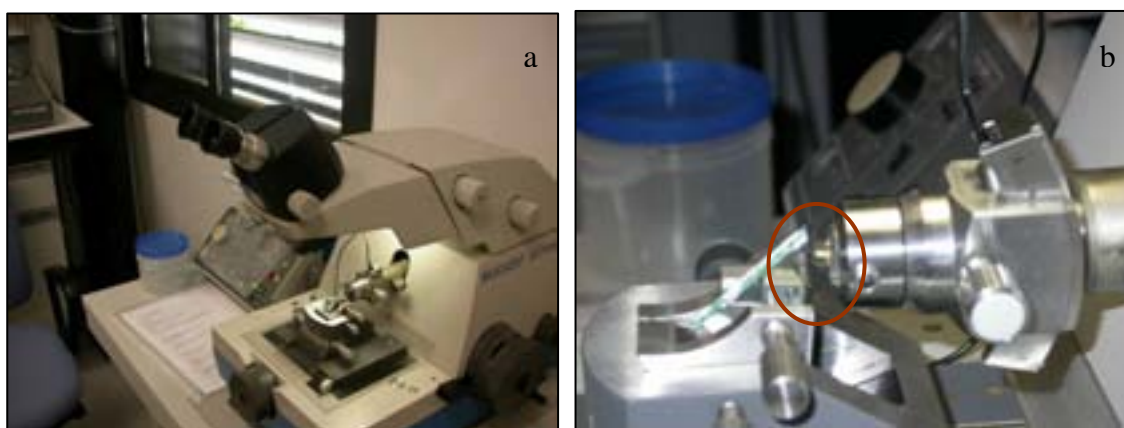


Fig. 2. a) Microtome for cutting the cross-sections of paintings. (Leica EM UC6rt microtome), b) Samples were embedded in a resin and then cut into slides.

*Raw fragments of the samples.* Small fragments of the samples were ground to a powder for examination by conventional XRD and for PY-GC/MS [14, 19].

*Single fibres* (a few micrometers in diameter) were carefully extracted from the canvas for textile identification by XRD.

### **I.1.3.2. Analytical techniques: instruments and methods**

Observations of the cross-sections were performed by Optical microscopy using a stereo microscope (Nikon HOPITHOT) with objectives of x20, x50, x100, x200 and equipped for microphotography using a digital camera (Nikon COOLPIX 4500), which was also used to identify the stratigraphy sequence of the different paint cross-sections.

The inorganic pigments have been characterized as cross-sections on a Jeol model JSM 5400 SEM. Semiquantitative analyses of elemental compositions of the different painting layers were obtained using EDX on a Link ISIS X-ray energy dispersive spectrometer equipped with an ultra-thin beryllium window, using an accelerating voltage of 20 keV. The cross-sections were coated with gold film before the SEM/EDX

investigations. X-rays analyzed with an energy dispersive detector (EDX) result in a semi-quantitative spectrum of the elements in the paint cross-section. Not all elements can be detected with EDX, because the detection threshold is relatively high and the X-ray energies of several elements overlap. In general, light elements in low concentrations are hard to detect with EDX. EDX is not a suitable technique for the detection of trace elements in pigments because their concentration is often below the detection limit (the detection limit is approximately 0.1 wt% for pure materials) [20].

The crystalline phases were characterized by X-ray diffraction (XRD), using a Siemens diffractometer, model Kristalloflex D-5000 using  $\text{CuK}\alpha_1$  radiation (40kV, 30mA), a diffracted-beam graphite monochromator and a scintillation counter. Measurements were carried out on powders of the sample in the range of  $3 < 2\theta < 65^\circ$  with steps of  $0.05^\circ$  and a 2 second counting time. Subsequently, the EVA data bank of standard X-ray powder diffraction patterns was used for phase identification. For textile identification by XRD, the fibers were introduced into a 0.3 mm glass capillary and these were then used to collect X-ray diffraction patterns in transmission mode on a Siemens D5000 dual diffractometer, equipped with a Ge monochromator in the incident beam and  $\text{CuK}\alpha_1$  radiation.

Fourier-transformed infrared spectroscopy FTIR is relevant for the identification of organic and inorganic compounds, but the surface of the cross-section must be totally planar in order to obtain good reflections [21]. Unfortunately, when organic compounds are mixed with large amounts of inorganic matter, such as in an argillaceous earth layer or lead white, the peaks representative of the inorganic components predominate in the FTIR spectrum. The organic constituents are often not visualized with FTIR, as their reflectance and relative concentrations are low [18], and the signal is reduced in a heterogeneous layer due to scattering of the infrared light within the cross-section. The Kramer-Krönig transformation is applied to the specular reflectance spectrum to transform it into an absorbance-like spectrum, which is more workable and easier to interpret. The FTIR spectra were registered on a Nicolet 510 spectrometer equipped with a nitrogen-cooled MCT detector and an Olympus optical microscope. The spectra were collected in reflectance mode, in the  $4000\text{-}700\text{ cm}^{-1}$  range, with a resolution of  $4\text{ cm}^{-1}$ . The final format of the data was in absorbance, where the background was collected through a gold film substrate. For each spectrum, at least 100 scans were accumulated. Peak positions were determined using the Nicolet Omnic software (based on a polynomial least squares

method). The advantage of infrared spectroscopy is to simultaneously obtain information on both organic and mineral compounds of the painting layers.

$\mu$ -X-ray diffraction and  $\mu$ -X-ray fluorescence were performed at the ID18F beamline, at the ESRF. This beamline is a high-energy multi-technique X-ray microscope. The double-crystal monochromator, equipped with both Si [111] and Si [311] crystals, offers a wide energy range (6-70 keV) for optimal excitation conditions of a broad range of elements [22] (Fig.3a). In this experiment, the excitation energy was fixed at 28 keV, corresponding to a wavelength of 0.44281 Å. The acquisition time was 20 seconds per pattern and the beam was focussed down to 15  $\mu$ m horizontal  $\times$  1  $\mu$ m vertical. A 2-dimensional CCD based X-Ray detector (refined detector distance 134.1967mm) was used to collect X-ray diffraction patterns in transmission mode. The X-ray fluorescence spectra were simultaneously detected with a Si(Li) detector. For these measurements, thin transversal cuts were mounted vertically, between two foils of Ultralen, and the whole set was raster-scanned horizontally and vertically to obtain two-dimensional images (Fig.3b). Thin transversal cuts were oriented horizontally such that the best resolution of the beam (1 $\mu$ m, vertical) was aligned with the axis of maximum sample heterogeneity, whereas the average in the horizontal direction (15 $\mu$ m) was obtained over the rather homogeneous colored layer. Three vertical line scans were acquired in each painting cross-section. X-ray fluorescence spectra were treated with PyMCA (Python multichannel analyzer) software [23] and used to identify the elemental composition of the different layers of the samples. In this program, a Levenberg-Marquardt algorithm is implemented to fit the spectra with constraints on the fitting parameters. A complete emission line series is fitted by taking into account theoretical line emission energies and theoretical energy ratios corrected by the experimental conditions (detector characteristics, detection geometry, matrix composition, excitation energy, etc.). A more detailed description of this code is given in [23]. The fitting configuration used to fit the average spectrum of a map is applied to each pixel of the 2D map to calculate the different elemental maps through a batch treatment. For each 2D X-ray diffraction pattern, the Debye-Scherrer diffraction rings were unwrapped and integrated versus the azimuthal angle to produce a 1D diffraction pattern using the ESRF package Fit2D [24]. The set of data thus generated has a format similar to fluorescence data, with a 1D diffraction pattern for each pixel.

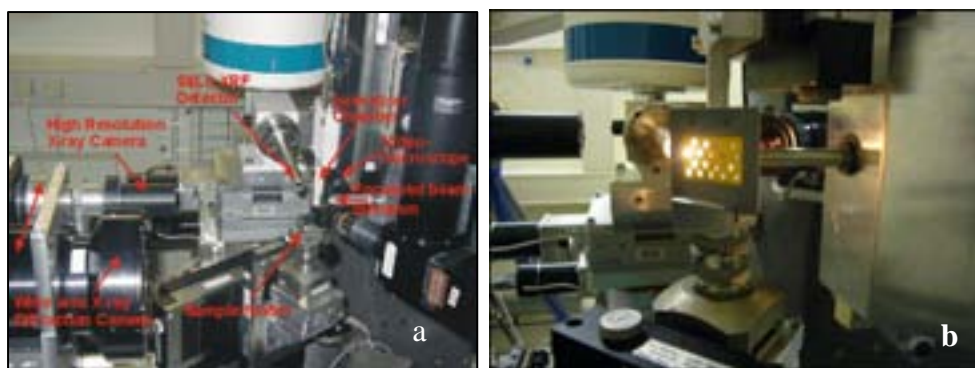


Fig. 3. a) ID18F microprobe setup at the ESRF, b) Detail of the measurements, thin transversal cuts were mounted vertically, between two foils of Ultralen.

Analytical pyrolysis was performed in the Dipartimento di Chimica G. Ciamician, Università di Bologna. Analytical pyrolysis, in-line with GC and Mass Spectrometry (PY-GC/MS) (Fig.4) was used to generate a qualitative characterisation of the organic components in a complex mixture such as the painting layers [25].



Fig. 4 Analytical pyrolysis, in-line with GC and Mass Spectrometry.

PY-GC/MS was carried out at 600°C for 10 seconds at the maximum heating rate using a CDS pyroprobe-heated filament pyrolyzer (CDS, Oxford, USA) directly connected to the injection port of a Varian 3400 gas chromatograph coupled to a Saturn II ion-trap mass spectrometer (Varian Analytical Instruments, Walnut Creek, USA) . A Supelco SPB% capillary column (30m, 0,32 mm I.D., 0,25  $\mu$ m film thickness) was used with a temperature programmed from 50° (held for 10 minutes) to 300°C at 5°C per min step intervals, with helium as the carrier gas. The temperature of the split/splitless injector and the PY-GC/MS interface were kept at 250°C. Mass spectra were recorded at 1 scan per min under electron impact at 70 eV in the mass range of 45 to 650 m/z (Fig. 5).

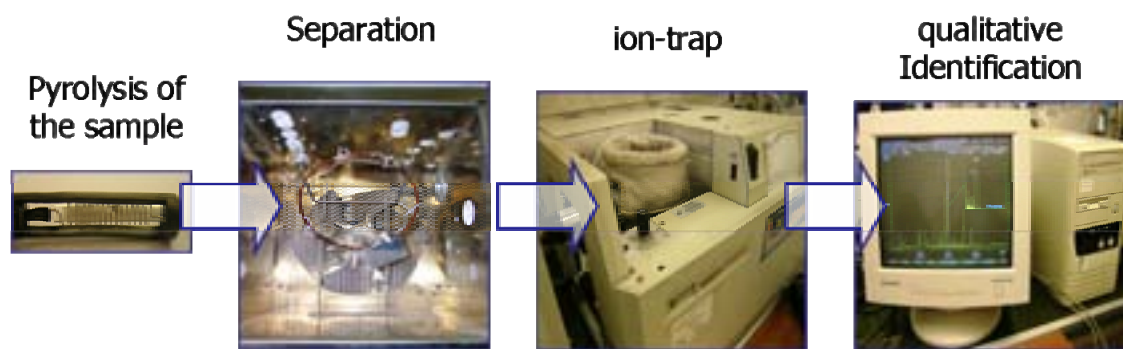


Fig. 5 set up of the Analytical Pyrolysis at the Bologna University Chemical Department.

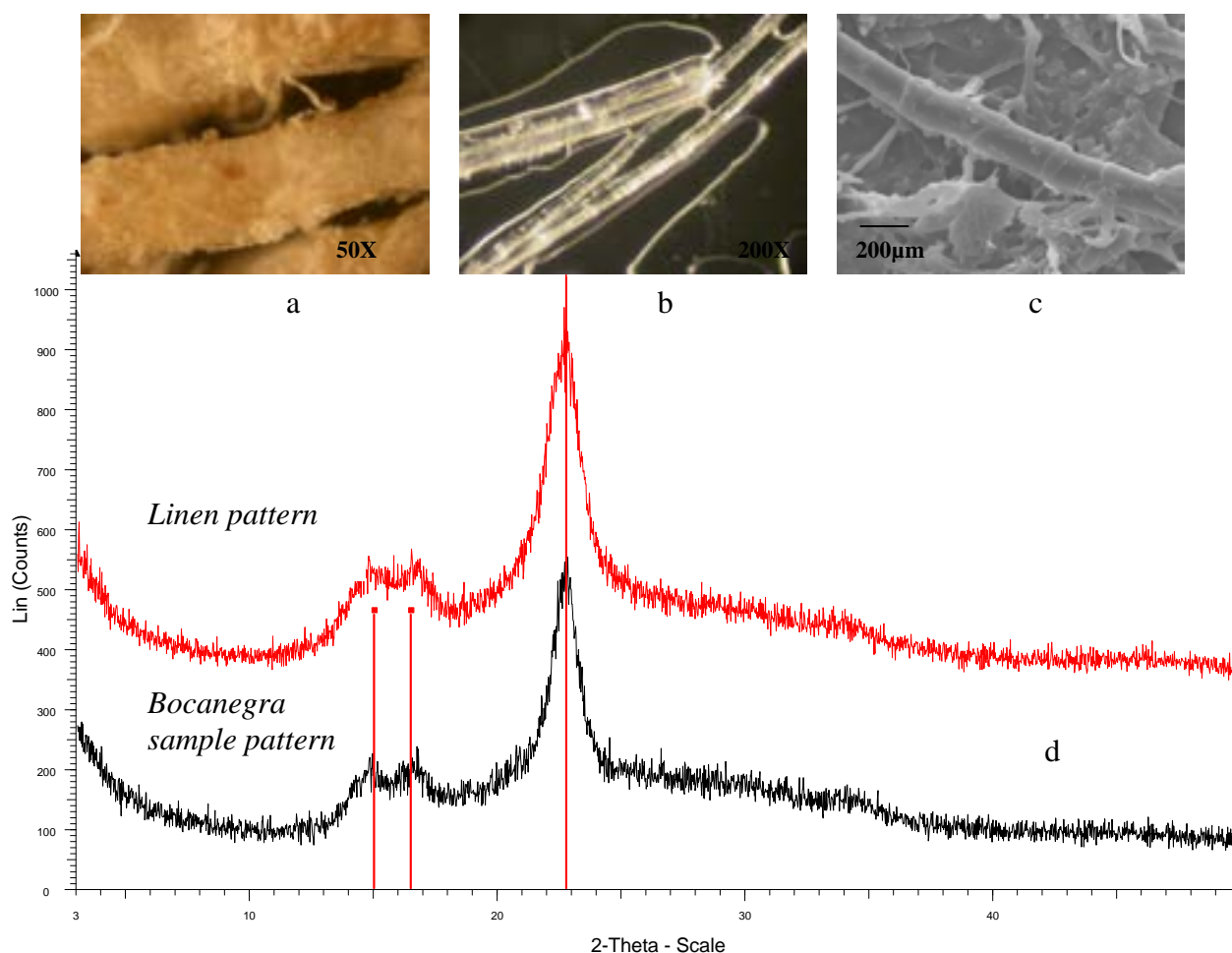
Structural assignment of the pyrolytical fragments was based on matching with the NIST mass spectra library. To improve the gas chromatographic behaviour of polar pyrolytic fragments, such as carboxylic or dicarboxylic acids, 10 microliters of tetramethylammonium hydroxide solution (TMAH 25% w/w in water) was added to the solid sample (few micrograms) before the pyrolysis. The study of the program, a gas chromatogram of the fragments of the volatile compounds of the sample, gives an indication about the organic chemical nature of the paint layer samples.

#### I.1.4. Results and discussion

##### I.1.4.1. Textile identification

The morphological studies of fibres were realized using optical and scanning electron microscopy. SEM images of single fibres from textile fragments are shown in Fig. 6a and 2b. The fibre has a diameter of 16.8-16.9  $\mu\text{m}$ , which, together with its morphology, is a very typical for linen (Fig. 6c) [26]. The XRD diffractograms of the fibre obtained from the painting and linen fibre used as a standard are included in Fig. 6d. The XRD pattern of the fibre sample recorded for  $2\theta$  in the range of 3-50° revealed pronounced Bragg peaks at  $2\theta$  values of around 15.2-16.6° and 22.8°, indicating the presence of a cellulose crystalline phase.

The linen used in these canvases contains a greater proportion of lignified material that has survived the retting process. This factor imparts strength and colour, but makes the linen more prone to deterioration. Factors that contribute to the deterioration of canvas can be summarized as follows: light, external pollution, and, to a lesser extent, the volatile acids trapped within a frame enclosure.



g. 6 Optical micrographs (a) without any clearing treatment and (b) after the organic compounds were removed by water with continuous heating for 24h (c) SEM image of the fibres of Bocanegra paintings (d) X-ray diffractogram of the fibres. Linen pattern and Bocanegra fibre pattern are shown.

These results show that Bocanegra used a traditional canvas support that normally consisted of stretched linen fabric, onto which was brushed an aqueous glue, which will be discussed later. Studies of paper and linen show that the oxidation products of cellulose are carboxylic acids, which can catalyse and promote the hydrolysis of cellulose [27]. However, the fibres studied in this work have not suffered from high alteration as indicated by the presence of crystalline phases of cellulose in the XRD patterns.

#### I.1.4.2. Identification of Preparation layers

The preparation layer of all twenty samples is composed of gypsum, argillaceous earth, iron oxides and animal glue mixed in different proportions. Gypsum was confirmed by FTIR spectroscopy (Fig.7) showing, respectively, the stretching and bending

absorptions of  $\text{SO}_4^{2-}$  groups at  $1146\text{-}1116\text{ cm}^{-1}$ , the water of hydration ( $\nu$  O-H at  $3403$  and  $3547\text{ cm}^{-1}$ , and the  $\delta$  O-H at  $1684$  and  $1622\text{ cm}^{-1}$ ), and animal glue was suspected by the protein bands ( $3239\text{ cm}^{-1}$ -stretching  $\nu$  N-H,  $1652\text{ cm}^{-1}$ -stretching  $\nu$  C=O amide I and  $1547\text{ cm}^{-1}$  bending  $\delta$  N-H amide II).

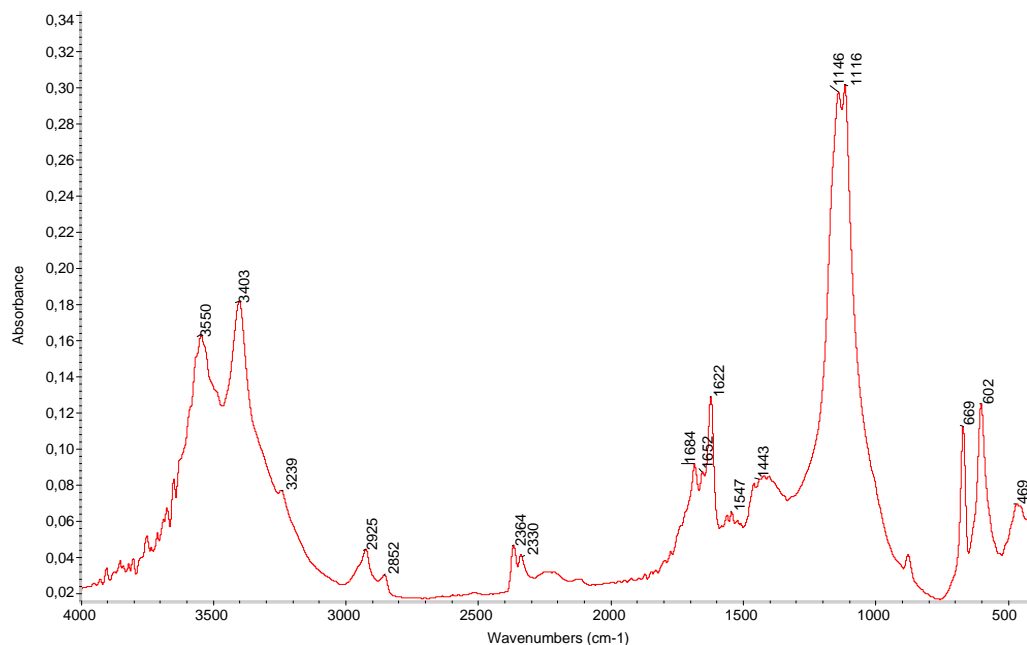


Fig. 7. FTIR spectra corresponding to the preparation layer of the Bocanegra painting sample.

Moreover, in Table 1, EDX analyses confirm the presence of C, O, Mg, Al, S, Si, K, Ca, and Fe. However, this technique is not sufficient to characterize the different phases.

Table 1. Analyses of the preparation layer of the six samples of the six paintings.

Painting	Sample	EDX	Phase identification (XRD)	Phase identification (SR $\mu$ XRD)
1	3	C, O, Mg, Al, S, Si, K, Ca, Fe	Gypsum	Calcite Quartz Goethite Gypsum anhydrite
2	6	C, O, Mg, Al, Si, S, K, Ca, Fe		
3	8	C, O, Mg, Al, Si, S, K, Ca, Fe		
4	1	C, O, Mg, Al, Si, S, K, Ca, Fe		
5	11	C, O, Mg, Al, Si, S, K, Ca, Fe		
6	4	C, O, Mg, Al, Si, S, K, Ca, Fe		

The separation of different layers is very complicated. For this reason, the samples (including all the layers) were ground for XRD characterisation. The XRD study is carried out in powder form using the conventional Bragg-Brentano method with a parafocusing geometry ( $\theta$  -  $2\theta$  coupled) that requires a very small quantity of sample. The

XRD pattern of the preparation layer (Fig. 8) confirmed the presence of calcium sulphate in two phases (mainly gypsum ( $\text{CaSO}_4 \cdot 2\text{H}_2\text{O}$ ) and anhydrite ( $\text{CaSO}_4$ )).

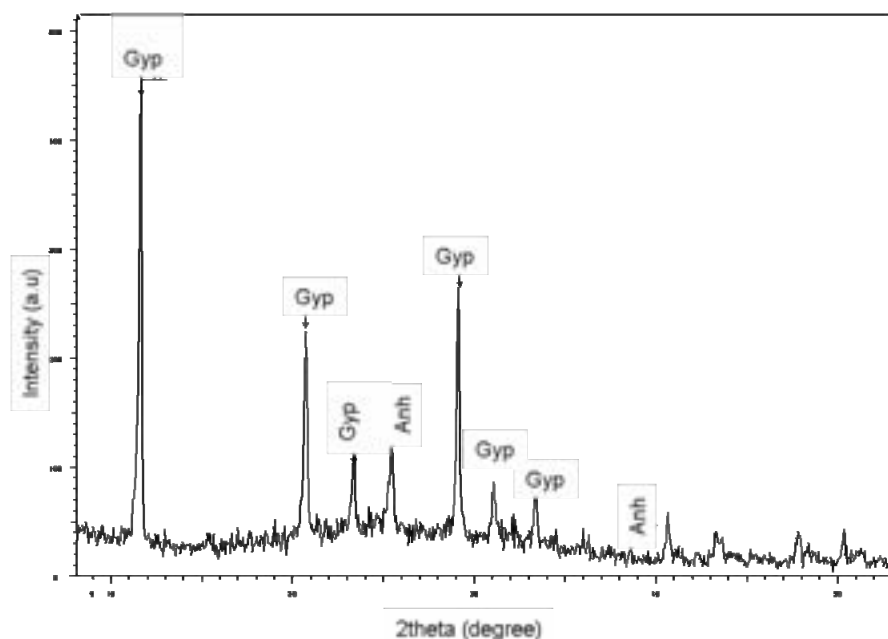


Fig. 8 The XRD pattern of the powder total sample whose peaks can be attributed the presence of gypsum (Gyp), calcite (Cal) and anhydrite (Anh).

The XRD and FTIR techniques confirm that the preparation layers were carried out with some pieces of textile mixture with animal glue associated to the support followed by the preparation of a lean character (animal glue and gypsum) layer. In some of the preparation layers, Bocanegra employs calcite and animal glue. In addition, a superficial colored layer in which iron compounds contribute to the yellow to ochre-reddish tone variation is present. However, in these samples, the iron compounds were only detected by EDX analyses and not by conventional XRD because this instrument may not be sensitive enough to detect minor phases of the cross-section. The iron phases are present in a low proportion in the preparation layer. In addition, the powder reflections are very small in comparison with the other minerals present in the mixture.

These facts are responsible for the difficult characterisation of the iron compounds by conventional X-ray diffraction. Experiments on thin cross-sections with combined SR  $\mu$ -XRF/ $\mu$ -XRD were performed. Fluorescence and diffraction data sets were simultaneously handled with PyMCA. This set-up shows high potential by concomitantly analysing element distribution ( $\mu$ -XRF) and structure information ( $\mu$ -XRD) in the cross-sections.

The elemental mapping distribution of iron in the preparation layer is shown in Fig. 9. Over the the same region, the diffraction pattern is calculated (Fig. 10) and shows the goethite phase mixture with calcite and quartz in the preparation layer. These results confirm that Bocanegra used goethite in the mixture of support preparation like other famous baroque painters such as Zurbaran and Murillo [28], and indicates that Bocanegra used a dark background due to the influence of the Tenebrism style.

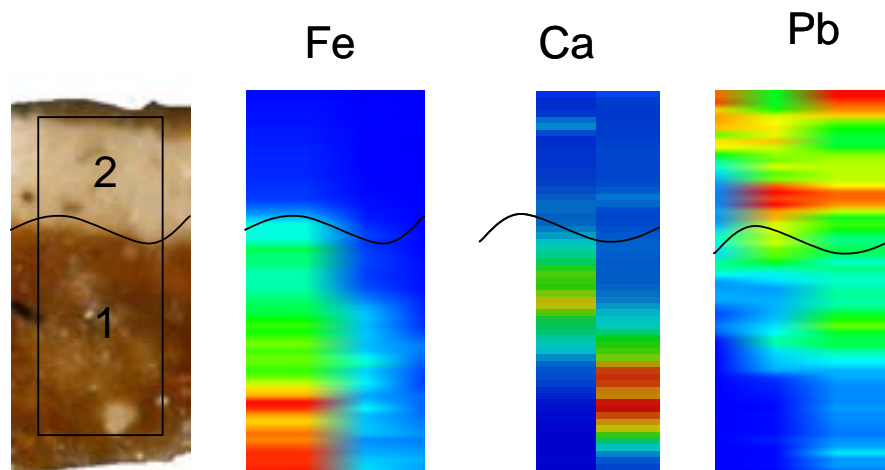


Fig. 9  $\mu$ XRF elemental mapping of the first layer: calcium and iron; elemental mapping of second layer: lead

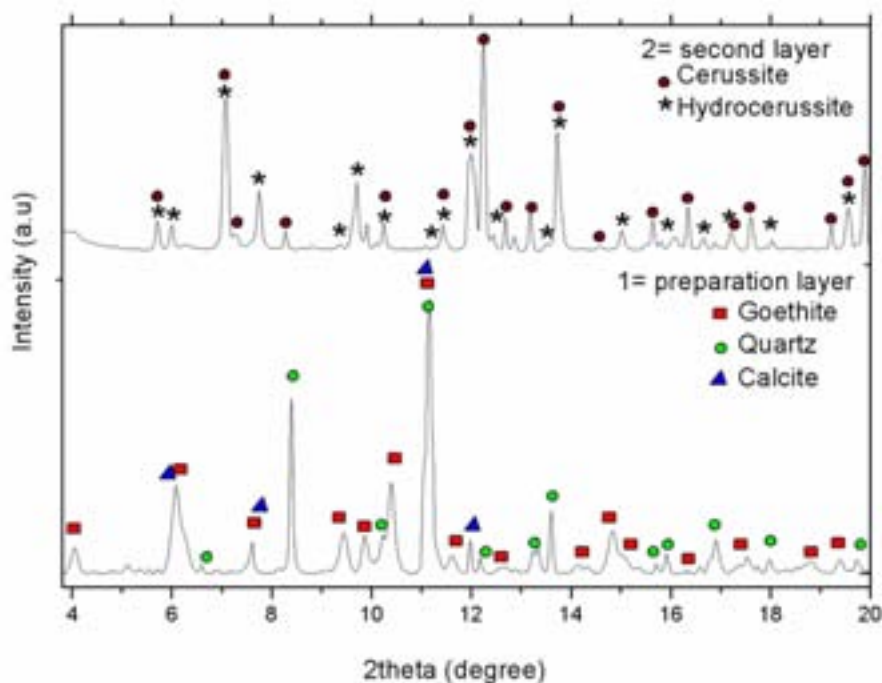


Fig. 10 SR  $\mu$ XRD of the first layer: goethite, calcite and quartz. SR  $\mu$ XRD of the second layer: cerussite and hydrocerussite.

The ruby red color, similar to vermilion [31] of the pictorial layer, is constituted of hematite in a higher proportion of goethite. The presence of only iron oxides suggests an artificial pigment. The mixture of goethite in a higher proportion together with silicates in the preparation layer suggests natural pigments with the calcite and quartz that Bocanegra used in the preparation layer.

#### I.1.4.3. Identification of pictorial layers

Above the preparation layers, different coloured layers were detected in the paintings such as red, blue, ochre, and white.

#### White pigment

The EXD analyses (Table 2) show that the white layers are constituted of C, Pb and O.

Table 2. Analyses of the third white layer of the six samples of the six paintings.

Painting	Sample	EDX	Pigment identification by SR $\mu$ -XRD
1	3	C,O, Pb, S, Ca	Lead white (cerussite, hydrocerussite), calcium carbonate
2	6	C, O, Pb, Ca, Fe, Si	
3	8	C, O, Pb, Ca	
4	1	C, O, Pb, Ca, Si, K,Fe	
5	11	C, O, Pb, Ca	
6	4	C, O, Pb, Ca	

The  $\mu$ XRF map shows the elemental distribution of lead (Fig. 9). In the white layer, mainly lead and calcium can be distinguished, with lead being the major constituent. In the lead region,  $\mu$ -XRD confirms the presence of lead white (Fig. 10) and shows the mineralogical phases of cerussite,  $Pb_3CO_3$ , and hydrocerussite,  $Pb_3(CO_3)_2(OH)_2$ . The presence of the organic binding media was revealed through FTIR spectroscopy (Fig. 11) carried out on the cross-section. The bands at 1738, 1162 and 1114  $cm^{-1}$  could be attributed, respectively, to the C=O stretching and C-O-C stretching of the drying oils.

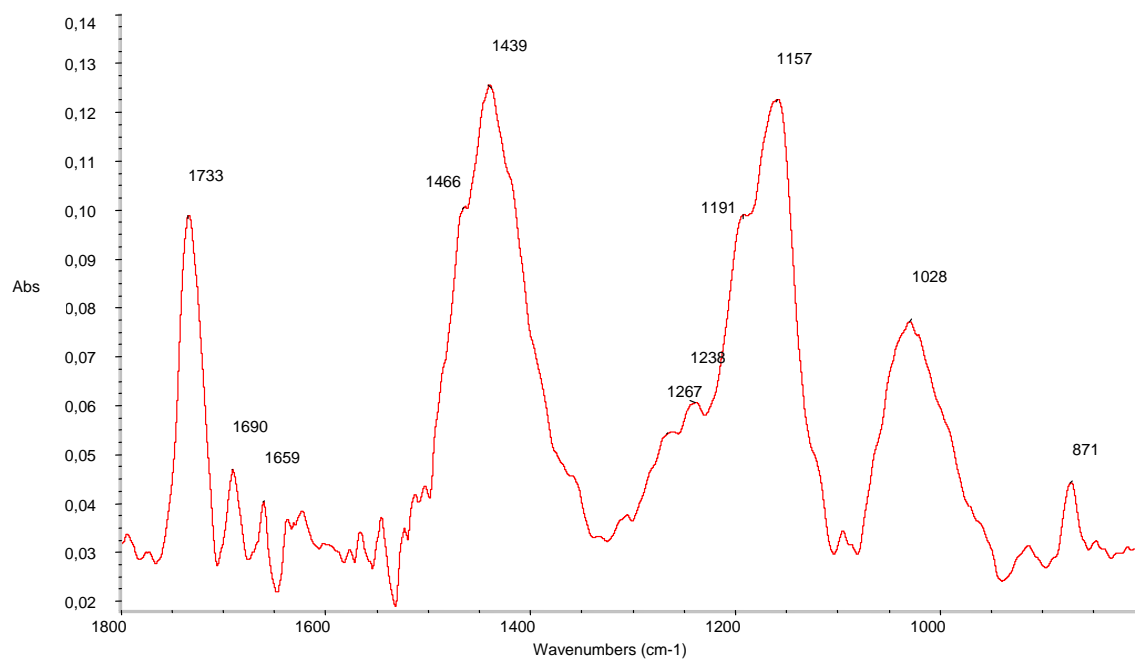


Fig. 11 FTIR spectra corresponding to: a) top pictorial layer, that shows the presence of bands of silicates ( $1097\text{ cm}^{-1}$ ), carbonates ( $1447\text{ cm}^{-1}$  and  $1471\text{ cm}^{-1}$ ), and drying oils ( $1738$  and  $1158\text{ cm}^{-1}$ ).

Py-GC/MS confirms the presence of siccative oils, which gave a chromatogram (Fig. 12) with high concentrations of palmitic, oleic, stearic and dicarboxylic acids (azelaic and suberic acids). These data show that the different pictorial layers were painted using drying oil as a ligand.

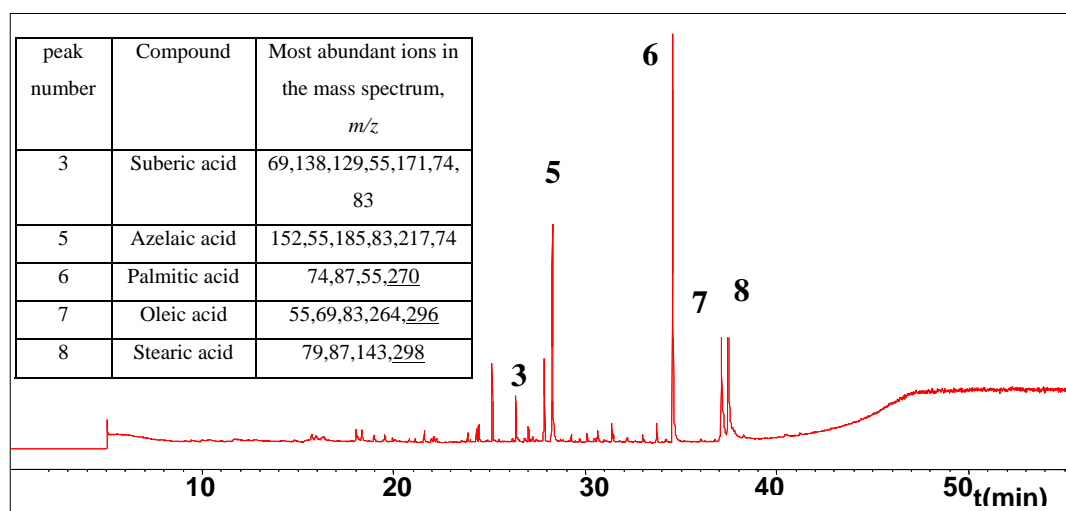


Fig. 12 Reconstructed ion chromatogram obtained from pyrolysis/methylation of Bocanegra painting sample. Numbers on top of peak refer to table (mass spectra characteristics of compounds evolved from pyrolysis methylation and structural attribution to peak numbers).

## Red pigment

### *Cinnabar (HgS)*

SEM/EDX and XRD give an approximation of the composition of the red pictorial layers in the different paint cross-sections. According to optical microscopy (Fig. 13a) observations, the red pigments in the pictorial layers are distributed as random aggregates of very thin particles. The EDX elemental analyses of these thin particles (Fig. 13b) identify Hg and S. The XRD diffraction pattern of the powder sample confirmed the presence of cinnabar (Fig. 13c).

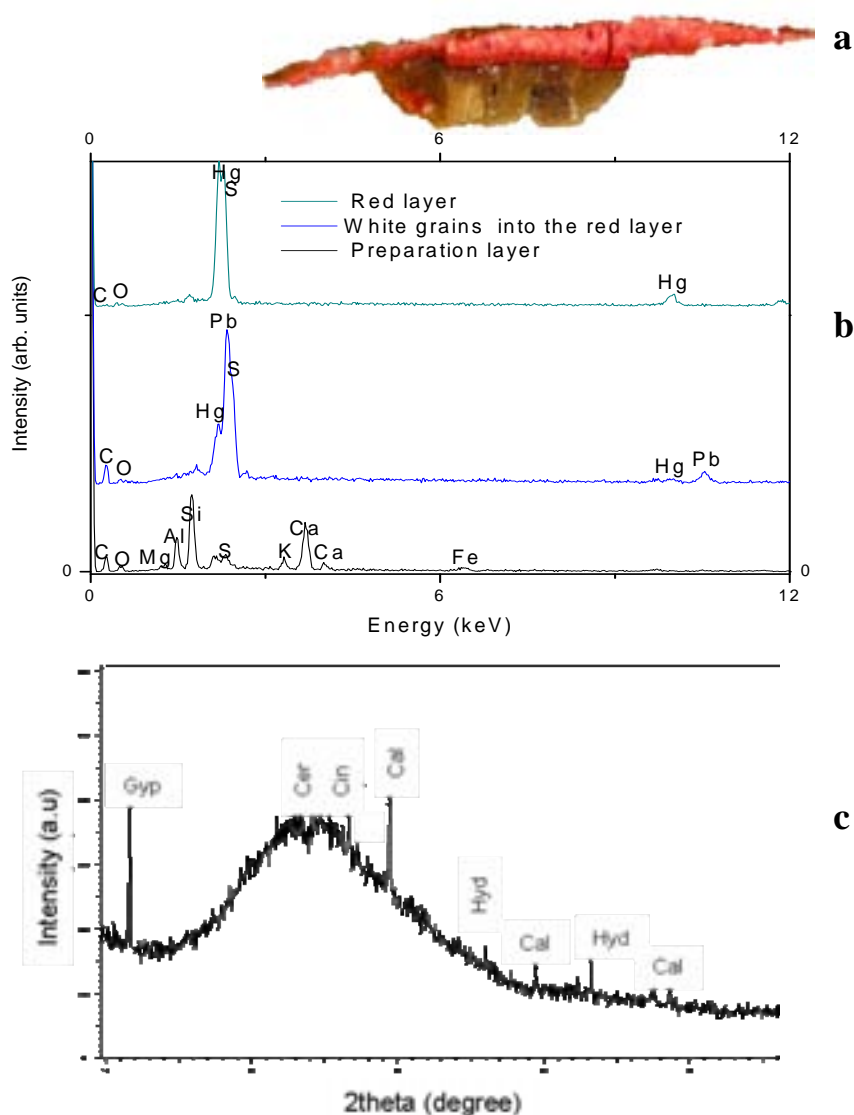


Fig. 13. (a) paint cross section originating from red San Ignacio's dress (b) EDX spectra of the different three layers of the cross section (c) the X-ray diffraction pattern of powder total sample obtained with under incidence angle  $1^\circ$  ( $\theta$ ), whose peaks can be attributed the presence of gypsum (Gyp), cerussite (Cer), hydrocerussite (Hyd), calcite (Cal) and cinnabar (Cin).

Pyrolysis shows the presence of siccative oils as a ligand, and at the same time shows the presence of cinnabar (Fig. 14a). In fact, as reported in a previous paper [19], HgS at a high temperature in a helium atmosphere decomposes, meaning that Hg atoms may be speciated in mass-spectrometry with the typical isotopic pattern (Fig.14b).

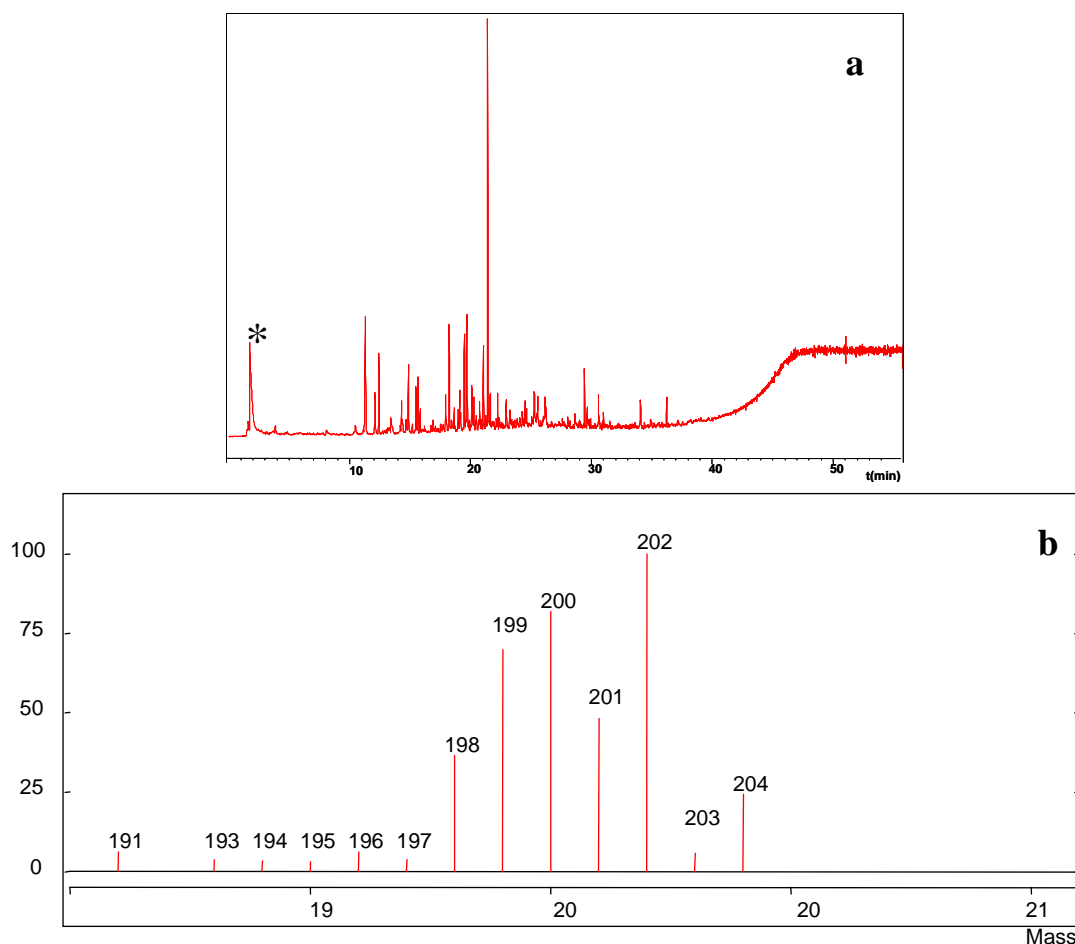


Fig. 14 (a) reconstructed ion chromatogram obtained from direct pyrolysis of the Bocanegra painting sample (b) \* single ion monitoring for  $m/z$  190 to  $m/z$  210 obtained from pyrolysis of a sample containing cinnabar.

The most important source of mercury is normally brilliant red, which has been used through our history as a pigment for paints. Cinnabar and vermilion are names assigned to a single chemical composition of different origin. The first is a natural compound while the second refers to the synthetic pigment. In both cases, there were no differences in structure and composition. In the Bocanegra samples, it was difficult to distinguish between cinnabar and vermilion. In Spain, the cinnabar mines in Almaden were already known from the Roman times, and the use of vermilion (artificial mercuric

sulphide) was described by the Arabs in the eighth-century. In China, vermilion has been used since antiquity [29].

### Iron oxide

Bocanegra used different ochre pigments that contained varying amounts of octahedral iron oxides, namely hematite ( $\alpha\text{Fe}_2\text{O}_3$ ) or/and goethite ( $\alpha\text{FeOOH}$ ), mixed with quartz and calcite. When hematite is the main iron oxide, a red colour is observed, whereas the ochre is yellow when the goethite dominates. These colours are due to the ion  $\text{Fe}^{3+}$  contained in both oxides, and more precisely to the charge transfer between  $\text{Fe}^{3+}$  and its ligands,  $\text{O}_2^-$  or  $\text{OH}^-$  [30]. In Fig. 15a, the scheme of the stratigraphy is superimposed with the iron mapping and diffraction patterns (Fig. 15b) calculated in the same areas. Using  $\mu\text{XRF}/\mu\text{XRD}$ , it was possible to distinguish between the composition of the iron phase present in the red layers of both the pictorial layer and the preparation layer.

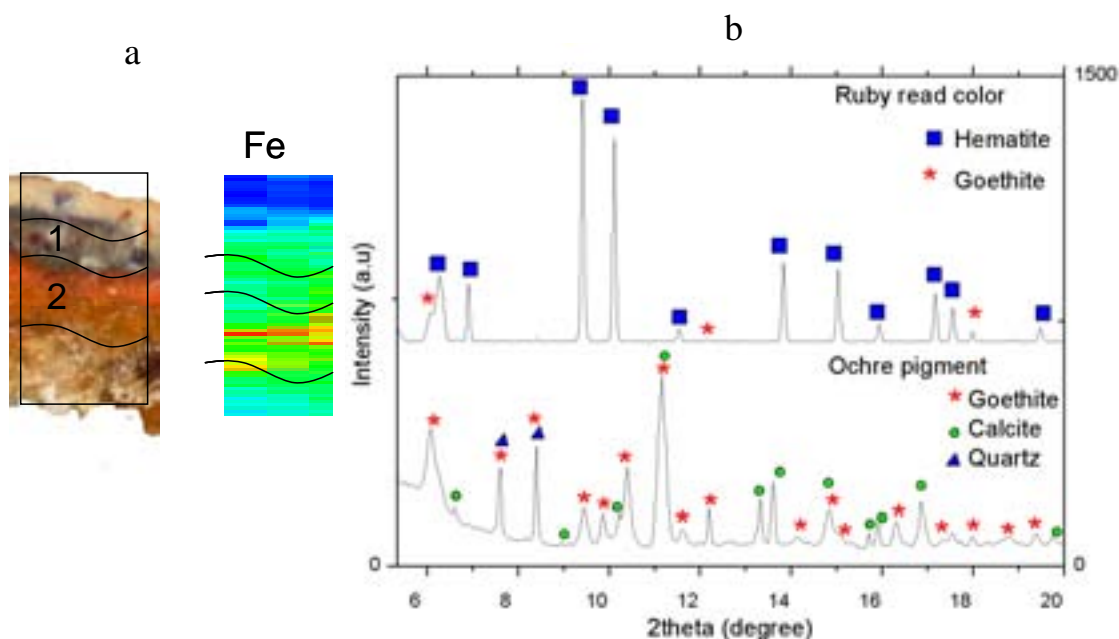


Fig. 15 (a) optical micrograph and  $\mu\text{XRF}$  elemental mapping of red particles in the layer: iron elemental mapping of the preparation layer: iron (b) SR  $\mu\text{XRD}$  of red particles: phases of mainly hematite with a low contribution of goethite. SR  $\mu\text{XRD}$  of red preparation layer: phases of goethite, calcite and quartz.

The ruby red color, similar to vermilion [31] of the pictorial layer, is constituted of hematite in a higher proportion than goethite. The presence of only iron oxides suggests an artificial pigment. The mixture of goethite in a higher proportion together with silicates

in the preparation layer suggests natural pigments with the calcite and quartz that Bocanegra used in the preparation layer.

## **Blue pigment**

### *Cobalt blue*

The use of cobalt as a blue pigment in the Iberian Peninsula was reported in the 13<sup>th</sup> century [32]. In Fig. 16a, the cross-section is shown and it is possible to observe the blue particles in the dark brown layer. In Fig. 16b, the blue particles were examined using SEM/EDX, which showed the presence of potassium, calcium, iron, cobalt, silicon and arsenic in low proportions. The thin cross-section was analyzed using  $\mu$ XRF/  $\mu$ XRD to confirm that this blue pigment was associated with a blue colored potassium glass (smalt).

The scheme of the distribution is superimposed with the arsenic and cobalt mappings (Fig. 16c), and the diffraction patterns were calculated in the same areas. The XRD pattern shows an amorphous phase with a small contribution of silicon oxide that is associated with a vitreous material (glass), as shown in Fig. 16d. The presence of arsenic in the blue pigment is reported from the 16<sup>th</sup> century [33]. The uses of the benefit of the brightness of synchrotron radiation in combination with both techniques ( $\mu$ XRD/ $\mu$ XRF) confirm that this blue pigment was prepared from cobalt-rich minerals, such as cobaltite and smaltite to form cobalt oxide (Zaffer) [34]. Added as cobalt oxide during the manufacturing, with much of the arsenic being volatilized [33]. When this cobalt blue glass pigment degrades, it not only loses its colour, but also causes yellowing of the oil so that the paintings become brownish-yellow. When smalt containing oil paint deteriorates, the alkaline component of the glass, which in the case of smalt is potassium, is lost from the pigment particles and migrates into the binding medium.

There it has the potential to cause concurrent alteration and degradation of the oil, with possible processes including reactions with carboxylic acids in the oil to form potassium fatty acid soaps, or with anion sources in the environment to form species such as carbonates and sulphates [35]. Bocanegra used this blue pigment that consists of a potassium silicate glass containing cobalt oxide and a low quantity of arsenic, which is still present in the cobalt matrix.

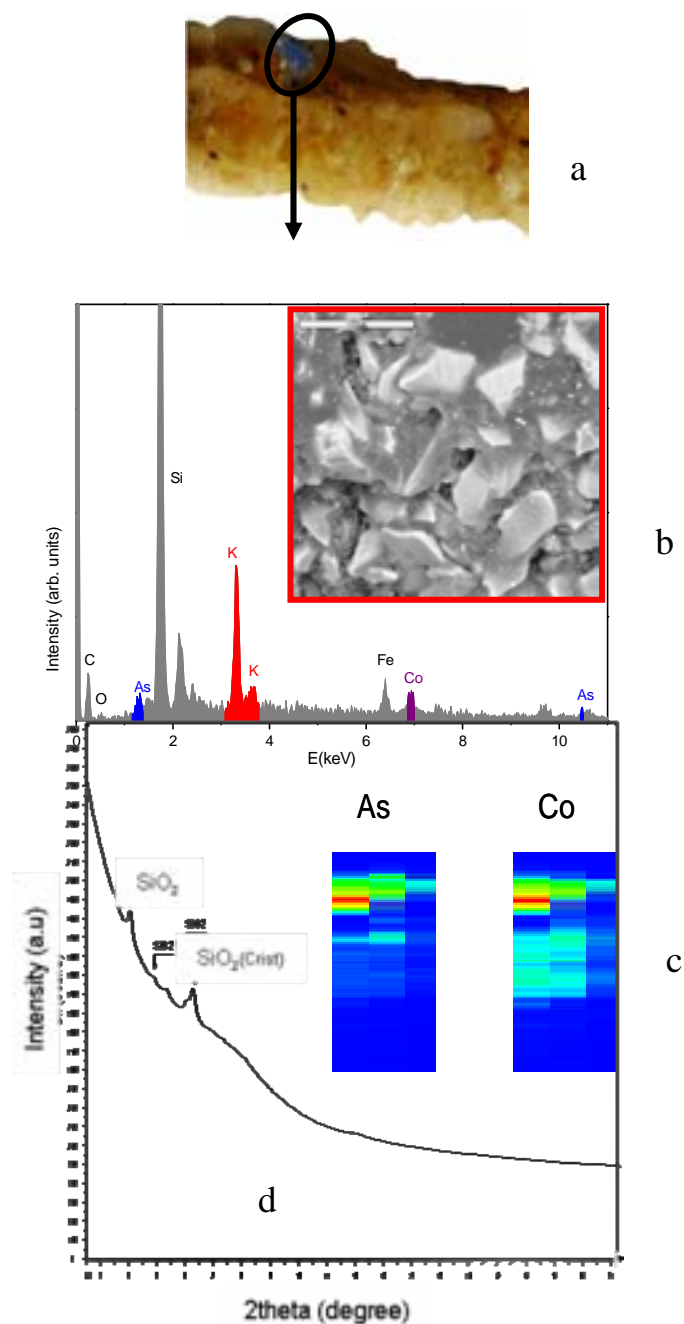


Fig.16 (a) Paint cross-section originating from ground. The cross-section shows the blue particles in the upper layer; the color of the pigment has faded, causing yellowing of the oil medium. (b) SEM/ EDX analyses show the presence of Co, As, and K in the blue particles. (c)  $\mu\text{XRF}$  elemental mapping of the blue particles: arsenic and cobalt (d) SR  $\mu\text{XRD}$  of the amorphous phases.

### Azurite

Azurite is a natural blue pigment that is derived from the mineral azurite, a basic copper carbonate. Bocanegra used it in the mixture of blue and red pigments. Using  $\mu\text{XRF}/\mu\text{XRD}$ , it was possible to obtain only the contribution of azurite without any

interference of the other pigments.  $\mu$ -XRD enables a more precise identification of the crystalline phase of azurite (Fig. 17).

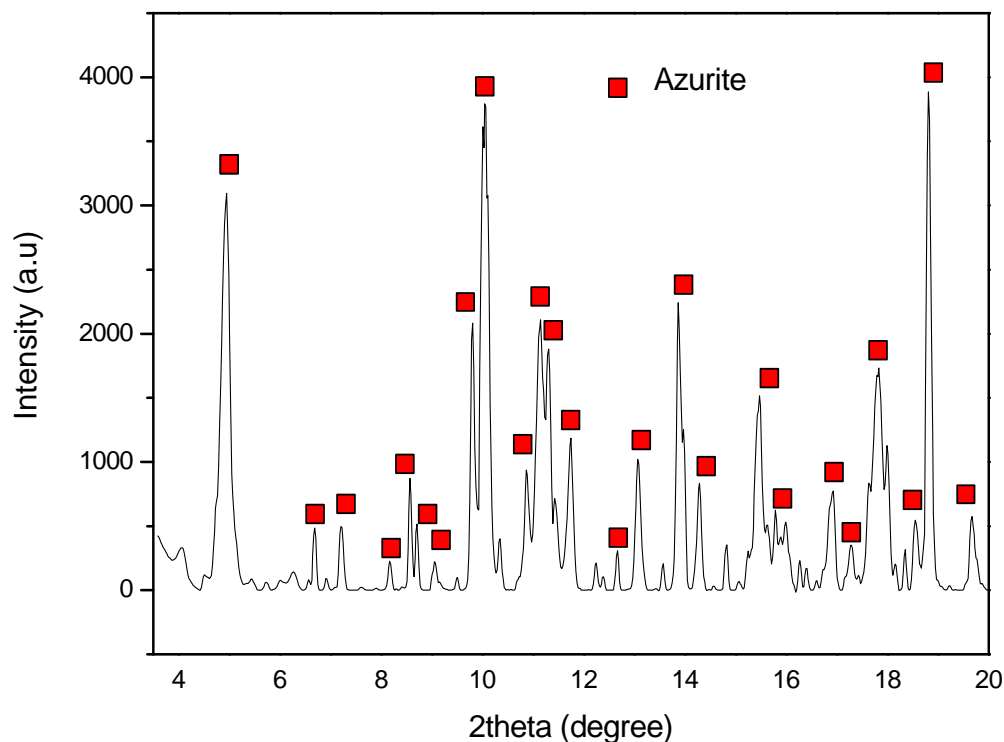


Fig.17  $\mu$ -XRD of crystalline phase of azurite.

#### I.1.4.4. Organic binding medium

Analytical pyrolysis shows that all of the samples of the six paintings have, as an organic ligand, siccative oils. This gives them a high content of dicarboxylic acids, particularly azelaic acid. These acids are considered, in high concentrations, markers of this type of material. Additionally, the egg used in tempera painting has glycerides with long chain aliphatic acids, but due the scarce content of polyunsaturated acids, reactions with oxygen and the polymerisation reaction of the siccative process is practically absent, and only a low concentration of azelaic acid is observed. Chromatographic peaks indicative of proteins are absent but their presence is not excluded because the pyrolytical degradation of proteinaceous materials generally gives insignificant fragments. Only in the presence of a high concentration of protein is it possible to identify markers such as diketopiperazines, as reported by Chiavari *et al.* [36].

### I.1.5. Conclusions

According to the analyses carried out in the Bocanegra painting of the San Ignacio of Loyola life we conclude that his palette contained different pigments. Some colors are employed with great intensity, for example the used cinnabar for the red dresses seeking a contrast that, at this time, his pictorial technique not remains intoned. Because of this, a double current of the light and color applied in these pictures is observed. In some works, he used a dark background that emphasized the figures, and in others, the figures are outlined on a translucent background generally of ochre (iron oxides pigments) and blue (azurite and smalt) tones. In the paintings of Bocanegra's second phase, from 1670-1676, typologies of the figures are set, and the palette is limited and acquires a sense of harmony in the colors. The brushstrokes are looser and the tendency towards strong contrasts is not present. Bocanegra also tries to melt the colors and smooth out the transitions between light and shadow. Besides the technical advance and the greater intensity of color that can be appreciated in the three canvases of "la vida de S. Ignacio", this phase demonstrated development of drama and expressiveness.

The results, obtained using different physical-chemical techniques and analytical methodology, and evaluating the relationships between them, gave useful information about the employed materials and painting techniques in the cultural heritage field.

Scanning electron microscopy, especially in combination with energy dispersive X-ray microanalysis, has been an indispensable tool and contributed extensively to the identification of the elements that constituted the different inorganic pigments of the conventional cross-sections of the paintings. FTIR supplied information on the organic components that the painter used in the preparation layers. The advantages of Py-GC/MS as a tool for the rapid screening of the organic composition of art objects is apparent from the results of this study; it permitted the identification of siccativ oils like those used in the organic medium in these paintings. The technique is capable of providing information on the presence of inorganic compounds such as HgS.

The non-destructive technique of XRD has been applied in the study of ancient textile fibres of Bocanegra paintings. Using a glass capillary, it was possible to use only one fibre of the material. The presence of crystalline parts of the cellulose possibly means that the fibres are only partially degraded.

Synchrotron-based  $\mu$ -XRD and  $\mu$ -XRF are particularly suited for the non-destructive study and micro-characterisation of the different materials present in multi-

layered paintings. This study demonstrated that synchrotron radiation micro-imaging techniques have yielded the ability to analyze pictorial layers, including grains, at the micrometer scale.  $\mu$ -XRD is very useful for the identification of phases that are present in low proportion in multilayer paintings with different inorganic pigments such as cerussite and hydrocerussite, and those with low powder reflection like azurite, cobalt blue, hematite, and goethite. Cinnabar has a high powder reflection and was identified by conventional XRD.

### I.1.6. References

- [1] E.Ciliberto., G. Spoto. (Eds.), *Modern analytical methods in art and archaeology*, Wiley-Interscience, New York, USA, 2000, p.763
- [2] D.C. Creagh., D.A.Bradley (Eds.), *Radiation in art and archaeometry*, Elsevier Science, Amsterdam, The Netherlands, 2000, p.297.
- [3] M.Cotte., J.Susini., A. Solé., Y.Taniguchi., J.Chillida., E. Checroun., P.Walter. *J.Anal. At. Spectrom.*, 23 (2008). 820.
- [4] L. Bertrand., D. Vantelon., E. Pantos. *Appl. Phys. A*, 83 (2006) 225.
- [5] E. Pantos. *Synchrotron radiation in archaeological and cultural heritage science*. In M. Uda, G. Demortier and I. Nakai (eds.) *X-rays for Archaeology*: London: Springer 2005. p.199-208.
- [6] M. Uda., G. Demortier., I. Nakai, I. *X-rays for Archaeology*. Springer-Verlag Netherlands 2005. p 459
- [7] D.C. Creagh. *The characterisation of artefacts of cultural heritage significance using physical techniques*. *Radiation Physics and Chemistry* 74 (2005) 426.
- [8] J. Cassar., C. Degriigny. *The philosophy of the workshop*, in: A. Adriaens., C. Degriigny., J. Cassar. (Eds.), *Benefits of non-destructive analytical Techniques for conservation*, office for the official publications of the European Union, Luxembourg, 2005, pp. 9 – 12.
- [9] K. Keune. *Binding Medium, Pigments and Metal Soaps Characterized and Localized in Paint Cross Sections*, Dissertation, Molart report, Archetype, London, 2005.
- [10] E. Dooryhee., Ph.Colomban. *Cultural heritage materials: Structural and spectroscopic evidence for ancient technologies*. *Phase Transitions* 81 (2-3) (2008) 139.
- [11] A. Von Haartman. *Metodología y técnicas en la restauración de obras pictóricas del Siglo de Oro español de la catedral de Almería*. Ed. Universidad de Granada. 1992, p. 85.

- [12] E. Orozco Diaz. Pedro Atanasio Bocanegra, Boletín Facultad de Letras. Granada. 1937, p. 24.
- [13] García Gutierrez F. San Ignacio de Loyola en la pintura y escultura de Andalucía, Boletín de las Artes 9, (1991) 49.
- [14] N. Khandekar, Preparation of cross-sections from easel painting. Rev Conser, 4, (2003) 52.
- [15] A. Duran., L.K Herrera., M<sup>a</sup>.D. Robador., J.L. Perez-Rodriguez. Color Study of Mudejar Paintings Of The Pond at the Palace of Reales Alcazares of Seville Color Research and Application 32 (6), (2007) 489.
- [16] M. Spring, C. Ricci, D.A.Peggie, S.G. Kazarian. ATR-FTIR imaging for the analysis of organic materials in paint cross sections: case studies on paint samples from the National Gallery, London. Analytical and Bioanalytical Chemistry (2008) 1-9
- [17] S. Kuckova, I. Nemeč, R. Hynek, J. Hradilova, T. Grygar. Analysis of organic colouring and binding components in colour layer of art works Analytical and Bioanalytical Chemistry 382 (2), (2005) 275-282
- [18] L.K Herrera., M. Cotte., M.C. Jimenez de Haro, A. Duran., A. Justo., J.L. Perez Rodriguez. Characterisation of iron oxide-based pigments by synchrotron-based micro X-ray diffraction. Appl Clay Sci DOI: 10.1016/j.clay.2008.01.021.
- [19] G. Chiavari., S. Prati. Analytical pyrolysis as diagnostic tool in the investigation of works of art. Chromatographia 58, (2003) 543.
- [20] J.I. Goldstein., D.E. Newbury., D.C Joy., C.E. Lyman., P. Echlin., E. Lifshin., L.C.Sawyer., J.R. Michael. Scanning electron microscopy and X-ray microanalysis, 3rd ed. Kluwer Academic/Plenum Publishers, New York, 2003, p. 40
- [21] J. Boon., S. Asahina., Surface preparation of cross sections of traditional and modern paint using the Argon ion milling polishing CP system. Microsc. Microanal., 12 (2), (2006)1322.
- [22] A. Somogyi., M. Drakopoulos., L. Vincze., B. Vekemans., C. Camerani., K. Janssens., A. Snigirev., F. Adams. ID18F: A new micro-x-ray fluorescence end – station at the European Synchrotron Radiation Facility: Preliminar results. X-Ray Spectrom., 30, (2001) 242.
- [23] V.A. Solé., E. Papillon., M. Cotte., P.H. Walter., J. Susini. A multiplatform code for the analysis of energy-dispersive X-ray spectra. Spectrochim. Acta, Part B, 62 (1) (2007) 63.
- [24] A.P.Hammersley., C. Riekel., Synchrotron Radiation News 2, (1989) 24.

- [25] G. Chiavari., S. Prati., G. Lanterna., C. Lalli., A. Cagnini. Diagnostic study of the materials and painting techniques in "The Dinner of Emmaus" by Gregorio (and Mattia?) Preti *Microchim Acta* 159 (3-4), (2007) 357.
- [26] A. Satta., R. Hagege., M. Sotton. Relationship between structure and behaviour of the elementary flax fibre. *Bull. Sci. ITF*, 15, (1986) 3.
- [27] G.F. Davidson., T.P. Nevell. The Auto-Hydrolysis of Acidic Oxy-celluloses. *J. Textile Inst.* 47 (1956) 439.
- [28] A. Duran. Metodología de Estudio y Análisis de diferentes tipos de obras pertenecientes a la Escuela Sevillana de los siglos XVII y XVIII. Ph.D. Universidad de Sevilla. 2006, 480 pp.
- [29] R.J. Gettens., R.L. Feller., W.T. Chase. Vermilion and Cinnabar, *Artists' Pigments. A Handbook of their History and Characteristics* 2 Roy, A. (ed) National Gallery of Art, Washington and Oxford University Press, Oxford, 1993, 159-182.
- [30] M. Elias., C. Chartier., G. Prévot., H. Garay., C. Vignaud. The colour of ochres explained by their composition. *Mater Sci and Eng B* 127, (2006) 70.
- [31] R.J. Gettens., G. L. Stout. *Painting materials: A short encyclopaedia*. Ed. Dover Publications, New York, 1966, 157-159.
- [32] C. Roldán., J. Coll., J. Ferrero... EDXRF analysis of blue pigments used in Valencian ceramics from the 14th century to modern times. *J. Cult. Herit.* 7 (2), 2006, 134.
- [33] G. Pappalardo., E. Costa., C. Marchetta., L. Pappalardo., F.P. Romano., A. Zucchiatti., P. Prati., P.A. Mandò., A. Migliori., L., Palombo., M.G. Vaccari. Non-destructive characterisation of Della Robbia sculptures at the Bargello museum in Florence by the combined use of PIXE and XRF portable systems, *J. Cult. Herit.* 5 (2004) 183.
- [34] B. Mühlethaler., J. Thissen. Smalt. In *Artists' pigments: A handbook of their history and characteristics*, vol. 2, ed. Ashok Roy. Washington, D.C.: National Gallery of Art. 1993, 113–130.
- [35] M. Spring., N. Penny., R. White., M. Wyld. Colour Change in the conversion of the Magdalen attributed to Pedro Campaña., *National Gallery Technical Bulletin*, 22, (2001) 54.
- [36] G. Chiavari., N. Gandini., P. Russo., D. Fabbri. Characterisation of standard tempera painting layers with proteinaceous binder by pyrolysis (methylation)-gas chromatography/mass spectrometry. *Chromatographia*, 47 (1988), 420.

## I. 2. Characterisation of iron oxide-based pigments by micro X-Ray diffraction

### Introduction

Pigments have been used as colouring materials since prehistoric ages. [1-7] One of the most frequently used pigments is a mixture of different iron oxyhydroxides and oxides. A very good and comprehensive review of iron oxides has been given by Cornell and Schwertmann (1996) [8]. Goethite ( $\alpha$ -FeOOH), lepidocrocite ( $\gamma$ -FeOOH) and hematite ( $\text{Fe}_2\text{O}_3$ ) are the phases most frequently found in the pigments. In addition, manganese oxide is sometimes present. The natural iron oxyhydroxides and iron oxides used as pigments are mixed with clay minerals (kaolinite, illite, smectite, etc.) [9].

Nowadays, most pigments are artificial in origin [3,8]. An excellent natural red oxide comes from the Persian Gulf. It contains about 70%  $\text{Fe}_2\text{O}_3$ . Usually, the Spanish red oxide contains more than 85% of  $\text{Fe}_2\text{O}_3$  [3]. The cross-section technique of sample preparation provides a wide variety of information and is one of the most common techniques in the work of the museum scientists [10-12]

Normally, the first technique that is used on the prepared cross-section is optical microscopy, which provides information about the morphology of the grains of pigments (homogeneity, size, form), including the aggregation state and optical characteristics [13,14]

The same cross-section is appropriated for the application of other analytical techniques, such as energy dispersive X-ray spectroscopy, micro-Raman, and micro-FTIR spectroscopy. Analyses carried out using these techniques allow identification of pigments, supports and binders with the removal of just one sample, thereby significantly reducing damage to the artwork [15-18]. These techniques also provide important information about the chemical composition of the ochre pigments used in the paints. However, it is not possible to characterize the different crystalline phases present.

The characterisation of these pigments (iron oxides and iron oxyhydroxides) by conventional X-ray diffraction is difficult because the phases are present at low concentration in a narrow layer, and often exhibit far weaker reflecting power than the other phases present throughout the sample.

### I. 2.1. Research aims

Synchrotron radiation provides information regarding the chemical composition and iron phases present in ochre pigments that is not possible to obtain by conventional XRD diffraction. This work, performed at the European Synchrotron Radiation Facility, reports the results of SR  $\mu$ -XRD and SR  $\mu$ -XRF of two samples taken from wall paintings of the ceiling of the San Agustin's Church in Cordoba (Spain). This technique has allowed characterisation of the iron oxyhydroxides and oxide phases in the dark brown layer seen in the cross-section of the paints.

### I. 2.2. Experimental

#### I. 2.2.1. Materials

Several small samples were taken from wall paintings at San Agustin's Church in Cordoba, most of them belonging to the ceiling (Fig. 1). This study focuses on samples 1 and 2. The composition of the other samples was similar to these two.

#### I. 2.2.2 Sample preparation

In conventional cross-section, the samples were prepared as cylinder moulds and were embedded in epoxy resin

*In thin cross-sections, the* samples were embedded in a resin (Leica Histo-resin) to prepare thin sections with a microtome.

The small fragments of the samples were ground to a powder form for examination by conventional X-ray diffraction.



Fig. 1 Photograph of a wall painting at ceiling in the San Agustin's Church in Cordoba, Spain.

### **I. 2.3. Analytical methods**

#### **I. 2.3.1. Conventional laboratory techniques**

Observation of conventional cross-sections was performed using a stereo microscope, Scanning electron micrographs were obtained with a JEOL JSM 5400. Semiquantitative analyses of the elemental compositions of the different layers were obtained using a Link ISIS energy dispersive X-ray spectrometer.  $\mu$ -Fourier Transform Infrared Spectroscopy ( $\mu$ -FTIR) (Nicolet 510) was employed to determine the inorganic anions and organic functional groups present in the compounds. The crystalline phases were characterized by X-ray diffraction (XRD) using a Siemens diffractometer, model Kristalloflex D-5000

#### **I.2.3.2. Synchrotron-based micro X-ray diffraction and micro X-ray fluorescence techniques**

$\mu$ -X-ray diffraction and  $\mu$ -X-ray fluorescence were performed at the ID18F beamline, at the European Synchrotron Radiation Facility in Grenoble (France). The geometry and the experimental parameters of this beamline were described in the previous section.

### **I. 2.4. Results and discussion**

In the conventional cross-section of sample 1 is shown in (Fig. 2a) two layers appear, one of white colour (60-80  $\mu\text{m}$ ) followed by another of dark brown colour (15-20  $\mu\text{m}$ ).

The EDX analysis of the dark brown layer (Fig. 2b above) shows the presence of Fe, Mn, Si, Al, S, Ca and O. These data suggest that the pigment could be attributed to Siena earth (mixture of silicoaluminates and iron and manganese oxides and/or oxyhydroxides) [3]. The Ca and S are attributed to the presence of gypsum, probably due to environmental contamination on the surface. EDX analysis of the white layer shows the presence of Pb and O (Fig. 2b bottom). The FTIR spectrum acquired in the dark brown layer (Fig. 2c bottom) shows bands attributed to sulphates ( $1040\text{-}1250\text{ cm}^{-1}$ ), silica or silicates ( $900\text{-}1100\text{ cm}^{-1}$ ), carbonates ( $1320\text{-}1530\text{ cm}^{-1}$ ) and oils ( $1700\text{-}1750\text{ cm}^{-1}$ ). FTIR study in the white layer confirms the presence of carbonates ( $1400\text{-}1410\text{ cm}^{-1}$ ) and

oils (Fig. 2c above). The presence of oil binders suggest that wall paintings were realized using “a secco” techniques.

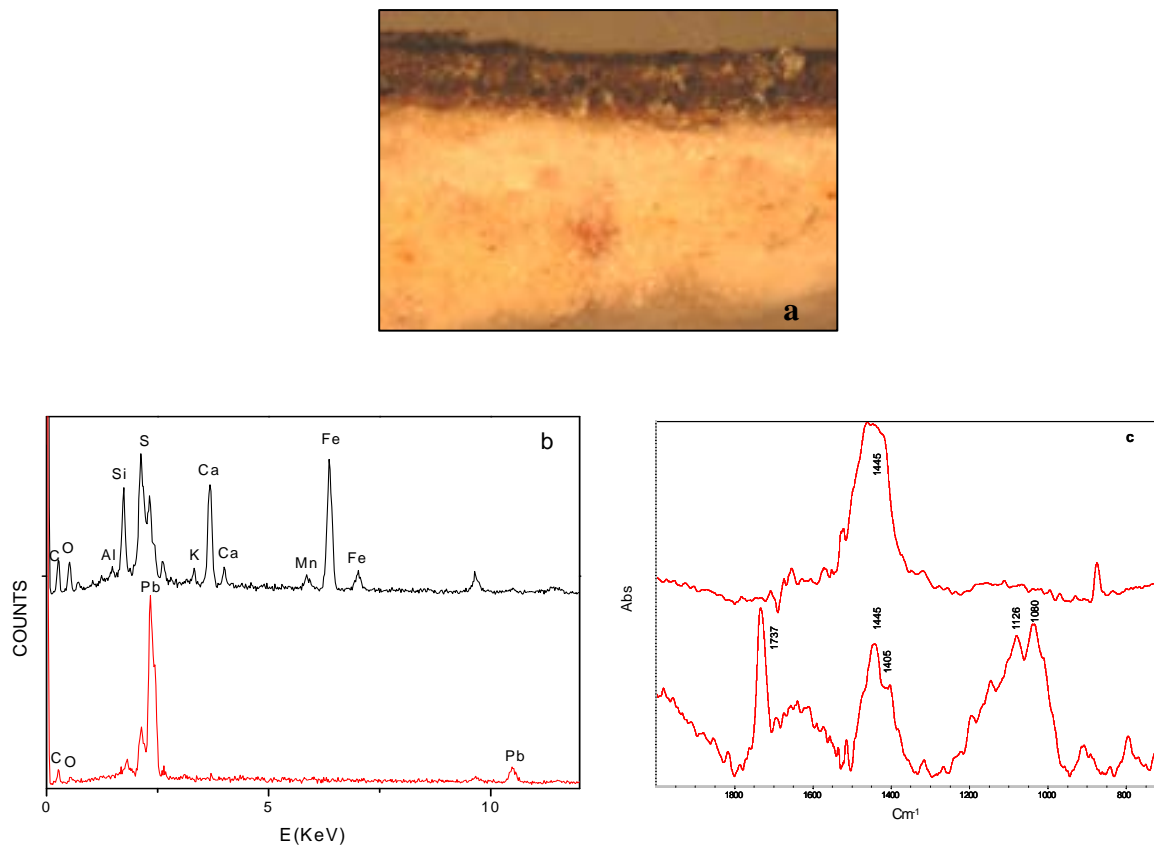


Fig. 2 (a) Cross-sections of sample 1 (b) EDX analysis of two layers (c) FTIR of the two layers.

A cross-section of sample 2 (Fig. 3a) shows a layer of white colour is present at the bottom, followed by another of dark brown colour and a thin layer at the top of the cross-section. The chemical composition of the dark brown layer and white layer is similar to those in the previously studied cross-section (Figs. 3b bottom and medium). The thin layer at the top of the sample is composed of gold (Fig. 3b above). FTIR study of the white layer shows bands at  $1420\text{-}1450\text{ cm}^{-1}$ , confirming the presence of carbonates (not shown).

Other samples from the same wall painting showed compositions similar to the two described above, and the results are not included.

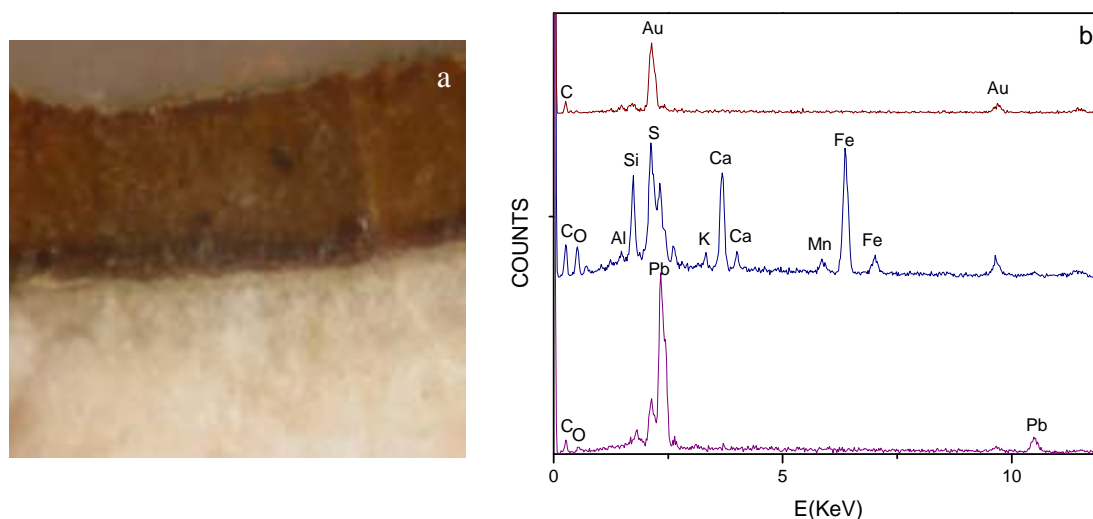


Fig. 3 (a) Cross-sections of sample 2, (b) EDX analysis of the external layer.

The samples taken for this study were very small and were composed of several layers. The separation of different layers was very complicated. For this reason the samples (including all the layers) were ground for XRD characterisation. The XRD study was carried out in powder form by the conventional Bragg-Brentano method with a focusing geometry ( $\Theta$ - $2\Theta$  coupled) that requires a very small quantity of sample. The conventional X-ray diffraction pattern of *raw fragment of* sample 1 was similar to sample 2 (Fig. 4) shows the presence of hydrocerussite  $\text{Pb}_3(\text{CO}_3)_2(\text{OH})_2$  (HyC) and cerussite  $\text{Pb}_3\text{CO}_3$  (Cer).

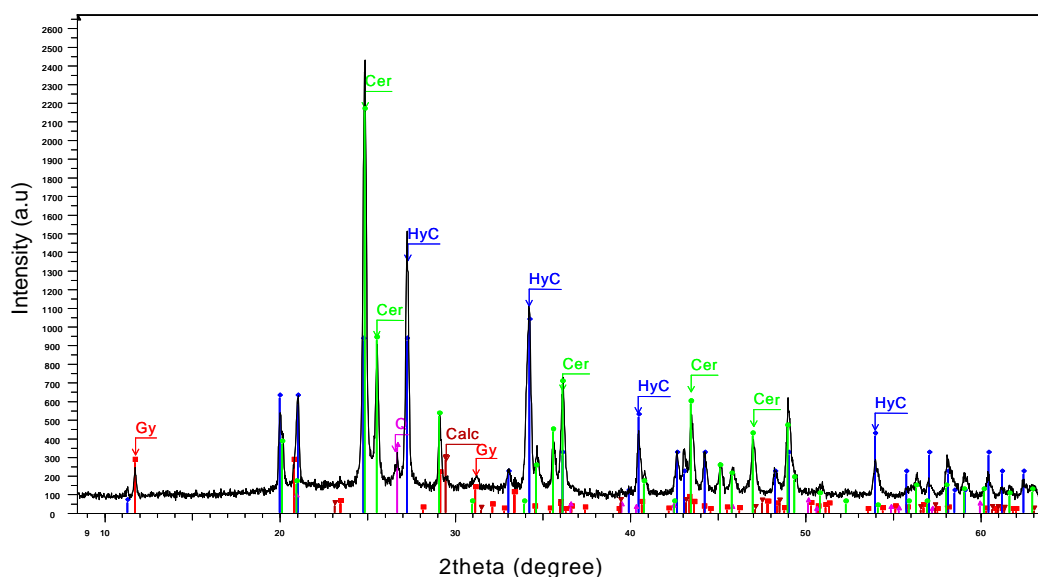


Fig. 4 The X-ray diffraction pattern of the powdered sample 1 obtained with conventional Bragg-Brentano geometry.

This result is in agreement with the presence of lead, oxygen, and carbonates identified by SEM-EDX and FTIR spectroscopy. Also, gypsum (Gy), calcite (Calc) and quartz (Q) appear. These results are in agreement with the composition found for the white layer by other techniques. However, the iron oxides and iron oxyhydroxides used as pigments were not detected in conventional XRD. These pigments are present in the thinnest layer of the sample at very low concentration relative to the other minerals present in the mixture. In addition, the iron oxides have weak diffraction intensity. These facts make characterisation of the iron compounds by conventional X-ray diffraction very difficult.

The development of methods for X-ray focusing and the development of synchrotron radiation sources have allowed the determination of relative elemental abundance with high precision and accuracy, and have illustrated correlations among the different elements. These developments have also permitted characterisation of the iron oxides and oxyhydroxides present in the dark brown layer of the painting. In Fig 5, the area of the micro cross-section analyzed and the sample slides designed for the study of microsamples by SR  $\mu$ -XRD and SR- $\mu$ -XRF are shown.

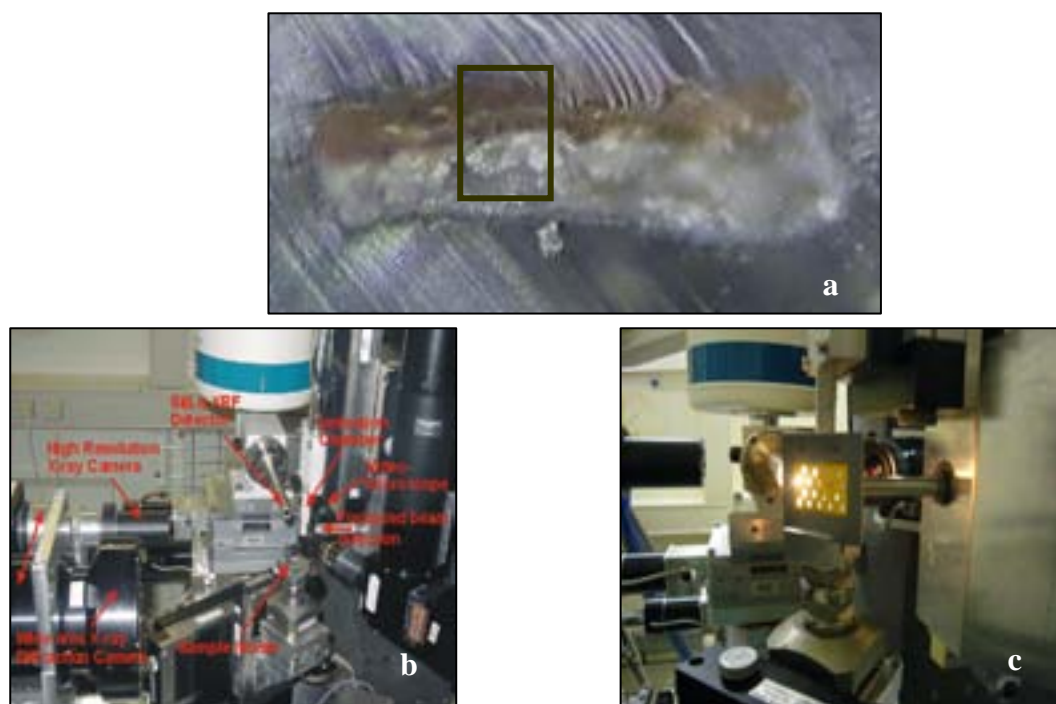


Fig. 5.(a) Area of the microsamples. Microanalysis of the brown layer ( $15\mu\text{m} \times 15\mu\text{m}$ ) (b) schematic layout of the microprobe setup ID 18F ESRF (c) sample holder of the microsample.

A typical X-ray fluorescence spectrum is shown in Fig. 6. It clearly illustrates the main problem faced when treating data: the numerous interferences of the K-lines of the low-Z elements, with the L or M lines of higher-Z elements.

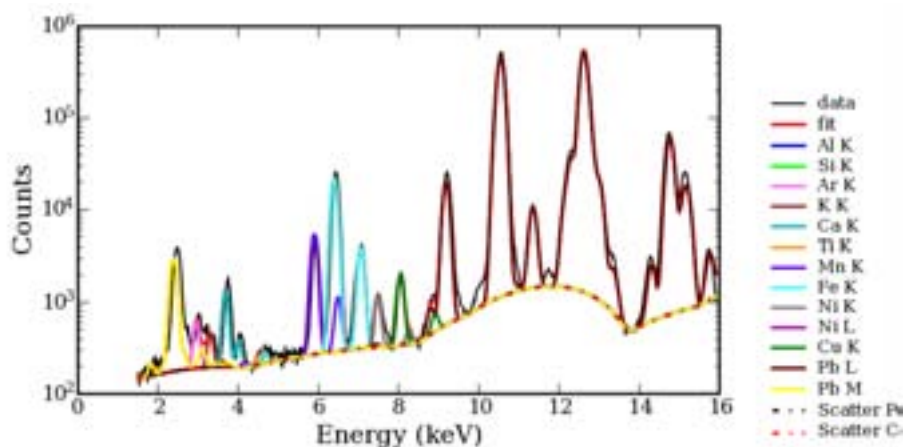


Fig. 6 Calibration of  $\mu$ -XRF spectrum, fitted with PyMCA of the sample 1.

A first approach to obtain the fluorescence image of each of the elements separately is by taking benefit from the energy tunability. For example, the distribution of iron can be obtained with an excitation beam of 7.2 keV. Then the energy is tuned above Pb L-edge (e.g.,  $E \approx 16$  keV) and the Mn K-edge 6.6 keV. X-ray fluorescence spectra are treated with PyMCA software and are used to identify elemental composition of the different layers of the samples with surprisingly good accuracy. This software implements a Levenberg–Marquardt algorithm to fit the spectra with constraints on the fitting parameters (detector characteristics, detection geometry, matrix composition, excitation energy, etc.). A complete emission line series is fitted by taking into account theoretical intensity ratios and line emission energies. A more detailed description of this code has been given by Solé et al. (2007) [19]. The fitting configuration thus obtained is applied to each pixel of 2D maps to calculate the different elemental maps through a batch treatment.

The XRF maps show the elemental distribution in the sample 1 (Fig. 7). Two layers can be distinguished from the base to the surface; the deeper layer contains mainly lead, calcium and sulphur, lead is the major constituent of this layer; calcium and sulphur are coming from the support of the painting. (Fig. 7b). In the region of lead (deeper layer)  $\mu$ -XRD confirms the presence of lead white and shows the mineralogical phases of hydrocerussite  $Pb_3(CO_3)_2(OH)_2$  (HyC) and cerussite  $Pb_3CO_3$  (Cer) (Fig. 8).

In the upper brown layer the XRF maps show the elemental distribution of iron and manganese. (Fig. 7a).  $\mu$ -XRD enables a more precise identification of crystalline phases of iron oxyhydroxides and iron oxides. Three patterns of characteristic scans confirm the presence of goethite ( $\alpha$ -FeOOH), lepidocrocite ( $\gamma$ -FeOOH) and hematite ( $\text{Fe}_2\text{O}_3$ ).

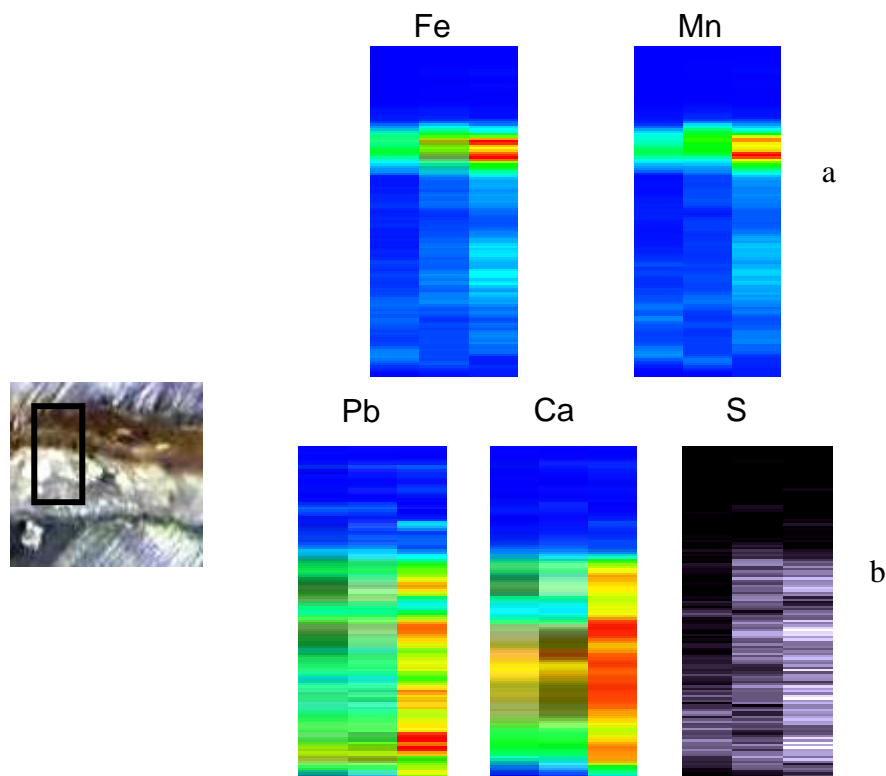


Fig. 7 Elemental mapping using  $\mu$ -XRF of the sample 1: (a) brown layer (b) white layer.

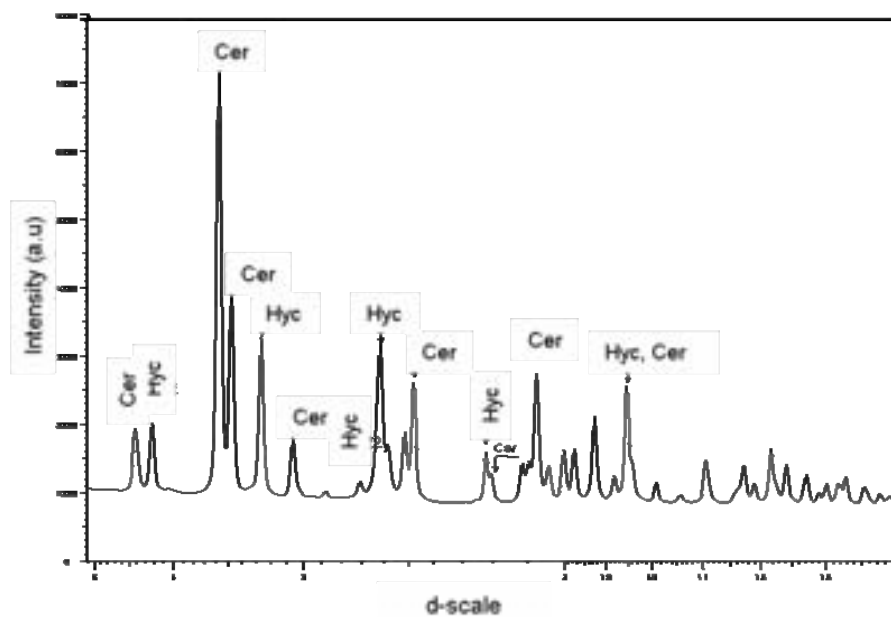


Fig. 8.  $\mu$ -XRD pattern of the white layer of sample 1.

In comparison with the patterns in Fig. 9b and c, Fig. 9a shows a higher amount of goethite (G). The peaks of lepidocrocite show similar intensity in the three patterns indicating a similar content in the brown layer. Hematite (H) is present in a very low concentration.  $\mu$ -XRD shows a heterogeneous mixture of the iron phases (goethite, lepidocrocite and hematite) present in the dark brown layer, indicating that iron oxide pigments used in the wall paintings of San Agustin's Church in Cordoba could be natural pigments. To further characterize the micro-physical properties of this pigment, additional experiments are necessary.

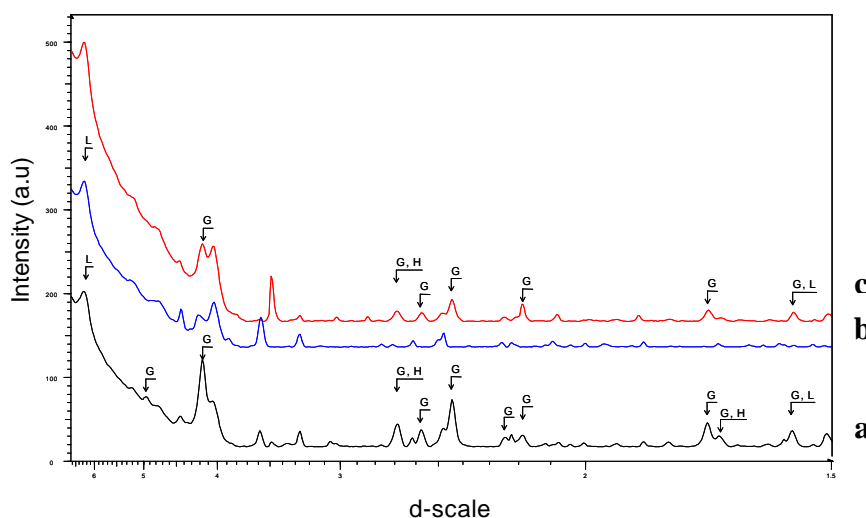


Fig. 9.  $\mu$ -XRD patterns of the dark brown layer of sample 1.

Gypsum, silica or silicates found in the external layer using conventional EDX analyses and FTIR are attributed to environmental contamination in the surface of the painting. The Ca and S detected by  $\mu$ -XRF in the deeper layer are the contribution of the support of the painting. In the raw fragments, the present of gypsum in the conventional XRD pattern may be associated to the mixture of support and contamination of the external layer of the painting.

### I. 2.5. Conclusions

Micro-infrared spectroscopy and energy dispersive X-ray elemental microanalysis are techniques that give important information about the chemical composition of the different components used in paints. It is impossible to characterize the different crystalline phases by conventional XRD because the pigments in the different layers are present at quite low concentrations relative to the bulk matrix components, and the

reflecting power of these iron containing pigments is weak relative to other components present in the sample.

For characterisation of iron oxide pigments by conventional XRD raw fragments of the paintings have to be used. It is rather difficult to identify the phases of thin paint layers (in the range of several tens of microns or even below). However, SR  $\mu$ -XRD made possible the identification of crystalline structure of the iron oxide and lead pigments in the cross-section of the paint layers. SR  $\mu$ -XRD technique has been proved to be a valuable tool for the accurate identification of the iron oxide and lead pigments.

Synchrotron Radiation  $\mu$ -XRD and  $\mu$ -XRF techniques are particularly suited to non-destructive study and micro-characterisation of the different materials present in multi-layered paintings.

### I. 2.6. References

- [1] Ch. L Eastlake. *Methods and Materials of the Great Schools and Masters*. Reprint from 1847. Dover Publications. New York 1960.
- [2] F. Pacheco. *Arte de la Pintura*. Reprinted from 1649. L.E.D.A Las Ediciones de Arte. Barcelona. Spain. 1966
- [3] R.J. Gettens, G.L. Stout *Painting Materials. A short Encyclopaedia*. Dover Publications, Inc., New York. 1996
- [4] C. Cennino. *Il Libro dell' Arte*. Thompson Jr., D.V. (translator), *The Craftsman's Handbook*. Reprint from 1437. Dover Publications, New York. 1978.
- [5] R.D. Harley. *Artist`s Pigments c. 1600-1835*. Butterworths Scientific, London. 1982
- [6] R.L. Feller, R.L. *Artists` Pigments, vol. 1* Cambridge Univ. Press, London. 1986
- [7] A. Roy(Ed.). *Artists` Pigments, vol. 2*. Oxford Univ. Press, New York 1993
- [8] R. Cornell, U. Schwertmann. *The iron oxide. Structure, properties, reactions, occurrence and uses*. VCH, Weinheim. 1996
- [9] D. Hradil, T. Grygar, J. Hradilova. *Clay and iron oxide pigments in the history of painting* *Applied Clay Science* 22 (5) (2003) 223-236.
- [10] J.S. Martin. *Observation on cross-section examination of painted and coated surfaces*, in *AIC Specially Group Postprints 1991*. Paper presented at the 19<sup>th</sup> Annual Meeting of the AIC. Albuquerque June 8, 1991 (C. Stravroudis, Ed.) AIC Washington, DC, 39-42. 1991
- [11] E.W. Fitzhugh. *Artists` Pigments, vol. 3* Oxford Univ. Press, New York. 1997

- [12] N. Khandekar. Preparation of cross-sections from easel painting. *Reviews in Conservation*, 4, 2003, 52-64.
- [13] J. Plester, Cross-section and chemical analysis of point samples. *Studies in Conservation*. 2, 1996, 110-157.
- [14] M<sup>a</sup>.L. Gomez. *La restauración. Examen científico aplicado a la conservación de obras de arte*. Ed. Catedra. 436 pp. 1998
- [15] F. Flieder. Mise on point des techniques d'identification des pigments et des liants inclus dans la couche picturale des enluminures de manuscrits. *Studies in Conservation* 13, 1968, 49-86.
- [16] E.H. Van't Hul-Ehrnreich E.H. Infrared microspectroscopy for the analysis of old painting materials. *Studies in Conservation*, 15, 1970, 175-182.
- [17] S. Rimaldi. Advantages and limits of X-ray fluorescence (XRF) in painting analysis. The case of Caravaggio, *Materiali e Structure: Problemi di conservazione* 4, 1994, 67-75.
- [18] S. Brieni, F. Cariati, F. Casadio, L. Toniolo. Spectrochemical characterisation by micro-FTIR spectroscopy of blue pigments in different polychromed works of art. *Vibrational Spectroscopy* 20, 1999, 15-25.
- [19] V.A Solé, E. Papillon, M. Cotte, PH. Walter, J. Susini, PyMCA: A multiplatform code for the analysis of energy-dispersive X-ray spectra. *Spectrochimica Acta Part B: Atomic Spectroscopy*, 62 (1), 2007, 63-68.

### **I. 3. Synchrotron-based X-ray experiments used for the study of an iron oxide micrometric pigment in 18th century paintings**

Earthy pigment colours varying from dull yellow to red-brown are commonly called “ochre” in paintings. This colour is created by the presence of different iron oxides and oxyhydroxides.

The characterisation of the phases present in ochre pigments by conventional x-ray diffraction is difficult because the analysis is performed in micro-samples (cross-sections). The pigments are present in a narrow layer, their concentration is very low and their reflecting power is weak in relation to other phases present. The first attempt to characterise samples using SR demonstrated that  $\mu$ -XRF and  $\mu$ -XRD are powerful techniques for the characterisation of the components of ochre pigment. These components included goethite and lepidocrocite in the narrow layer, which were identified with good spatial resolution.

#### **I. 3.1. Research aims**

This work reports the presence of monazite, reddish-brown cerium, lanthanum phosphate [(Ce,La)PO<sub>4</sub>], and iron oxide pigments. These compounds were identified using synchrotron-based micro-imaging techniques.

#### **I. 3. 2. Experimental**

SR- $\mu$ XRF and  $\mu$ -XRD data were collected at the ID18F beam line in the European Synchrotron Radiation Facility (ESRF) [1]. One sample of earth-based pigment extracted from Gospel in San Agustin’s Church in Cordoba, Spain (Fig.1) was studied. The sampling was carried out by scraping off different areas of the paintings. This study only referred to one sample.



Fig. 1 Photograph of a wall painting located at the nave of Gospel in San Agustín's Church in Córdoba, Spain.

### I. 3. 3. Results and discussion

An area of micro cross-section was analysed. The study of the microsamples by SR  $\mu$ -XRD and SR- $\mu$ -XRF is shown in Fig 2a. X-ray fluorescence spectra treated with PyMCA [2] code revealed the main components of the brown layer (Fig 2b). This study identified the distribution of the main elements in the different layers of the sample (Fig 2c).

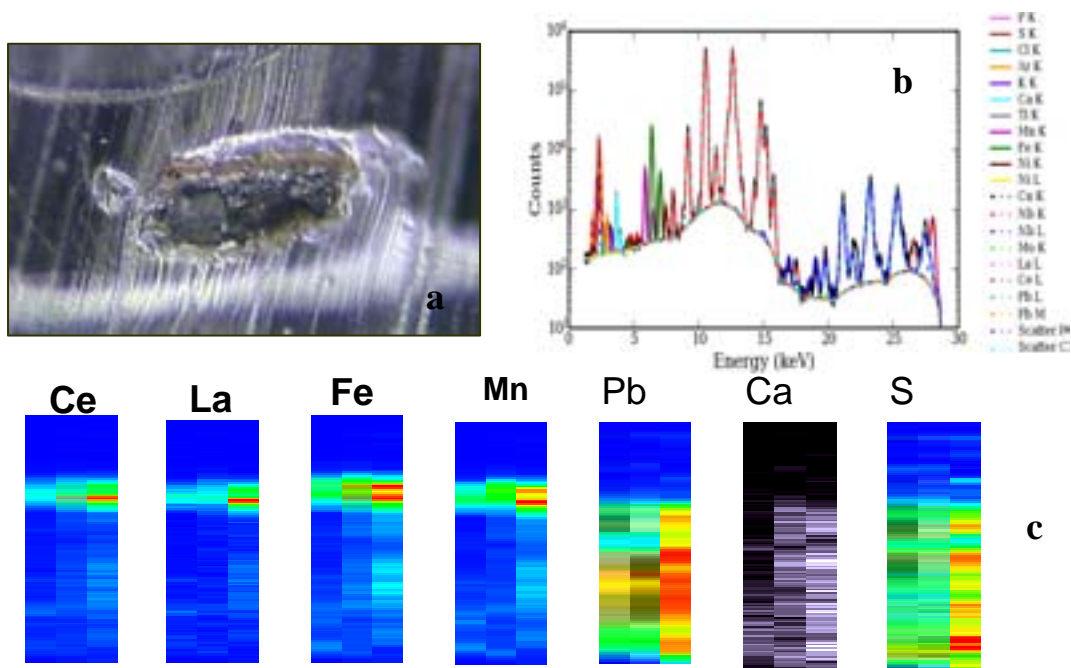


Fig. 2. (a) Area of the microsamples. Microanalysis of the brown layer (15 $\mu$ m  $\times$  15  $\mu$ m) (b) Calibration of the  $\mu$ -XRF spectrum, fitted with PyMCA of the sample (c) Elemental mapping using  $\mu$ -XRF of the sample

The zone of the X-ray fluorescence spectra where cerium appeared is shown in Fig. 3a. This zone is further illustrated by the pictorial layer shown in the 2D mappings (Fig 3b). The results had surprisingly good accuracy.

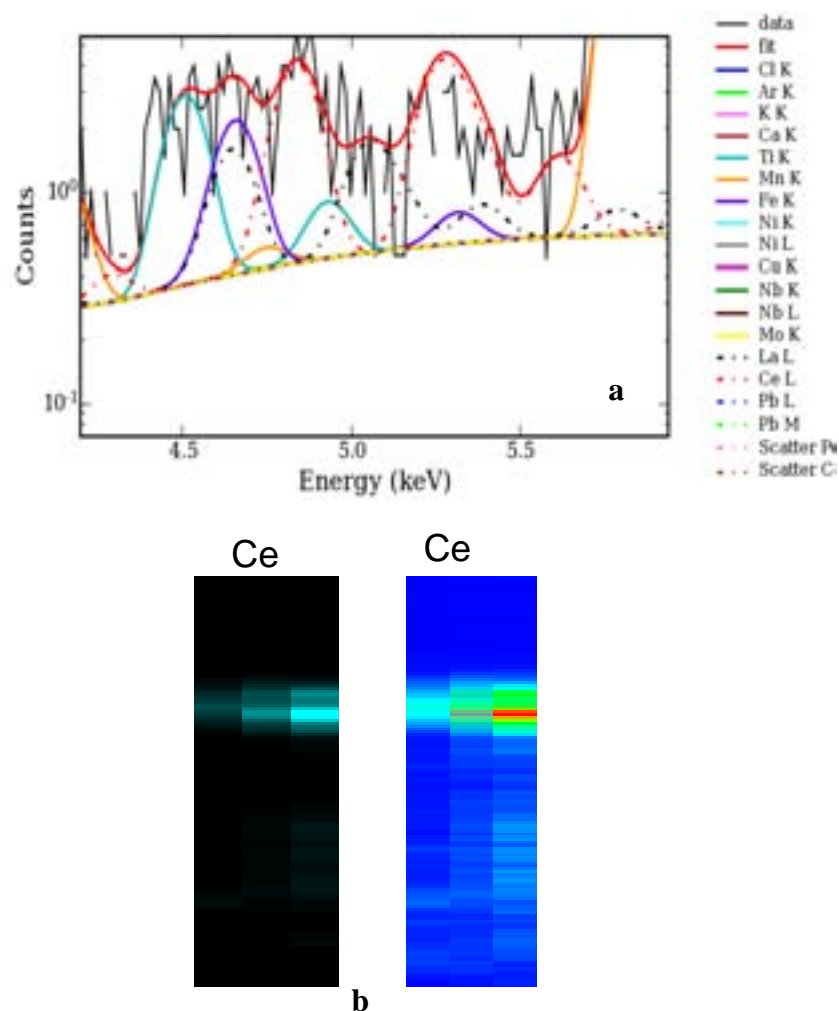


Fig. 3 (a) Area of the microsamples and microanalysis of the brown layer ( $15\mu\text{m} \times 15\mu\text{m}$ ) (b) Calibration of the  $\mu$ -XRF spectrum in the Ce L-edge (c) Elemental mapping of Ce in the sample

It was possible to determine the relative amounts of iron phases embedded in the heterogeneous matrix of the brown layer. The XRD patterns show the intensity variations of the peaks that are attributed to iron oxide and oxyhydroxides in the dark brown layer. The iron compounds found were goethite (Goe) and lepidocrocite (Lep) (Fig 4).

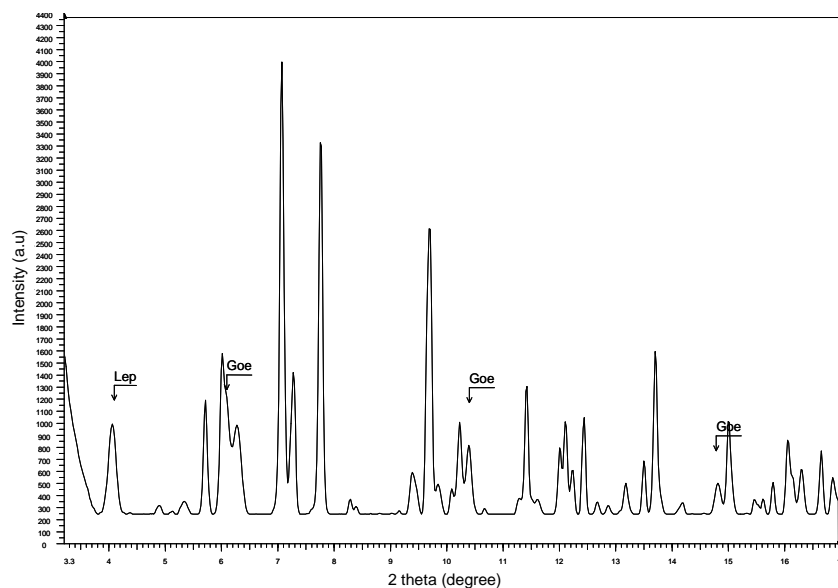


Fig. 4  $\mu$ -XRD patterns of the dark brown layer of sample

The most important finding of this study is the presence of monazite, which includes reddish-brown cerium and lanthanum phosphate  $[(\text{Ce},\text{La})\text{PO}_4]$ . The combined use of synchrotron- based image techniques allowed us to identify monazite in the brown layer of the samples from the nave of Gospel in San Agustin's Church in Cordoba, Spain (Fig 5).

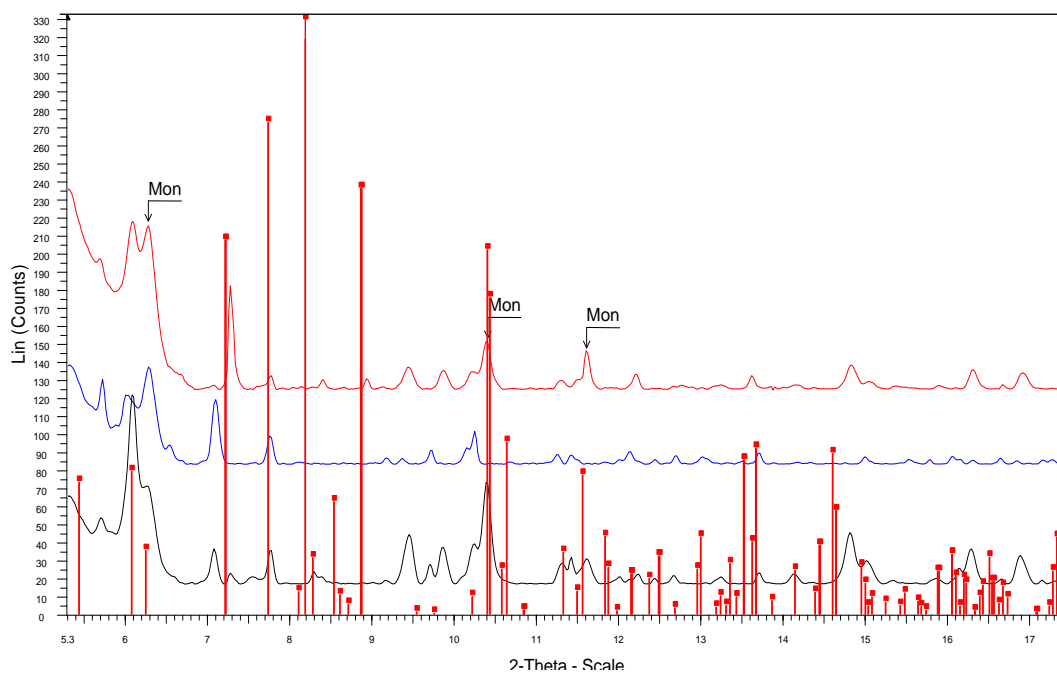


Fig. 5  $\mu$ -XRD pattern of the enrichment zone of Ce from the dark brown layer

### **I. 3.4. Conclusion**

These techniques have been demonstrated that are available for the study of painting layers in cross-sections. It's the first time that monazite (Mon) reports in the literature as a accompanying phase in the ochre ancient pigments together with iron oxide.

### **I. 3. 5. References**

[1] Bohic, S., Simionovici1, A., Biquard, X., et al. Synchrotron X-ray Microfluorescence and Microspectroscopy: Application and Perspectives in Materials Science. Oil & Gas Science and Technolog - Rev. IFP, Vol. 60 (2005), No. 6, pp. 979-993.

[2] Solé, V.A., Papillon, E., Cotte, M., Walter, PH., Susini, J. 2007. PyMCA: A multiplatform code for the analysis of energy-dispersive X-ray spectra. Spectrochimica Acta Part B: Atomic Spectroscopy 62 (1), 63-68.

## **I. 4. Characterisation of azurite and malachite pigments by combined application of $\mu$ -X-ray diffraction/ $\mu$ -X-ray fluorescence in cross sections from Spanish Baroque paintings**

### **Introduction**

There is a great deal of interest in copper minerals formed in numerous environmental situations. Two of the copper carbonate minerals, azurite  $2\text{CuCO}_3 \cdot \text{Cu}(\text{OH})$  and malachite  $\text{CuCO}_3 \cdot \text{Cu}(\text{OH})_2$ , are important both as pigments and as corrosion products. This work focuses on the use of these copper carbonates as pigments during the Spanish Baroque period. Azurite is a natural blue pigment that is derived from the mineral azurite and was the most important blue pigment in Europe beginning in the Middle Ages, but particularly from the fourteenth to the seventeenth century [1]. The pigment was prepared by carefully selecting material and then subjecting it to grinding, washing, levitation and flotation processes [1]. Malachite is perhaps the oldest known bright green pigment [2]. It is a basic copper carbonate similar in chemical composition to azurite, except that it contains a larger amount of water. The minerals, however, were used extensively for paintings in many different media from antiquity until relatively recently. Azurite's primary use since prehistoric times has been as a pigment [3]. Other authors [4] report that the blue and green pigments were never used in Paleolithic cave art, but it is possible that some of the black pigments observed on such drawings today could have been malachite or azurite pigments that decomposed into tenorite by heating [5]. Malachite and azurite must be ground quite coarsely to retain good colour as a pigment; the minerals become progressively paler as the particle size is reduced.

The copper pigments are usually detected by SEM/EDX [6, 7]. However the different phases cannot be characterised using this technique. The small quantity of copper phases in the pictorial layers, the use of mixture compounds, and the low crystallinity of compounds make their characterisation difficult with laboratory techniques. Other techniques, such as micro-infrared and micro-Raman spectroscopy and X-ray diffraction (XRD), have been used to determine the composition of copper pigments in the layers of paint in artwork [8, 9, 10]. Microanalytical methods using synchrotron radiation take advantage of properties such as the source of the brightness, which enable the beam size to be focused close to the diffraction limit (a few microns of the mid-infrared, down to submicron for X-rays) without compromising the flux. This

allows for the possibility of acquiring signal on a reduced pixel size with a smaller dwell time (less than one second for  $\mu$ XRF or  $\mu$ XRD). The combination of these two properties is a major asset when studying complex systems, such as copper phases in ancient paintings, and is essential while acquiring high-resolution 2D maps.

During the Baroque period, the most important painters, such as Zurbaran, Palomino and Bocanegra, received some of the most important contracts for painting many religious pieces of art in Andalusia. These paintings are characterised by their ability to highly control pigments, binders, and supports. In previous works [11, 12], the use of several pigments such as hematite, goethite, cerussite, hydrocerussite, cinnabar, and blue cobalt was identified [13], and binders such as animal glue, secative oils, mixtures of proteins and secative oils were also observed [11,13]. Copper pigments were very widely used (for the colour of the sky, clothing, etc.) in these paintings. Some of the blue colours made with azurite have turned greenish over time, which may be partially attributable to the hydration of this mineral to form malachite. Azurite is less stable than malachite, and is hence replaced by it over time [14]. Azurite can also be converted to other products by certain environmental factors, impacting the preservation of the materials that incorporated this mineral. For example, azurite can be darkened by exposure to sulphur fumes, perhaps due to sulphide formation, as seen especially in mural paintings. Gettens [1] reported cases of suspected azurite conversion to malachite and rarely to paratacamite; Riederer [15] found the azurite pigment in the facades of the elder temple of Aphaia at Aegina, Greece, which had been partially transformed to paratacamite. Azurite and malachite react with chlorine ions in the presence of moisture to form copper salts [4]. Some samples containing copper show the presence of atacamite due to NaCl coming from environmental pollution [14]. A clear example of a decaying process is presented by Dei et al. [16]. They exposed how the application of ammonium carbonate and barium hydroxide to some wall paintings induced the degradation of azurite to paratacamite and copper hydroxide, leading to a remarkable colour change. In general, the presence of atacamite may be attributed to the transformation of azurite by the chloride ion due to the slow ingress of a saline solution or groundwater into the wall paintings [17]. Castro et al. [18] presented another interesting example where the presence of moolooite (copper oxalate) was found in different artwork as a degradation product of malachite after biological attack. The interactions of copper pigments with oil-binding media have also been studied [19, 20]. The thick layers of azurite in oil paintings

often become greenish or dark with age, which probably results from the reaction of the copper with an oil medium to produce a variety of copper organometallic compounds, such as copper resinates or oleates. Studies focused on the degradation of copper pigments into oil media are not very common in field of the wall paintings.

#### **I. 4. 1. Research aims**

The main objective of this work is:

Characterise the azurite pigment and its possible degradation to malachite in Spanish Baroque paintings from the seventeenth century.

To demonstrate the advantages of using combined Synchrotron-based  $\mu$  X-ray diffraction and  $\mu$  X-ray fluorescence over conventional X-ray diffraction in the identification of paintings and in the analysis of pictorial layers, including grains, at the micrometer scale, will be demonstrated.

The relative abundance of carboxylic acids present in the binding medium was also evaluated in the azurite transformation.

#### **I. 4.2. Experimental**

The paintings used for the sampling of the green colours included works by some of the most important Andalusian Baroque painters (Fig.1), such as: Francisco Zurbaran, with one sample taken from the “*San Pascual*” canvas (1640) and another from the “*Jesus Coronando a San Jose*” canvas (1630), which are part of the important collection of the Fine Arts Museum of Seville; Antonio Palomino, with two samples from the “*Inmaculada*” canvas (1672-1676) from the Fine Arts Museum of Granada; and Pedro Atanasio Bocanegra, with one sample taken from “*San Ignacio herido en las puertas de Pamplona*” (1668), which belongs to the collection located in the San Justo y Pastor church in Granada.

##### **I. 4.2.1. Sample preparation**

Sample preparation is often a tricky point for the study of micrometric fragments of paintings [21]. It may be difficult to carry out all the experiments of a unique sample; conversely, when the quantity of painting fragment is enough, different sample preparations may be followed to fit the technical requirements of each analytical technique.



Fig. 1 Cavases paintings: (a) “*San Pascual*” (b) “*Jesus Coronando a San Jose*” (c) “*Inmaculada*” (d) “*San Ignacio herido en las puertas de Pamplona*”

Three types of sample preparation were performed. The first one consisted of polishing a cross section after embedding in a resin the sample was cut to expose a face showing the cross sections of the paint layer. Finally, the surface was carefully polished on a rotating disc covered with abrasive SiC paper with a grain size from 800 to 1200 mesh and finished with a cloth. This method was useful for using optical microscopy, SEM/EDX, and FTIR spectroscopy, which require a more careful preparation of the polished surface.

The second way was by preparing thin cross sections obtained using a microtome to cut the samples that were embedded in a resin (Leica Histo-resin). Several slice thicknesses were tested, and 20-30  $\mu\text{m}$  was chosen as the appropriate thickness. The presence of the embedding resin was not an inconvenience for the SR  $\mu\text{XRF}/\mu\text{XRD}$  analyses [22]. Finally, small fragments of the samples were ground to a powder form for examination by conventional XRD and for PY-GC/MS [23].

### **I. 4.3. Results and discussion**

#### **I. 4.3.1 Analysis of the blue-green layer in the samples**

Figure 2a depicts the light-optical micrograph of the blue cross section taken from the Inmaculada Virgin dress painted by Palomino (sample 1). This cross section shows the mixture of the blue grains with the white grains in the upper layer; the sizes of the blue grains are bigger than the other grains observed in this layer. The thickness of this layer is about 100  $\mu\text{m}$ . The EDX analyses (Fig. 2b) of blue layer showed the presence of carbon, oxygen, copper and lead; in addition, silicon, calcium and iron peaks appeared with low intensities. The blue particles are only comprised of copper, carbon and oxygen; the conventional XRD pattern of the blue layer (Fig. 2c) allowed for identification of the azurite, hydrocerussite, cerussite and quartz phases.

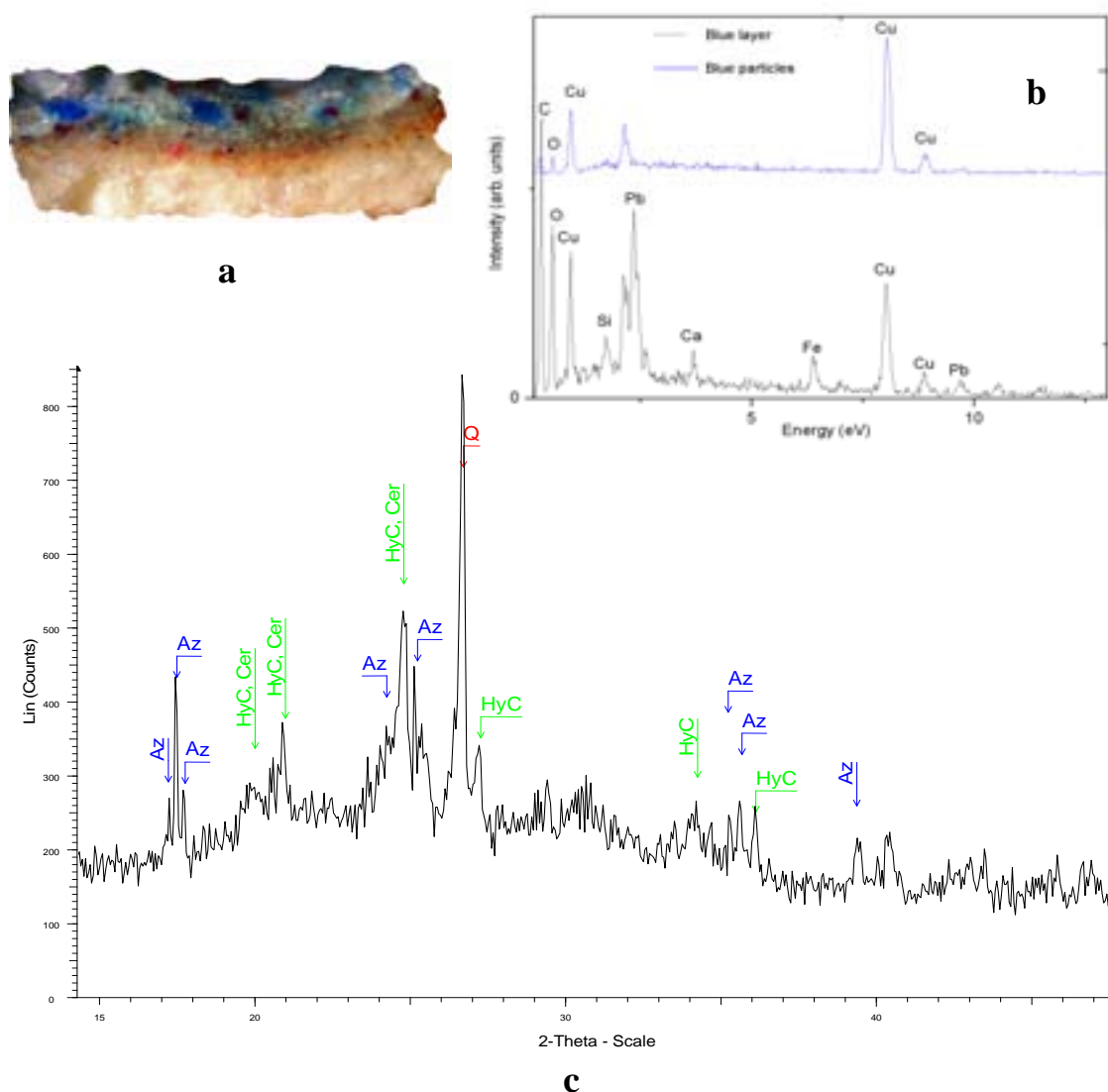


Fig. 2 Conventional cross section of paint samples (a) Micrographs originating from Inmaculada Virgin's dress by Palomino. (b) EDX spectra of the blue layer. (c) X-ray diffraction pattern of powder blue layer, obtained with a  $1^\circ$  incidence angle and whose peaks can be attributed to the presence of azurite (Az), cerussite (Cer), hydrocerussite (Hyc), and quartz (Q).

Sample 2 was taken from the sky of the "Inmaculada Virgin" painted by Palomino (Fig. 3a). The EDX analysis of the blue/green layer showed the presence of carbon, oxygen, copper, silicon, lead and iron. Different particle sizes of pigments were present in this sample. The punctual analysis carried out by EDX reported that these layers are comprised of copper, carbon and oxygen (Fig. 3b). The Conventional XRD pattern did not show the presence of the copper phases, but hydrocerussite and cerussite being the only phases identified (Fig. 3c).

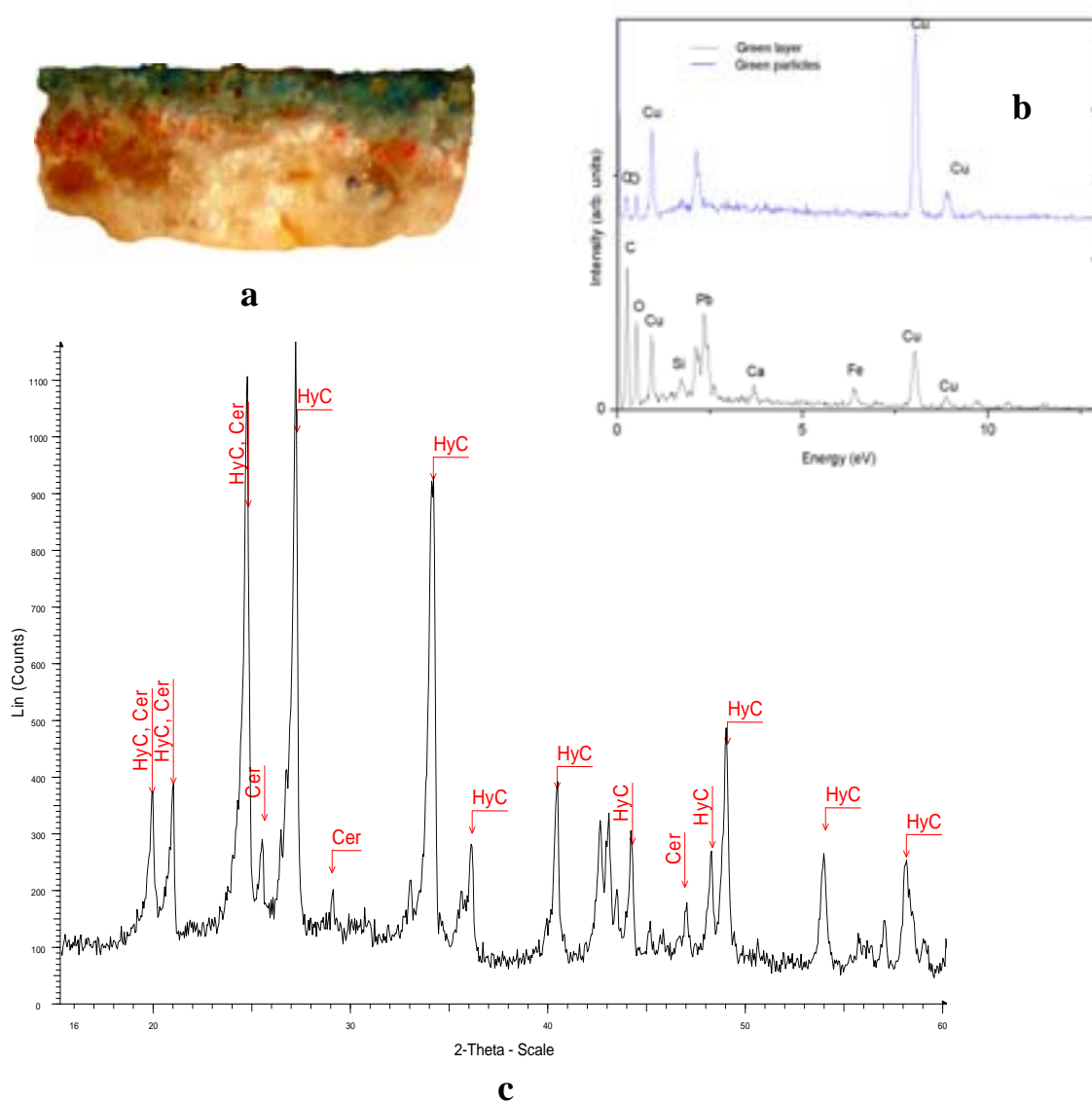


Fig. 3 Conventional cross section of paint samples (a) Micrographs originating from Inmaculada Virgin by Palomino. (b) EDX spectra of the blue layer. (c) X-ray diffraction pattern of total powder sample, obtained with a  $1^\circ$  incidence angle and whose peaks can be attributed to the presence of cerussite (Cer) and hydrocerussite (Hyc).

Sample 3, taken from the dress of “San Jose” (Zurbaran canvas), was also a blue coloured layer (Fig.4a), but was thinner and with smaller grains than sample 1. Copper and lead were also detected by EDX analysis (Fig.4b). However, the main element of the blue grains was copper. Meanwhile, the Conventional XRD data from these samples detected only the presence of hydrocerussite, anhydrite and quartz (Fig.4c). The copper pigments may be present as minor phases, and the classical XRD lab instrument may not be sensitive enough to detect these phases.

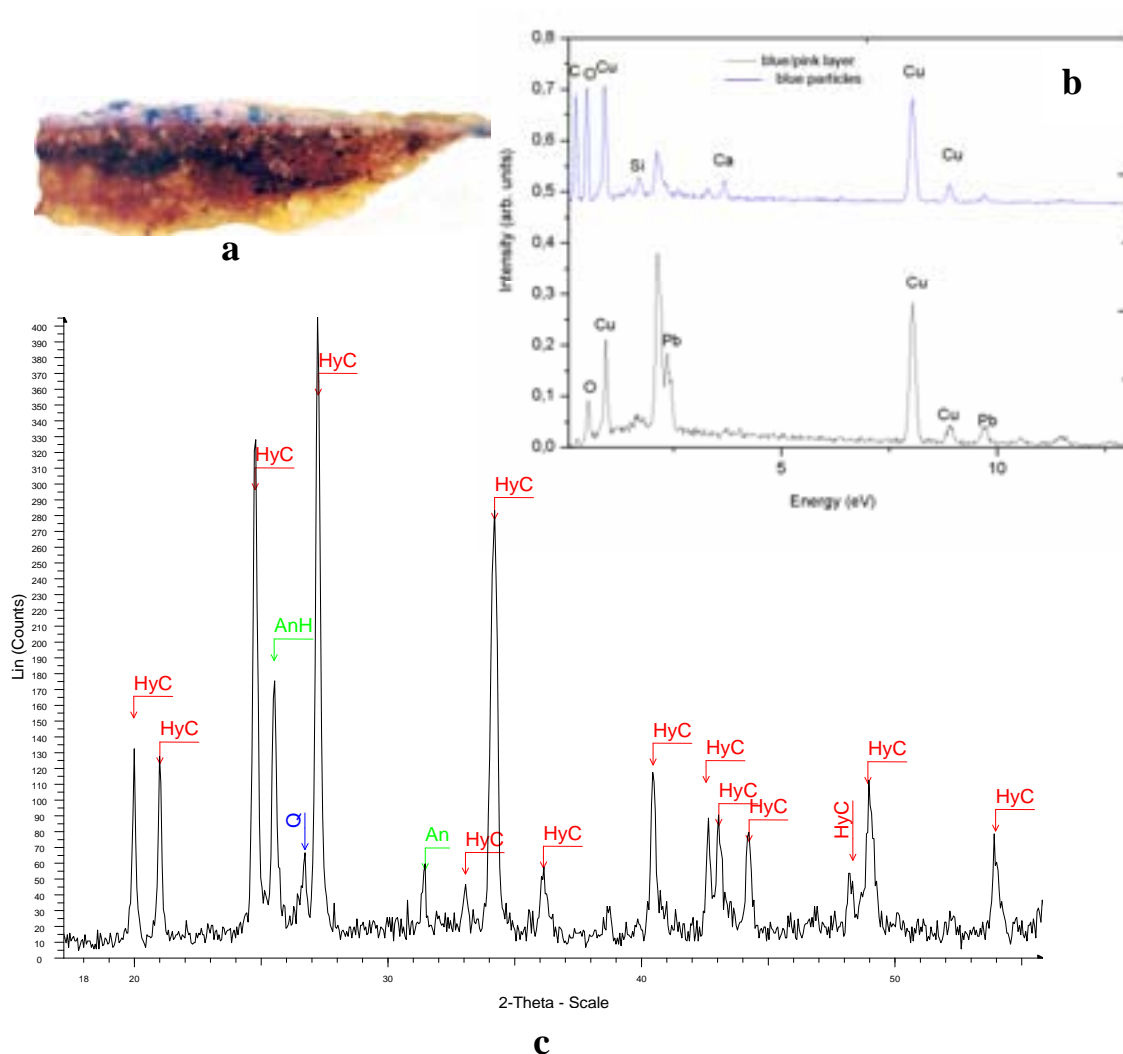


Fig. 4 Conventional cross section of paint samples (a) Micrographs originating from *San Jose's* dress in the *Jesus Coronando a San Jose* by Zurbaran. (b) EDX spectra of the blue layer. (c) X-ray diffraction pattern of the total powder sample, obtained under a  $1^\circ$  incidence angle and whose peaks can be attributed to the presence of hydrocerussite (Hyc), anhydrite (Ah) and quartz (Q).

Sample 4, coming from the “San Pascual” canvas painted by Zurbaran, exhibited a green coloured layer (Fig. 5a) that was mainly comprised of copper and lead in the upper layer. Calcium was also present in this layer (Fig.5b). Hydrocerussite and gypsum phases were revealed by conventional XRD patterns of the total powdered sample (Fig.5c).

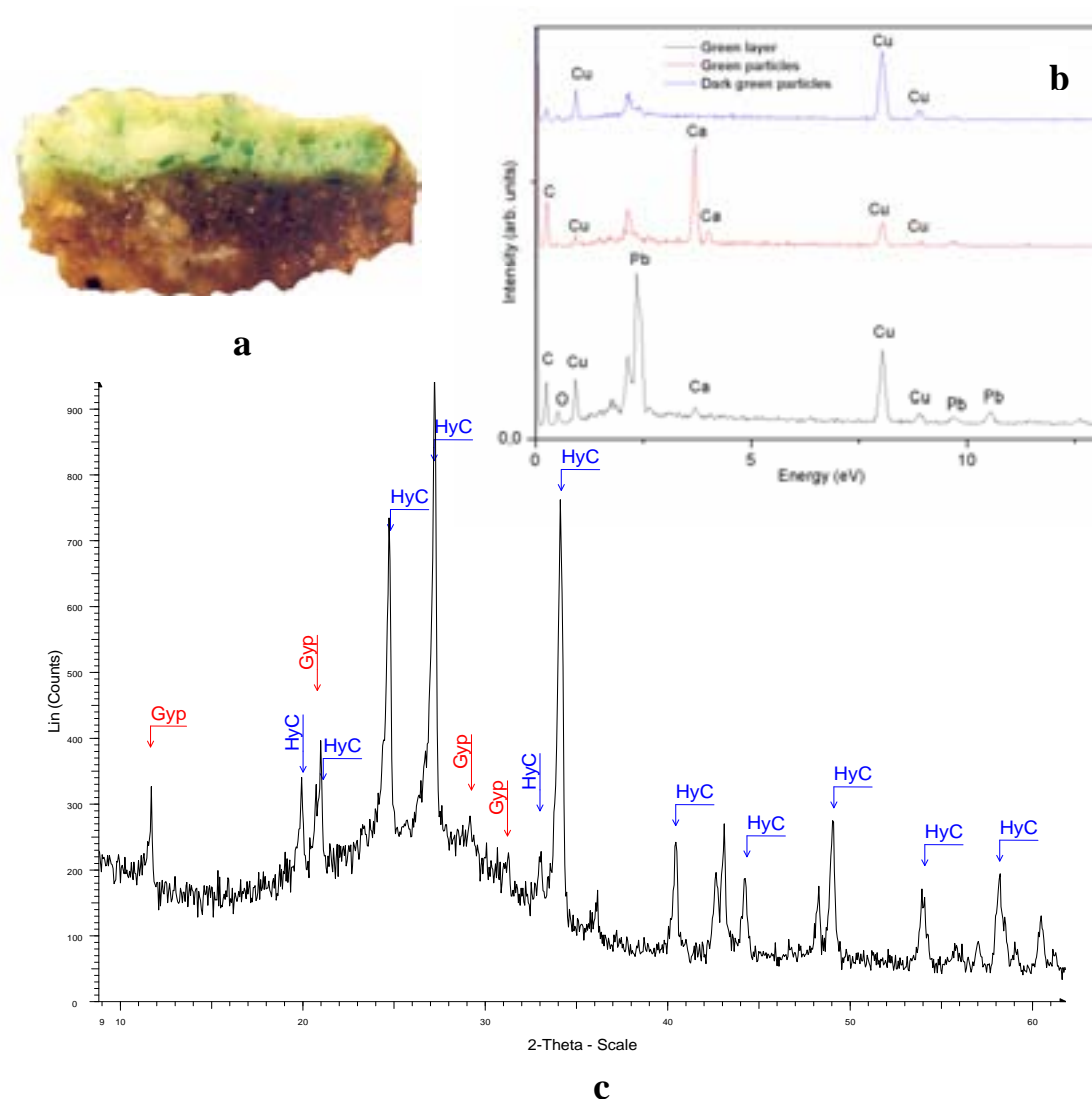


Fig. 5 Conventional cross section of paint samples (a) Micrographs originating from *San Pascual* by Zurbaran. (b) EDX spectra of the green layer. (c) X-ray diffraction pattern of the total powder sample, obtained at a  $1^\circ$  incidence angle and whose peaks can be attributed to the presence of gypsum (Gyp) and hydrocerussite (Hyc).

EDX analyses of samples 3 and 4 showed similar elemental composition of the blue/green grains, however the colours were different, which suggested that the phases present were not the same. Figure 6a illustrates a cross section microphotograph taken from “*San Ignacio herido en las puertas de Pamplona.*” This sample was selected due to the complex undefined colour used by the painter Bocanegra. In the thin cross section it is possible to identify blue, green and red grains with different particle sizes that were distributed in the colour layer. The elemental analysis of the colour layer revealed carbon, oxygen, silicon, copper, lead, potassium and iron. Punctual EDX analyses detected copper from the blue and green particles and iron from the red particles (Fig. 6b).

The XRD pattern only provided information about the support layer (gypsum, calcite and anhydrite) (data not shown).

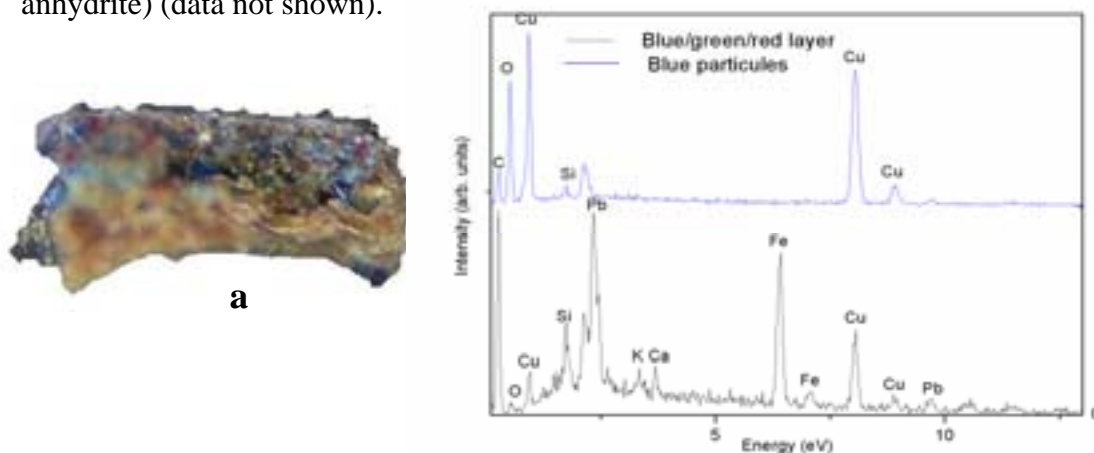


Fig. 6 Conventional cross section of paint samples (a) Micrographs originating from *San Ignacio Herido en las Puertas de Pamplona* by Bocanegra. (b) EDX spectra of the green / blue/ red layers.

The micro Raman studies of the blue layer (Fig. 7a) of samples 1, 2 and 3 revealed the presence of azurite (absorption bands at 395, 760, 830, 931 and 1094  $\text{cm}^{-1}$ ). The green grains of sample 4 were identified as malachite (Fig. 7b). The characteristic bands (around 217, 265, 350, 430, 531  $\text{cm}^{-1}$ ) and the characteristic stretching vibration of carbonates (1050-1100  $\text{cm}^{-1}$ ) are identified around

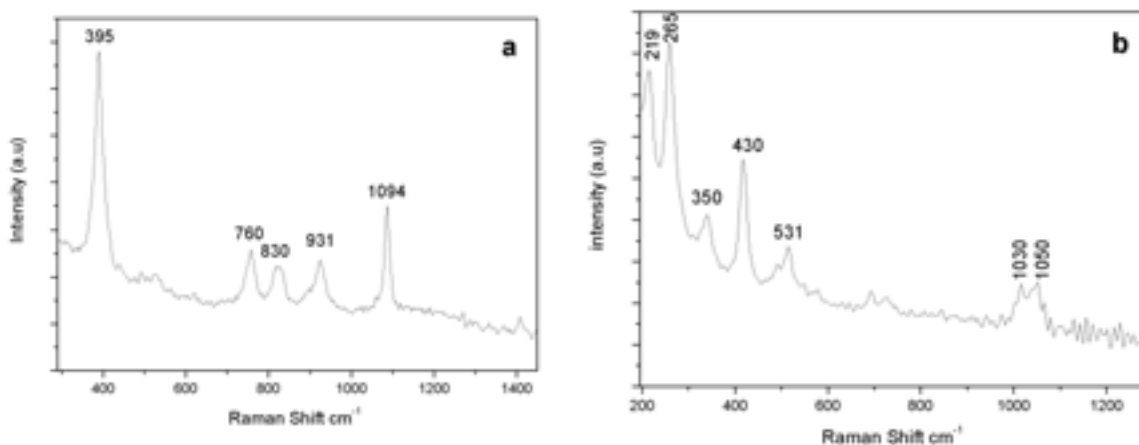


Fig. 7 (a) Micro Raman spectra in the blue layer of sample 2 and (b) Micro Raman spectra in the green layer of sample 4.

Due to the high complexity of sample 5 the study by Raman showed some difficulty to assign the different absorption bands for the pigment identification. Consequently the obtained information was not enough to carry out a precise characterisation.

### I. 4.3.2 Identification of organic components in the blue layers of the samples

The FTIR spectrum acquired from the blue/green/red layer of sample 5 (Fig.8a) showed bands that could be attributed to carbonates in a smaller proportion ( $1400\text{-}1449\text{ cm}^{-1}$ ) than oils ( $1700\text{-}1730, 1149\text{ cm}^{-1}$ ). In the FTIR spectrum of sample 1 (Fig 8b), it was possible to distinguish the carbonate and oil bands, but in different proportions than in sample 5. The other samples studied in this work contain carbonates and oils in the colour layer. These results were not very conclusive because the copper pigment was not identified. A small absorption band in samples 5 that appear at  $1580\text{ cm}^{-1}$  may be attributed to the presence of some carboxylates compounds. The chromatograms obtained from analytical pyrolysis (Fig.8c) of all the samples were dominated by peaks associated with the methyl esters of long chain aliphatic monocarboxylic acids, such as palmitic and stearic acids. These are typical compounds derived from the TMAH pyrolysis-methylation of lipid materials containing fatty acid derivatives, such as natural waxes, eggs and drying oils [24]. The detection of high concentrations of dimethyl esters of azelaic acids (nonanedioic acid), together with the presence of suberic (octanedioic acid) dimethyl ester, suggested the use of secative oils as a binding medium. Dicarboxylic acids, such as azelaic and suberic acids, are formed during polymerization and ageing of the secative oils. Nevertheless, the detection of these acids is a common finding in the PY-GC/MS analysis of different aged secative oils in the presence of TMAH; however, it is not possible to unambiguously assign the results to a specific secative oil.

### I. 4.3.3 $\mu$ XRF/ $\mu$ XRD analysis of a thin cross section

XRD has been proven to be a valuable tool for the clear identification of inorganic pigments. However, with conventional XRD, it is rather difficult to acquire all of the information from these samples due to the thinness of the blue/green colour layers, which are in the range of several tens of microns. Furthermore, the contributions of the small quantities of the copper pigments to the total sample are very low. It was only possible to identify the presence of azurite in sample 1 because the blue layer was in a higher proportion compared with the other samples. The phase was straightforwardly identified, but the peaks from each phase showed a significantly different broadening. Azurite was characterised in the blue layer in samples 2 and 3, and malachite was identified in the

green layer of sample 4 using micro Raman spectroscopy. Due to the small grains present in sample 5, it was difficult to identify the blue, green, and red pigments that appeared mixed within a single layer.

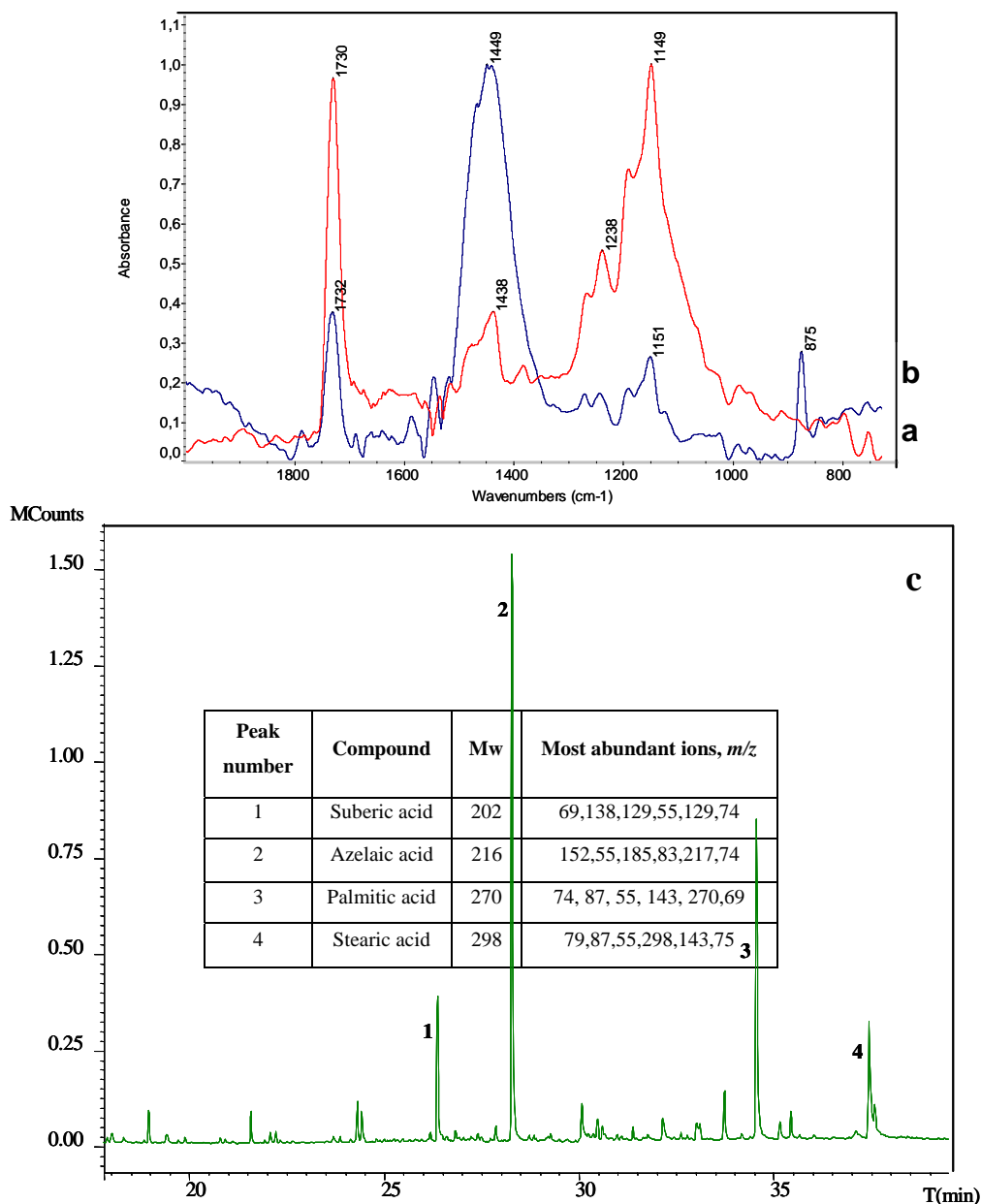


Fig. 8 FTIR spectra corresponding to: (a) the blue/green/red layer of sample 5, showing the presence of bands corresponding to carbonates ( $1400\text{-}1449\text{ cm}^{-1}$ ) and drying oils ( $1730$  and  $1149\text{ cm}^{-1}$ ) (b) blue layer of sample 1, showing the presence of carbonates ( $1400\text{-}1438\text{ cm}^{-1}$ ) and drying oils ( $1732$  and  $1151\text{ cm}^{-1}$ ) (c) reconstructed ion chromatogram obtained from pyrolysis/methylation of sample 5. The numbers on top of the peaks refer to the table (mass spectra characteristics of compounds evolved from pyrolysis methylation and structural attribution to peak numbers).

To solve the difficulties involving the characterisation of different pigments coexisting in the same color layer of sample 5, experiments using  $\mu\text{XRF}/\mu\text{XRD}$  on the

thin cross sections of this sample were conducted to illustrate the potential of the combination of these techniques [25] (Fig 9a). Two-dimensional mapping was performed with the simultaneous acquisition of diffraction patterns (in transmission) and fluorescence spectra (at 90° from the incoming beam, in the horizontal plane) at each pixel of a 2D-array. This sample was selected due to the complexity of the pictorial layer containing the different pigments (red, blue and green). In addition, the high concentrations of carboxylic acids suggested possible changes in the copper pigments. Fluorescence and diffraction data sets were simultaneously handled with PyMCA. There is clear complementary in analyzing the parallel elemental and structural information provided by XRF and XRD. In Fig 9b, an  $\mu$ XRF spectrum shows the K lines for Cu and Fe. The thin cross section is superimposed on some of the elemental mapping (Cu and Fe). The average diffraction patterns were calculated over the same identified areas (see Fig 9c). In the pictorial layer of this sample, it was possible to identify the different grains. The use of this technique allowed for the determination that the blue grains had an azurite pattern (Fig.9d). The green and the red grains were identified as malachite and hematite phases, respectively (Fig. 9e and Fig. 9f). The presence of hematite in this layer demonstrated that this pigment was extensively used during this period. The painter Bocanegra mainly used the ruby red colour in the pictorial layers reported in other paintings [13].

These results reveal a complex painting technique, due to the contribution of the inorganic pigments and the binding medium in the thin pictorial layer. This information was used to try to explain the mixture of azurite and malachite in the same layer. Azurite turns greenish, which may be partially attributed to the hydration of this mineral to malachite. Malachite has a similar composition to azurite, except that it contains a larger amount of water. Azurite is less stable than malachite, and hence, is replaced by it. Gunn et al. [26] report some changes in the copper pigments in the painting layers. Carboxylic and fatty acids present in the oil media of the paintings interact with the copper ions associated with azurite or/and malachite. These interactions could contribute to the formation of copper carboxylates due to the complexation of copper ions with the carboxylic acid groups of the polymeric network in oil paintings. FTIR shows a small absorption bands at 1580  $\text{cm}^{-1}$  that confirm the presence of carboxylates. The formation of copper carboxylates can not be rejecting in the Spanish baroque paintings studied in this work.

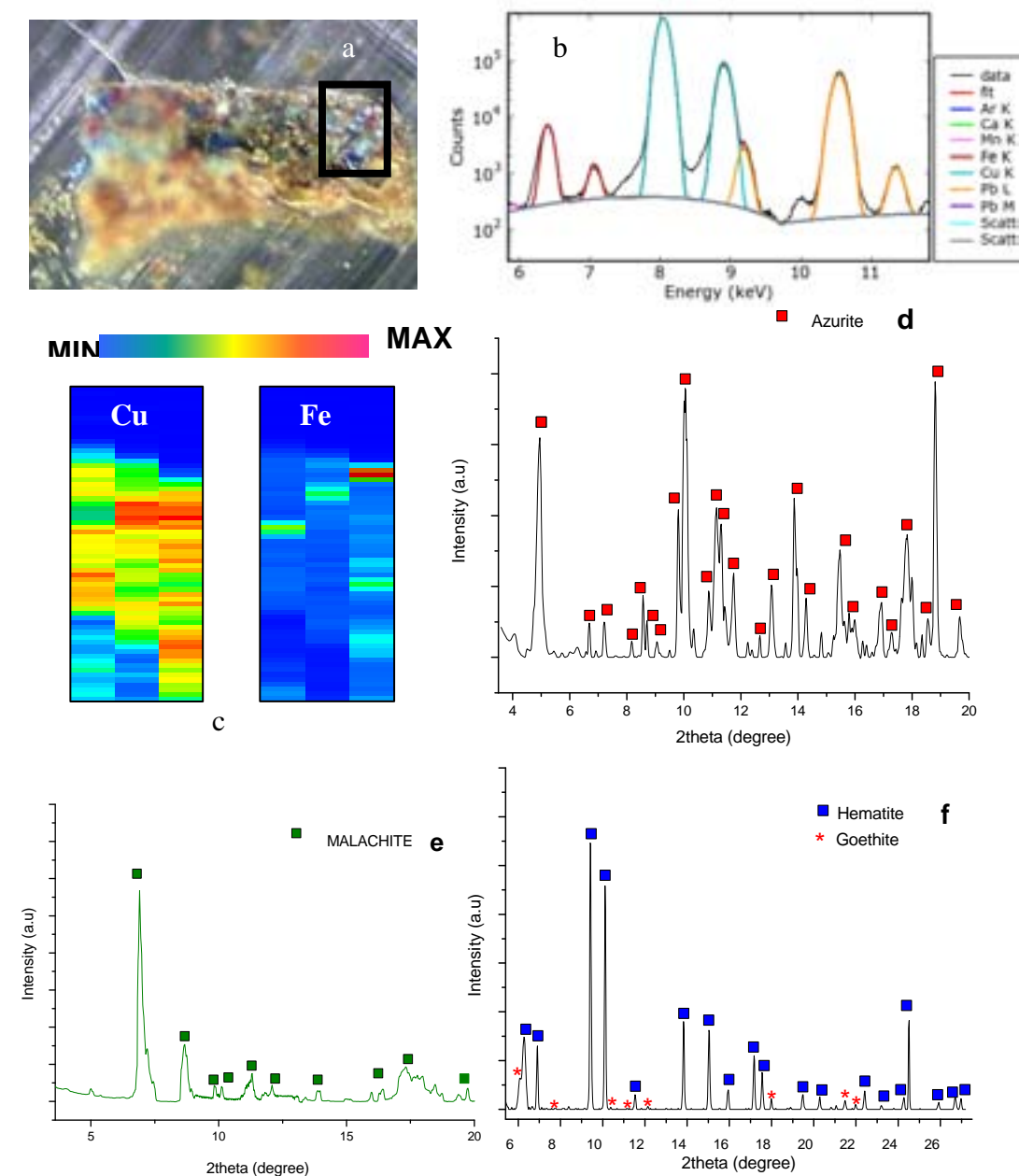


Fig. 9 (a) Thin cross-section micrographs of sample 5, (b)  $\mu$ XRF spectrum, (c) elemental maps of Cu and Fe obtained in the pictorial layer, (d) SR  $\mu$ XRD pattern of blue grains, (e) SR  $\mu$ XRD pattern of green grains, and (f) SR  $\mu$ XRD of red grains.

The presence of a mixture of these two copper pigments in the same layer could be attributed to a mixture of both pigments carried out by the painter to find a different blue/green tone. The information obtained using  $\mu$ XRF/ $\mu$ XRD allowed us to conclude that the green grains could be attributed to malachite phases and the blue grains could be attributed to azurite phases. The mixture of the two phases in the same grain was never detected. Also, copper carboxylates have been detected suggesting the possible transformation of the copper pigments.

#### I. 4.4. Conclusions

Synchrotron-based  $\mu$ -XRD and  $\mu$ -XRF are particularly suited to the study and micro-characterisation of the different materials present in multi-layered paintings. This study demonstrated that synchrotron radiation micro-imaging techniques have ability to analyze pictorial layers, including grains, at the micrometer scale, which present some difficulties to achieve with other laboratory techniques.  $\mu$ -XRD is very useful for the identification of phases that are present in low proportion in multilayer paintings with different inorganic pigments, such as cerussite and hydrocerussite, and those with lower reflecting powder, like azurite, malachite, hematite, and goethite. The azurite to malachite conversion was not observed. The mixture of both phases into the same grains was not detected. The possible presence of copper carboxylates identified by FTIR suggests the possible interaction between carboxylic acids and copper pigments. Micro Raman spectroscopy has been very useful for the identification of copper pigments. Some difficulties have been detected by Raman study that was solved by synchrotron-based  $\mu$  X-ray diffraction and  $\mu$  X-ray fluorescence in sample 5 where the pigments was observed as small grains and mixture with other pigments.

#### I. 4.5. References

- [1] R.J. Gettens, G.L. Stout: *Painting materials*. (Dover Publications, Inc., New York 1966) p. 350
- [2] J.R. Barnett, S. Miller, E. Pearce: *Opt. Lasers Eng.* 38, 445 (2006)
- [3] P. Ucko, A. Rosenfeld: *Arte Paleolítico*. (Ed. Guadarrama Madrid 1967), p.185
- [4] D.A. Scott: *copper and bronze in* (Getty Publications., Los Angeles 2002) p.513
- [5] I. A. Kiseleva, L. P. Ogorodova, L. V. Melchakova, M. R. Bisengalieva and N. S. Becturganov: *Phys. Chem. Miner.* 19, 322 (1992)
- [6] N. Salvadó, T. Pradell, E. Pantos, M.Z. Papiz, J. Molera, M. Seco, M. Vendrell-Saz, M. J. Synchrotron Radiat. 9, 215 (2002)
- [7] N. Salvadó, PhD Thesis, Barcelona University, Spain (1998), p. 351
- [8] M.L. Franquelo, A. Duran, L.K. Herrera, M.C. Jimenez de Haro, J.L. Perez Rodríguez: *J. Mol. Struct.* (2009) *in press*

- [9] S. Bruni, F. Cariati, F. Casadio, L. Toniolo: *Vib. Spectrosc* 20,15(1999)
- [10] R. L. Frost, W. N. Martens, L. Rintoul, E. Mahmutagic, J. T. Kloprogge: *J. Raman Spectrosc.* 33, 252 (2002)
- [11] A. Duran, PhD Thesis, Seville University, Spain (2006), p.480
- [12] L.K. Herrera, A. Justo, J.L. Perez Rodriguez, A. Duran. Technical report (ICMSE-CSIC, 120p. 2007)
- [13] L.K. Herrera, S. Montalbani, G. Chiavari, M. Cotte, V.A. Solé, J. Bueno, A. Duran, A. Justo, J.L. Perez Rodriguez: *Talanta* (2009) Submitted
- [14] J.L. Pérez-Rodríguez, C. Maqueda, M.C. Jiménez De Haro, P. Rodríguez-Rubio: *Atmos. Environ.* 32, 993 (1998)
- [15] J. Riederer: *Archaeometry* 16, 102 (1974)
- [16] L. Dei, A. Ahle, P. Baglioni, D. Dini, E. Ferroni: *Stud. Conserv.* 43, 80 (1998)
- [17] K. Castro, A. Sarmiento, I. Martínez-Arkarazo, J. M. Madariaga, L. A. Fernández: *Anal. Chem.* 80,4103 (2008)
- [18] D.A. Scott: *Stud. Conserv.* 45, 39 (2000)
- [19] G. Gautier, M.P. Colombini: *Talanta.* 73, 95 (2007)
- [20] E. Ioakimoglou, S. Boyatzis, P. Argitis, A. Fostiridou, K. Papapanagiotou, N. Yannovits: *Chem. Mater.* 11, 2013 (1999)
- [21] M. Cotte, E. Checroun, V. Mazel, V. A. Solé, P. Richardin, Y. Taniguchi, P. Walter, J. Susini: "Combination of FTIR and X-rays synchrotron-based micro-imaging techniques for the study of ancient paintings. A practical point of view", e *PRESERVATIONScience*, *in press*
- [22] L.K. Herrera, M. Cotte, M.C. Jimenez de Haro, A. Duran, A. Justo, J.L. Perez Rodriguez: *Applied Clay Science* 42, 57 (2008)
- [23] G. Chiavari, S. Prati: Analytical pyrolysis as diagnostic tool in the investigation of works of art. *Chromatographia* 58, 543 (2003)
- [24] G. Chiavari, D. Fabbri, S. Prati: *J. Anal. Appl. Pyrolysis.* 74, 39 (2005)
- [25] M. Cotte, J. Susini, A. Solé, Y. Taniguchi, J. Chillida, E. Checroun, P. Walter: *J. Anal. At. Spectrom.* 23, 820 (2008)
- [26] M. Gunn, G. Chottard, E. Rivière, J.J. Girerd, J.C Chottard *Stud. Conserv.* 47, 12 (2002)

## II. Hg/Sn amalgam degradation of ancient glass mirrors

### Introduction

From the sixteenth to the beginning of the twentieth century, the most widely used mirror was a pane of glass backed with a tin-mercury amalgam, commonly called the amalgam mirror [1,2]. It is difficult to determine when the tin amalgam mirror processing technique was discovered; however, the first known production centre of these mirrors was Venice in 1507. The Dal Gallo brothers from Murano Island [2] had developed a new method to make mirrors [3, 4] where the metals used were in fact an amalgam of tin and mercury. The amalgam was a two-phase system: crystals of tin-mercury compounds were surrounded by a mercury rich liquid phase [2]. Their method entailed backing a plate of flat glass with a thin sheet of reflecting metal. This technology became widespread in Venice, with the Venetian mirror industry ultimately dominating the market until the middle of the seventeenth century.

The technology for the production of tin amalgam mirrors is described in [2,5]. First, a tin film of about 0.1 mm is laid on a perfectly flat plate of marble. Thereafter, mercury is poured onto the tin film. For a mirror with a surface area of 30 to 40 cm<sup>2</sup>, a large amount of mercury, between 75 to 100 kg, is necessary [6]. Then, a mechanically polished and cleaned glass pane is slid over the mercury, with the leading edge dipped into the mercury, but without scraping the tin film. Afterwards the glass is pressed down, and the table with the marble plate is tilted slowly so that the excess mercury can flow off. Within 24 hours, the tin foil is completely transformed into the amalgam alloy [6]. The complete hardening process takes up to one month, depending on the size of the mirror.

Corrosion of the tin-mercury alloy surface of amalgam mirrors produces tin dioxide and tin monoxide and releases liquid mercury from the solid phase. In order to gain further insight into these surfaces, the microstructure of the tin amalgam mirror layers have been investigated by preparation of metallographic cross-sections. This chapter presents the analytical approach, which combines techniques including scanning electron microscopy (SEM), X-ray analysis (EDX), Raman spectroscopy, Fourier transform infrared spectroscopy (FTIR), grazing incidence diffraction (GID), surface-spectroscopic methods (XPS and REELS), and transmission electron microscopy (TEM), and synchrotron radiation based X ray diffraction (SR-XRD) used to characterize five

amalgam surfaces, with different alteration degrees, dated between the XVII–XVIII centuries from historical buildings in Andalusia, Spain.

### II.1. Research aims

The main objectives of this chapter are to:

- (i) Characterize the alloy in order to identify the elements and compounds (Sn, Hg, Sn–Hg alloys, SnO, SnO<sub>2</sub>) possibly involved in the corrosion processes. Also, qualitatively analyze the corrosion phases from ancient tin-mercury mirrors by measuring the changes in diffraction profiles as a function of the thickness of the alloy.
- (ii) Contribute to a better understanding of the degradation of amalgam mirrors present in historical buildings. Specific emphasis has been made on the study of corrosion products and the alloying element. The knowledge of these mechanisms will help to find measures to better preserve these art objects.

### II.2. Samples studied

Among all the baroque mirrors, collected from historic buildings and belonging to the cultural heritage of the south of Spain (Fig.1), five were selected in this work as representative examples of four unique situations (Table 1).

Table-1. Description of the mirrors

Sample	Century	Location and description
1	XVII	The samples were obtained from the Hermitage of the “ <i>Cristo del Llano</i> ” (17 <sup>th</sup> Century), which is located in a village of the northern district of Jaén, in the middle of the <i>Sierra Morena</i> mountains. The mirror was mounted in the wood frame of a large baroque altarpiece. The amalgam layer was scarcely corroded. The environment was classified as a rural atmosphere.
2	XVIII	The samples were obtained from “ <i>Camerin Virgen del Rosario</i> ” in the <i>Santo Domingo</i> Convent in Granada. The mirror fragments were enclosed in different frames of baroque ornamentation in the <i>Camerin</i> , and the back side of the mirror was in contact with a gypsum wall. The amalgam layer was completely corroded. The environment was classified as an urban atmosphere
3	XVIII	The samples were obtained from mirrors of the “ <i>Santiago</i> ” church in <i>Écija</i> . The mirror was mounted in a wooden frame. The amalgam layer was completely corroded and no longer adhering to the glass. The environment was classified as an urban atmosphere that was exposed to very high temperatures in the summer.
4	XVIII	The samples were taken from the “ <i>Santa Ana</i> ” parish church in Seville. The mirror was mounted in a wooden frame, and its back was covered with a wooden panel. The dust behind the mirror contained drops of mercury. The amalgam layer was corroded. The environment was classified as an urban atmosphere; however, in the past, it was an industrial atmosphere with ceramic factories
5	XVII	These mirror fragments were obtained from the same altarpiece as sample 1. These pieces of mirror exhibited a small corroded area.



Fig .1 (a) Sample 1: Hermitage of the “*Cristo del Llano* (Jaen) (b) Sample 2: “*Camerin Virgen del Rosario*” in the *Santo Domingo* Convent (Granada). (c) Sample 3: “*Santiago*” church (*Ecija*). (d) Sample 4: “*Santa Ana*” church (Seville).

### II.3. Experimental methods

The mirrors were studied using optical and scanning electron microscopy. Prior to SEM/EDX investigation using a JEOL JSM 5400 microscope, the samples were coated with a gold film. Semiquantitative analyses of the elemental composition of the amalgams were obtained using a Link ISIS Energy Dispersive X-Ray Spectrometer and an accelerating voltage of 20 keV. For the spectroscopic characterisation of the amalgams,

Micro-Raman measurements were performed using a Horiba / Jobin Yvon LabRaman system, cooled charge coupled device (CCD) detection, and 632.8 nm He–Ne laser excitation. Micro-Raman spectra were obtained by scanning across a sample using 10× and 50× objectives with spatial resolutions of 100  $\mu\text{m}$ .

FTIR spectra were recorded with a resolution of 4  $\text{cm}^{-1}$  in transmission mode in the 750-400  $\text{cm}^{-1}$  range with a Nicolet 510 FTIR spectrometer. The spectra were obtained

from KBr pressed pellets of 2 cm diameter, which were prepared by mixing 5 mg of powder material with 100 mg of KBr.

For the X-Ray Diffraction (XRD) study of the most external layers of the amalgam, the conventional Bragg-Brentano parafocussing geometry ( $\theta$ - $2\theta$  coupled) was not found to be useful [7]. Due to the penetration of the X-ray beam, the diffracted intensity of the most external layers is very weak, making it impossible to measure the crystalline composition [7]. Therefore, Grazing Incidence X-Ray Diffraction (GID), with a reduced penetration depth, was used to provide very precise information on surface and interface of atomic arrangement in crystalline structures [8, 9, 10, 11]. By varying the angle of incidence, the penetration of the x-ray beam into the material can be controlled allowing the acquisition of non-destructive crystalline composition depth profile as well the analysis of surfaces and buried interfaces.

The data were collected on a Siemens D5000 diffractometer with Cu target and equipped with a grazing incidence attachment. The excitation energy was fixed at 8050 eV, corresponding to a wavelength of 1.5406 Å. The grazing incidence attachment consists of a long soller slit with a 0.4° divergence and a LiF (100) monochromator crystal and used a parallel configuration. The parallel mode was chosen since it produced a higher diffracted intensity. The X-ray beam impinges on the sample at a small angle (at  $\gamma = 1^\circ$  and  $5^\circ$ ) and remains fixed during the detector scan. Due to the small incidence angle, only X-ray signals of the sample surface are registered.

Additional GID measurements were performed using the six-circle diffractometer installed at the Spanish CRG beamline (Fig. 2a) at the European Radiation Facility (ESRF) [12,13]. Diffraction measurements were performed using the grazing incidence mode with a fixed energy of 14.050 KeV (wavelength 0.855 Å). The vertical geometry was used in order to efficiently take advantage of both the linear polarization of the bending magnet synchrotron radiation and the low beam vertical divergence. The set-up used (diffractometer + X-Ray beam divergence) provides an incident angle accuracy of  $5 \cdot 10^{-3}$  degrees, which enables an accurate control of the sampling depth. The incidence angle was varied between 0.4 and 3 degrees in order to change the penetration depth between a few nanometers up to several micrometers. The X-Ray beam spot size was 300  $\mu\text{m}$  (horizontal) x 500  $\mu\text{m}$  (vertical), allowing discrimination between the amalgam and corroded regions of the samples. Finally, it was necessary to develop additional experiments for Sample 5 because this sample exhibited a small dark area beyond the

undamaged amalgam layer. Grazing incident diffraction with the X-ray synchrotron beam using the seven-circle diffractometer installed at the French CRG beamline (D2AM-BM2) [14] at the European Radiation Facility (ESRF) was performed (Fig. 2b) with a monochromatic beam at the energy  $E = 13.555$  keV ( $\lambda = 0.8279 \text{ \AA}$ ) due to the high-resolution of BM02. By moving the beam impact from a small dark area beyond the amalgam layer to the undamaged amalgam layer itself, Sn oxidation was observed. In order to obtain a more quantitative analysis of the different phases present in the small dark area, Rietveld refinement was performed.

In the grazing incidence geometry, the X-ray beam impinges on the surface at small incidence angles ( $\gamma$ ). For all materials, the refractive index at x-ray energies is slightly less than one, and there is a critical angle  $\gamma_c$  below which total external reflection occurs.

For incidence angles lower than  $\gamma_c$ , the X-rays are evanescent within the solid and penetrate only a few tenths of an angstrom. As the incident angle increases and becomes equal to  $\gamma_c$ , the X-ray penetration depth rapidly increases, and for an incidence angle above  $\gamma_c$ , it approaches that expected from absorption [15]. Since the diffracted beams originate in this region of variable depth, the diffraction pattern from the sample with depth-dependence on the structure will depend on the angle of incidence [15-18].

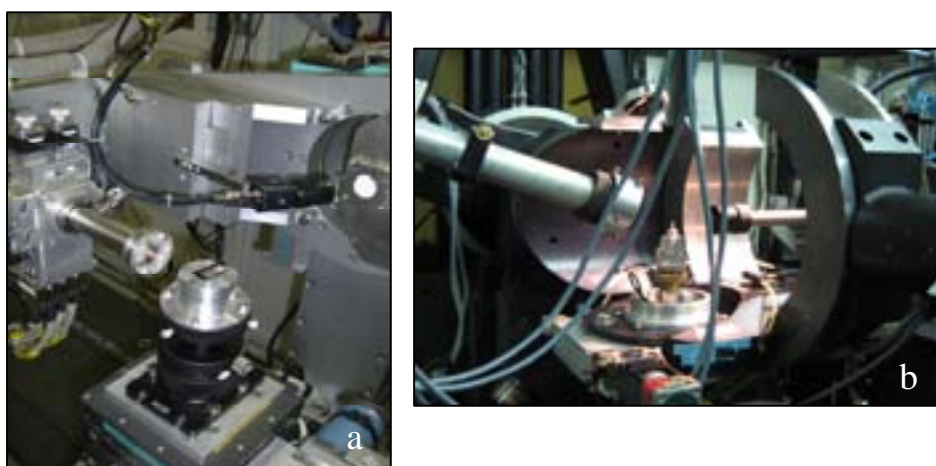


Fig. 2. (a) BM25A configuration (b) BM02 Configuration

X-ray photoelectron spectroscopy (XPS) and reflection electron energy-loss spectroscopy (REELS) are powerful surface-sensitive analytical techniques that are well suited for the analysis of materials. The corrosion products of the tin mercury alloy were SnO and SnO<sub>2</sub>. Some difficulties have been found for the characterisation of the chemical

state for Sn oxides using XPS. However, Jimenez *et al.* [19] report the preparation of SnO<sub>2</sub> and SnO thin films and their characterisation by surface-spectroscopic methods.

The XPS and REELS spectra were recorded on an ESCALAB 210 spectrometer operating in the pass energy constant mode at 50 eV for XPS and at 20 eV for REELS. The base pressure during measurements was typically  $5 \times 10^{-10}$  Torr. The Al K $\alpha$  radiation was used as the excitation source. The binding energy scale was referenced by using the Sn 3d<sub>5/2</sub> peak at 487.55 eV. The sensitivity factors from the apparatus were used for the quantification of the XPS spectra [20,21].

## II.4. Results

### II. 4.1. General microanalysis of the glasses

EDX analysis of all the glass pieces backed with the tin amalgam indicated the presence of O, Na, Mg, Al, Si, Cl, K, Ca, Mn, and Fe. (Fig. 3) This composition is typical for a silicate glass [22] with some impurities, such as Fe and Mn due to the manufacturing methods [22].

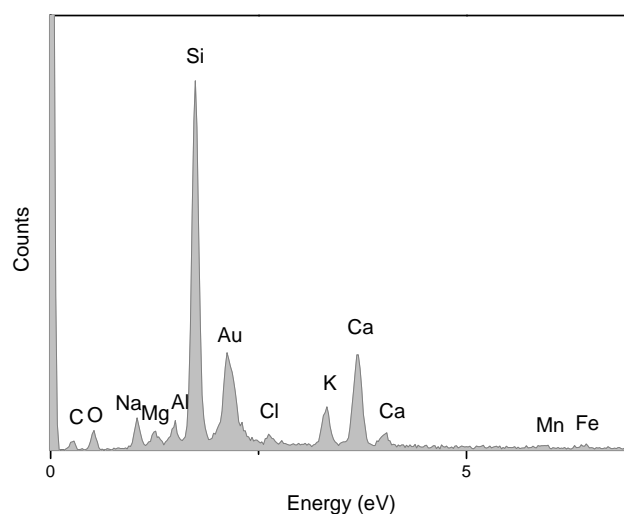


Fig. 3 EDX analysis of the supporting glasses of sample 1, 2, 3, 4, showing typical Elements of a silicate glass.

### II.4.2. Conventional studies of the amalgam surfaces

The Sn-Hg equilibrium phase diagram [23], as depicted in Fig. 4, shows that the alpha and beta phases are pure tin and that the gamma, delta, and epsilon phases are solid phases containing both tin and mercury. Both metals react to form a layer composed of 19 wt% Hg (12.02 at %), and the voids between the crystals are filled with the remaining liquid phase, which is constituted by a liquid dissolution of 0%–5% tin in mercury [2].

The average composition of the amalgam was approximately 75 wt% tin and 25 wt% mercury.

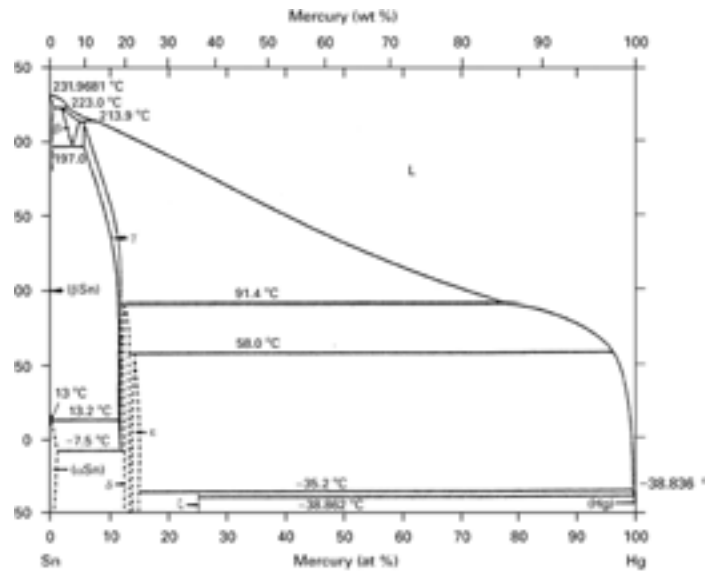


Fig. 4 Hg-Sn equilibrium phase diagram from reference. [23]

#### II.4.2.1. Sample 1

An example of the visual appearance of the uncorroded alloy using an optical microscope is shown in Fig. 5a. EDX analysis detected two phases in the amalgam, a mercury-rich phase (Fig. 5b) and a tin-mercury phase (Fig. 5c). The presence of a mercury-rich phase suggested minimal alteration of the reflecting layer.

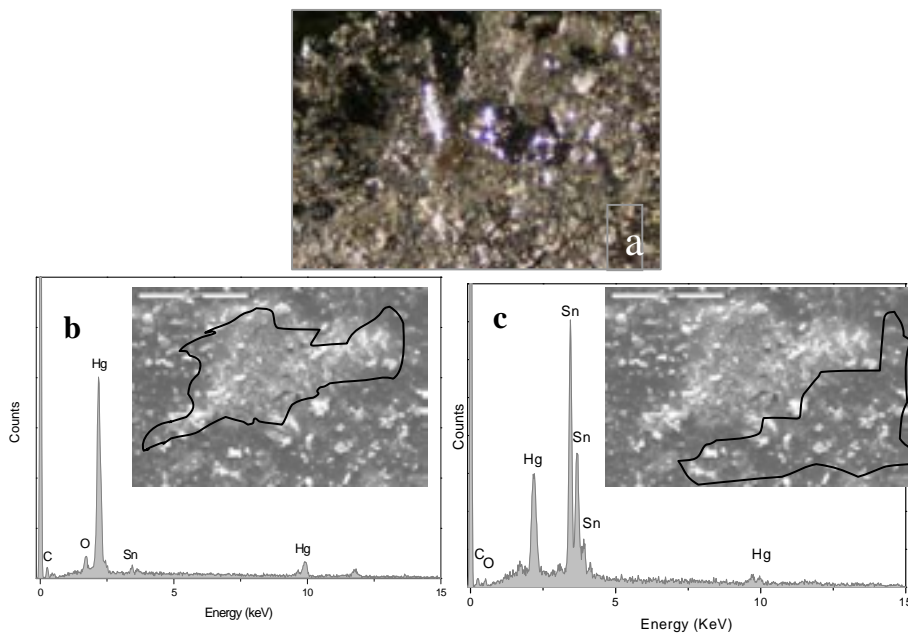


Fig. 5 Microphotographs of sample 1 showing (a) the morphology of the amalgam (100x). SEM/EDX analysis of the two phases present in sample 1: (b) mercury – rich phase; (c) tin-mercury phase.

The initial XRD studies used Bragg-Brentano geometry and showed only the presence of the Sn-Hg amalgam ( $\text{Hg}_{0.1}\text{Sn}_{0.9}$ ) and metallic tin ( $\beta\text{Sn}$ ), which is in agreement with the sixteenth century method of mirror manufacturing (Fig. 6).

For the GID studies, it was essential to calculate the penetration depth of the beam, which is dependent on the wavelength ( $1.5406 \text{ \AA}$ ) the chemical composition, the density and the incidence angle ( $\gamma = 1^\circ$  and  $\gamma = 5^\circ$ ). First, the critical angles ( $\gamma_c$ ) for the different compounds found on the surface of the alloys were calculated to be:  $\gamma_c \text{Hg}_{0.1}\text{Sn}_{0.9} = 0.37^\circ$ ,  $\gamma_c \beta\text{Sn} = 0.36^\circ$ , and  $\gamma_c \text{SnO}_2 = 0.35^\circ$  (following the work of Vineyard, G. H. [24]).

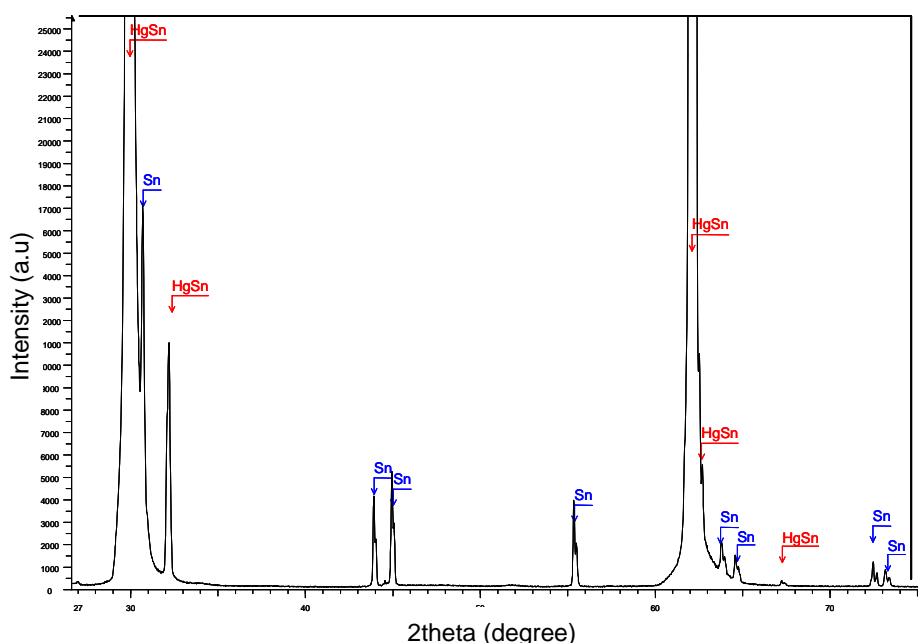


Fig. 6 XRD diffractogram of the reflecting layer of Sample 1 obtained with conventional Bragg-Brentano geometry

The penetration depths were then calculated from the equation give by Vineyard [24] and absorbDX software [25]. Table 2 shows the penetration depth of tin dioxide.

Normally we can consider that the analyzed thickness corresponds to the layer which gives a fraction equal to 0.9 (90 % of the signal), the analyzed depth is described as follows:

$$X = -\ln(1 - 0.90) \times \left( \mu(\lambda) \cdot \rho \cdot \left( \frac{1}{\sin \gamma} + \frac{1}{\sin(2\theta - \gamma)} \right) \right)^{-1}$$

Where  $\mu$  is the mass absorption coefficient ( $\text{cm}^2/\text{g}$ ),  $\rho$  is the density ( $\text{g}/\text{cm}^3$ ),  $\gamma$  is incidence angle (degree) and  $2\theta$  is the diffraction angle for the strongest peak. In order to get the depth of the analyzed layer of these amalgams surface is for the  $\text{SnO}_2$  (110) peak (Strongest peak,  $2\theta = 26.61$ ) the depth for 90 % contribution of the measured intensity for  $\gamma = 1^\circ$  is  $0.27 \mu\text{m}$  and for  $\gamma = 5^\circ$  is  $1.17 \mu\text{m}$ .

Table 2 Calculation of penetration depths ( $I$ )

Compound	$\gamma = 1^\circ$ penetration depth ( $I$ )	$\gamma = 5^\circ$ penetration depth ( $I$ )
$\text{SnO}_2$	$0.27 \mu\text{m}$	$1.17 \mu\text{m}$

GID using  $\gamma = 1^\circ$  and  $5^\circ$  was used to identify the composition of the reflecting layer of Sample 1, which is shown in Fig. 7. The pattern at  $\gamma = 1^\circ$  provided information about the most external layer; the peaks were attributed to  $\text{Hg}_{0.1}\text{Sn}_{0.9}$  and metallic tin, which is in agreement with the Hg-Sn phase diagram showed in Fig. 4. In addition, small broad peaks appear, which are due to a very low proportion of tin oxide, possibly associated with cassiterite ( $\text{SnO}_2$ ). However, it is also evident that the diffractogram evolves from the surface to the middle of the amalgam. In particular, the pattern at  $\gamma = 5^\circ$  shows the presence of  $\text{Hg}_{0.1}\text{Sn}_{0.9}$  and metallic tin in higher proportions than in the XRD pattern acquired at  $\gamma = 1^\circ$ . These results show a very low degree of alteration, with the reflective layer remaining practically intact ( $\text{Hg}_{0.1}\text{Sn}_{0.9}$  and metallic  $\beta\text{Sn}$ ).

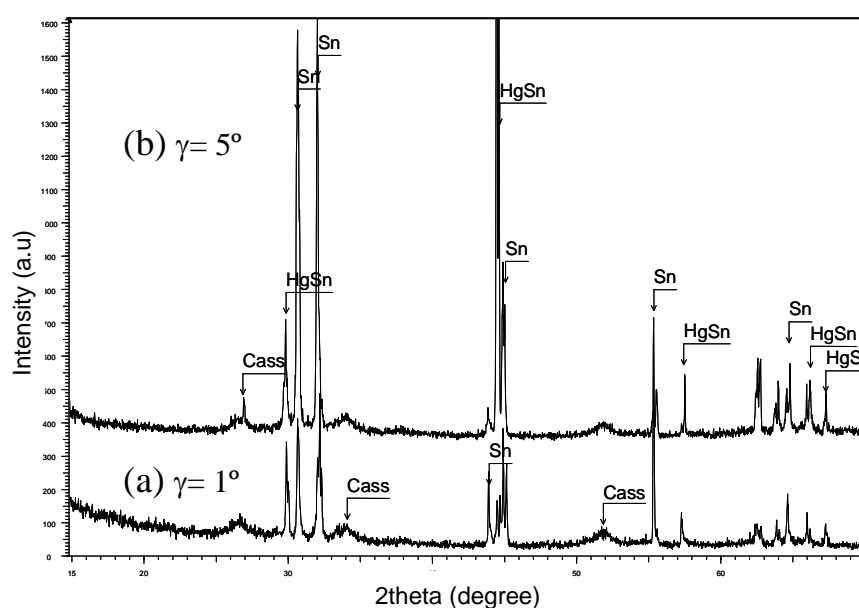


Fig. 7 XRD patterns of the reflecting layer of Sample 1 under incidence angles: a)  $\gamma = 1^\circ$ ; b)  $\gamma = 5^\circ$ . Cass (cassiterite), HgSn (amalgam corresponding to  $\text{Hg}_{0.1}\text{Sn}_{0.9}$ ) and  $\beta\text{Sn}$  (metallic tin).

### II.4.2.2. Sample 2

Fig. 8a reveals the morphology of the reflecting layer of Sample 2 where some areas are surrounded by a globular formation of corrosion products. The EDX analysis showed the presence of Sn on the surface; the presence of silicates is due to dust. The dust and other environmental factors determined the different levels of decay of the amalgam.

The diffraction profiles of Sample 2, shown in Fig. 9, were acquired using  $\gamma = 1^\circ$  and  $\gamma = 5^\circ$ . The pattern at  $\gamma = 1^\circ$  gives information about the most external layer; the diffraction patterns can be attributed to tin oxides, as  $\text{SnO}_2$ , and gypsum. In particular, the pattern at  $\gamma = 5^\circ$  showed that the presence of tin oxide proportion was little more than gypsum.

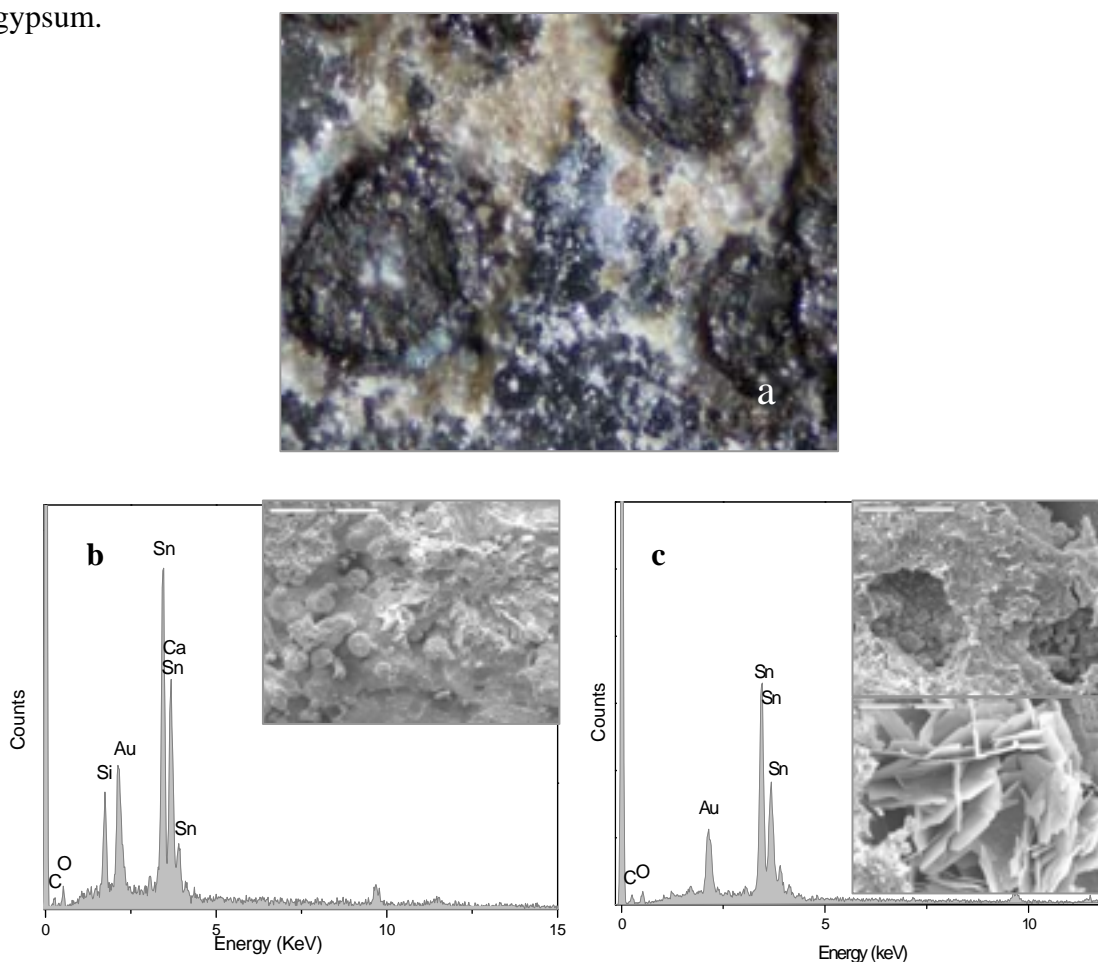


Fig. 8 (a) microphotographs of sample 2: corroded areas of the amalgam (100x). (b) EDX analysis (Sn, Ca, Si, C and O) and morphology of the corroded areas of the amalgam (c) EDX analysis (Sn, C and O) and morphology of the tin oxides. The presence of Au is due to the metallization process.

These results showed a very high degree of surface alteration. The amalgam ( $\text{Hg}_{0.1}\text{Sn}_{0.9}$ ) and metallic Sn ( $\beta\text{Sn}$ ), which were the original phases of the unoxidized amalgam, practically disappear.

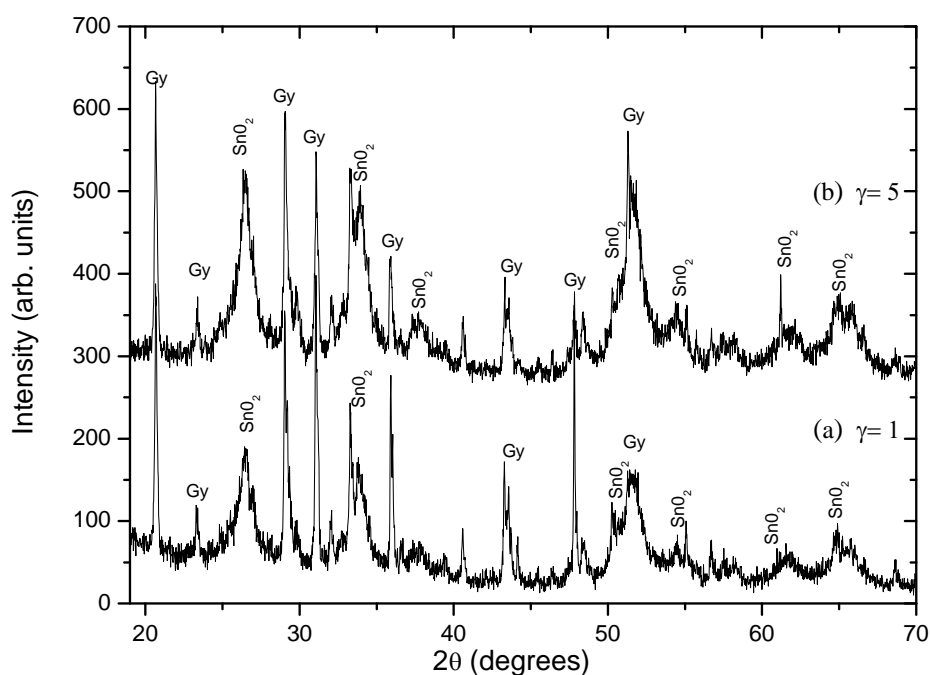


Fig. 9 XRD patterns of the reflecting layer of the mirror from sample 2 under incidence angles: (a)  $\gamma = 1^\circ$ ; (b)  $\gamma = 5^\circ$ .

#### II.4.2.3. Sample 3

Two amalgam surfaces were studied: the dull surface (protected with a wooden panel) and the glossy one (kept together with the glass). An example of the visual appearance of the dull surface and glossy using an optical microscope is shown in Fig. 10.

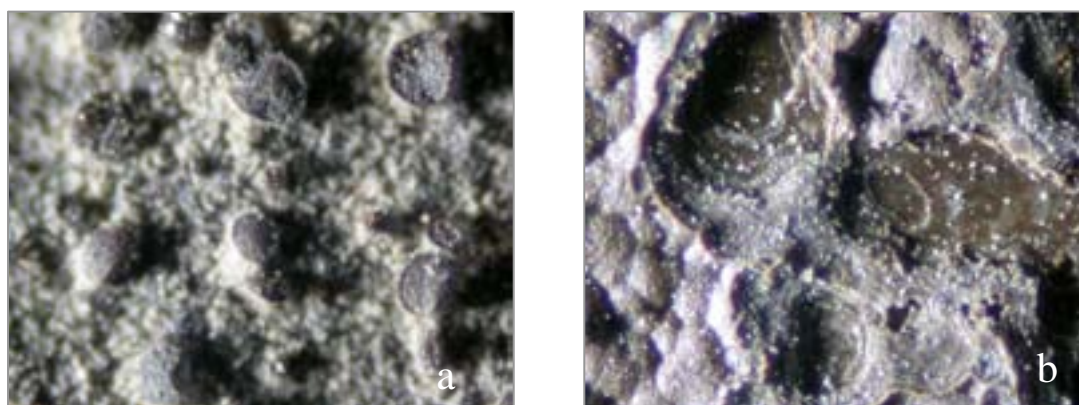


Fig. 10 Microphotographs of sample 3 (a) morphology of dull surface (b) morphology of glossy surface (100x).

The decorative border that appears over the glass of the mirror from Sample 3 was made with gold. The EDX analysis detected the presence of Sn and Hg in some areas of both of the amalgam surfaces of the ancient mirror. Due to the heterogeneous complexity of the surface, the microstructure of the dull surface was investigated by preparation of

metallographic cross sections. The thickness of the layers ranged from 60 to 130  $\mu\text{m}$ . In the cross-section, mainly two different phases were recognized, which appear light grey and white due to the atomic number contrast of backscattered electrons (Fig. 11a). The predominately light grey phase identified by semi-quantitative EDX analysis contains approximately 80 wt% tin and 20 wt% mercury (Fig. 11b). The grain size varies from 20 to 50  $\mu\text{m}$ . These crystallites are surrounded by the white phase, which is composed of 98 wt% mercury and 2 wt% tin, as identified by semi-quantitative EDX analysis (Fig. 11c).

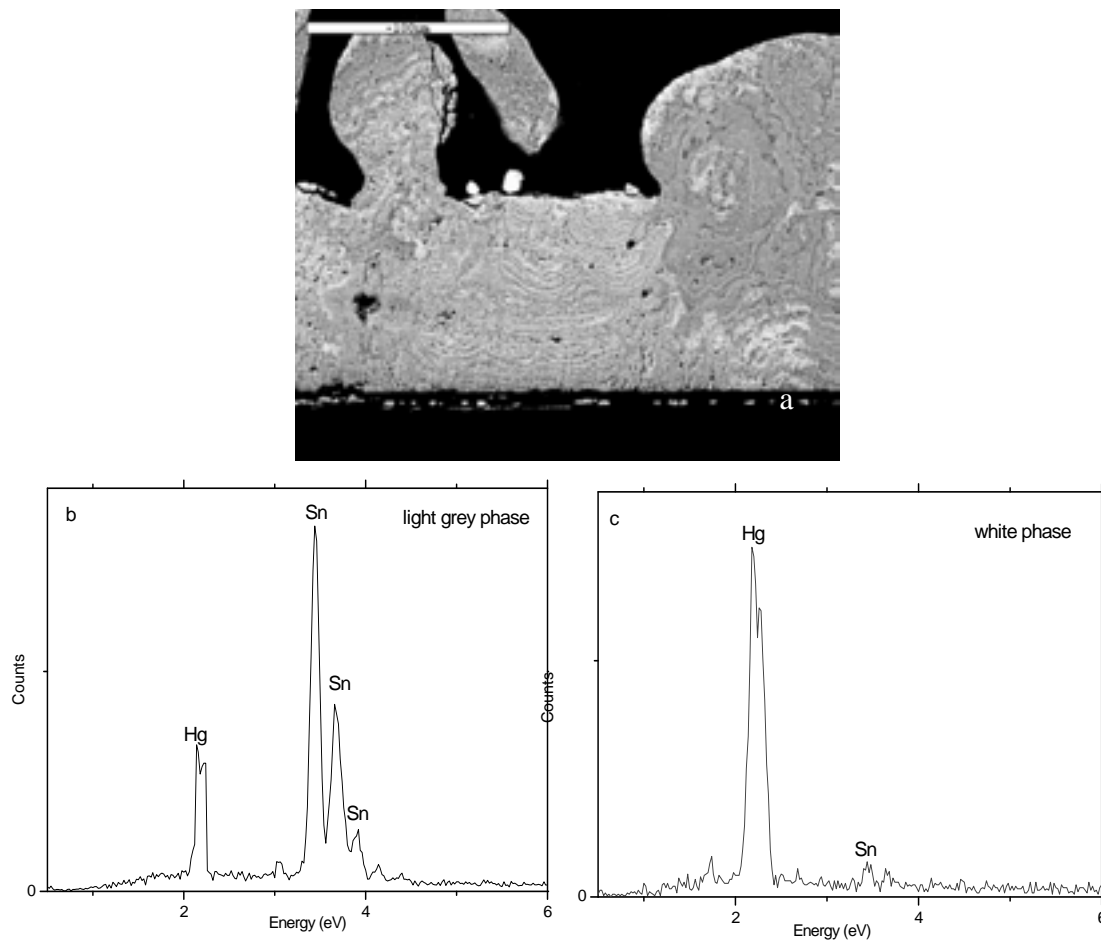


Fig. 11 (a) SEM image of the microstructure of a glossy surface of sample 3. (b) EDX light grey and (c) white phases

This result is in agreement with a former investigation of Hadsund [2], who also identified tin-mercury crystallites containing about 19 wt% mercury surrounded by a liquid mercury phase with a low tin content. The corrosion products frequently had the shape of hemispherical concentric bands (Fig. 12a) composed of tin oxide (Fig. 12b).

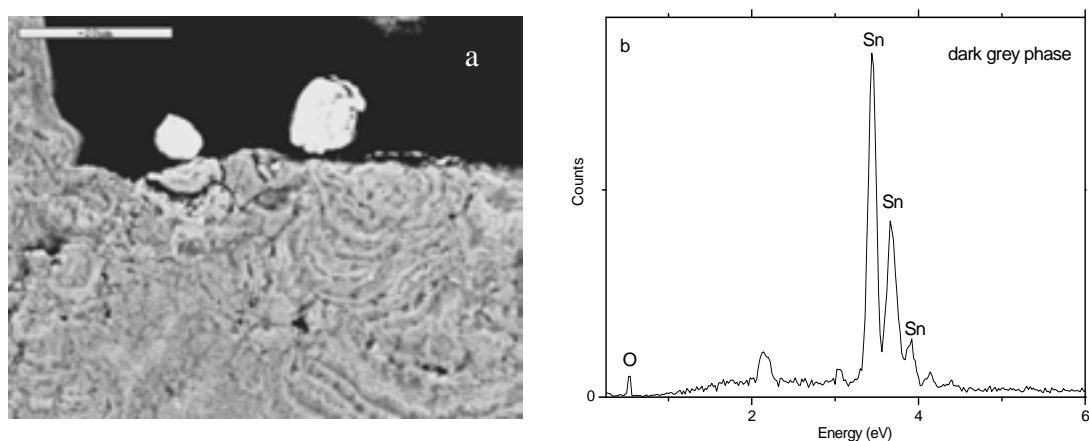


Fig. 12 (a) SEM image of the microstructure of a dull surface of sample 3 (b) EDX of the concentric bands.

The characterisation of the dull surface of sample 3 carried out at  $\gamma = 5^\circ$ , Fig. 13a, showed the presence of  $\text{SnO}_2$  in a much higher proportion than  $\text{SnO}$ ; however, the glossy surface at  $\gamma = 5^\circ$ , Fig. 13b, showed tin oxide ( $\text{SnO}$ ) in a higher proportion than  $\text{SnO}_2$ .

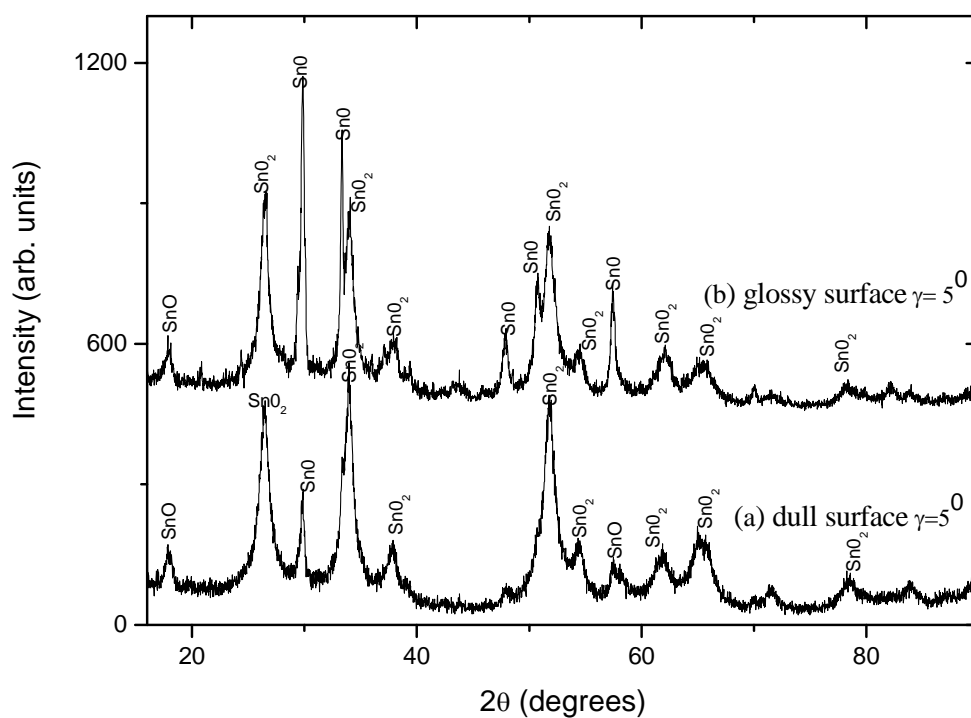


Fig. 13. GID patterns of the (a) dull and (b) glossy surface of Sample 3

#### II.4.2.4. Sample 4

In Sample 4, there was no evidence of amalgam ( $\text{Hg}_{0.1}\text{Sn}_{0.9}$ ) and metallic tin ( $\beta\text{Sn}$ ), due to the high alteration degree. The typical morphology of the corroded parts of the sample can be observed in Fig. 14, which shows the concentric bands that can be

attributed to the formation of tin oxide after mercury release [26]. The EDX analysis shows the presence of Sn on the surface; the presence of silicates is due to dust coming from the environmental contamination. The dust and other environmental factors determined the different levels of decay of the amalgam.

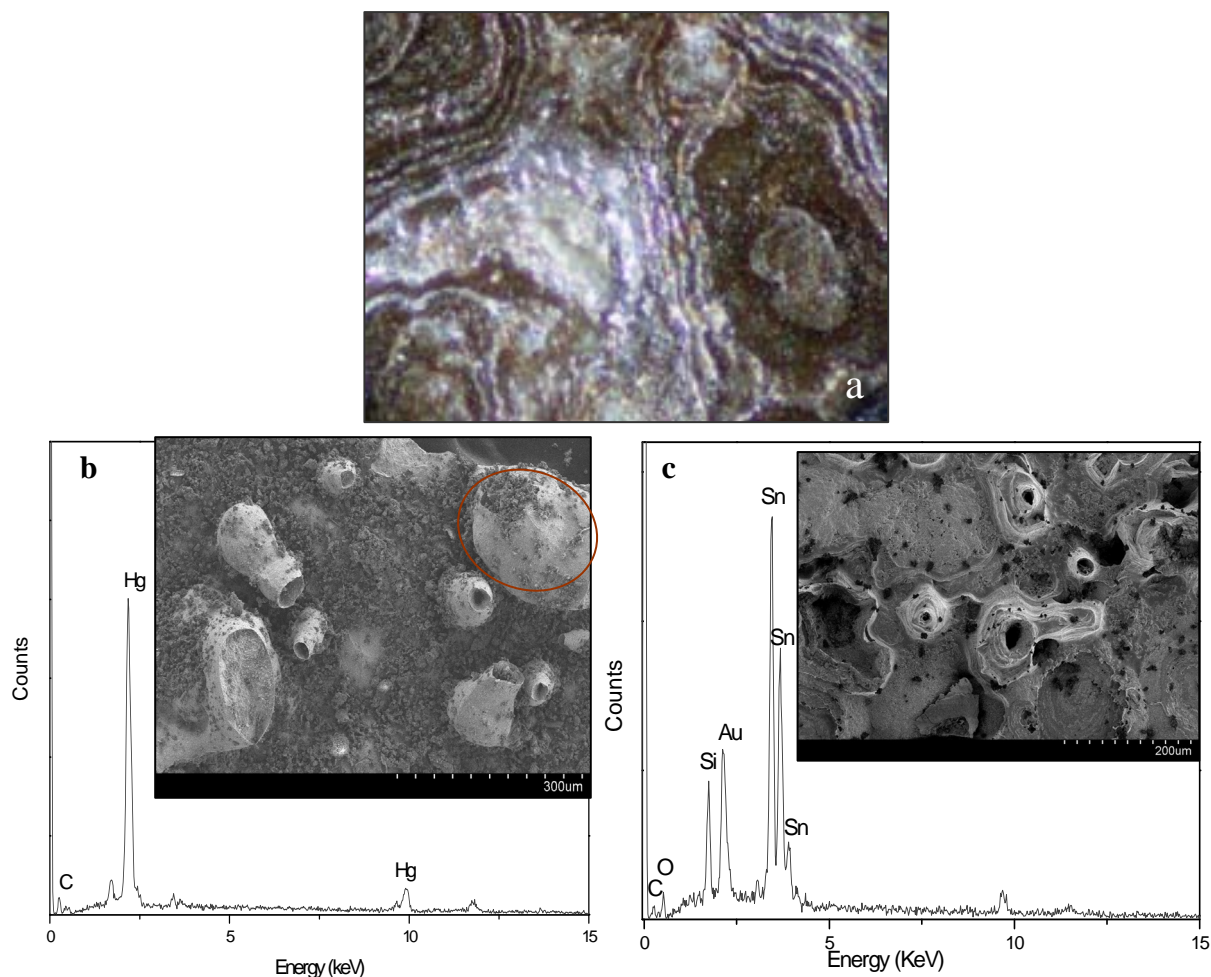


Fig. 14 (a) microphotographs of sample 4. corroded areas of the amalgam (100x). (b) EDX analysis of a drop of mercury and morphology of the corroded areas of the amalgam (c) EDX analysis (C, O, Si, and Sn) and concentric bands of the tin oxides.

The characterisation of Sample 4, as shown in Fig. 15, carried out at  $\gamma = 1^\circ$  and  $5^\circ$ , showed cassiterite ( $\text{SnO}_2$ ) and romarchite ( $\text{SnO}$ ). There was no evidence of  $\text{Hg}_{0.1}\text{Sn}_{0.9}$  or metallic tin due to the high degree of corrosion. SEM micrographs show many protuberances with holes on the top of them, resembling ‘craters.’ In some of these craters, spheres of Hg are still present and fill the pores, as shown in Fig. 16a. Fig. 16b shows the typical appearance of corrosion: the crater seems to have broken, leaving a series of concentric bands that show the different layers of the amalgam.

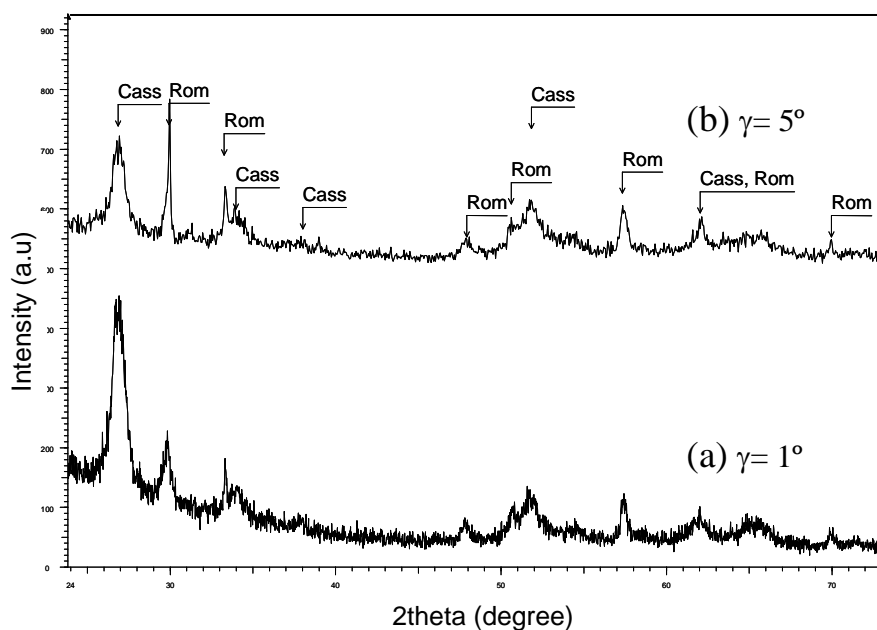


Fig. 15 GID patterns of Sample 4 using incidence angles: (a)  $\gamma = 1^\circ$ ; (b)  $\gamma = 5^\circ$ . Cass (cassiterite), Rom (romarchite).

The amalgam probably had an excess of liquid phase that gradually disappeared during the aging process.

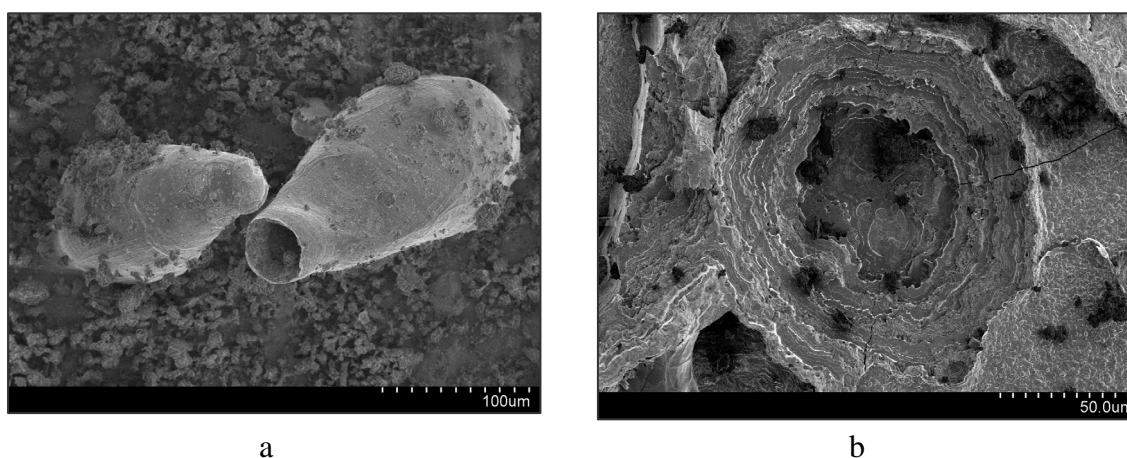


Fig. 16 SEM images of the corroded areas of the amalgam of sample 4. Protuberances resembling 'craters' are observed on the surface (a) The left shows a drop of Hg arising and the right is empty because the Hg has been released; (b) the 'crater' disappeared, leaving only the hole remaining; different layers of the solid phase are visible as concentric colouring bands. Edges are mainly formed by tin oxides.

#### II.4.3. XPS studies of the amalgams surfaces

The X-ray photoelectron spectrum of the amalgam surface ( $\sim 5$  nm) is shown in Fig. 17. The core-level lines Sn4d, Sn4s, C1s, Sn3d, O1s, Sn3p<sub>3/2</sub>, Sn3p<sub>1/2</sub>, and the Auger lines SnMNN and OKVV can be seen clearly for Samples 1, 3 and 4. Similar core-levels appear in Sample 2, together with Si2p, Si2s, S2p and Ca2p. Hg traces have not been

detected by XPS. This fact suggests that Sn could be enriched in the outer layer (~5 nm) of the amalgam, whereas Hg remains in deeper layers that are not reached by the XPS radiation.

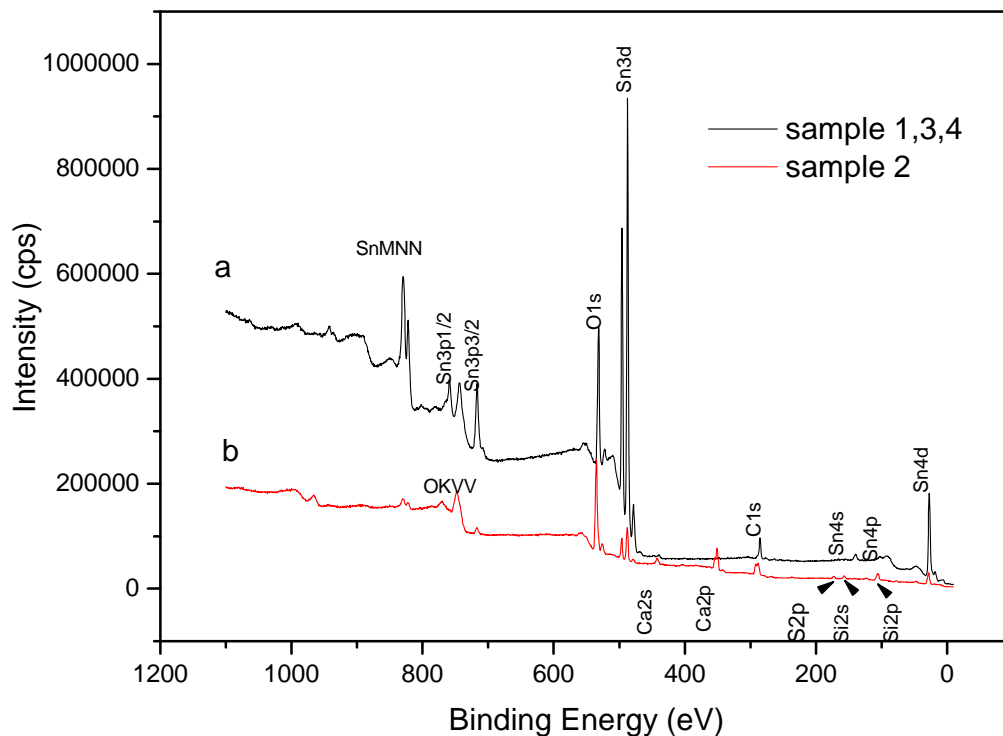


Fig. 17 XPS spectra of amalgam layer (~5 nm) of Samples: (a) 1, 3, and 4, (b) 2.

The surface analysis of Samples 2, 3 and 4 by XPS shows a unique chemical species for tin:  $\text{Sn}^{4+}$ . This species is characterized by a Sn 3d  $_{5/2}$  peak at 487.55 eV of binding energy (Fig.18a) and a SnMNN Auger peak at 431.30 eV of kinetic energy (Fig.18b) (modified Auger parameter, 918.85 eV). These energetic values confirm that, at the surface, tin is oxidized to SnO or SnO<sub>2</sub>, since the values for Sn<sup>0</sup> are quite different: 484.90 eV (BE) and 437.3 eV (KE), respectively. In addition, the experimental Auger parameter is closer to that expected for bulk SnO<sub>2</sub> (918.60 eV) than for bulk SnO (919.3 eV). Finally, the absence of an energy loss peak at -27 eV in the REELS spectra of these samples confirm that SnO is not present (Fig.18c). By contrast, in Sample 1, the main Sn3d  $_{5/2}$  peak, which could be ascribed both to SnO<sub>2</sub> and to SnO, is accompanied by a small shoulder at 488.4 eV that must be attributed to metallic Sn due to the low alteration degree. (Fig not shown).

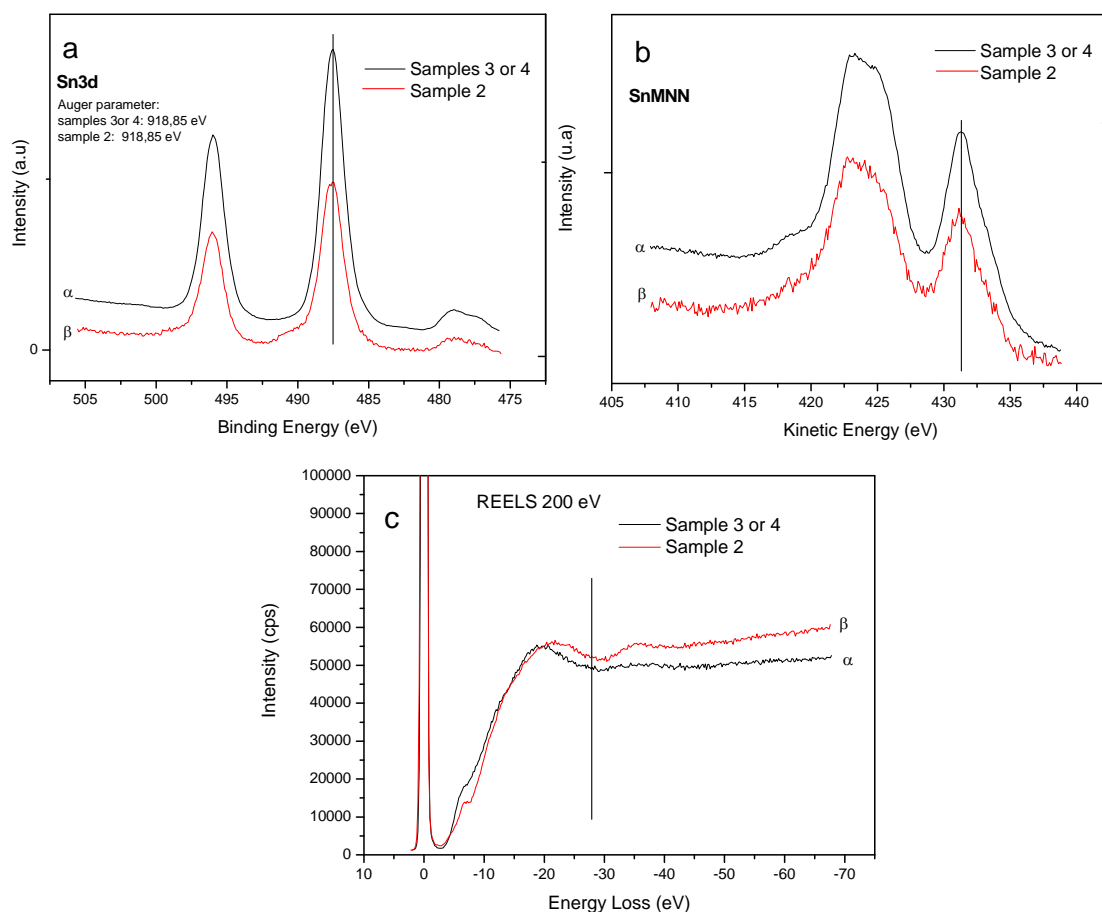


Fig. 18 (a) Sn 3d photoelectron peaks for (α) Samples 3 and 4, (β) Sample 2. (b) Sn Auger peaks of amalgam surface attributed to (α) Samples 3, 4 and (β) Sample 2 (c) Electron energy loss spectra at  $E_0=200\text{eV}$  of (α) Samples 3, 4 and (β) Sample 2.

#### II.4.4. Spectroscopic studies of tin in the amalgams surfaces

The Raman technique has become increasingly available in the field of cultural heritage studies [27]. In this chapter, Raman spectroscopy was used, as a complementary technique, to characterize the corrosion products. In order to identify the surface compositions, Raman spectra on the surfaces, shown in Fig. 19, were collected. The spectra of Samples 3 and 4 display the two more intense bands characteristic of  $\text{SnO}_2$  at  $633\text{cm}^{-1}$  and  $636\text{cm}^{-1}$  [28] and  $725\text{cm}^{-1}$ . The intensity of the band at  $630\text{cm}^{-1}$  varies with the high level of amalgam corrosion stage [28,29]. The bands at  $470\text{cm}^{-1}$ ,  $513\text{cm}^{-1}$  and  $750\text{cm}^{-1}$  could be attributed to the presence of  $\text{SnO}$  [29]. The differences in relative intensity of the bands characteristic of the  $\text{SnO}_2$  phase could be explained in terms of the different crystallinity of the tin oxide [28,29].

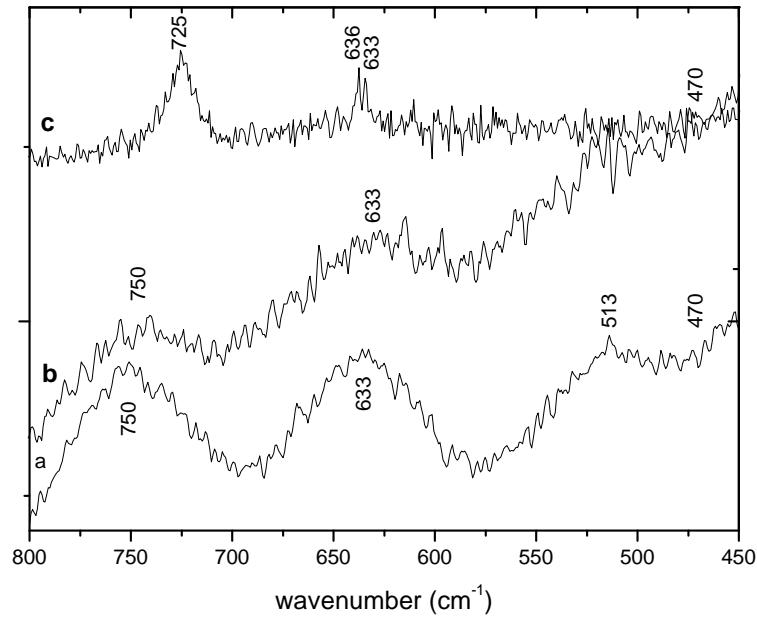


Fig. 19 Raman spectra of corroded amalgam: (a) dull surfaces of Sample 3 (b) glossy surfaces of Sample 3 (c) surfaces of Sample 4.

Samples 3 and 4 were ground to a powder form for examination by FTIR. Fig. 20 displays the FTIR spectra of Samples 3 and 4. The bands of tin oxide are summarized in Table 3. These results, similar to those collected by Huang, et al. [29], Ocaña et al. [28], and De Rinck et al. [31], suggest that the corrosion surface of tin was composed of a comparable amount of  $\text{SnO}_2$  and  $\text{SnO}$ . However, the  $\text{SnO}_2$  content increases with time.

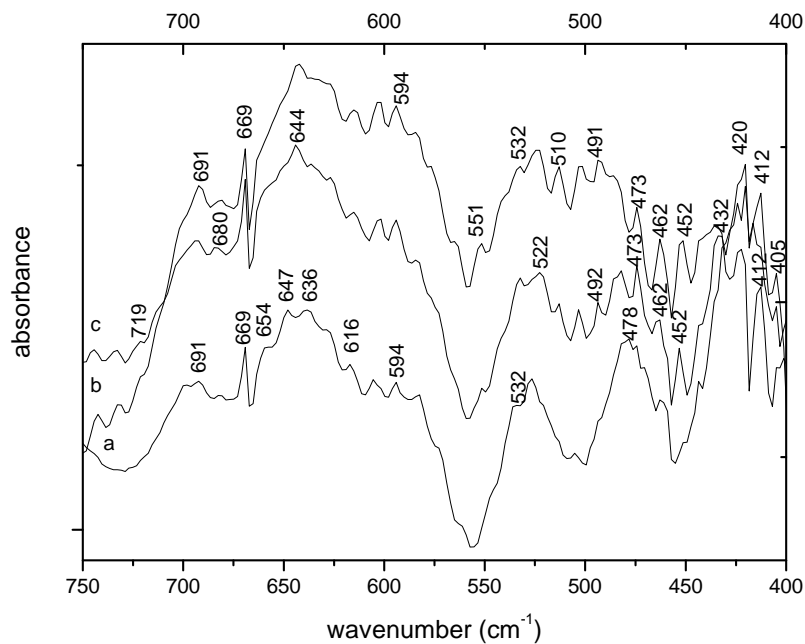


Fig. 20 FTIR spectra of the corrosion amalgam: (a) Dull surfaces of Sample 3 (b) Glossy surfaces of Sample 3, and (c) Surfaces of Sample 4.

The FTIR measurements are in good agreement with those from the Raman spectroscopic study.

Table 3 Major FTIR bands of tin compounds

Compound	FTIR bands (cm <sup>-1</sup> )	Ref
SnO <sub>2</sub>	405,412,452,594,616, 636,644,647,654 669,680	29,30,31
SnO	420,432,473,478,492 510,522,532,719	29,30,31

## II.5. Synchrotron experiments

Synchrotron radiation has become a generic term to describe the electromagnetic field radiated by relativistic accelerated charged particles [31]. Synchrotron radiation is usually produced in storage rings where electrons or positrons are subjected to applied magnetic fields that force them to travel along curved paths. In a storage ring, the synchrotron radiation is produced either in the bending magnets needed to keep the electrons in a closed orbit or in insertion devices such as wigglers or undulators situated in the straight sections of the storage ring [31]. In the insertion devices, an alternating magnetic field forces the electrons to follow oscillating paths rather than moving in a straight line; as a result, a narrow cone is emitted, which constitutes the synchrotron radiation. The beamlines are placed tangentially to the storage ring when dealing with a bending magnet and parallel to the straight section of the storage ring when dealing with an insertion device. Several aspects of an X-ray source determine the quality of the X-ray beam it produces. The Figure of merit is brilliance rather than flux. Brilliance is determined by the number of X-ray quanta per area of the source, per solid angle, per second, and often per spectral interval. Such a quantity allows one to compare the quality of the X-ray beam from different sources. It should be noted that the maximum brilliance from third generation undulators is about 10 orders of magnitude higher than that from a rotating anode.

### II.5.1. Grazing incident diffraction using synchrotron radiation

In GID measurement, the depth penetration  $\Lambda$  of the beam is dependent on the wavelength and incidence angle and is calculated from the Beer-Lambert's law [32]. For calculating the depth of penetration  $\Lambda$  of the beam into the sample, it is necessary to first

calculate the critical angles ( $\gamma_c$ ) for different compounds found on the surface of the amalgams:  $\gamma_{c\beta\text{sn}}=0.20^\circ$ ,  $\gamma_{c\text{Hg}_{0.1}\text{Sn}_{0.9}}=0.67^\circ$ ,  $\gamma_{c\text{SnO}_2}=0.20^\circ$ , and  $\gamma_{c\text{SnO}}=0.19^\circ$  following the work of Toney M.F *et al.* [24,33] Different incidence angles were chosen for the GID measurement:  $\gamma$  of  $0.4^\circ$ ,  $0.5^\circ$ ,  $0.8^\circ$ ,  $1^\circ$  and  $3^\circ$  above the critical angle ( $\gamma_c$ ), as the surfaces of the amalgam were very rough; these incident angles allow the depth profile characterisation. Fig. 21 shows the diffraction patterns of Sample 1 for increasing incidence angles greater than  $\gamma_c$ . The XRD shows the presence of  $\text{Hg}_{0.1}\text{Sn}_{0.9}$  according to JCPDS files (481546, 40673 and 411445 respectively) [ $2.99 \text{ \AA}$  ( $001$ ),  $2.78 \text{ \AA}$  ( $100$ ),  $2.04 \text{ \AA}$  ( $101$ ),  $1.60 \text{ \AA}$  ( $110$ ),  $1.39 \text{ \AA}$  ( $200$ )]. In addition, diffractions corresponding to  $\beta$ - Sn appear [ $2.91 \text{ \AA}$  ( $200$ ),  $2.79 \text{ \AA}$  ( $101$ ),  $2.06 \text{ \AA}$  ( $220$ ),  $2.02 \text{ \AA}$  ( $211$ ),  $1.66 \text{ \AA}$  ( $301$ ),  $1.48 \text{ \AA}$  ( $112$ ),  $1.44 \text{ \AA}$  ( $321$ )]. Some broad peaks corresponding to  $\text{SnO}_2$  [ $3.35 \text{ \AA}$  ( $110$ ),  $2.64 \text{ \AA}$  ( $101$ ) and  $1.76 \text{ \AA}$  ( $211$ )] were also identified.

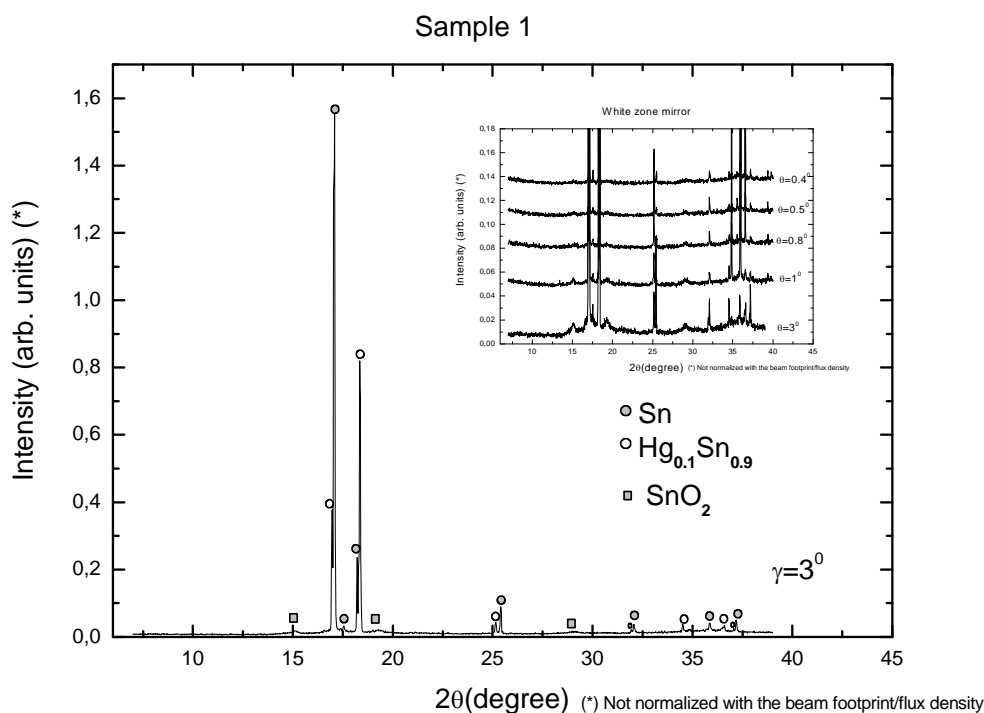


Fig. 21 XRD profile at different incidence angles  $\gamma = 0.4^\circ$  to  $3^\circ$  of Sample 1

The XRD patterns show similar characteristic peaks and intensities at different incidence angles. Very small broad peaks of  $\text{SnO}_2$  appear at  $0.5^\circ$  to  $3^\circ$ . These data suggest a similar composition along the depth profile associated with a low degradation of the amalgam layer and were in agreement with those from conventional GID.

The XRD pattern of Sample 2 (Fig. 22) only identifies the  $\text{SnO}_2$  phase along the profile according to JCPDS file 411445 [ $3.35 \text{ \AA}$  ( $110$ ),  $2.64 \text{ \AA}$  ( $101$ ),  $2.37 \text{ \AA}$  ( $200$ ),  $1.76 \text{ \AA}$  ( $211$ ),  $1.67 \text{ \AA}$  ( $220$ ),  $1.50 \text{ \AA}$  ( $310$ )]. The presence of  $\text{SnO}_2$  confirms that this sample shows the highest alteration degree of all the samples studied in this work. The  $\text{SnO}$  first formed was thermodynamically unstable and slowly oxidized to  $\text{SnO}_2$ . In addition [ $\text{CaSO}_4 \cdot 2\text{H}_2\text{O}$ ]  $7.63 \text{ \AA}$  was also present in a very low proportion because the mirror was in contact with a gypsum wall and the sulphates ions contributed to an acceleration of the corrosion of the amalgam [34].

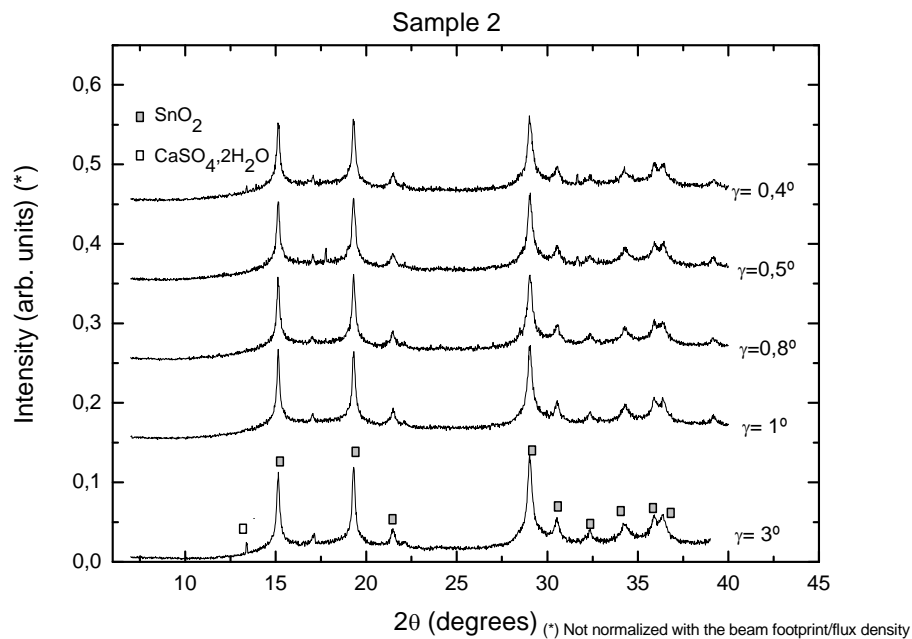


Fig. 22 XRD profile at different incidence angles  $\gamma = 0.4^\circ$  to  $3^\circ$  of Sample 2

Figs. 23a and 23b show the XRD patterns of Samples 3 and 4.  $\text{SnO}_2$  and  $\text{SnO}$  according to JCPDS file 60395 [ $2.99 \text{ \AA}$  ( $101$ )  $2.69 \text{ \AA}$  ( $110$ ),  $1.80 \text{ \AA}$  ( $112$ ),  $1.60 \text{ \AA}$  ( $211$ )] phases appear, while  $\text{Sn}_{0.9}\text{Hg}_{0.1}$  and  $\beta\text{-Sn}$  phases were not found, due to the high corrosion of these samples. Important changes of the phases along the depth profile at different incident angles were not detected. The diffraction peaks obtained with  $\gamma = 0.4^\circ$  are broader than those obtained with  $\gamma = 3^\circ$ , which can probably be attributed to the less crystalline tin oxide phases.

This fact is due to the higher alteration at the top of the amalgam layer. From the analysis of the relative intensity of different peaks, it is possible to obtain information about the different alteration degree in both samples.

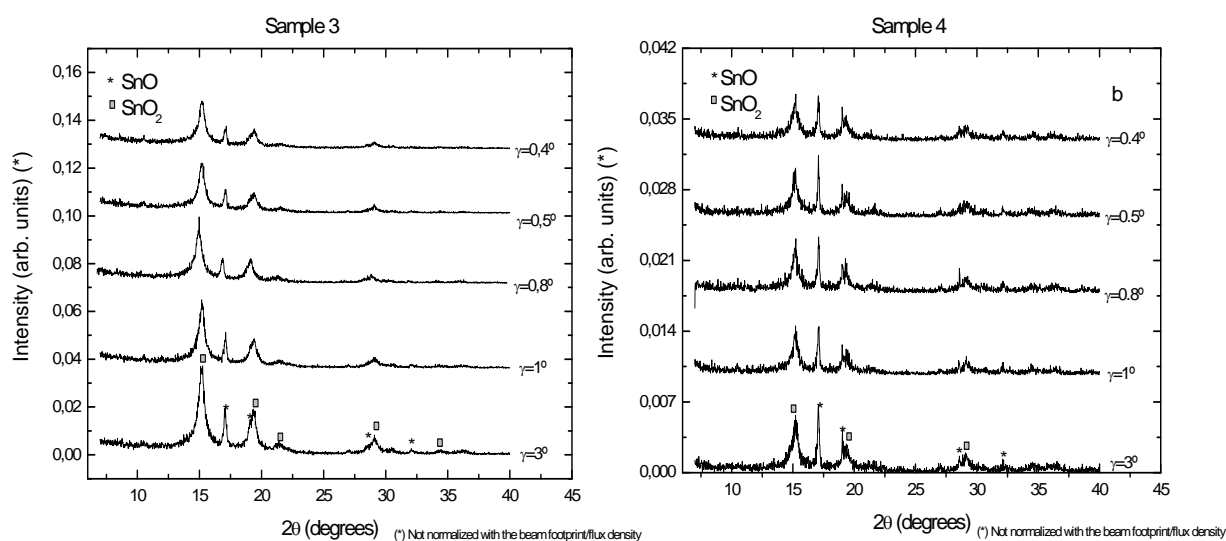


Fig. 23 XRD profile at different incidence angles  $\gamma = 0.4^\circ$  to  $3^\circ$  of (a) Sample 3 and (b) Sample 4.

### II.5.2. Composition by semi-quantitative X-Ray diffraction

For a better knowledge of the mechanisms of alteration of the amalgams, it is very important to obtain high quality diffractograms in order to be able to detect the remainders of the amalgam in addition to the very low proportions of SnO in the most external layers and SnO<sub>2</sub> in the bulk. Sample 5 presents a small dark area outside the undamaged amalgam layer. Using conventional XRD, it is not possible to obtain separated information about phase identification of both areas of the amalgam. The high-resolution of BM02 permits a sub-mm beam that it necessary for separating out the corroded and uncorroded parts of the layer. To obtain the different composition of the small dark area ( $\phi$  1mm), it was necessary to use a high intensity and well collimated incidence beam that is only obtained using synchrotron radiation (Fig. 24). The small dark area measurement at:  $\gamma = 5.0^\circ$  shows the presence of Hg<sub>0.1</sub>Sn<sub>0.9</sub>; in addition, diffractions corresponding to  $\beta$ - Sn and SnO phases appear. The small dark area measurement at  $\omega = 1.0^\circ$  shows the presence of SnO, SnO<sub>2</sub>, and Hg<sub>0.1</sub>Sn<sub>0.9</sub>; meanwhile,  $\beta$ -Sn was not present due to the complete transformation of the tin oxides. The XRD patterns change at different incidence angles. The tin oxide proportion increases down to the profile of the layer. For quantitative analysis of the different phases present in a small dark area, Rietveld refinement of the XRD patterns was performed at  $\gamma = 1.0^\circ$  and  $\gamma = 5.0^\circ$  using the fullprof software [35]. A semi-quantitative analysis of the phase compositions was obtained using the Rietveld refinement modeling. Average patterns corresponding to

the specific layers in the small dark areas ( $\gamma=5.0^\circ$  and  $\gamma=1.0^\circ$ ) have been plotted, which provide patterns with better statistics that permit a correct Rietveld refinement analysis for quantitative information.

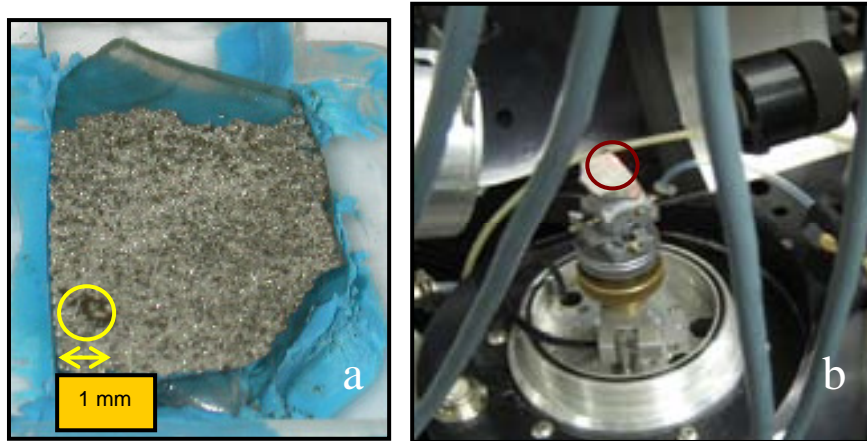


Fig. 24 (a) small dark area detail of Sample 5 (b) Image of SR-XRD device used for focalized XRD with laser the dark area the D2AM-BM2 beamline

The pattern with  $\gamma=5.0^\circ$  (Fig. 25) gives the information for the internal layer inside the dark spot. The amount of cassiterite ( $\text{SnO}_2$ ) is relatively high, about 82 %, romarchite is relative low 16%, and the contribution of  $\text{Hg}_{0.1}\text{Sn}_{0.9}$  is about 0.89%.

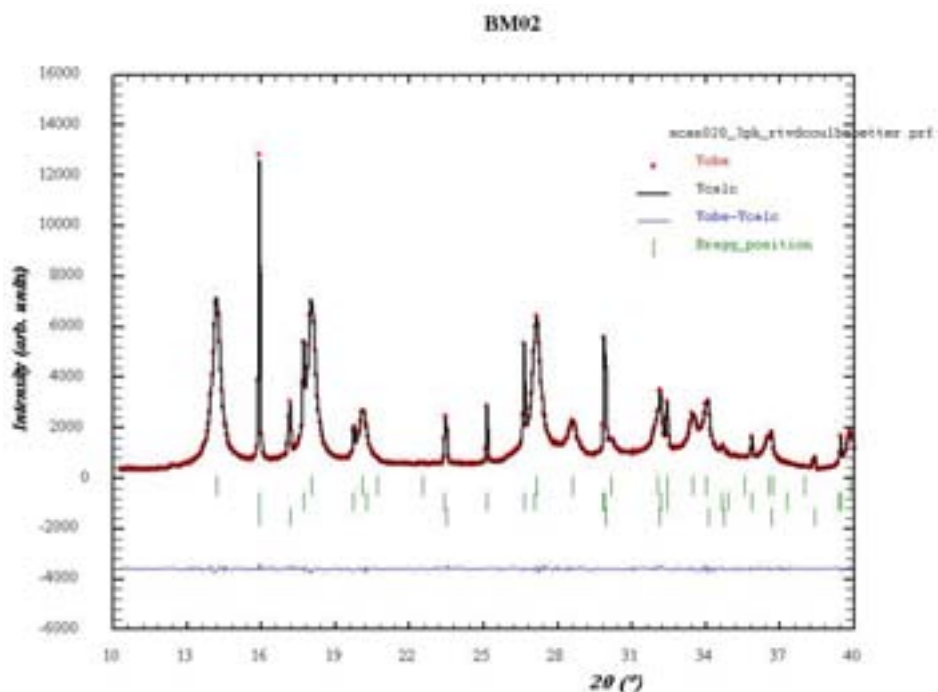


Fig. 25 Rietveld plot of small dark area at  $\omega=5.0^\circ$  obtained with FULLPROF [35] ( $R_{wp} = 8.7$ ,  $\chi^2 = 4.43$ ). Observed (dots) and calculated (solid line) synchrotron diffraction patterns are shown together with the difference curve below. The vertical ticks indicate the reflection positions for the three phases: (1)  $\text{SnO}_2$  (2)  $\text{SnO}$  (3)  $\text{Hg}_{0.1}\text{Sn}_{0.9}$

The pattern with  $\gamma=1.0^\circ$  provides information on the most external layer of the dark area (Fig. 26). The amount of cassiterite ( $\text{SnO}_2$ ) is very low, about 4.69%, romarchite ( $\text{SnO}$ ) is relative high, 82.68%,  $\text{Hg}_{0.1}\text{Sn}_{0.9}$  is about 4.51%, and  $\beta\text{-Sn}$  is about 8.12%.

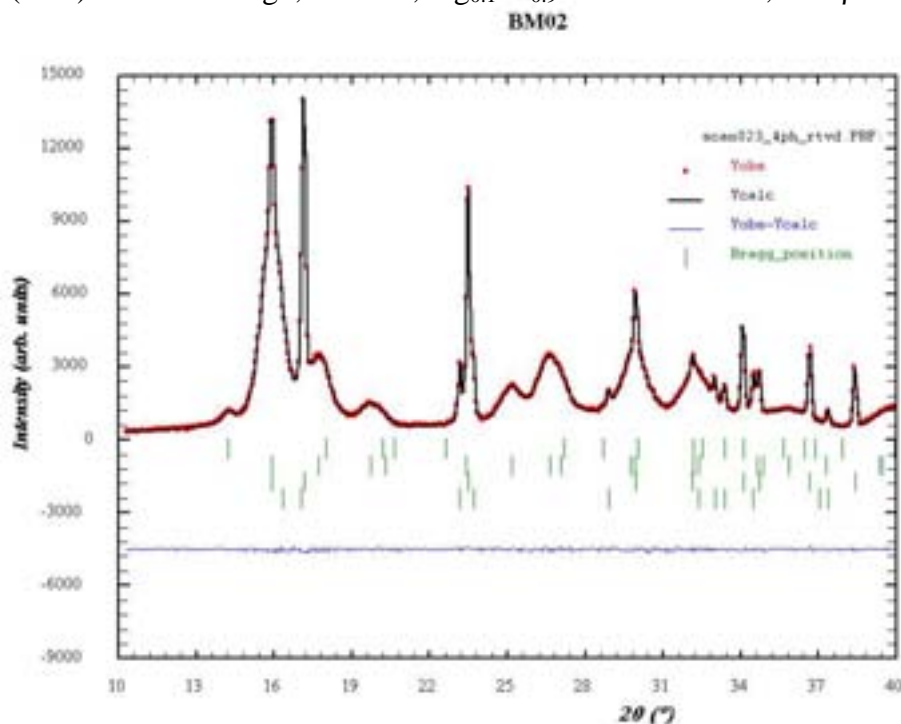


Fig. 26 Rietveld plot of small dark area at  $\omega=1.0^\circ$  obtained with FULLPROF [35] ( $R_{wp}=9.3$ ,  $\chi^2=3.96$ ). Observed (dots) and calculated (solid line) synchrotron diffraction patterns are shown together with the difference curve below. The vertical ticks indicate the reflection positions for the three phases: (1)  $\text{SnO}_2$  (2)  $\text{SnO}$  (3)  $\text{Hg}_{0.1}\text{Sn}_{0.9}$  (4)  $\beta\text{-Sn}$ .

## II.6. Discussion

The XRD study, using the GID method, provided information on the amalgam surface [36]. Small changes in the angle resulted in a large variation in the depth profile of the tin oxides and cannot be sensitively controlled at the nanometre scale. However, this provides a depth profile on a larger micrometer scale. The ancient mirrors studied presented different degrees of alteration. The manufacturing process, the environment, and the onset of corrosion at the most exposed amalgam layer are the factors that determine the different levels of amalgam decay [37].

The two tin oxides ( $\text{SnO}$ ,  $\text{SnO}_2$ ) are normal products due to environmental corrosion, and they correspond to the tin oxides reported due to indoor exposure [38, 39].

The high level of relative humidity is a determining factor of corrosion; furthermore, dust has an acidic character, which also retains humidity, thereby contributing to the acceleration of the corrosion process.

Sample 1 presented such a low stage of degradation that not only metallic tin but also  $\text{Hg}_{0.1}\text{Sn}_{0.9}$  was identified in all of the diffraction patterns. The diffractograms using GID with conventional and synchrotron radiations also showed a small proportion of tin oxides in the upper layers. No traces of Hg were detected by XPS, but Hg was identified by EDX, whose penetration depth is higher than that of XPS. However, this discrepancy creates an important problem in the characterisation of the amalgam layer in Sample 1. Two hypotheses are suggested to explain why Hg was not detected by the XPS: (i) Hg evaporated in the vacuum of the XPS chamber, which could have damaged its detector; (ii) Sn could be enriched in the outer layer of the amalgam, whereas Hg remained in deeper layers that are not reached by the XPS radiation. The XPS confirmed the presence of the  $\text{Sn}^{2+}$  and  $\text{Sn}^0$  species at the most external surfaces of the amalgam. On the other hand, Sample 2 shows a high degree of alteration. Gypsum was also present in the dull surface of the amalgam, coming from the wall in contact with the mirror. Such presence suggests that sulphates accelerated the corrosion of the amalgam [40].

Sample 3 also presents a high degree of corrosion of the dull surface, clearly shown by the higher presence of  $\text{SnO}_2$  than SnO. However, in the glossy surface, the increase of SnO is in agreement with a lower corrosion degree. The contribution of gypsum and calcite, associated with environmental contamination, and the organic acid coming from the degradation of the wood frame, may be responsible for the higher degradation of the dull surface.

Sample 4 presented such a high degree of corrosion that romarchite (SnO) and cassiterite ( $\text{SnO}_2$ ) could be identified in the inner layers. Meanwhile, the amount of  $\text{SnO}_2$ , relative to the amount of SnO, increased in the outer layers. These data suggest a gradual increase of tin degradation along the outer layers of the amalgam.

These results confirm the high degree of alteration of Samples 3 and 4, perhaps due to the organic acids coming from the wood frame. A predominant role of atmospheric pollutants such as sulphates was detected in Sample 2 that accelerated its corrosion process. The amalgam of Sample 1 is the least altered sample. However, the XPS shows the presence of  $\text{Sn}^0$  and  $\text{Sn}^{4+}$ , confirming the oxidation process of the surface that was not clearly detected by GID. FTIR and Raman spectroscopic methods provide clear

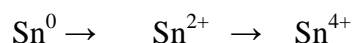
information about the SnO<sub>2</sub> and SnO present on the surfaces of the amalgam. The Raman spectra of the glossy surfaces of Sample 3 have very few bands revealing that the compounds are very poorly crystallised at the surfaces in comparison with Sample 4.

The mercury-rich liquid phase present in these samples, detected only by SEM/EDX analyses, accelerated the corrosion of the tin-rich solid phase due to the de-alloying process and involves the selective leaching of mercury that slowly evaporates. Gravity also could have played a role in the formation and release of mercury drops [2]. These facts are responsible for the presence of the liquid mercury phase on the top of the craters and at the bottom edge of the mirrors.

#### Corrosion process of the mirrors

The mercury evaporation is closely related to the corrosion state of the amalgam. In order to reveal the relationship between the mercury release and the tin oxides formed on the most external layer it is necessary to determine the composition and the chemical state of the components of the amalgam surface. Tin oxide layer formed on the amalgam surface suppresses the mercury evaporation. The Gibbs formation energy ( $\Delta G^{\circ}_{298(\text{Kj/mol})}$ ) of tin oxides are: SnO = -252 Kj/mol and for SnO<sub>2</sub> = -519 Kj/mol. This information suggests the favourable formation of SnO<sub>2</sub> at the surface of the amalgam. The XPS suggest that the high content of Sn at the surface of the amalgam is the result of the mercury evaporation that has a high diffusion coefficient compared to tin. Consequently the tin is oxidizing to SnO<sub>2</sub> at the surface.

The chemical analysis carried out by XPS at the surface (~5nm) showed the presence of Sn<sup>4+</sup>. The XRD information showed that the phases present between 0.25µm and 1.17µm are tin dioxide (Sn<sup>4+</sup>) and tin monoxide (Sn<sup>2+</sup>). The original amalgam was constituted by Sn<sup>0</sup>. Therefore corroded mirrors studied in this work show a similar corrosion process, that is, the oxidation of tin in the following way:



The mercury-rich liquid phase present in the amalgam accelerates the corrosion of the tin-rich solid phase through may be also attributed to the galvanic action. Tin has an electrochemical potential of -0.136 volts, corroded preferentially over mercury, which has an electrochemical potential of 0.854 volts [41]. In addition metallic mercury has a relatively high vapour pressure at room temperature (25°C), this produces the slow evaporation of the mercury from the amalgam disappearing from the reaction media;

however, there is still liquid phases in both mirrors, appearing drops of Hg at the bottom of the frame. Here one would expect oxidation of the surface of the metal, to form a passive tin oxide film which would protect metal from further corrosion. However when the amalgam is corroded, mercury is released as tin oxidizes thus, two phases are present and galvanic corrosion can take place between the two phases [7]. The tin-rich solid phase would be expected to oxidize with the release of mercury, which causes the softening of the amalgam of the corroded area. The SnO firstly formed is thermodynamically unstable but oxidizes very slowly to the SnO<sub>2</sub> [26]. The two tin oxides are normal products due to atmospheric corrosion and correspond to the reported ones of tin exposed indoors [42, 43, 44], and the long time elapsed from the mirrors manufacture (XVII Century).

Semi-quantitative analysis of the depth-dependent distribution of the crystalline phases of the amalgam surface of Sample 5, using the grazing incidence X-ray diffraction technique was performed. The GID method using synchrotron radiation supplies important information of the degraded process of the amalgam. The use of a large beam with a high angle resolution provides an accurate means for semi-quantitative analysis and the use of a sub-mm beam opens a way for separating the dark corroded and uncorroded part of the amalgam. The heterogeneous formation of the dark area causes some errors in the quantitative analysis (estimated to be 8%). However, it was possible to distinguish between the four main phases in the most external layer ( $\gamma=1.0^\circ$ ) of the small dark area corresponding to SnO<sub>2</sub>≈4.69 %, SnO≈82.68% %, Hg<sub>0.1</sub>Sn<sub>0.9</sub>≈4.51% and  $\beta$ -Sn≈8.12%. The small percentage of Hg<sub>0.1</sub>Sn<sub>0.9</sub> is due to the contribution of some particles that are present near the border that separated the corroded from the uncorroded areas. The  $\beta$ -Sn phase was not totally transformed to the tin oxide due to the low percentage found at the surfaces. The high percentage of SnO is due to the first oxidation stage of tin (Sn<sup>2+</sup>); some of the SnO was oxidized to Sn<sup>4+</sup>. Moreover, in the internal layer of the dark area, it is possible to distinguish the three main phases corresponding to SnO<sub>2</sub> ≈82 %, SnO≈16%, and Hg<sub>0.1</sub>Sn<sub>0.9</sub> ≈0.89%. In the dark area,  $\beta$ -Sn was totally transformed into the tin oxides. The high percentage of SnO<sub>2</sub> is due to the stability of this oxide. The present of SnO<sub>2</sub> in a high portion is similar to the corroded surface amalgam that was previously studied.

The ancient mirrors studied presented such a high degree of corrosion that the amount of SnO<sub>2</sub> increased in the outer layers. These data suggest a gradual increase of tin degradation along the outer layers of the amalgam. The mercury-rich liquid phase present in the amalgam accelerated the corrosion of the tin-rich solid phase. Here, one would expect oxidation of the surface of the metal to form a passive tin dioxide film which would protect the metal from further corrosion. However, the mercury is volatile and slowly disappears from the tin-mercury compound leaving finely divided particles of tin that are oxidized forming nanocrystals that are explain in the next chapter.

### II.7. Conclusions

The combined use of SEM/EDX, XPS, FTIR, Raman and XRD provides good insight into the surface chemical information and corrosion products of ancient mirrors. The combination of all these techniques is able to clearly determine the corrosion state of the former mirror.

The combined use of GID and XPS provides good insight into the surface's chemical structure and the degradation of different amalgam mirrors. GID enables a notable increase in the volume of studied samples, allowing a large irradiated area of the sample at small X-ray penetration depths. GID is a potential and useful non-destructive research tool for studying cultural heritage artifacts.

The developed SRXRD experimental set-up used on the amalgam surfaces offers an unique opportunity to obtain, on the same sample and under identical conditions, a depth profile analysis that allows the correlation of information between the surface and bulk properties of the mirrors. XPS analysis reinforces the information obtained by GID.

The use of a large beam with a high angle resolution provides an accurate mean for semi-quantitative analysis and the used of sub-mm beam opens a way to separate the dark corroded and uncorroded parts of the amalgam.

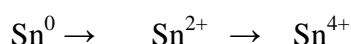
The structure of the tin amalgam mirror is composed of a binary alloy of tin and mercury. X-ray diffraction identifies this structure as Hg<sub>0.1</sub>Sn<sub>0.9</sub> with a primitive hexagonal structure and special group P6/mmm.

Sample 1 presents a very low degree of alteration, whereas Sample 2 was largely degraded, to an extent that the reflecting layers Hg<sub>0.1</sub>Sn<sub>0.9</sub> and metallic β-Sn had disappeared. Mercury is volatile and slowly evaporates; ultimately leaving finely divided

particles of tin that are easily oxidized first to SnO (romarchite) and then to SnO<sub>2</sub> (cassiterite).

In Samples 2, 3 and 4, a unique chemical species, Sn<sup>4+</sup>, was found and, on the other hand, for Sample 1 the XPS analysis is the only technique that confirmed the formation of Sn<sup>4+</sup> at the surface. SnO<sub>2</sub> is the most typical and stable corrosion product of the tin.

The corroded mirrors studied in this work show a similar corrosion process, that is, the oxidation of tin at the surface (~5 nm), in the following way:



Semi-quantitative composition analysis of the different phases found using Rietveld refinement modeling contributed to the knowledge of the corrosion mechanisms produced on the amalgam surfaces of the ancient mirrors.

## II.8. References

- [1] Morser F, *A study of glass surface deterioration by moisture*, The Glass Industry 42 (1961) 244-286
- [2] Hadsund P. 1993 *The Tin-Mercury Mirror: Its Manufacturing Technique and Deterioration Processes*, Studies in Conservation 38-3-16.
- [3] Navarro J.M.F. 1991 *El Vidrio*. 2nd Ed., CSIC, Madrid.
- [4] Römich H. Historic glass and its interaction with the environment, in: Tennent N.H. (Ed.). 1999 *The conservation of glass and ceramics. Research, Practice and Training*. James and James Science Publishers, London. 5-14.
- [5] Adams F, Adriaens A, Aerts A, De Raedt I, Janssens K, Schalm O. 1997 *Micro and surface analysis in art and archaeology*: Plenary lecture, Journal of Analytical Atomic Spectrometry 12 (3) 257-265.
- [6] Shoukamg Z, Tangkun H. Studies of ancient Chinese mirrors and other bronze artefacts, in: La Niece S, Craddock P(Ed.). 1993 *Metal Plating and Patination: Cultural, Technical and Historical developments*, Chapter 5. Butterworth Heinemann oxford.
- [7] Herrera L.K, Duran A, Jimenez de Haro M.C, Perez-Rodriguez J.L, Justo A. 2007 *Study of baroque artworks by non-destructive techniques*. Coalition Electronic Newsletter 14 10-14.
- [8] Rubio-Zuazo J, Castro G.R. 2005 *Hard X-ray photoelectron spectroscopy (HAXPES) ( $\leq 15$  keV) at SpLine, the Spanish CRG beamline at the ESRF*. Nucl.Inst Meth A. 547 (1) 64-72.

- [9] Rubio-Zuazo J, Castro G.R. 2007 *Probing buried interfaces by simultaneous combination of X-ray diffraction (SXRD) and hard X-ray photoelectron spectroscopy (HAXPES, up to 15 KeV)*. Reviews on advance material. science. 15, (1) 79-86
- [10] Skrzypek, S.J., Goły, M., Ratuszek, W., Kowalski, M. T. 2007. *Non-destructive phase analysis and residual stresses measurement using grazing angle X-ray diffraction geometry*. Diffusion and Defect Data Pt.B: Solid State Phenomena 130, 47-52
- [11] Kötschau, I.M., Schock, H.W. 2006 *Compositional depth profiling of polycrystalline thin films by grazing-incidence X-ray diffraction*. Journal of Applied Crystallography 39 (5), 683-696
- [12] <http://www.esrf.eu/UsersAndScience/Experiments/CRG/BM25/>
- [13] Rubio-Zuazo, J., Castro, G.R. 2008 *Non-destructive compositional depth profile analysis by hard x-ray photoelectron spectroscopy*. Journal of Physics: Conference Series 100 (1), art. no. 012042
- [14] Simon, J.P., Arnaud, S., Bley, F., Berar, J.F., Caillot, B, Comparat, V. , Geissler, E., De Geyer, A., Jeantey, P., Livet, F, Okuda, H. 1997 *A New Small-Angle X-ray Scattering Instrument on the French CRG Beamline at the ESRF Multiwavelength Anomalous Scattering/Diffraction Beamline (D2AM)* Journal of Applied Crystallography 30 (6), 900-904
- [15] Breiby, D.W., Bunk, O., Andreasen, J.W., Lemke, H.T., Nielsen, M.M. 2008 *Simulating X-ray diffraction of textured films* Journal of Applied Crystallography 41 (2), 262-271
- [16] Samant, M.G., Toney, M.F., Borges, G.L., Blum, L., Melroy, O.R. 1998 *Grazing incidence X-ray diffraction of lead monolayers at a silver (111) and gold (111) electrode/electrolyte interface* Journal of Physical Chemistry 92 (1), 220-225
- [17] Goehner R.P, Eatough M.O. 1992 *A Study of Grazing Incidence Configurations and Their Effect on X-Ray Diffraction Data*. Powder Diffraction, 7 (1)2-5.
- [18] Singh, M., Low, I.M. 2002 *Depth-profiling of phase composition and preferred orientation in a graded alumina/mullite/aluminium-titanate hybrid using X-ray and synchrotron radiation diffraction*. Materials Research. Bulletin 37 (7), 1279-1291
- [19] Jiménez V.M, Mejías J.A, Espinós J.P, González-Elipe A.R. 1996 *Interface effects for metal oxide thin films deposited on another metal oxide III. SnO and SnO<sub>2</sub> deposited on MgO (100) and the use of chemical state plots*. Surface. Science. 366, 545.-563
- [20] Reiche R, Oswald S, Yubero F, Espinós J.P, Holgado J.P, and Gonzalez-Elipe A R. 2004. *Monitoring Interface Interactions By XPS At Nanometric Tin Oxides Supported on Al<sub>2</sub>O<sub>3</sub> and Sb<sub>2</sub>O<sub>3</sub>*. Journal of Physical Chemistry B 108 (28), 9905-9913
- [21] Gonzalez-Elipe, A.R, Yubero F. 2001 *Spectroscopic Characterisation of Oxide/Oxide Interfaces*. Handbook of Surfaces and Interfaces of Materials. USA Academic Press. 147-191.

- [22] Schreiner, M. 1991 Glass of the past: *The degradation and deterioration of medieval glass artifacts* Mikrochimica Acta 104 (1-6), 255-264
- [23] Massalsky T.B (ed.) 1992. in Binary Alloys Phase Diagrams, Vol. 3 Edn (ASM International, Metals Park, Ohio, 2168.
- [24] Vineyard, G.H. 1982 *Grazing-incidence diffraction and the distorted-wave approximation for the study of surfaces*. Physical Review B 26 (8), 4146-4159
- [25] Simulation performed using the absorbDX, (v1.1.2) software, provided with the bruker-AXS D8 Advance x-ray diffractometer
- [26] Herrera L.K, Duran A, Franquelo M.L, Jimenez de Haro M.C, Justo A, Perez-Rodriguez J.L. 2008 *Studies of Deterioration of the Tin-Mercury Alloy within Ancient Spanish Mirrors* Journal of Cultural Heritage 9, 41-46
- [27] Robinet L, Eremin K, Cobo del Arco B, Gibson L.T. 2004 *A Raman spectroscopic study of pollution-induced glass deterioration*. Journal of Raman spectroscopy. 35, 662-670
- [28] Ocaña M, Serna C.J, Matijevic E. 1993 *A vibrational study of uniform SnO<sub>2</sub> powders of various morphologies*. Solid Stated Ionic. 63-65, 170-177.
- [29] Hagan B.X, Tornatore P, Li Y.S. 2000 *IR and Raman spectroelectrochemical studies of corrosion film on tin*. Electrochemical Acta. 46, 671-679.
- [30] De Ryck I, Van Biezen E, Leyssens K, Adriaens A, Storme P, Adams F. 2004 *Study of tin corrosion: the influence of alloying elements*. Journal of Cultural Heritage. 189-195
- [31] Rubio-Zuazo, J. 2005 Doctoral thesis: Synchrotron X-ray radiation applied to the study of thin films: The case of La<sub>0.7</sub>Ca<sub>0.3</sub>MnO<sub>3</sub>/SrTiO<sub>3</sub>(001). 399pp
- [32] Klug H, L.E Alexander 1974. In: X-Ray diffraction procedures for polycrystalline and amorphous materials, Wiley/Interscience, New York, 94pp
- [33] Toney M.F, Brennan S, J. 1989 *Structural depth profiling of iron oxide films using grazing incidence asymmetric Bragg X-Ray diffraction*. Journal Applied. Physics. 65,(12) 4763-4768.
- [34] De Rick I, Adriaens A, Storme P, Adams F. 2004 *The tin mercury inlay of a cabinet manufactured by Hendrik Van Soest: A case study*. e-preservation science Ed, Morana 1, 9-14
- [35] Carvajal J.R, Roisnel T, Fullprof V. 2008. <http://www.fullprof.com>
- [36] Herrera L.K, Duran A, Franquelo M.L, González-Elipe A.R, Espinós J.P, Rubio-Zuazo, J, Castro G, Justo A, Perez-Rodriguez J.L. 2008 *Study by grazing incident diffraction and surface spectroscopy of amalgam from cultural heritage ancient mirrors*. in press DOI 10.2478/s 1111532-008-0089-1

- [37] Corbeil M.C. 1998 *A note on the use of tin amalgam in marquetry*, Studies in Conservation 43, 265-269.
- [38] Kossolapv A; Twilley J 1994 *A decorative Chinese dagger: evidence for ancient amalgam tinning*, Studies in Conservation 39, 257-264
- [39] Robbiola L, Rahmouni K, Chiavari C, Martini C, Prandstraller D, Texier A, Takenouti H, Vermaut P. 2008 *New insight into the nature and properties of pale green surfaces of outdoor bronze monuments*. Applied Physics A Materials Science and Processing. 92, 161-169
- [40] Bartolla J, Rfhrsb S, Erkoç A, Firsovc A, Bjeoumikhovd A, Langhoff N. 2004 *Micro-X-ray absorption near edge structure spectroscopy investigations of baroque tin-amalgam mirrors at BESSY using a capillary focusing system* Spectrochimica Acta part B. 59, 1587-1592.
- [41] R.C. Weast(ed). CRC Handbook of Chemistry and Physics 70th edn (Boca Raton, FL: CRC Press). 1989.
- [42] A.V. Echavarria, F.E. Echeverria, C.A. Arroyave, E. Cano, J.M. Bastidas J.M *Corros. Rev.* 21 (5-6), 395 (2003)
- [43] L. Pilosi (Ed.), *Guidelines for the conservation and restoration of stained Glass*, 2nd International Corpus Vitrearum , Nuremberg (2001).
- [44] Newton, G., Davison, S., *Conservation of Glass*, Butterworths, London, 1989.

## II. 1. Study of nanocrystalline SnO<sub>2</sub> particles formed during the corrosion processes of ancient amalgam mirrors

### Introduction

Tin oxides have been used in a variety of applications, such as ceramic materials [1], gas sensors [2], dye-based solar cells [3], electronic materials [4] and catalysts [5]. The synthesis of nanomaterials with well controlled sizes, morphology and chemical composition may open new opportunities in the exploration of new and enhanced physical properties [6,7]. The preparation of nanocrystalline SnO<sub>2</sub> of narrow size distribution has been widely reported [8-10].

In the field of cultural heritage, cassiterite was used in the tin-based opacifiers (lead stannate yellow and tin oxide white) in glass production for a short period in Europe from the second to the first centuries BC, and throughout the Roman and Byzantine Empires from the fourth century AD. Tin oxide was also used in the production of Islamic opaque glazes from the ninth century AD, and subsequently in enamels applied to Islamic and Venetian glasses from the 12<sup>th</sup> century AD [11,12]. Wang et al. [13] have proved that the surface layers of black mirrors in ancient china were mainly composed of nanometer-sized particles of Sn<sub>1-x</sub>(CuFePbSi)<sub>x</sub>O<sub>2</sub> with cassiterite structure.

Other interesting subjects included in cultural heritage materials are tin-mercury amalgam mirrors that were explain in the last section of this chapter The Sn<sup>0</sup> can be converted to SnO and SnO<sub>2</sub> [14]. The two tin oxides are the normal products of atmospheric corrosion of tin objects, i.e. tin, tin alloys, bronze, amalgams and pewter artifacts [15, 16, 17]. SnO<sub>2</sub> is by far the most typical and most stable corrosion product of tin. The SnO<sub>2</sub> layer is formed by passivating the surface in the environment studies [18]. In the corrosion-inhibitive effect, amorphous tin oxide is assumed to form a protective barrier on the bronze surfaces [19]. In the case of amalgam mirrors, the mercury is volatile and slowly disappears from the tin-mercury compound, leaving finely divided particles of tin that are oxidised, probably forming nanocrystalline SnO<sub>2</sub> particles.

### II.1.1. Research aim

Study of the formation of SnO<sub>2</sub> nanometric particles in the alteration process of ancient amalgam mirrors has been studied.

### II.1.2. Materials

Corroded amalgam sample was taken from Andalusian Baroque mirror

### II.1.3. Experimental method

To separate the SnO<sub>2</sub> particles of sample, ultrasonic treatment was used, which was performed with a Misonic ultrasonic liquid processor of 750 W output with a 20 kHz converter and a tapped titanium disruptor horn of 12.7 mm in diameter that produces a double (peak to peak) amplitude into a cylindrical jacketed cooling cell of 5 cm in internal diameter, where a few grams of SnO<sub>2</sub> powder was mixed with 20 ml of freshly deionised water. The dispersions were sonicated for 1h. The temperature reactor was kept constant at 20 °C during the entire treatment by means of a cooling recirculator. After treatment, samples were lyophilised to remove the water of suspension. The average crystal size of SnO<sub>2</sub> separated from the surface of the corroded mirror using the sonication method and the SnO<sub>2</sub> particles found directly on the surface of the corroded mirror without the sonication method [20] were estimated using the Scherrer formula [21]. Transmission electron microscopy was performed with a TEM Philips CM200 microscope operating at 200kV to analyse the morphology, particle size and crystallographic parameters of the tin dioxide particles.

### II.1.4. Results and Discussion

#### II.1.4.1. Corroded amalgam

An example of the visual appearance of sample using an optical microscope is shown in Fig. 1a. The SEM micrograph shows many protuberances with holes on the top of them resembling 'craters'. In some of these craters, spheres of Hg are still present and fill the pores (Fig. 1b). The EDX analysis of the corroded amalgam surface detected the presence of two segregated phases, one constituted by Sn and other one by Hg. The total surface contains approximately 80 wt% tin and 20 wt% mercury.

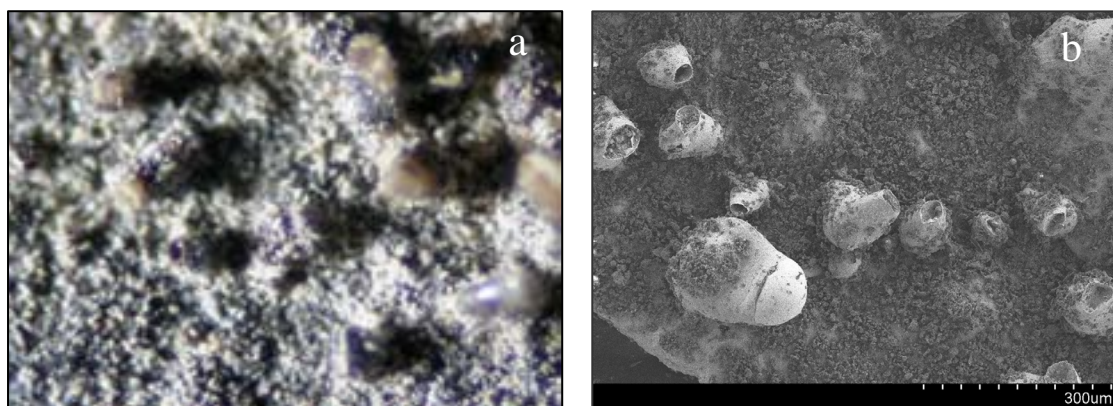


Fig. 1. Microphotographs of the morphology of corroded mirror (a) craters observed on the surface (500X) (b) SEM image shows a drop of Hg arising from the crater and other craters empty because the Hg has been released.

Due to the heterogeneous complexity of the surface, the microstructure was investigated by the preparation of a metallographic cross-section. The thickness of the layers ranged from 100 to 130  $\mu\text{m}$ . In the cross-section, mainly two different phases were recognised, which appear light grey and white due to the atomic number contrast of backscattered electrons (Fig. 2a). The semi-quantitative EDX analyses depend on the zone that has been analysed due to the heterogeneous corrosion process of the tin amalgam mirror along the cross section. For this reason, we identified three different zones: zone 1 contains approximately 80 wt% tin and 20 wt% mercury (Fig. 2b); zone 2 is composed of 98 wt% mercury and 2 wt% tin (Fig. 2c). Corrosion products on the surface of the mirror frequently had the shape of hemispherical concentric bands composed of tin oxide. Zone 3 is composed of these bands, and these are the most frequently found in the corroded amalgam (Fig. 2d).

The diffraction profiles of the surface (Fig. 3) were acquired using  $\gamma = 1^\circ$  and  $\gamma = 5^\circ$ . The pattern at  $\gamma = 1^\circ$  gives information about the most external layer; the diffraction patterns can be attributed to tin oxides, such as  $\text{SnO}_2$ . The pattern at  $\gamma = 5^\circ$  showed a similar composition. These results showed a very high degree of surface alteration.

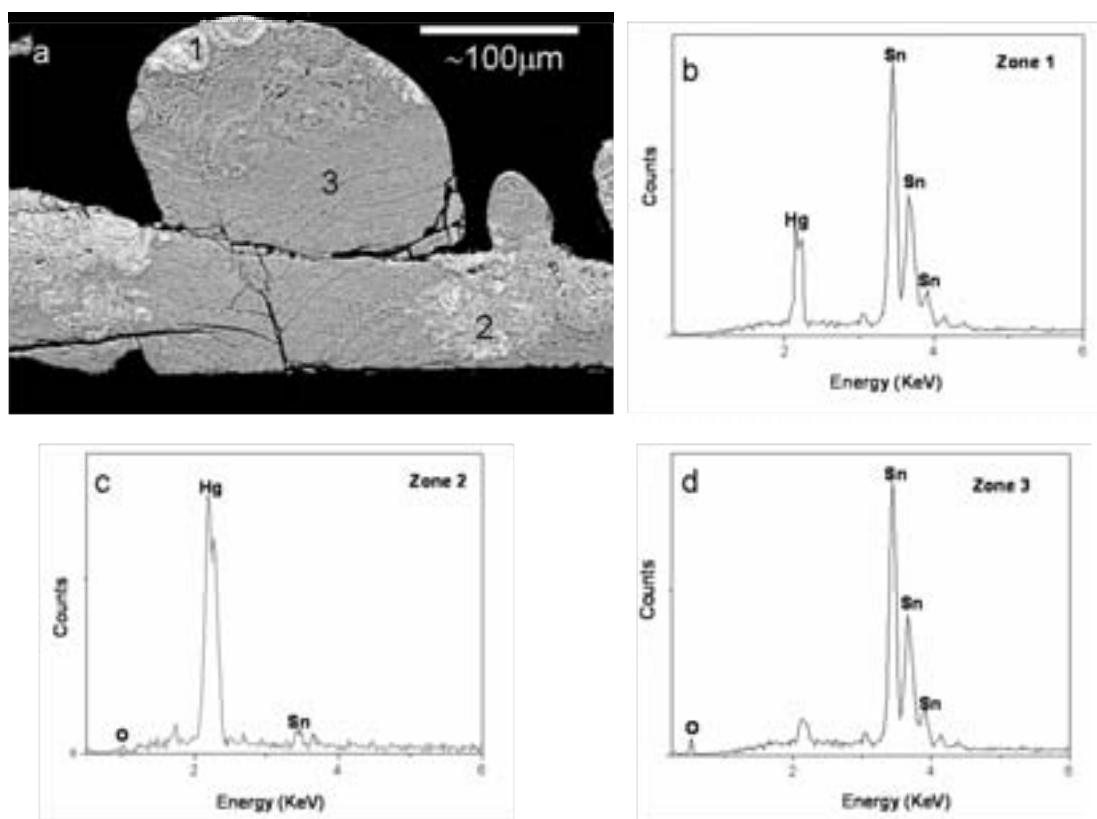


Fig. 2. (a) SEM image of the microstructure of the cross section of the corroded mirror (sample 2) (b) zone 1 (c) zone 2 (d) zone 3.

The amalgam ( $\text{Hg}_{0.1}\text{Sn}_{0.9}$ ) and metallic Sn ( $\beta\text{Sn}$ ), which were the original phases of the unoxidised amalgam, were not found due to corrosion of the original alloy. These data suggest a high alteration degree of the tin-mercury mirror and the formation of very small particle sizes of  $\text{SnO}_2$ .

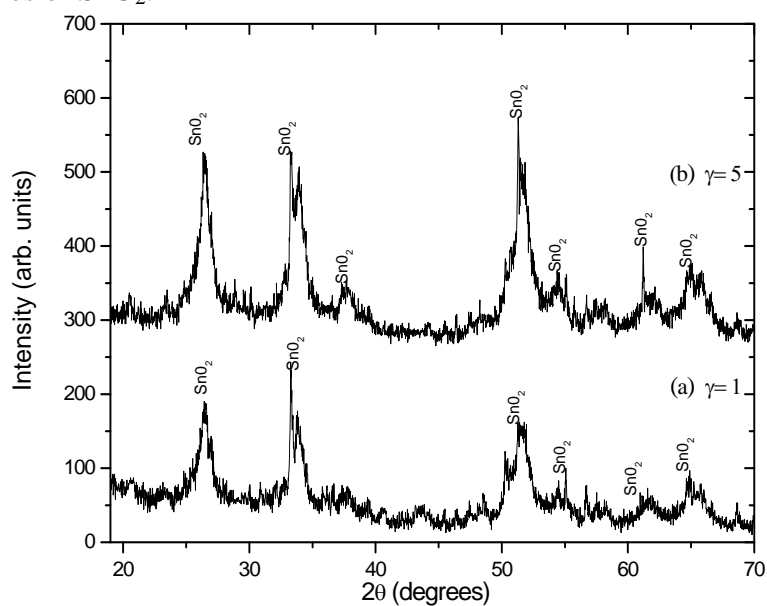


Fig. 3. XRD diffractograms of sample 2 under incidence angles: (a)  $\gamma = 1^\circ$ ; (b)  $\gamma = 5^\circ$ .

### II.1.4.2. Characterisation of tin dioxide nanoparticles

The SnO<sub>2</sub> phase was straightforwardly identified by XRD (Fig.4). The average crystal sizes of the SnO<sub>2</sub> particles were estimated by the Scherrer formula based on the (1 1 0) reflection of the XRD [21 , 22]. The measurements were done in the XRD patterns obtained directly on the corroded mirror and on the SnO<sub>2</sub> powders separated from the surface.

$$\langle d \rangle = K\lambda/\beta\cos\theta$$

where  $d$  is the average crystalline size,  $K$  is a grain shape dependent constant (0.9),  $\lambda$  is the wavelength of the incident beam,  $\theta$  is a Bragg reflection angle and  $\beta$  is the full width at half-maximum [21]. The average crystallite size of the SnO<sub>2</sub> powder separated from the surface was estimated from the XRD pattern, and the value obtained was 4 nm. The XRD measurement directly on the corroded surface showed a similar value of 5 nm.

These values are in agreement with the results reported by Wang et al. [13], who studied the presence of SnO<sub>2</sub> in ancient Chinese black mirrors and also synthesized SnO<sub>2</sub> particles.

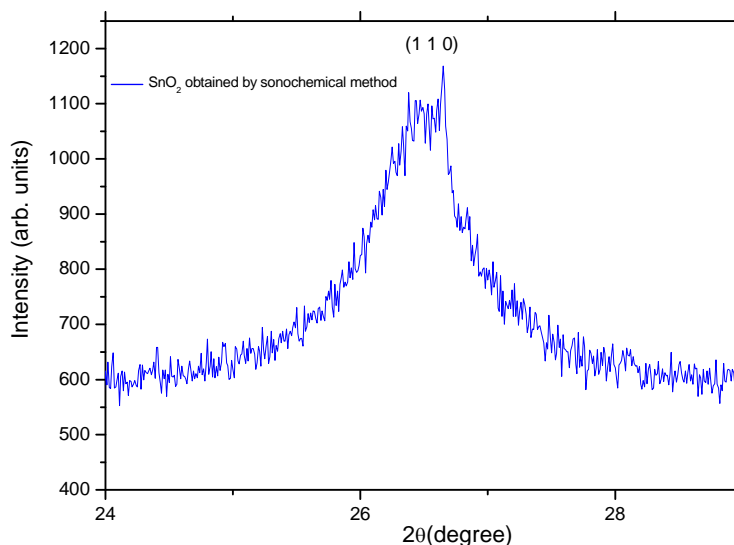


Fig. 4. XRD profile at incidence angle  $\gamma = 5^\circ$  of SnO<sub>2</sub> powder separated from the surface of sample 2 by the sonication method.

To confirm the particle sizes obtained by XRD, the samples were studied by TEM. A drop of the suspension obtained by sonication treatment containing these nanoparticles was dropped onto a copper grid and transferred to a transmission electron microscope (TEM). TEM images of the SnO<sub>2</sub> particles formed during the corrosion process of the ancient mirrors were acquired together with the Selected Area Electron Diffraction (SAED). Figures 5a and 5b show a polycrystalline matrix formed by irregular small

particles with a crystalline size of about 4-5 nm. The SAED of both samples (Figs. 8a1 and 8b1) showed bright spots with a d-spacing of 3.44, which can be assigned to the SnO<sub>2</sub> (110) planes. The second and third rings are in agreement with the expected values of the SnO<sub>2</sub> (110) and (200) planes. All of the spots of both samples could be indexed to the cassiterite structure.

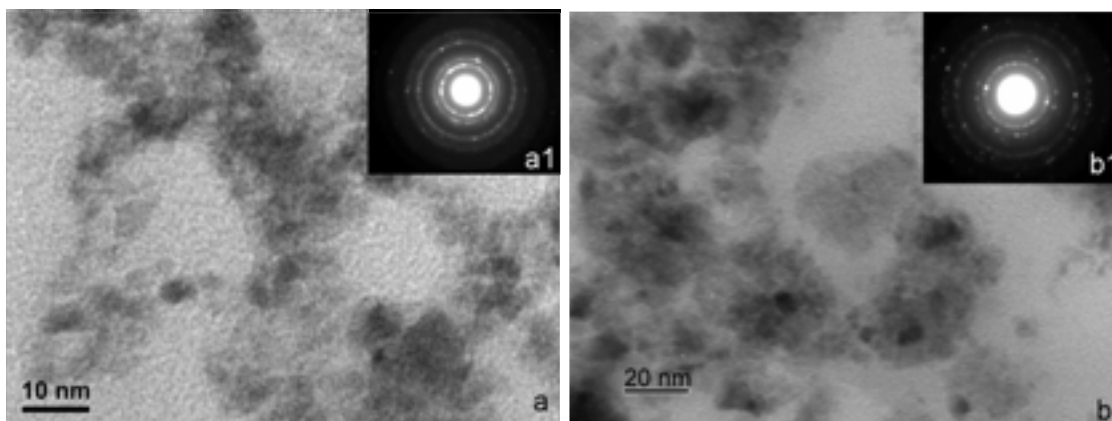


Fig. 5. TEM image (a) from SnO<sub>2</sub> nanoparticles (b) aggregates of SnO<sub>2</sub> nanoparticles found on the surface of sample (a1) electron diffraction pattern of the sample (b1) electron diffraction pattern of the sample.

The amalgam presented a high degree of corrosion, in that the amount of SnO<sub>2</sub> was increased in the outer layers. These data suggest a gradual increase of tin degradation along the outer layers of the amalgam. In this sample, the SnO<sub>2</sub> phase was straightforwardly identified by XRD using different incidence angles. The average crystalline size of the nanoparticles was evaluated using the Scherrer formula and was estimated in the range of 4 to 5 nm, which is in a good agreement with the size estimated by TEM. The electron diffraction pattern of the nanoparticles could be indexed to the cassiterite (SnO<sub>2</sub>) structure, which is the most typical and stable corrosion product of tin.

The mercury-rich liquid phase present in the amalgam accelerated the corrosion of the tin-rich solid phase. Here, one would expect oxidation of the surface of the metal to form a passive tin dioxide film that would protect the metal from further corrosion. However, the mercury is volatile and slowly disappears from the tin-mercury compound, leaving finely divided particles of tin that are oxidised to SnO<sub>2</sub> nanocrystals.

### II.1.5. Conclusion

The investigation of the corrosion processes of amalgam layers on a microscopic scale has been done using different techniques. Sn-Hg alloys, Hg and SnO<sub>2</sub> could be identified within the corrosion areas studied. Therefore, the corrosion process most likely

starts with a segregation of mercury and tin leading to the formation of Hg drops on the surface of the alloy layer. These nanoparticles are formed due to the oxidation process of the Sn polycrystalline layer remaining behind and still in contact with the Hg drops. Most likely, first SnO, and then SnO<sub>2</sub> is formed. The mercury drops eventually evaporate, leaving behind a “crater” surrounded by SnO<sub>2</sub> that is filled with a thin layer of SnO<sub>2</sub> nanoparticles, which eventually fall out of the “crater”.

### II.1.6. References

- [1] H. Torvela and S. Leppävuori: Intern. High Technol. Ceram. Vol. 3 (1987), p.309.
- [2] A. Cirera, A. Vila, A. Dieguez, A. Cabot, A. Cornet, and J.R. Morante: Sens. Actuators, B. Vol. 64 (2000), p. 65.
- [3] S. Chappel and A. Zaban: Sol. Energy Mater. Sol. Cells. Vol. 71 (2002), p.141.
- [4] D. Aurbach, A. Nimberger, B. Markovsky, E. Levi, E. Sominsky, and A. Gedanken: Chem. Mater. Vol. 14 (2002), p.4155.
- [5] M. Miyauchy, A. Nakajima, T. Watanabe, and K. Hashimoto: Chem. Mater. Vol. 14 (2002), p. 2812.
- [6] Y. Rusen and W. Zhong. Lin: J. Am. Chem. Soc. Vol. 128 (2006) p. 1466.
- [7] A. P. Alivisatos: J. Phys. Chem. Vol. 100 (1996), p13236.
- [8] L.M. Cukov, T. Tsuzuki, and. McCormick : Scr. Mater. Vol. 44 (2001), p.1787.
- [9] M.Ocaña, C.J.Serna, and E. Matijevic: Mater Lett. Vol. 12 (1991), p 32.
- [10] K.C. Song, J.H. Kim : Powder Technol. Vol. 107 (2000), p 268.
- [11] M. Tite, T. Pradell, and A. Shortland: Archeometry Vol. 50 (2008), p. 67.
- [12] J. Molera, T. Pradell, N. Salvadó, N., and M.Vendrell-Saz: J. Am. Ceram. Soc. Vol. 82 (1999), p 2871.
- [13] C. Wang, B. Lu, J. Zuo, S. Zhang, S. Tan, M. Suzuki, and W.T. Chase: Nanostruct. Mater. Vol. 5 (1995), p 489.
- [14] I. De Ryck, E. Van Biezen, K.Leyssens, A. Adriaens, P. Storme, and F.Adams: J.Cult. Herit. Vol. 5 (2004), p 189.
- [15] L. Robbiola, K. Rahmouni, C. Chiavari, C. Martini, D. Prandstraller, A. Texier, H. Takenouti, and P. Vermaut: Appl. Phys. A: Mater. Sci. Process. Vol. 92 (2008), p 161.

- [16] R.A Ramik, R.M Organ, and J.A Mandarin: *Can. Mineral.* Vol. 41 (2003), p 649.
- [17] L.K. Herrera, A Duran, M.C Jimenez de Haro, J.L Perez-Rodriguez and A. Justo: *Coalition Electronic Newsletter.* Vol. 14 (2007) p, 10.
- [18] S.E Dunkle, J.R. Craig, J.D. Rimstidt, and W.R Lusardi: *Geoarchaeology.* Vol. 19 (2004), p 531.
- [19] L. Robbiola, J-M Blengino, and C. Fiaud: *Corros. Sci.* Vol. 40 (1998), p 2083.
- [20] J.L. Perez-Rodriguez, A. Wiewiora, V. Ramirez-Valle, V., A. Durán, and L.A. Pérez-Maqueda, L.A: *J. Phys. Chem. Solids.* Vol. 68 (2007) 1225
- [21] T. Krishnakumar, N. Pinna, K. Prasanna, K. Perumal, and R. Jayaprakash: *Mater Lett.* Vol. 62 (2008), p 3437.
- [22] X. Liujiang, Q. Dong, T. Xincun, and C. Chunjiao: *Mater. Chem. Phys.* Vol. 108 (2008), p 232.

### **III.1 Chemical composition of the metal pipes of Spanish baroque organs as determined by laboratory and synchrotron techniques.**

#### **Introduction**

An organ is artwork symbolic of a period. It is the union of tradition and innovation, craftsmanship and technology, music and architecture. Taken together, these elements form a marvellous structure that fills churches and concert halls with sound. Historical organs are an important part of European Cultural Heritage [1]. No other musical instrument can compare with the pipe organs in power, timbre, dynamic range, complexity of tone and sheer majestic sound. Recent interest in baroque music has generated demand to produce new organs with old sound. Old technology based on intuition and the family traditions of organ masters has been lost. New technology is based on the latest developments in analytical techniques and materials science. This new technology must be developed to obtain detailed information concerning chemical composition. The importance of such knowledge is that the alloy composition and properties of the pipes strongly influence the organ's sound.

An organ consists of hundreds to thousands of pipes arranged in different "stops" (sets of pipes with similar tone quality). Different alloys can be used to manufacture metal pipes. The metal pipes in organs are usually made out of tin, lead or a varying percentage of these two elements. The percentage of tin and lead changes the function of the typed pipes within the organ [2]. Lead has been the standard material of organ pipes for a very long time [3]. Its availability, low cost, high density and softness make it easy to work with and allow it to dampen unwanted resonance [4]. However, because modern lead is so pure and has a low strength/weight ratio, it is particularly prone to creep. To compensate for this, during casting most organ builders replace trace elements removed during refining. These trace elements generally consist of small amounts of antimony, bismuth, copper, and silver. It has been hypothesized that traces in 17<sup>th</sup> century lead made the pipes sturdy enough to stand for many years. Together, all of these trace elements produce the desired stiffness [5]. While lead has universal application, tin has been avoided almost completely. This is usually due to cost.

Nonetheless, tin has been considered the metal *par excellence* for strings and facades. Pipes manufactured with tin-rich alloys have a bright sound and typically look shinier than pipes manufacture with lead-rich alloys.

### III.1.2 Organ description

A pipe organ is a musical instrument that produces sound by blowing air through a series of hollow tubes controlled by keyboards. Pipe organs are distinguished from reed organs. In reed organs, air causes thin strips of metal to vibrate. They are also distinguished from electronic organs that use electrical devices to produce sounds similar to pipe organs. The large pipe organs used in public buildings are by far the biggest and most complicated musical instruments ever built.

A pipe organ consists of four basic parts. The console contains keyboards, foot pedals, and stops. The pipes, which may be as short as 1 in (2.5 cm) or as long as 32 ft (10 m), produce the sound. A complex mechanism operated by the console controls the flow of air into the pipes. A wind generator supplies air to the pipes.

A very small pipe organ may have a console with only one keyboard. Each key might control the flow of air to one pipe. However, most pipe organs have consoles with two to five keyboards, a set of foot pedals and a set of stops. Stops are controls that open or close the air supply to a group of pipes, known as a rank. In this way, each key can control the flow of air to several pipes.

The pipes exist in two basic forms. About four-fifths of the pipes in a typical pipe organ are flue pipes. A flue pipe consists of a hollow cylinder with an opening in the side of the pipe. The rest of the pipes are reed pipes. A reed pipe consists of a hollow cylinder containing a vibrating strip of metal connected to a hollow cone.

The action may be mechanical, pneumatic, electrical, or electropneumatic. A mechanical action links the console to the valves. The valves control the flow of air to the pipes with cranks, rollers, and levers. A pneumatic action uses air pressure, activated by the console, to control the valves.

The earliest known ancestor of the pipe organ was the hydraulus. The hydraulus was invented by the Greek engineer Ctesibius in Alexandria, Egypt, in the third century B.C. This device contained a reservoir of air that was placed in a large container of water. Air was pumped into the reservoir, and the pressure of the water maintained a steady supply of air to the pipes. Pipe organs with bellows appeared about four hundred years later. Medieval pipe organs had very large keys and could only play diatonic notes (the notes played by the white keys on modern keyboards). By the fourteenth century, keyboards could also play chromatic notes (the notes played by the black keys on modern keyboards). Keys were reduced in size by the end of the fifteenth century. By the year 1500, pipe organs in northern Germany had

all of the basic features found in modern instruments. Germany led the world in organ building for three hundred years.

### **III. 1.3 Spanish baroque organ**

Spanish organ culture is unique and special [6]. The organ has always been the most expensive and innovative instrument in musical history [6]. Everything related to the organ has improved over time. A wide Spanish project studied the composition of twenty-five Spanish Baroque Organs [7]. This chapter focuses on a Spanish baroque organ (Anonymous, c.a.1785) in the church of *San Andrés de Baeza*. Baeza is located in southern Spain in *Jaén* County.

In order to gain insight into the surface composition of the Spanish pipe samples, different experimental analyses were carried out. One such analysis was a microstructural characterisation of the samples. The most appropriate laboratory technique is Scanning Electron Microscopy combined with X-ray Energy Dispersive Spectrometry (SEM/EDX) and Grazing-Incidence X-ray Diffraction (GIXRD).  $\mu$ X-ray Fluorescence ( $\mu$ XRF) mapping using synchrotron radiation sources and a micro/submicron X-ray fluorescence probe were carried out with excitation energies in the ID 18F and ID 21 beamlines at the European Synchrotron Radiation Facility (ESRF) [8,9].

#### **III.1.4. Research aim**

The aim of this work was to identify the distribution and correlation of the trace elements present in the tin and lead phases of the Spanish pipe baroque organ. This was accomplished using a combination of laboratory techniques. New microanalytical methods employing the ID 18F and ID21 beamlines at the ESRF were used to obtain elemental and chemical imaging of the main phases and the trace elements at a sub-micrometer scale.

#### **III.1.5. Materials**

Four historical samples were collected from a baroque organ of San Andres (Fig 1a). Sample 1 is the horizontal resonator f2". Sample 2 is the "front flue pipe n°18". Sample 3 is the interior pipe "flue d #3" (Fig. 1b). Sample 4 is the interior "flue pipe Violon c2".



Fig.1 (a) Spanish baroque organ from Baeza, Jaen, (Anonymous, c.a.1785). (b) detailed view of the “flue pipe” (sample 3).

### III.1.6. Experimental

#### III.1.6.1. Sample preparation

Two types of sample preparation were completed:

(i) Untreated samples - Samples underwent no preparation in order to keep them intact for the determination of the chemical nature of the surface.

(ii) Metallographic cross-sectional samples - Samples were prepared into metallographic transversal cross-sections. These sections were analysed to understand the nature of the metallic composition of the alloy. The main alloying elements and trace elements were identified. The transverse cross-sections of the pipe samples for metallographic observation were cold mounted, polished and etched for microstructural examination. Abrasive particles frequently become embedded in the surface due to the ductile properties of these binary alloys (Pb-Sn). These particles can be dislodged with polishing and scratching of the metal sample. Prolonged polishing with intermittent etching and ultrasonic cleaning were applied to all of the samples.

### III.1.6.2. SEM/EDX investigation

The study of the morphology of the untreated sample surfaces was carried out using Optical Microscope, Scanning Electron Microscopes (JEOL JSM5400 and HITACHI S-4800). The elemental chemical analysis of the surface was done with a JEOL JSM5400 using Energy Dispersive X-Ray spectroscopy (Link ISIS). Semi-quantification of Sn and Pb were carried out by EDX analysis of the metallographic cross-sections samples.

### III.1.6.3. XRD analysis

A Siemens D5000 diffractometer with a Cu target and removable Grazing Incident Diffraction (GIXRD) device was used for the non-destructive characterisation procedure. This procedure identifies crystalline phases present at the surface and the metallographic cross-sections of the pipe metal samples. The diffractometer was equipped with a GID device and the measurements were carried out at low fixed incidence angles. These angles were used to characterise the alteration layer. Since the organ pipes are not flat, it was necessary to use a parallel x-ray beam. The beams diffracted by the sample were collimated using a parallel slit analyser rather than the divergent beam typically obtained with Bragg-Brentano geometry.

### III.1.6.4. $\mu$ XRF measurements

#### III.1.6.4.1. $\mu$ XRF elemental mappings at high excitation energy

$\mu$ XRF mapping was performed by synchrotron radiation at microprobe station ID18F on the metallographic cross-section (Fig. 2). The beam line is equipped with three undulator sources and a fixed-exit double Si (111) crystal monochromator with an energy resolution of  $\Delta E/E \sim 10^{-4}$ . The monochromatic beam is focused on the sample surface by means of Al compound refractive lenses ( $\sim 10^9$  phot/sec in the focused beam at 28 keV) excitation energy value. The optical stack uses 112 lenses with a parabolic profile and a radius of curvature of 196  $\mu\text{m}$ . [10] The intensity of the incident x-ray beam is monitored with a mini-ionization chamber [11]. A single element solid state Si(Li) detector (150 eV/Mn-K $\alpha$  energy resolution at 4 ms shaping time; 30 mm<sup>2</sup> active area; 4 mm active thickness) collects the characteristic X-ray fluorescence lines. By creating a secondary source using the beam line slits (0.1  $\times$  0.1 mm), the beam dimensions estimated by the Au knife-edge scan method [12] are 1.5  $\times$  5  $\mu\text{m}^2$  (V  $\times$  H) at 28 keV.

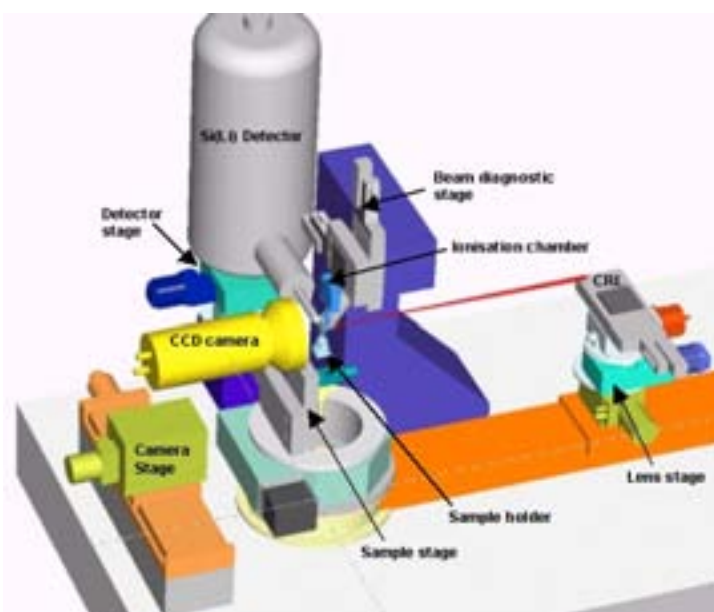


Fig. 2 ID18F microprobe setup at the ESRF.

#### III.1.6.4.2. $\mu$ XRF elemental mappings at low excitation energy

$\mu$ X-ray fluorescence mapping was performed in untreated and cross-sectional samples using the x-ray microscopy beam line ID21 (Fig. 3). The scanning x-ray microscope is optimised for very low background and a low detection limit.

The energy values are 4.05 and 7.3 keV. The energy beam is determined with a fixed-exit, double crystal Si (111) monochromator that is located upstream of the microscope. It has an energy resolution of  $\Delta E/E = 10^{-4}$ . The beam size is reduced to  $80\mu\text{m}^2$  (horizontal x vertical) thanks to the Fresnel zone plates and a geometrical demagnification of the synchrotron sources [9]. At fixed energy, the beam remains fixed while the sample is raster-scanned horizontally and vertically to obtain two-dimensional images.

The microfluorescence signal was collected in the horizontal plane perpendicular to the incident beam direction by using a small area. An HpGe solid-state, energy dispersive detector with an energy resolution of 135eV at 6keV was used. Possible flux variation of the incoming beam was corrected with a normalization detector. The detector was inserted just upstream of the sample. The instrument was operated under vacuum to avoid the scattering from air and to minimize air absorption, which is significant for light-element fluorescence lines.

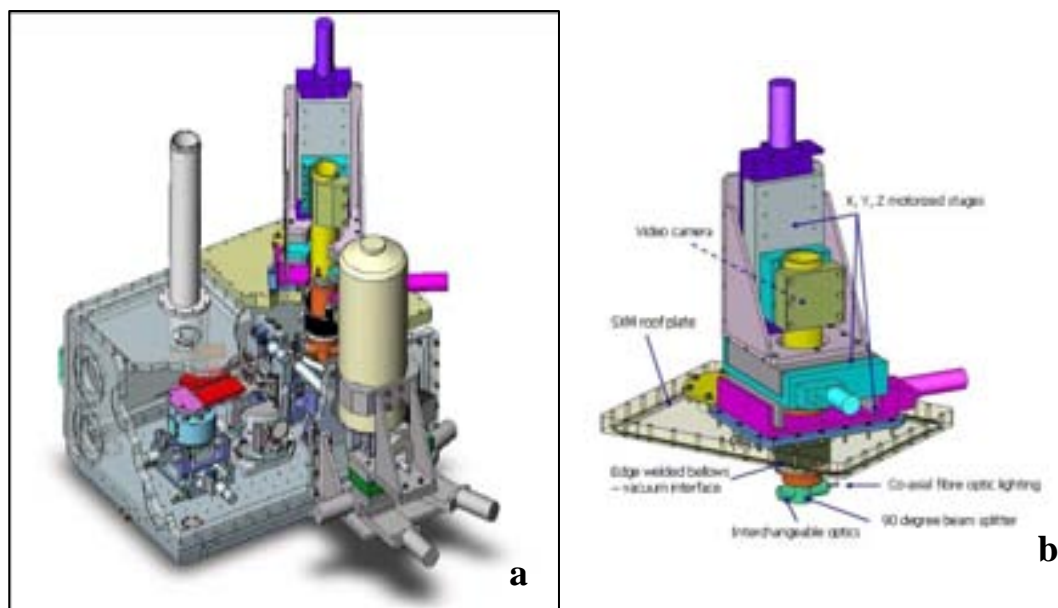


Fig. 3 (a) ID21 microprobe setup at the ESRF (b) the scanning x-ray microscope of the ID21

### III. I.7. Data treatments

Different two-dimensional maps (2D) were acquired in the untreated and the cross-sectional samples of Sample 3. X-ray fluorescence spectra were treated with PyMCA code [13]. This method was used to identify the elemental composition and distribution of the major elements and trace elements of the sample with good accuracy. X-ray imaging implements a Levenberg-Marquardt algorithm to fit the spectra with constraints on the fitting parameters (detector characteristics, detection geometry, matrix composition, excitation energy, etc.). The complete emission line series was fitted using theoretical intensity ratios and line emission energies. A more detailed description of this code was given by Solé, V.A; *et al* (2007) [13]. The fitting configuration obtained was applied to each pixel of the 2D maps to calculate the different elemental maps through a batch treatment.

### III.1.8. Results and discussion

#### III.1.8.1. Characterisation and analysis of untreated samples using laboratory techniques

The morphology of the surface is shown in Fig. 2a. The chemical analyses show Pb and Sn (expected) as well as the presence of small amount of Cl, Ca and Si, since these elements were not components of the initial matrix of Pb and Sn, they should come from

surface contamination (Fig. 2b). Crystalline corrosion products were analysed in the four samples. The alteration layer of the organ pipe is very thin. This study was completed using coupled  $\theta$ - $2\theta$  diffraction. Therefore, the peaks of the bulk components (tin-lead) are very intense compared to that of the alteration products. The use of a fixed low-incidence angle ( $\gamma$ ) increases path length through the sample and decrease X-ray penetration. This method provides better sample peak detection. This allows for analysis of outer most layers and observation of the products of alteration. In organs pipe samples, the application of a low-incidence angle while recording x-rays revealed interesting information without scraping the thin corrosion layer. The pattern at  $\gamma = 1^\circ$  provides information about the most external layer. The crystalline phases are  $\alpha$ -Pb,  $\beta$ -Sn as well as a new unexpected phase laurionite  $\text{PbCl}(\text{OH})$  (Fig.2c).

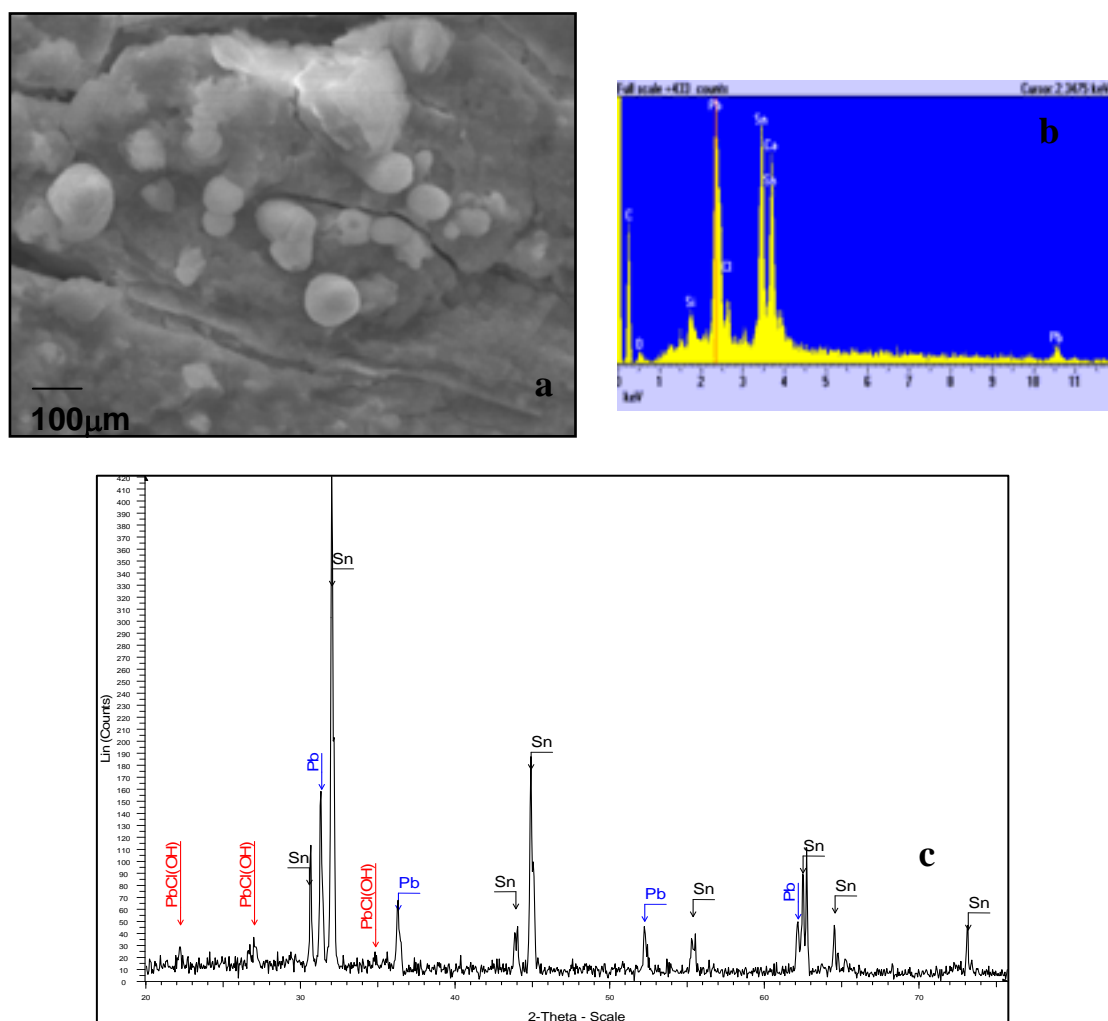


Fig. 2 (a) surface morphology of the untreated Sample 3 (b) detail of Sample 3 EDX analysis of this surface (c) XRD pattern of the surface layer of Sample 3 under incidence angle  $\gamma = 1^\circ$

In agreement with these results the EDX analyses show a significance amount of Cl at the surface, from this results it can deduced that the main surface product of lead corrosion is laurionite. The presence of laurionite suggests an incorrect cleaning procedure using chlorine cleaning compounds (bleach).

### III.1.8.2. Characterisation and analysis of metallographic cross-sections using laboratory techniques

During the metallographic optical examination of the bulk samples, important information of the metallic fragments was found. The transverse cross-sections revealed that the microstructure of the four samples consists of two segregated phases. One phase is tin-rich and the other is lead-rich (Fig.3).

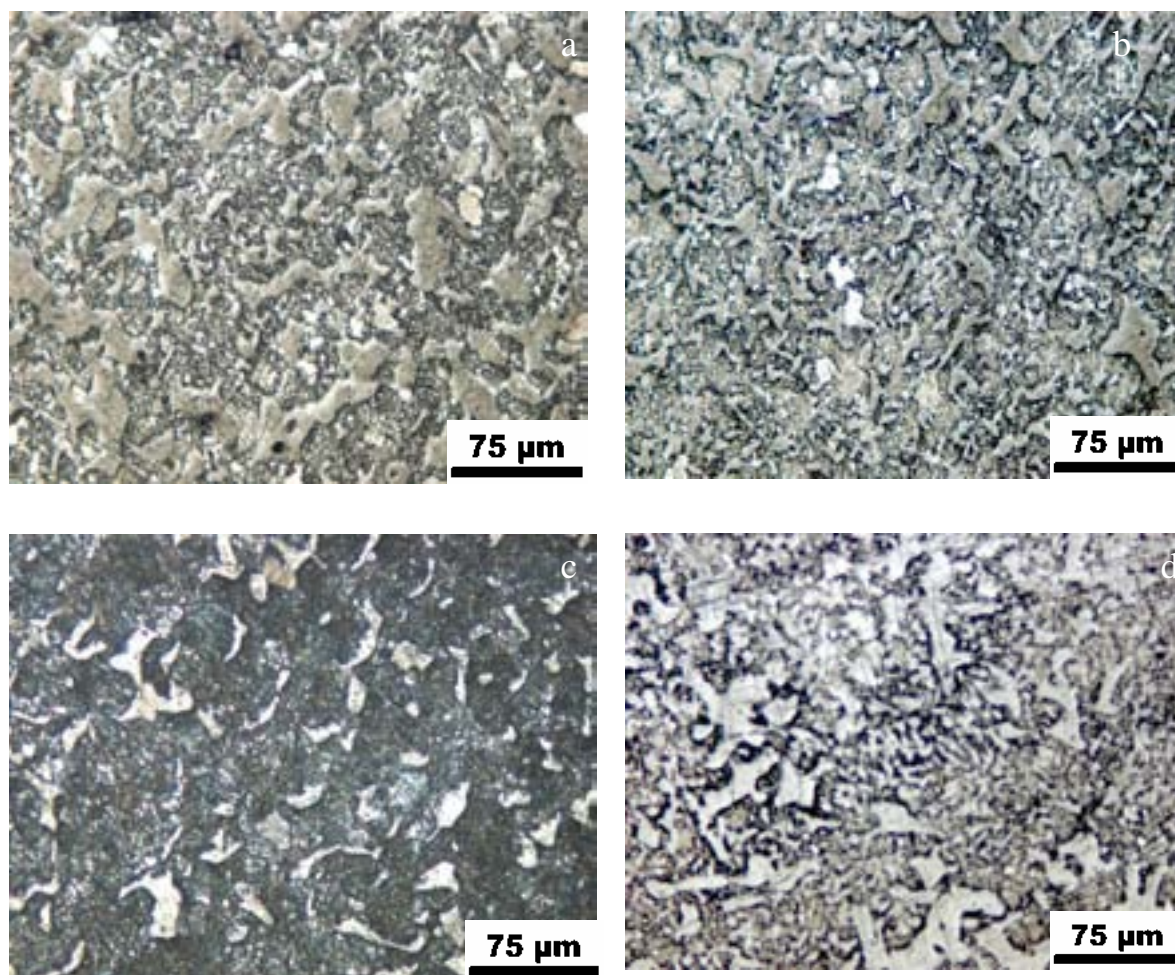


Fig. 3 Different aspects of the metallographic structure. Metallographic etching: chloride in alcohol. (a) Sample 1 (b) Sample 2 (c) Sample 3 (d) Sample 4

EDX semi-quantification analyses of the four cross sections are presented in Table 1. Table 1 shows the major elements (Sn and Pb). The pipe metal samples have a high portion of tin (60%) and a significant amount of lead.

Table 1. Major elements present in the pipe metal samples

Sample	Description of the pipes	% Lead (Pb)	% Tin (Sn)
1	Horizontal resonator f2).	40.1	59.9
2	Front flue pipe n° 18.)	33.5	66.5
3	Interior flue pipe Flue d #3	20.2	79.8
4	Interior flue pipe. Violon c2.	37.5	62.5

The crystallographic structure of the samples after etching treatment was determined by x-ray diffraction (XRD). Bragg–Brentano or grazing incidence configurations were used. Fig. 4 shows the XRD diagram for Sample 3 at  $\gamma = 5^\circ$ . It shows the absence of crystalline products at the surface arising from contamination and corrosion processes. The figure only shows the two-phase system for tin and lead of the bulk.

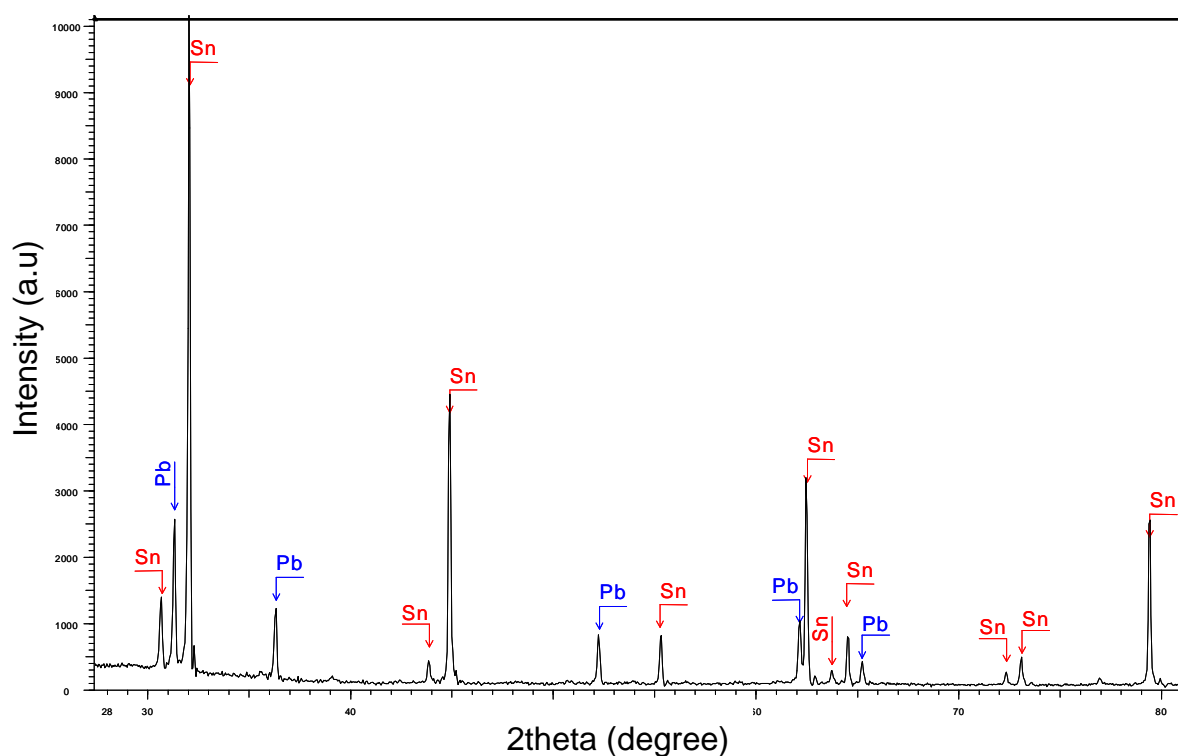


Fig. 4 XRD pattern of metallographic preparation after etching of sample BAE 3 under incidence angle  $\gamma = 5^\circ$

### III.1.8.3. Synchrotron Radiation Studies

Synchrotron radiation is an increasingly important tool for research in cultural heritage. It is particularly useful in the analysis of metal objects. The information obtained using this laboratory technique is critical to the microstructure characterisation and crystallographic structure determination of the two major elements. Using SR-  $\mu$ -XRF (high brightness, low divergence and highly linear polarization) [13], it was possible to obtain additional information and detect trace elements as well as distribution information. Normally this information is not readily available in the laboratory framework.

In order to study the trace elements, quantify their concentration in the bulk, and quantify their distribution within major phases, one of the four samples was chosen. This sample had a structural composition similar to the surface (untreated sample) and the bulk (cross-section). XRF analysis was carried out using a synchrotron radiation microbeam as the excitation source. In general, EDX microanalysis of the major elements was quantitatively determined. However, accurate determination of the minor elemental composition and trace concentration levels cannot be done by this technique because bremsstrahlung radiation restricts the detection limits. By using a synchrotron radiation source, species and multi-elemental densities can be detected at the micrometer scale.

#### III.1.8.3.1. $\mu$ XRF elemental mapping at high excitation energy

The spectra were recorded at an incident angle of  $\theta = 45^\circ \pm 5^\circ$  with respect to the sample surface. The average XRF data recorded over the  $80 \times 80 \mu\text{m}^2$  sample surface from Sample 3 are shown in Fig. 5. The spectrum consists of a well-defined background on which X-ray characteristic emission lines and spectral artefacts (escape peaks) are superimposed.

The L and K shells of the major elements Sn and Pb (as well as Ar from the air) are displayed at 28 keV excitation energy. The study of the distribution of the elements shows that the organ pipes are spotted metals. In other words, they are a mixture of lead and tin (Fig. 5). The escape peaks generated from the Si(Li) solid state detector at 1.74 keV (Si  $K_\alpha$  energy) from the parent lines are also included.

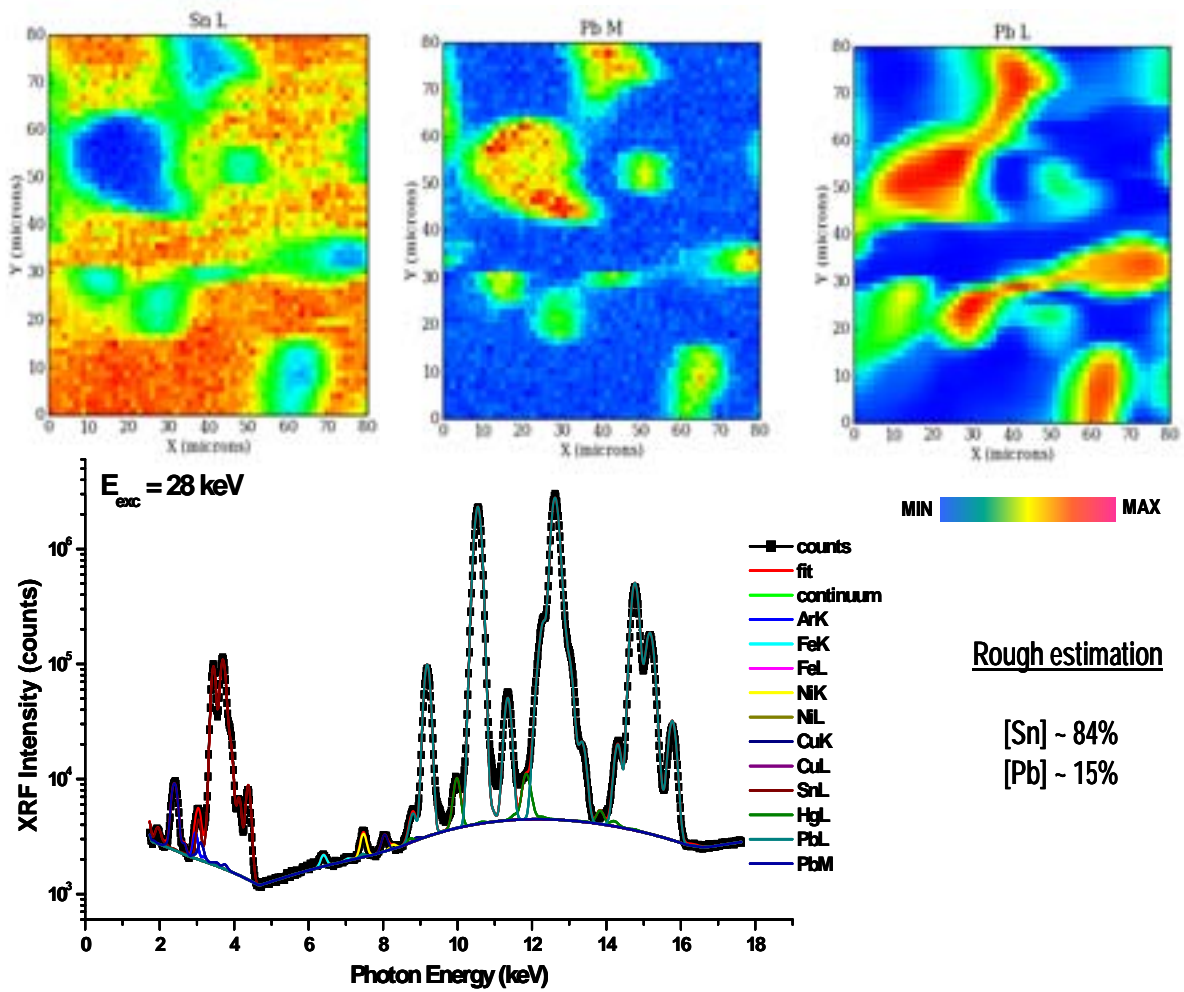


Fig 5 Distribution of the major elements of the cross-section of Sample 3 and the XRF spectra at high excitation energy.

The peak-like structures are statistically significant in the considered energy range. Therefore, the presence of trace elements such as Fe, Ni, Cu and Hg was revealed. By designating regions of interest around the dominant fluorescence lines and taking advantage of the scanning capabilities of the microprobe ID18F station, the compositional homogeneity of the samples was analysed in the length scale of the beam size. Elemental maps of Sn and Pb were obtained by measuring their respective  $k_{\alpha}$  fluorescence line intensities over an  $80 \times 80 \mu\text{m}^2$  area. Non-uniform patterns with strong intensity changes were observed, showing the inhomogeneous distribution of both elements. The results indicate the presence of segregation effects and their counter-balanced localization at the micrometer scale. The resulting spatial variations of the different elemental traces and the mean average XRF spectrum are displayed in Fig. 6.

The spatial distributions of atomic species not detectable through conventional EDX are illustrated. These species became apparent during  $\mu$ -XRF spectral analysis [8].

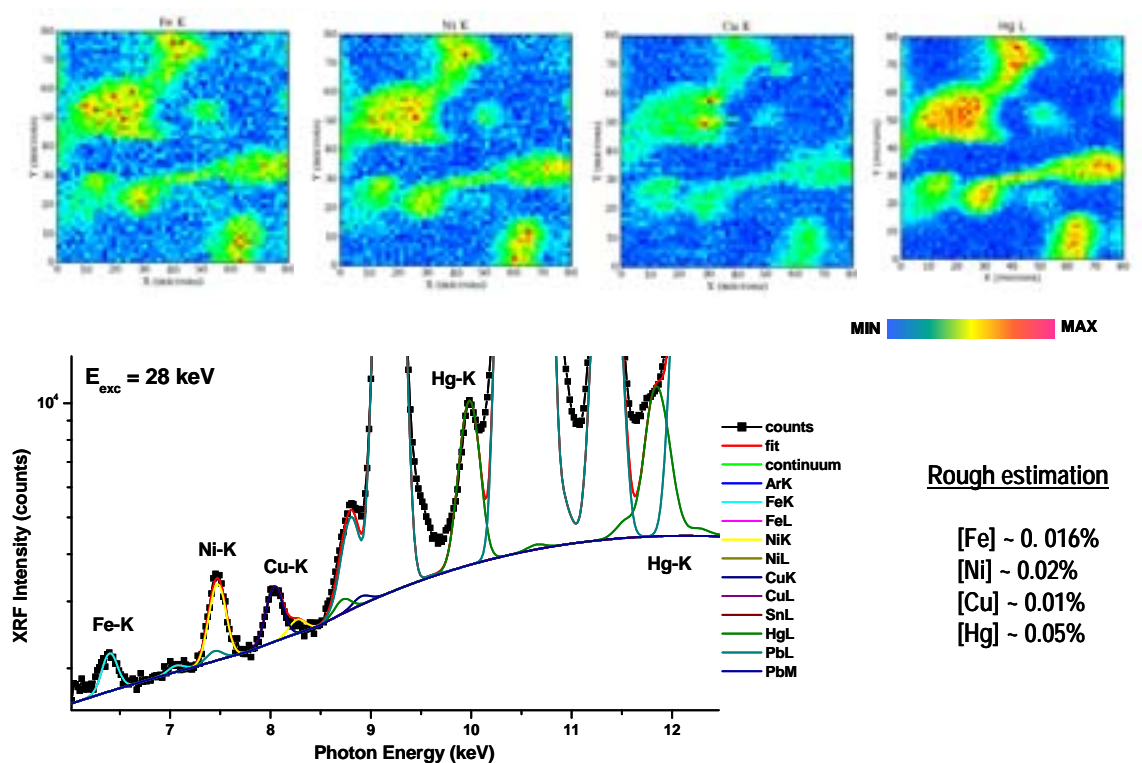


Fig 6 Distribution of the trace elements of the cross-section of Sample 3 and the XRF spectra at high excitation energy

A quantitative analysis using PyMCA code was computed based on the assumption that the incidence of the monochromatic beam on the flat sample occurred without secondary excitation. The fits yielded an elemental concentration around 85% [Sn] and 15% [Pb] for the major elements. Values ranging from 0.05% [Hg], 0.02% [Ni], 0.016% [Fe], and 0.01% [Cu] were found for these trace elements. For the remaining elements, the quantification derived very low concentrations (below to 0.01%) that were within the detection limits of the ID18F station. All elements exhibited an inhomogeneous distribution with spatial co-localization consistent with Pb incorporation.

### III.1.8.3.2. $\mu$ XRF elemental mappings at low excitation energy

To ascertain the percentages of tin and lead elements  $\mu$ XRF were recorded at low energies (7.3 and 4.03 keV). The spectrum recorder at 7.3keV has a smaller number of peaks than the one obtained at 28keV allowed to refined analysis of the major elements Sn and Pb

that showed an heterogeneous distribution of both elements; depending upon the region searched the percentage of lead range from 15to 43% (Fig.7)

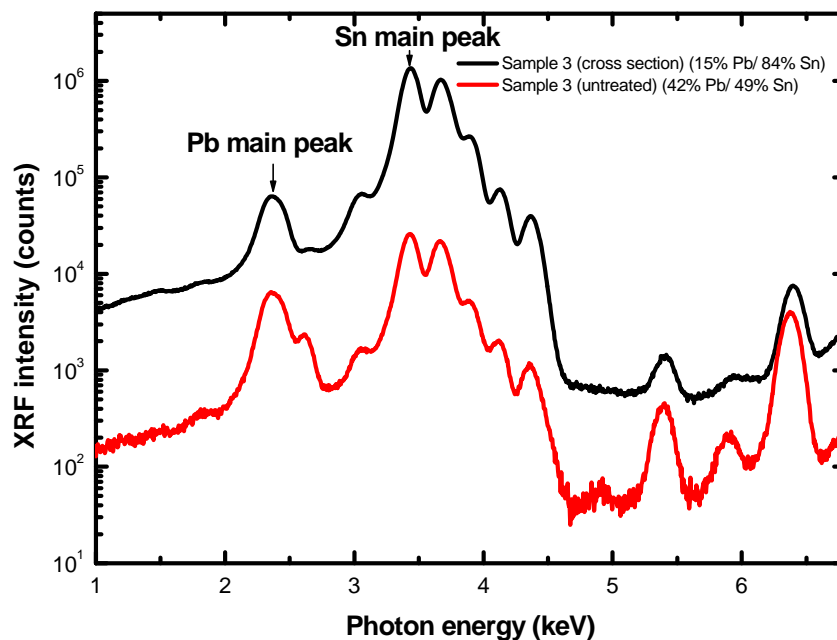


Fig. 7 Comparison between high Pb content and low Pb content region of sample 3 (untreated and metallographic cross section preparations)

These measurements showed the additional presence of elements appearing at low energies such as Cl k edge at 2.82 keV, as well as Cr appearing at medium energies (5.98 keV) but not visible in the high energy spectrum (28 keV) due to its low concentration while its detection in the spectrum including all elements.

The distribution of the two phases was resolved with the fitting program PyMCA. 2D mapping highlighted the presence of traces of Fe and Cr in the bulk of the sample. These elements were associated with lead and tin phases. A typical X-ray fluorescence spectrum, obtained at the Fe K-edge (7.3 keV), is given in Fig. 8. It illustrates the good fit obtained in the absence of low interference from the K-lines of low Z elements. The fit was obtained from the fluorescence image of each element using energy tunability.

For the untreated sample, the distribution of Cl on the surface was obtained. Precise mappings were acquired to highlight these regions with better resolution using low energy excitation energy (4.05 keV).

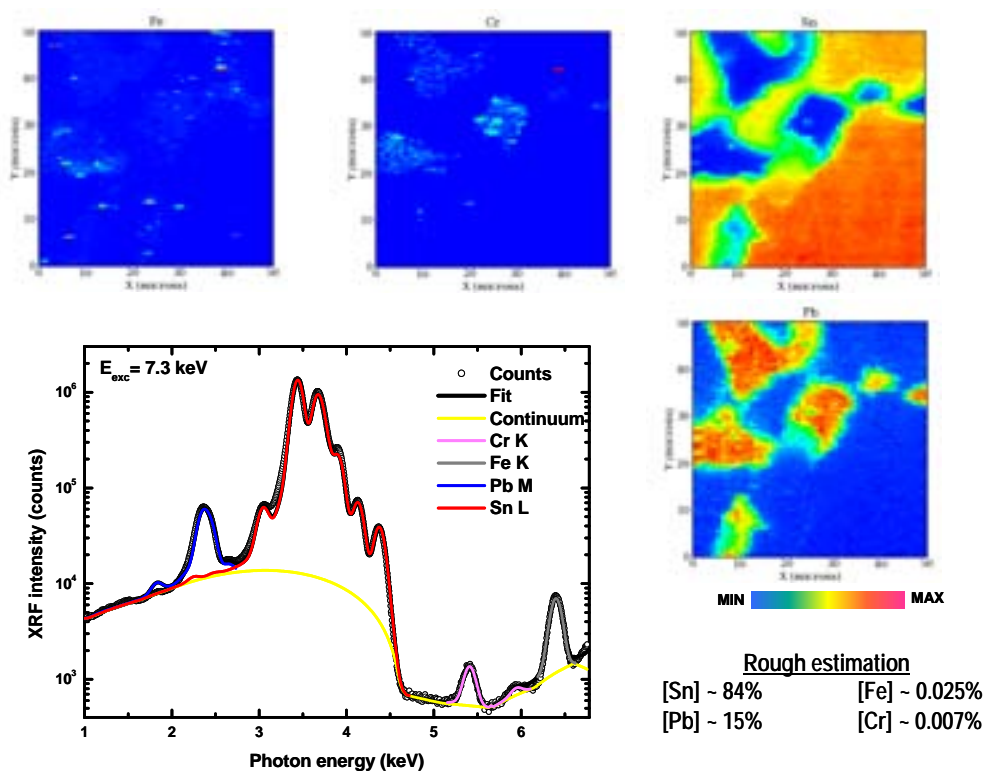


Fig. 8 Distribution of the main and trace elements of untreated Sample 3 as well as the XRF spectra at low excitation energy

Maps of Cl and Pb are given for untreated Sample 3 in Fig. 9. They show a correlated Pb and Cl distribution embedded in the tin-led matrix.

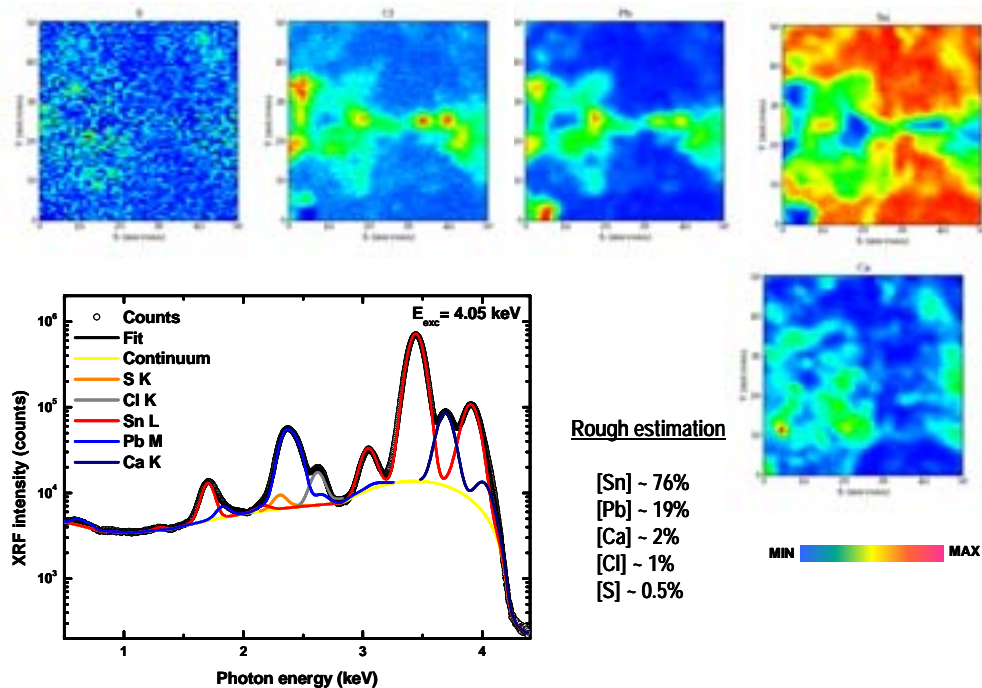


Fig. 9 Distribution and correlation of Pb, Cl and other elements of the untreated Sample 3 as well as the XRF spectra at low excitation energy

These results confirm the presence of laurionite  $\text{PbCl(OH)}$  detected by GID in the untreated samples. These findings corroborate the preferential attack of Cl on the lead phase and not the tin phase.

### III.1.9. Conclusions

This study reveals the different trace elements and their localization in the two segregated areas using  $\mu$ -XRF. Ancient builders built organs based on intuition and family tradition. Lead in the 17<sup>th</sup> century may be reproduced by adding the impurities that come naturally in old “pure” lead. These results are important for the new organ builders because today’s lead is totally pure. Adding trace elements may reproduce antique technology to make better pipe organs. Based on these results, builders should try to create pipes with trace elements that were present in the past.

### III.1.10. References

- [1] C. Chiavari, C. Martini, D. Prandstraller, A. Niklasson, L.G. Johansson, J.E. Svensson, A. Aslund, C.J. Bergsten: *Corros. Sci.* 50, 2444 (2008)
- [2] A. Eckert: *Materials and Corrosion.* 59, 254 (2008)
- [3]. L.K. Herrera, A. Duran, M.C. Jiménez de Haro, J.L. Perez-Rodriguez, Á. Justo: Coalition. CSIC Thematic Network on Cultural Heritage (Electronic Newsletter) 14, 10 (2007)
- [4] A. Justo, M.C. Jiménez, M.B. Sigüenza, A. Durán, J.L. Pérez-Rodríguez: Internal report “Estudio científico de muestras procedentes del Órgano de la Catedral de Zaragoza”. CSIC, 40 (2004)
- [5] W.R. Lewis: *The metallurgy of tin lead alloys for organ pipes.* ISO information. 767 (1974)
- [6]. G. Grenzing, E. Zindel: *Organ Journal.* 1, 7 (2007)
- [7] A.Justo. L.K Herrera, M.B. Sigüenza: Ministry of Science and Technology of Spain (MAT 2007-63234)
- [8]. A. Somogyi, M. Drakopoulos, L. Vincze, B. Vekemans, C. Camerani, K. Janssens, A. Snigirev, and F. Adams: *X-ray Spectrometry* 30, 242 (2001).
- [9] J. Susini, M.Salomé, B.Fayard, R. Ortega, B. Kaulich: *Surf. Rew. Lett.* 9, 203 (2002)
- [10]. B. Lengeler, C. Schroer, J. Tmmler, B. Benner, M. Richwin, A. Snigirev, I. Snigireva and M. Drakopoulos: *J. Synchrotron Rad.* 6, 1153 (1999).

- [11]. M. Kocsis M, and A. Somogyi: *J. Synchrotron Rad.* 10, 187 (2003).
- [12]. G. Martinez-Criado, A. Somogyi, S. Ramos, J. Campo, R. Tucoulou, M. Salome, J. Susini: *J. Synchrotron Rad.* 12, 208 (2005)
- [13] V.A. Solé, E. Papillon, M. Cotte, P.H. Walter, J. Susini: *Spectrochim. Acta, Part B*, 62, 63 (2007).
- [14] D. Creagh: *Synchrotron Radiation and its Use in Art, Archaeometry, and Cultural Heritage Studies*. In: *Physical Techniques in the Study of Art, Archaeology and Cultural Heritage* 2, 95 (2007)

### III. 2. Chemical composition of the red pipes of a Spanish baroque organ

#### Introduction

An organ contains flue and reed pipes constructed mostly of tin and lead spotted metals (described in previous section). There are no moving parts within a flue pipe organ. Reed pipes contain an additional vibrating part, the Cu-based alloy tongue that vibrates on the shallot. The tongue crucially influences and produces sounds [1,2] (Fig. 1). In most cases, both tongues and shallots are made of brass (a copper–zinc alloy).



Fig.1 (a) base of a reed pipe (b) tongue (c) shallot from the organ of Alcala de los Gazalez, Cadiz (XVIII century)

### **III.2.1. Research aim**

The composition and microstructure of historic tongues from reed pipes of a baroque organ and a modern organ were studied. The presence of lead and other trace elements in the two brass alloys were of prime interest in this part.

### **III.2.2. Experimental**

#### **III.2.2.1. Analytical technique**

The metallographic samples were ground and polished using standard techniques [2]. They were etched for 30 to 60 s by swabbing with a solution of 57 mL HNO<sub>3</sub>, 17 mL H<sub>3</sub>PO<sub>4</sub>, and 66 mL acetic acid. Different kinds of experimental analyses were carried out. Analyses included microstructural characterisation of the tongues by optical (OM) and scanning electron microscopy (SEM). Semiquantitative chemical analyses were obtained by energy dispersive spectroscopy (EDX) in the SEM. The phases contained in the alloys were determined by x-ray diffraction (XRD). Identification and distribution of the trace elements using synchrotron radiation-based  $\mu$ X-ray fluorescence (SR- $\mu$ XRF) was completed.

#### **III.2.2.2. Samples**

A historical tongue from the organ of the church of San Lorenzo, Cadiz (sample 1) and a modern brass alloy used by organ builders to make new organs (sample 2) were selected.

### **III.2.3. Results and discussion**

#### **III.2.3.1. Microstructural Observations**

The grain structure of the old brass tongue (sample 1) is illustrated in Fig 2. The metallographic cross-section revealed a typical microstructure of grains. SEM/EDX made it possible to determine that these inclusions are associated with lead and bismuth.

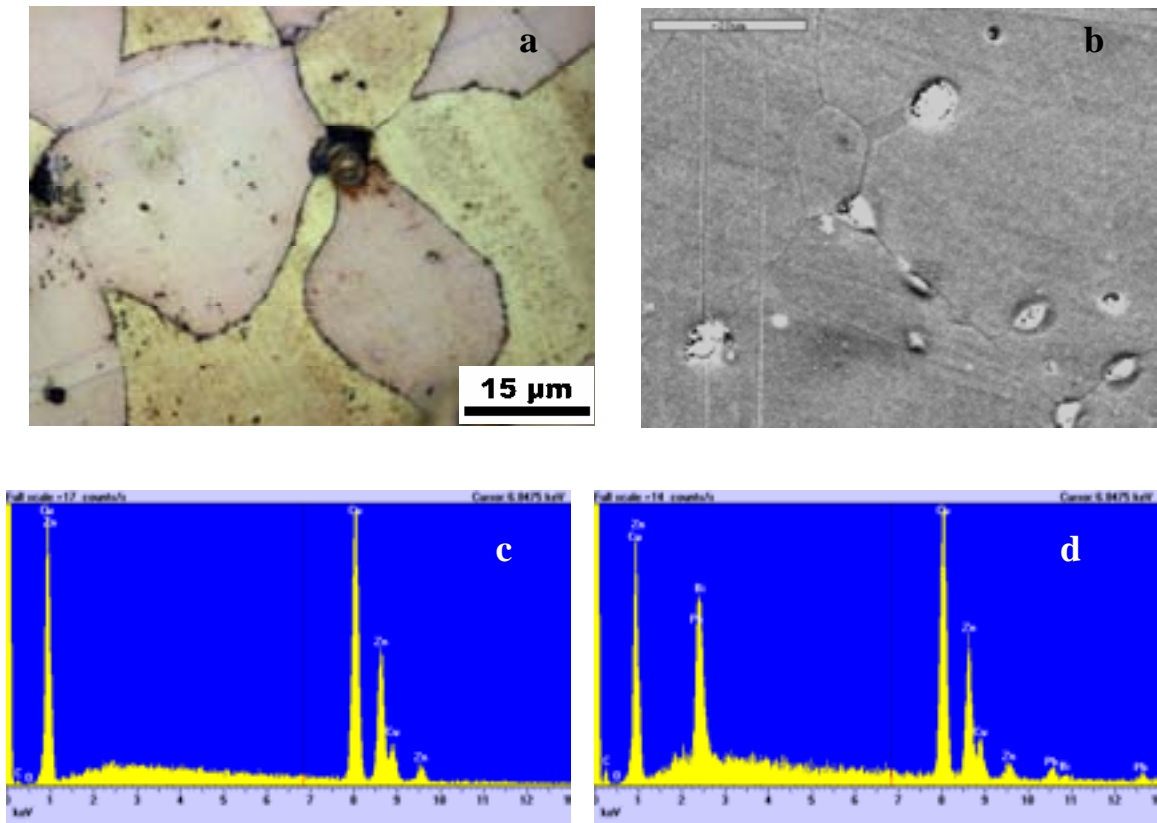


Fig. 2 (a) microstructure of Sample 1 (b) SEM image of Sample 1 (c) Cu and Zn elements of the old tongue (d) Inclusions of lead and bismuth

Fig. 3 illustrates the microstructure of the modern tongue (Sample 2). This metallographic cross-section shows that the grain structure is different than Sample 1. This sample was clearly casted. Only the inclusion of lead in the microstructure was found.

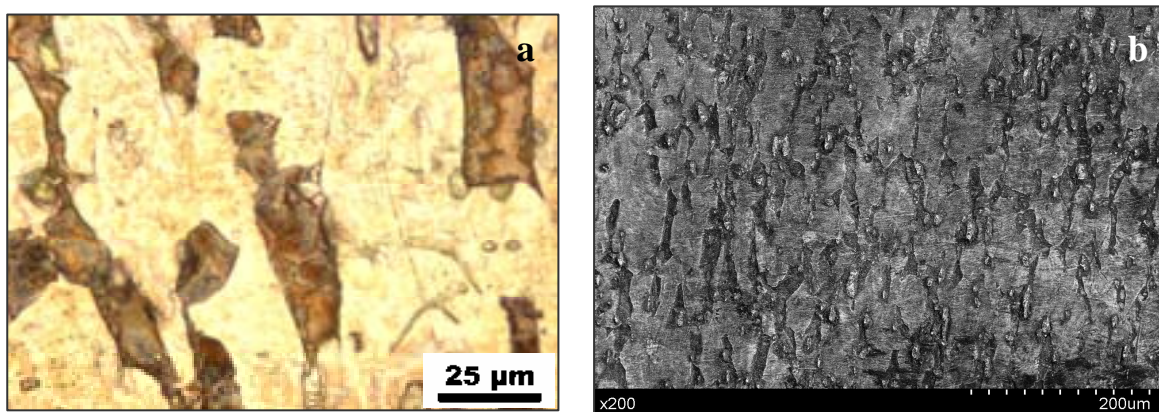


Fig. 3 (a) microstructure of Sample 2 (b) SEM image of Sample 2

X-ray diffraction analyses were carried out to characterise the microstructure of the old and modern alloys used to make tongues. The diffraction pattern in Fig. 4 was obtained

from the old tongue. The reflections can be indexed according to literature data [3]. The results correspond to Cu<sub>0.64</sub>Zn<sub>0.36</sub> (wt%).

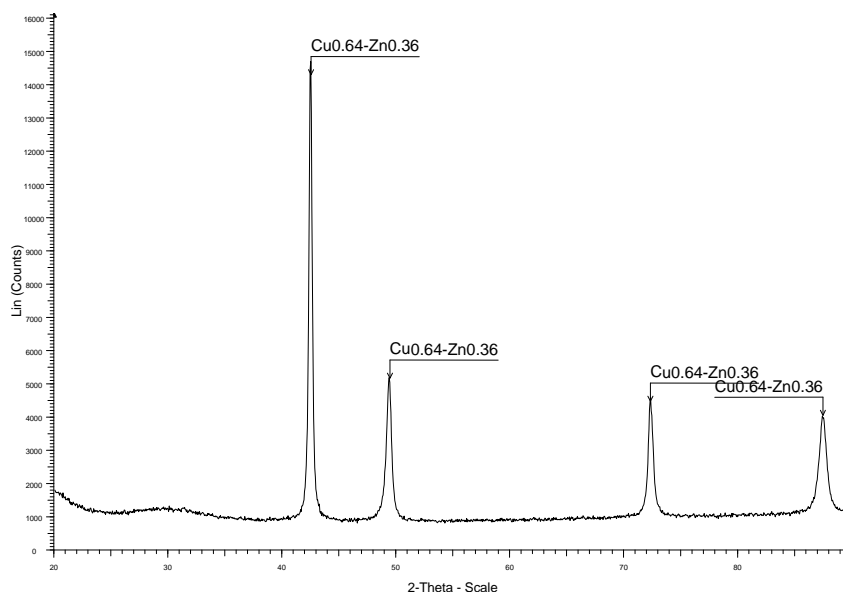


Fig. 4 XRD pattern of the old tongue.

The modern tongue had the same composition as the old tongue alloy. It also included new phases, such as metallic lead and phases of Cu- Zn (Fig.5)

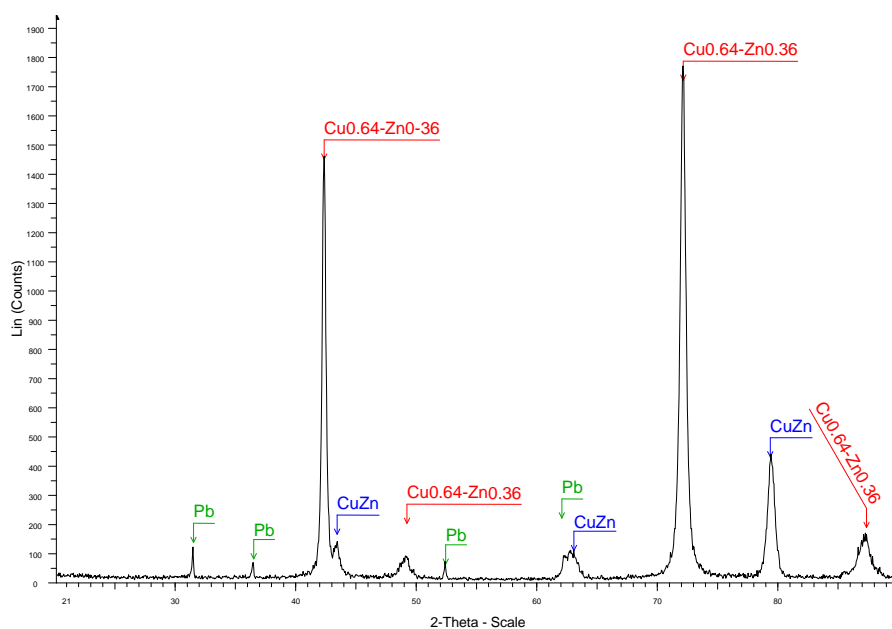


Fig. 5 XRD pattern of the new tongue.

Quantification of these elements by EDX analysis is difficult due to the technique's detection limits. To overcome this problem, a more sensitive SR- $\mu$ XRF analysis was carried out in the ID18F beam line at the ESRF. The PyMCA code indicates that the old historical

brass tongue has a fitted elemental concentration yield of around 64% [Cu] and 34% [Zn] for the main elements (Fig 6).

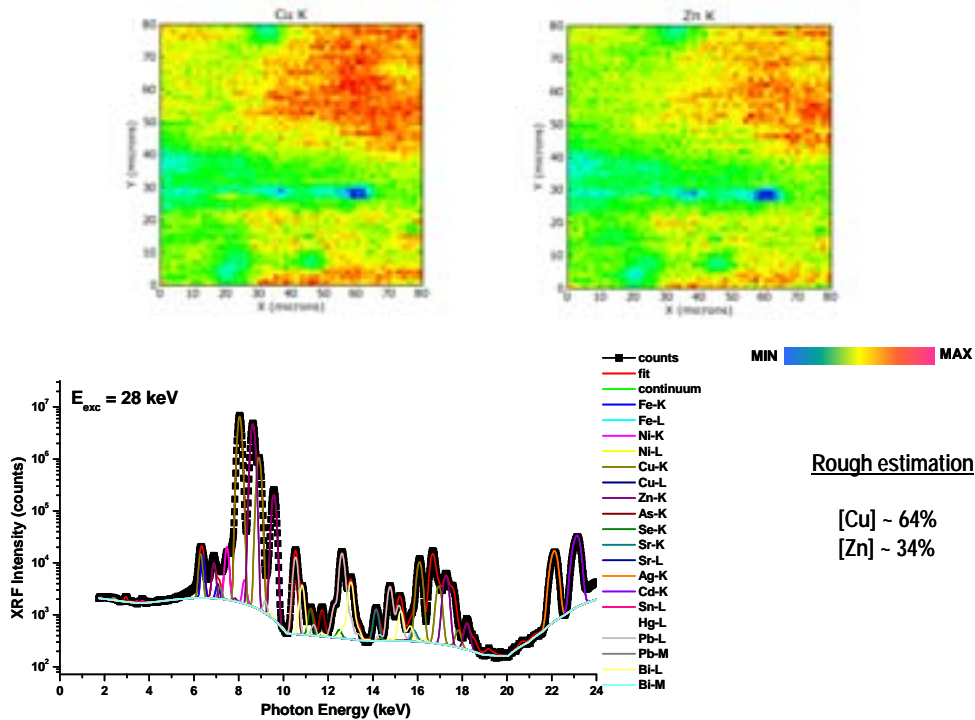


Fig. 6 Distribution of the major elements of the old tongue and the XRF spectra at high excitation energy.

Further analysis revealed the presence of other minor elements. Concentrations included 0.4% [Pb], 0.2% [Ni], 0.2% [Fe], and 0.2% [Sn] (Fig 7).

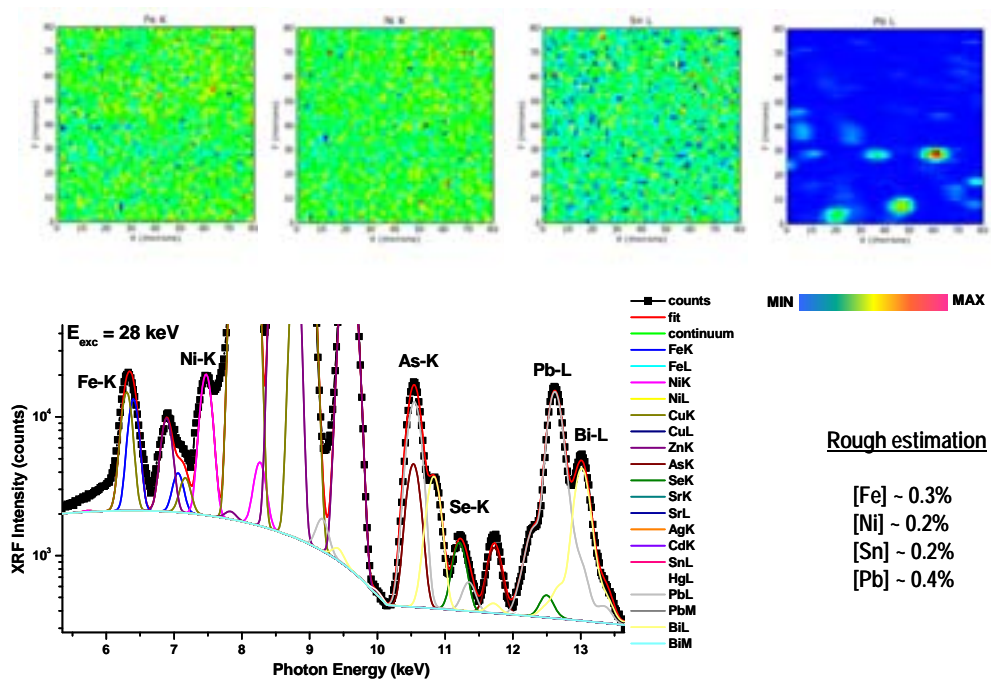


Fig 7 Distribution of the trace elements of the old tongue and the XRF spectra at high excitation energy

The elements below 0.01% concentration, such as 0.08% [As], 0.01% [Se], 0.006% [Sr], and 0.1% [Bi], were quantified (Fig 8). It is interesting that the higher zinc concentration found in this tongue is similar to the organs dated around 1750 [4]. Another important finding of this analysis was the confirmation of the role of metallic Pb in the final microstructure of the tongue. Unlike zinc, lead is not soluble in copper. This means that the lead atoms in a lead-copper melt are not equally distributed throughout the copper. Organ builders formed little droplets that were not good for brass because they were brittle. Since it doesn't anneal, lead causes internal stresses that can lead to material failure [4]. Brass alloy used for make tongues before 1750 always contained lead due to the manufacturing process [5].

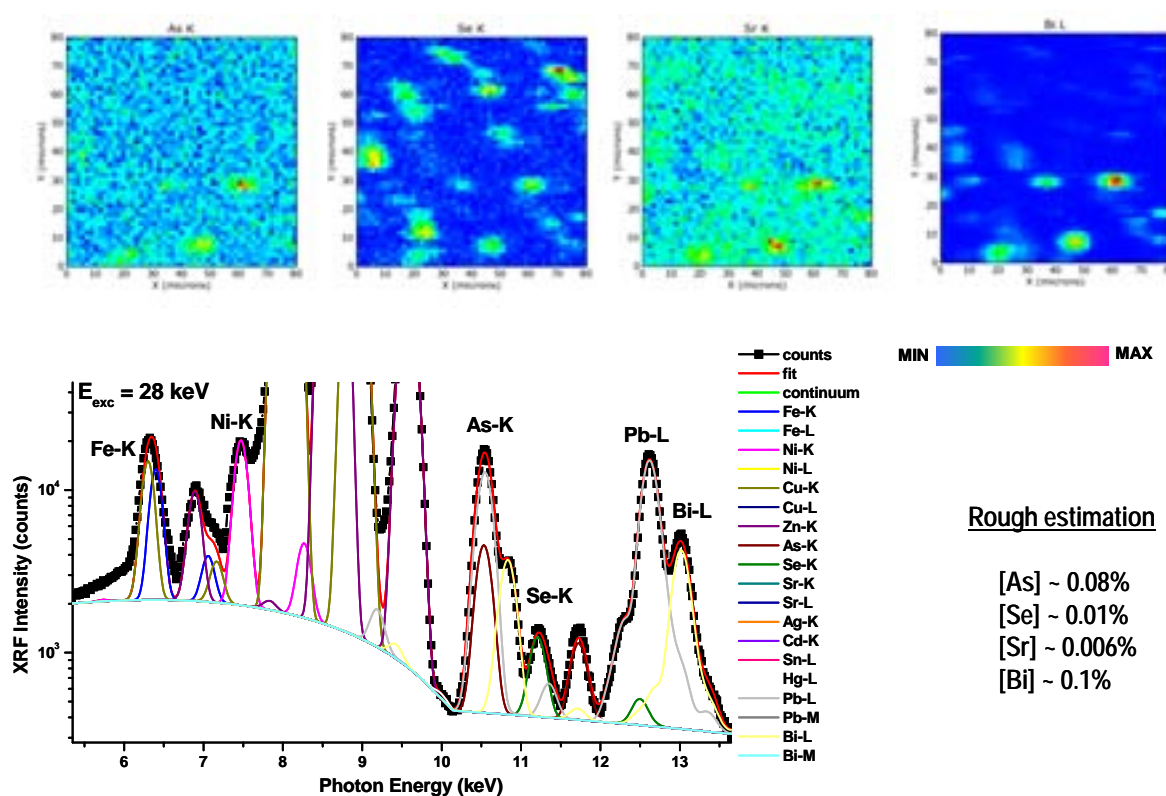


Fig 8 Distribution of the trace elements below 0.01% in the old tongue as well as the XRF spectra at high excitation energy.

These analyses show an excellent correlation between the XRD patterns of the old tongue, the quantification obtained with the PyMCA code, and the distribution of the main elements using the synchrotron-based  $\mu$ XRF imaging. The information obtained about the modern tongue using these laboratory techniques was sufficient for identification.

#### III.2.4. Reference

- [1] M. Kob Acta Acoust. 86 642–8 (2000)
- [2] Kluge W Acta Organol. 15 181–212 (1981)
- [3] S. Gialanella, L. Lutterotti Journal of Alloys and Compounds 317–318, 479 (2001)
- [4] B. Baretzky, The metal sets the tone Max Planck Research (2007)
- [5] A Manescu, F Fiori, A Giuliani, N Kardjilov, Z Kasztovszky, F Rustichelli, B Strauma Journal of Physics: condensed matter 20 (2008) 104250

## **IV. Identification of cellulose fibres belonging to Spanish cultural heritage using synchrotron x-ray diffraction and laboratory techniques**

### **Introduction**

Cellulose-based plant fibres play an important role in diverse industrial applications [1], especially in automotive parts, as well as in construction and food packaging materials [2]. Nevertheless, extensive research is still required to exploit the full potential of these cellulose fibres. In the field of cultural heritage, historical textiles require the best preservation possible based on current information and resources to ensure longevity. Cellulose fibres are used in important historical artefacts such as canvas [3, 4] documents [5], filling materials [6], etc. In this work, several cellulose fibres were investigated by synchrotron radiation X-ray diffraction (SR-XRD). The information obtained by SR-XRD was confirmed by laboratory techniques including scanning electron microscopy (SEM) and Fourier transform infrared spectroscopy (FTIR).

### **IV.1. Research aims**

The aim of these experiments was to identify the morphology and structure of the textile fibres found in an important Spanish artwork and to identify any possible degradation of these fibres.

### **IV.2. Structure of fibres**

The fibre is composed of layers of cuticle, primary and secondary walls, and a lumen (the hollow central core). The cuticle is the outer skin, which provides protection against chemical and degrading processes. The primary cell wall contains cellulose microfibrils, and these microfibrils are found in a spiral configuration. The secondary cell wall consists of concentric layers of spiralling cellulose macrofibrils. Most of the cellulose is concentrated in the secondary wall. The lumen or hollow canal forms at a certain growth stage when aqueous solution of proteins, sugar, and minerals evaporate, causing differential pressure within the fibre. [7]

The morphological structure of cellulose fibres makes them analogous to modern reinforced rigid matrix composites [8]. The morphology and interfaces of fibres affect the physical, mechanical and chemical properties of these cellulose materials. The polymers

involved in the composition of the fibres are cellulose, hemicellulose, lignin and pectin. Lignin and pectin act mainly as bonding agents [8].

#### IV.2.1. Hierarchical description of natural fibres

The microstructure of cellulose fibres is extremely complicated, in that it comprises different hierarchical organisations [8] at different length scales, and the different materials are present in variable proportions. Fig. 1 shows the structure of fibres, which can be described in different terms depending on the level of hierarchy taken into consideration [9]. The elemental units of the microstructure are microfibrils of cellulose; they are in assemblies of up to 20 elementary fibrils called micelles. Every micelle is composed of 50-100 molecules of cellulose. The distance between two micelles is about 1 nm, and there is about 100 nm between microfibrils. In the wild, the cell wall is swollen, and the space between the micelles and microfibrils is filled with water. The microfibrils are thousands of nanometres (nm) in length and 5-50 nm in diameter. These microfibrils, impregnated with hemicelluloses, form the primary and secondary cell wall layers. Agglomerates of such microfibrils constitute a macrofibril, which in turn constitute a single fibre cell. These single fibre cells, or elementary fibres, are 10-30  $\mu\text{m}$  in diameter. They are bonded together with pectins and small amounts of lignin, constructing the next level of the microstructure, the technical fibres, with diameters of about 40-100  $\mu\text{m}$ . The technical fibres adhere together within a pectin-lignin matrix that frames the fibres bundles [10].

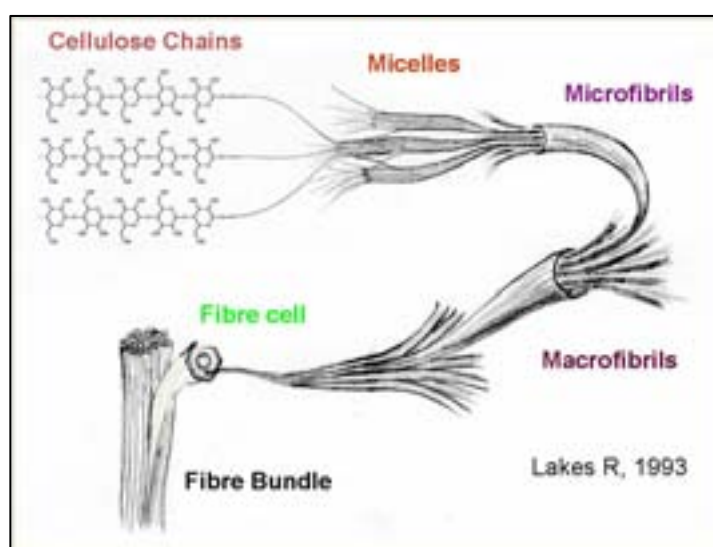


Fig. 1. Different hierarchical organisations contained in the fibres. [8]

#### **IV.2.2 Flax description**

Flax, or linen, is a bast fibre derived from certain varieties of *Linum usitatissimum* [11]. It is the first plant known to have been used for the production of fibres, dating back several thousand years B.C. Linen fibres have good mechanical properties, including relatively high strength and low extensibility; these factors, combined with the increase in fibre strength observed on wetting, make linen a good choice for the production of canvas supports [12]. All plant fibres share a similar composition and structure. The fibres are cellular in nature, being composed predominantly of cellulosic cell walls around a hollow lumen. In the case of flax fibres, bundles of these cells are cemented together by the lignaceous middle lamella [12]. The cell walls of flax, as with all plant fibres, are largely composed of polysaccharides – principally cellulose (62.1%), along with hemicelluloses (16.7%), pectin (1.8%), and smaller proportions of lignin (2.0%), proteins, pigments, waxes and minerals [13,14,15,16].

#### **IV.2.3. Cotton description**

Cotton, an Old–World fibre, may have grown in Egypt in 12000 B.C and India in 3000 B.C. [17] India is generally recognised as the centre of cotton production from 1500 B.C. until the early 16<sup>th</sup> century. Cotton, whether wild or domesticated, belongs to the genus *Gossypium* of the family Malvaceae [18]. Among other traits that the members of this genus have in common, they present epidermal hairs, or fibres, covering the seeds. It was certainly the usefulness of these hairs that first drew the attention of ancient populations, which eventually led to the domestication and cultivation of several of the *Gossypium* species [19]. Today, cotton is the most important fibre-crop in the world and is cultivated in more than forty countries. A fundamental understanding of cotton fibre structure and properties is important because cotton is nature's purest form of cellulose, and cotton fibres are economically significant in the global market. Cotton fibres are single-celled outgrowths from individual epidermal cells on the outer integument of the ovules in the cotton fruit [20]. Four distinct but overlapping stages are involved in cotton fibre development: initiation, elongation, secondary wall thickening, and maturation [20].

#### **IV.2.4. Cellulose degradation**

Cellulosic materials are susceptible to a range of degradation processes including those associated with chemical attack, photolysis, microbial and fungal metabolism, and

thermal degradation. As cellulose comprises the major structural component of the fibres, its degradation may dictate the altered performance with ageing. In general, the deterioration of the material is due to oxidative processes or hydrolysis, leading to the scission of the cellulose polymer.

Moisture plays an important role in the stability of the fibres; cellulose is most stable within a relative humidity (RH) range of 45–46% [15, 14, 11]. Water is readily absorbed through the pre-existing network of pores, where it acts as a plasticiser, particularly in the amorphous regions, and may disrupt hydrogen bonds. High humidity and excess water may cause swelling, leading to a deterioration in mechanical properties as well as rendering the fibres more prone to biological and chemical attack due to the opening of the polymer structure. Desiccation and shrinkage may occur at low humidity, resulting in the formation of additional hydrogen bonds and loss of flexibility; in more extreme conditions, condensation reactions between adjacent hydroxyl groups can occur, leading to cross-linking and further rigidity. Dissolved salt affects the way in which the fibres absorb water due to the presence of the hydrated ions, and upon subsequent drying; the crystallisation of salt within the material can lead to microstructural disruption.

Free radical thermal oxidation reactions may result in cross-linking and chain scission, as well as discolouration [22, 21, 15, 14, 12, 11]. These reactions occur slowly at normal temperatures but are accelerated by the presence of pre-existing free radicals, such as those arising from photoreactions. Lignin and, to a lesser extent, hemicelluloses are both more susceptible to thermal damage than cellulose is. Cellulose is susceptible to attack by acids (e.g., those present as atmospheric pollutants or the products of oxidative degradation via the mechanism of acid hydrolysis). This occurs rapidly and randomly throughout the chain, particularly in the amorphous regions, leading to the scission of the glycosidic ether bond and the formation of hydrocellulose fragments. The resulting material is highly crystalline, rigid and mechanically weak [23, 15, 14, 12, 11]. Flax fibres are susceptible to damage by light, especially radiation in the ultraviolet (UV) region [12]. With UV exposure, cellulose undergoes various photodegradative reactions, including direct photolysis, photochemical and radical oxidation and photosensitised degradation [24, 22, 21, 15, 14, 12, 11]. These processes are accelerated by the presence of moisture and catalysts such as trace metals. Extensive photodegradation will lead to depolymerisation and the formation of a variety of small, water-soluble acidic species, which tend to be yellow or brown in colour, thus leading to discolouration. As a

consequence of their solubility, they can readily be washed out of degraded fabrics, but this also risks further weakening the fabric itself. Finally, cellulose is also susceptible to damage by a range of microorganisms, which break the polymer down to yield metabolites [15, 14, 12, 11]; by-products of these reactions, such as hydrogen peroxide and organic acids, may cause additional damage to the polymer. As with other forms of attack, microbial attack will preferentially occur when there is improved access to the polymer chain, specifically in the amorphous regions and in areas of pre-existing damage, such as that caused by photodegradation or swelling. Hemicelluloses and pectins are also the targets of biological degradation, but lignin appears to exhibit some resistance.

#### IV.2.5. Crystalline index

It has long been recognised through X-ray diffraction that cellulose is part crystalline and part amorphous [25]. In the crystalline regions, the cellulose chains are held by mutual H-bonding, whereas the cellulose chains do not form hydrogen bonds in the amorphous region. The fundamental unit of this lattice, referred to as the unit cell, was derived by Meyer and Misch [26] and is reproduced in Fig. 2. The cell is monoclinic with three principal planes of reflection shown as (002), (101), and  $(10\bar{1})$ .

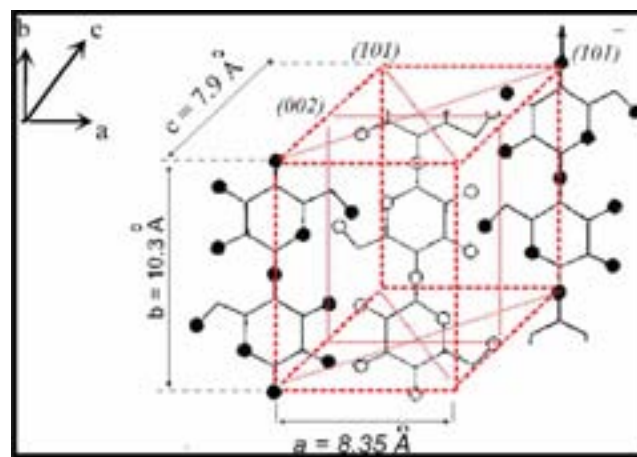


Fig. 2. The cell is monoclinic with three principal planes of reflection, shown as (002), (101), and  $(10\bar{1})$  [26]

Segal and Conrad and Segal [27, 28] developed an empirical method for estimating the degree of crystallinity of native cellulose (Cellulose I). The amount of crystalline Cellulose I in the total cellulose can be expressed by the X-ray “crystalline index” (CI), defined by

$$CI=100[(I_{002}-I_{am})/ I_{002}]$$

where  $I_{002}$  is the intensity of the principal Cellulose I peak at  $2\theta = 12.11^\circ$  and  $I_{am}$  is the intensity attributed to amorphous cellulose given at  $2\theta = 8.95^\circ$ . More detailed methods utilising multipeak resolution and profile fitting of X-ray diffraction data have been followed by Hiseh et al and Hu and Hiseh [29, 30], who applied these to determine the crystallinity of developing cottons. Non-diffraction methods of determining the crystallinity of cellulose include both FTIR and solid-state nuclear magnetic resonance (NMR) spectroscopies, which have been used to measure the crystalline of cellulose [31].

### IV.3. Experimental

#### IV.3.1. Samples Selection

The textile samples selected for this work were collected from different Spanish artworks. Fig. 3 shows the origins of the samples. One sample extract comes from a very important canvas collection (*La vida de S. Ignacio of Loyola, 1668*) by Pedro Atanasio Bocanegra, and one sample was collected from a canvas painted by Pablo Legot (*La Transfiguración, 1631*). Two samples from an anonymous painter were collected from the altarpiece of *Huerca Overa, Almeria*.

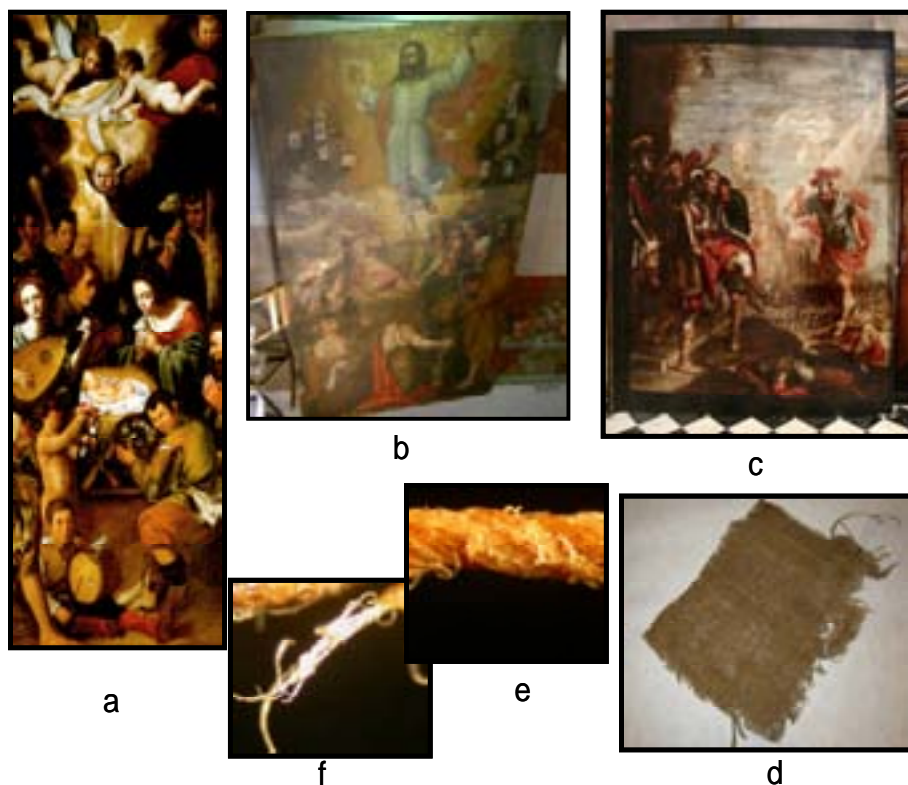


Fig. 3. Pablo Legot paintings: (a) *La adoración De Los Pastores*, 1631-1636; (b) *Transfiguración*, 1631. Bocanegra paintings: (c) *San Ignacio herido en las puertas de Pamplona*, 1668; (d) textile fragment of Bocanegra canvas; (e) optical microscope image of fibre bundles; (f) macrofibrils wound into bundles.

One sample taken in the *Sala de los Reyes in the Alhambra* found as a filling material in the wooden ceiling (Fig. 4).

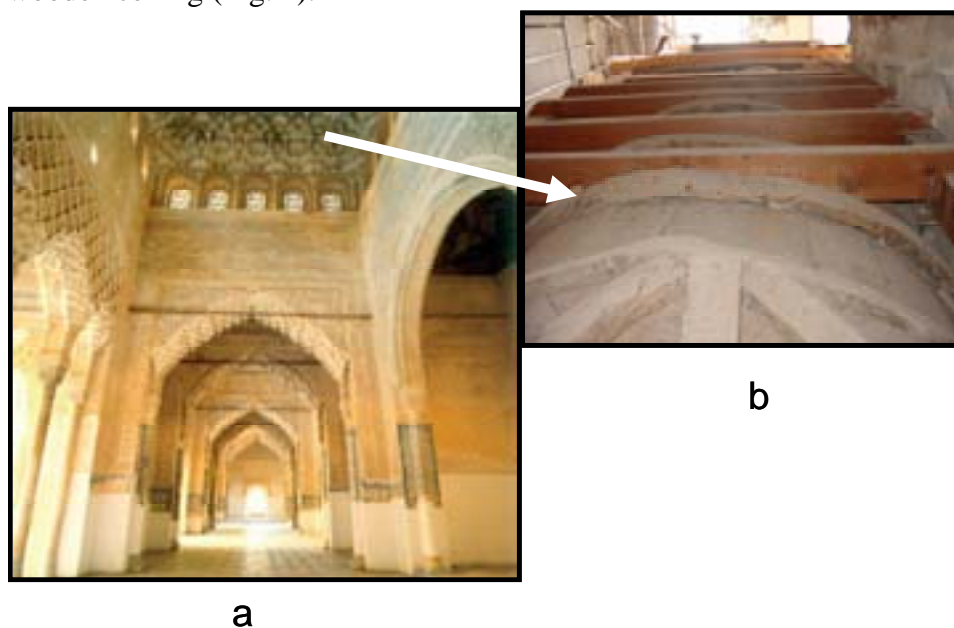


Fig. 4. (a) *Sala de los Reyes, Alhambra* where sample 5 was extracted. (b) The fibre was a filling material on the surface at the top of the ceiling.

The textiles are listed in Table I. All these samples were characterised and compared to modern fibres to provide a deeper knowledge of these textile samples and their degradation stage.

Table I. Description of the samples studied.

Sample	Artwork	Location	Type	Century
1	Canvas	Granada	Flax	XVII
2	Canvas	Seville	Flax	XVII
3	Altarpiece canvas	Almeria	Cotton	XVII
4	Altarpiece canvas	Almeria	Cotton	XVII
5	Filling material	Granada	Plant material	XIV

#### IV.3.2. Sample preparation

Two types of sample preparation were performed. Fibre bundle: fibres of a few millimetres in length were carefully extracted using tweezers from the different samples under an optical microscope.

Cross-section: fragments of textile samples were embedded in an epoxy resin, and the fibre was cut. The surface was carefully polished on a rotating disc covered with

abrasive SiC paper, which covered a grain size from 800 to 1200 mesh, and then finished with a cloth.

### IV.3.3. Analytical techniques

A combination of optical microscopy (OM) and scanning electron microscopy (SEM) was used to reveal the diagnostic features of the fibres necessary for their identification. SEM micrographs of the fibres were recorded with different magnifications by means of a HITACHI S-4800. The surface morphology of the textile samples was observed on a fibre bundle and in the cross-section coated with gold.

The FTIR spectra of the fibre samples were used to distinguish the broad categories of celluloses fibres based on the relative lignin content with respect to the other cellulose components. The samples were investigated with a Nicolet 510 spectrometer in transmission mode with a detector at a  $4\text{cm}^{-1}$  resolution with 64 scans. The samples were cut into pieces less than 1mm long, mixed with approximately 100mg powdered KBr and ground KBr disc die and pressed at approximately 8 MPa pressure for 2 min. The infrared spectra of the samples were then recorded in the wavenumber range from 400 to  $4000\text{ cm}^{-1}$ .

The use of synchrotron facilities improves the experimental conditions considerably, allowing the direct measurement of the fibre samples due to the availability of very intense XRD microbeams. SR X-ray diffraction (SR-XRD) patterns were carried out at the beamline (BM25A) of the European synchrotron radiation facility (ESRF) (Fig. 5a). Patterns were collected with a fixed wavelength of  $0.8263\pm 0.0003\text{Å}$  (15 KeV) at room temperature. The synchrotron radiation was focused to a spot size of 1 mm. The fibre was placed into a glass capillary of  $\phi=0.2\text{mm}$ , which was rotated during the exposure (Fig. 5b). Two pairs of slits were used, one just after the capillary and one just before the scintillator detector, in order to achieve the required resolution. Data collection was done between  $4\text{-}14^\circ$  ( $2\theta$ ) in the scan mode with  $0.02^\circ$  steps and a 10 s acquisition time per point.

The third harmonic was rejected by slightly detuning the second Si (111) crystal of the monochromator.

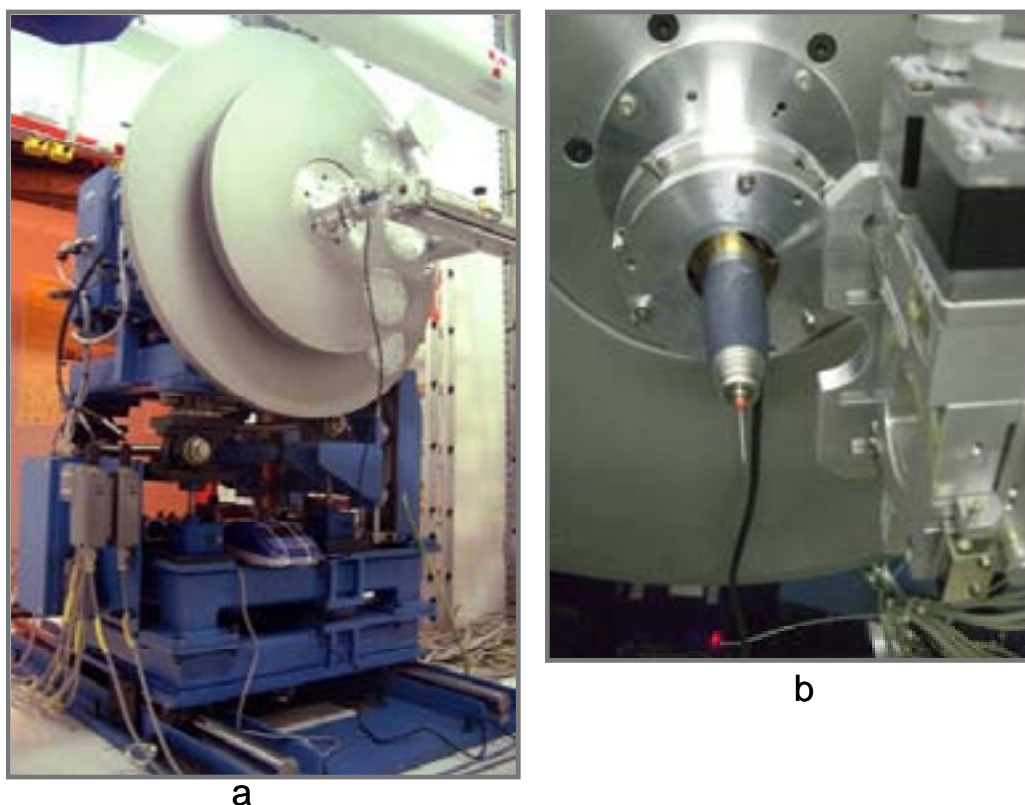


Fig. 5. (a) SR-powder diffraction set up installed at the beamline (BM25A) of the European synchrotron radiation facility (ESRF). (b) The fibre was placed into a glass capillary.

#### IV.4. Results and discussion

##### IV.4.1. Optical and Scanning electron microscopes investigations

A textile is defined initially through its characteristic fibre type—the morphology or intrinsic features and dimensions, and the chemical properties. Once this base knowledge has been established, the next and fundamental step in the identification of textile materials is to determine the state of the textile. Morphology analyses carried out with microscopy techniques allowed us to detect microscopic features peculiar to the natural fibre components of each sample and thus identify them [4,32]. The SEM micrographs in Fig. 6 show longitudinal (Fig. 6a) and cross-sectional (Fig. 6b) views of flax fibres of sample 1. As shown in Fig. 6b, the fibre cross-section is irregular, showing a variety of fibre cells in the bundles of flax fibre cells with the lumen in the middle. The fibre cells of samples 1 have diameters of 13.6-19.6  $\mu\text{m}$ , which are very typical values for flax (Fig. 6c) [33].

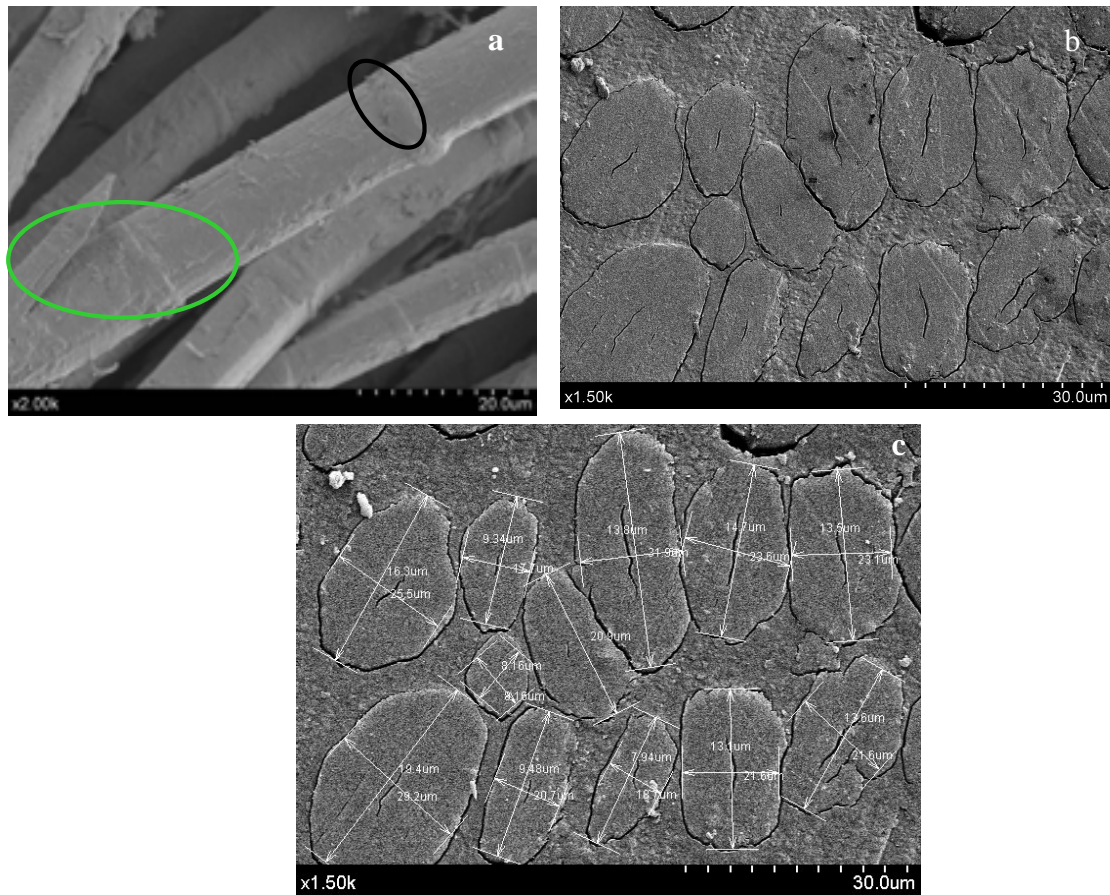


Fig. 6. SEM micrograph of the fibres composing sample 1: (a) identified as flax, showing full kink bands. (b) Cross-section of the sample 1 showing bundles of flax fibre cells with a lumen in the middle. (c) The bundles of flax are irregular, with diameters of 13.6-19.6  $\mu\text{m}$ .

SEM observation shows kink bands along the single fibre of sample 2 (Fig. 7a). The kinks are the spots where the fibres are starting to break and fibrillate, leading to deterioration of the flax texture. It is, however, interesting to look at the deformation process that takes place in the kink bands of the flax fibre of sample 2 (Fig.7b).

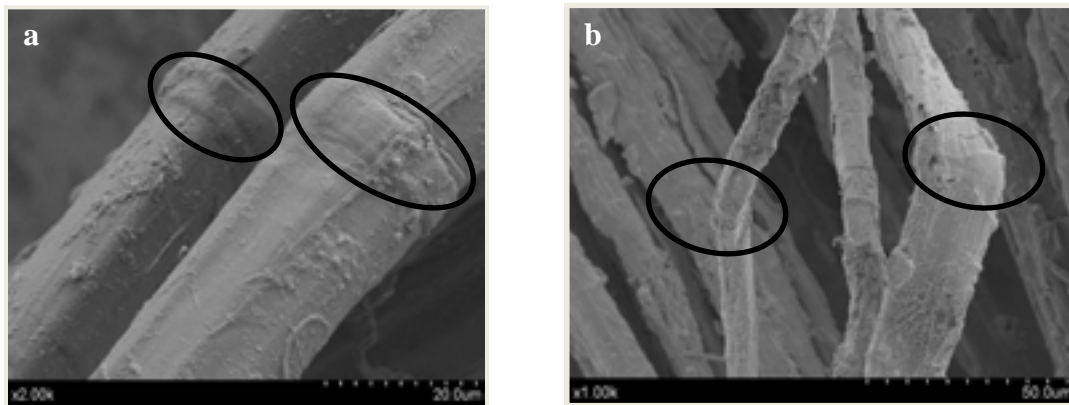


Fig. 7. SEM micrographs of the fibres composing sample 2: (a) Fully developed kink band in an elementary flax fibre. (b) Fracture initiates on the fibre. The primary and secondary cell walls have separated.

In the case of sample 3, SEM observation shows that fibres are isolated and look like a ribbon with raised edges, rolled in a helicoidal manner around the axis (Fig. 8a). These morphological characteristics are peculiar to cotton fibres [4, 32, 34, 35]. The morphological analysis made by SEM observation also shows that sample 4 (Fig. 8b) was composed of cotton fibres, but it is possible to observe that these fibres were breaking down in their structural macrofibrils into the fibre bundle.

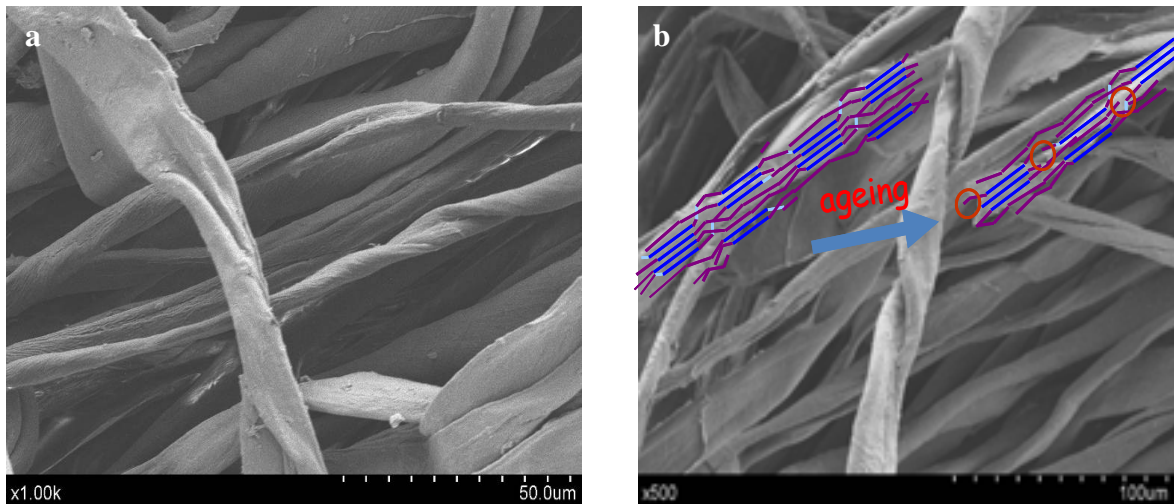


Fig. 8. SEM micrograph of the fibres composing sample 3: (a) fibres identified as cotton, and (b) fibres showing the signatures of the ageing process of sample 4.

The SEM image of sample 5 (Fig. 9a) shows that these fibres are organised in a very compact (fibres are grouped in several bundles) and tight manner; moreover, they are cylindrical in shape. The fibre diameters were smaller than those of the other samples. In the cross-section (Fig. 9b), it was possible to observe only the presence of bundle fibres. In this sample, the fibre cells were not observed as clearly as those in the other samples studied in this work due to the fact that most of the cellulose content was not concentrated in the secondary wall cell, as occurs in flax and cotton fibres. This fibre may be associated with a primary wall cell related to unprocessed plant material, because macro- and microfibrils were not detected. Only the undefined shape of possible internal interfaces of the fibre cells was observed (Fig. 9c).

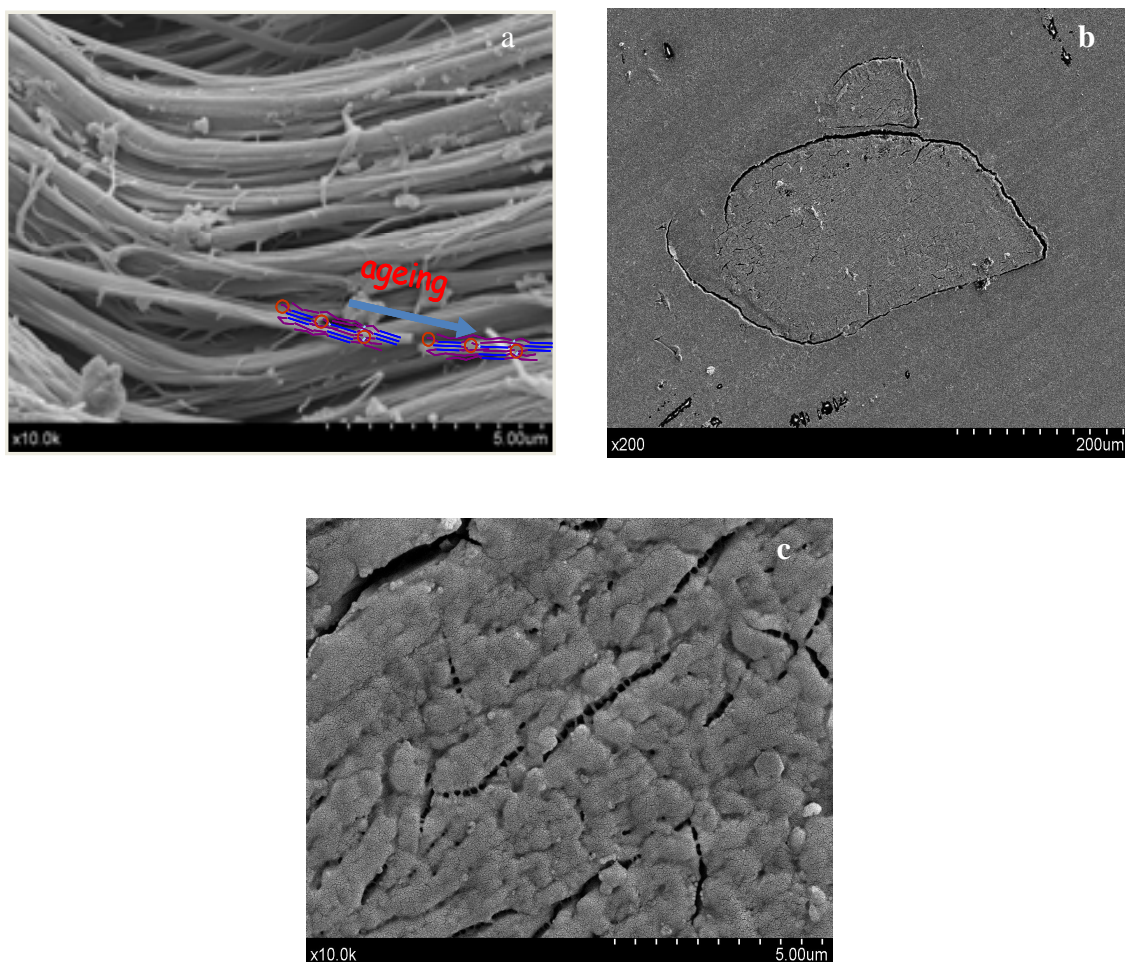


Fig. 9 SEM micrograph of fibre composing sample 5: (a) fibrous part of the flock from the sample, showing signatures of the ageing process; (b) cross-section showing a bundle of a single fibre; (c) undefined shape of a bundle of possible fibre cells.

#### IV.4.2. FTIR Spectroscopy

Spectroscopic methods (infrared spectroscopy) to distinguish between different classes of fibres are shown. Two ratios were calculated according to Garside and Wyeth [36] and Duran [4] for all fibres based on either the lignin-to-cellulose ratio ( $R_1$ ), or the lignin to organic matter ratio ( $R_2$ ).  $R_1 = I_{1595}/I_{1105}$  and  $R_2 = I_{1595}/I_{2900}$  bands in spectra situated at  $1595\text{ cm}^{-1}$  are assigned to groups C=C of lignin, bands at  $1105\text{ cm}^{-1}$  to glycoside bonds C-C in polysaccharides (cellulose compounds), and bands situated at  $2900\text{ cm}^{-1}$  are assigned to general organic material (groups  $-\text{CH}_2$ ,  $-\text{CH}_3$ , methyl and ethyl). Depending on the theoretical percentages of cellulose, hemicelluloses, pectin and lignin, and the ratios  $R_1$  and  $R_2$ , four different regions are defined, corresponding to the

most used cellulose fibres in artworks: flax, cotton, jute, hemp [4, 36, 37]. Fig. 10 shows the FTIR spectra of samples 1, 3 and 5.

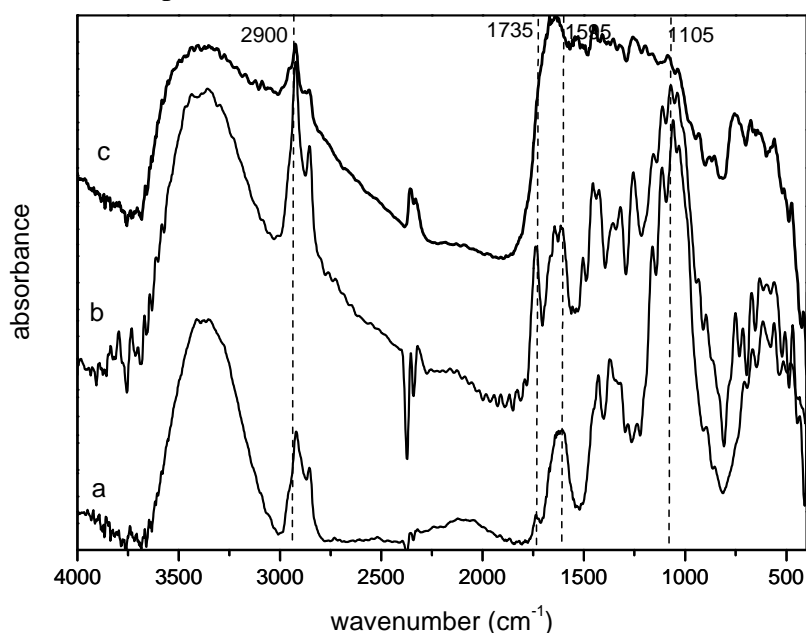


Fig.10 FTIR spectra of (a) sample 1, (b) sample 3 and (c) sample 5

We then calculated the ratios  $R_1$  and  $R_2$  for each of the samples and compared them with the theoretical values. Samples 1 and 2 show values of  $R_1$  and  $R_2$  corresponding to flax. For samples 3 and 4, the values are attributed to cotton (Table II). Sample 5 shows high intensity absorption bands in the range of 1637-1735  $\text{cm}^{-1}$ . The intensity increase and broadening of these bands can be attributed to strengthening by the carbonyl groups of oxycelluloses found due to the degradation process of this sample [37]. The ratios of sample 5 are very difficult to determine due to the low intensity of the absorption bands at 1595  $\text{cm}^{-1}$ . This fact is attributed to the low lignin concentration in this sample and the fact that this organic compound is a poorly characterised material.

Table II. The different theoretical values for cotton and flax samples

Samples	R1	R2	Assignment	Theoretical values [4,37]	
				R1	R2
1	0.48	0.57	Flax	~ 0.25-0.75	~ 0.10-0.80
2	0.57	0.66	Flax		
3	0.17	0.25	Cotton	~ 0.05-0.25	~ 0.10-0.60
4	0.17	0.24	Cotton		

#### IV.4.3. X-ray diffraction studies by synchrotron radiation

The use of a small beam for the investigations of fibres has a number of advantages [38]. The accuracy and reliability of the determination of the preferred orientation are significantly enhanced when using single fibres because, in fibre bundles, a tilt of fibres within the bundle cannot be separated from the tilt of the layers within the fibres [39]. The high brilliance of the radiation enables short exposure times, allowing in situ experiments during the loading of single fibres [40, 41, 42]. The isolation of a fibre from the bundle is possible even when the fibre has not been separated when using synchrotron radiation. The diameter of the microbeam was defined as 1mm; for this reason, X-ray diffraction data collection was performed for the microfibrils of all the samples. The possibility of performing X-ray diffraction with a beam size equal to that of the fibre diameter is advantageous for gaining better insight into the microfibril structural details across the bundle fibre. This information will allow us to characterise the different types of fibres used in Spanish cultural heritage and their crystalline index (CI) and crystallite sizes.

Fig.11 shows three peaks for native Cellulose I for the all flax samples. The 002 reflection is the most intense interference in all the diffractograms. It corresponds to the lattice planes of the glucosidic rings, which are the most densely charged structure in Cellulose I.

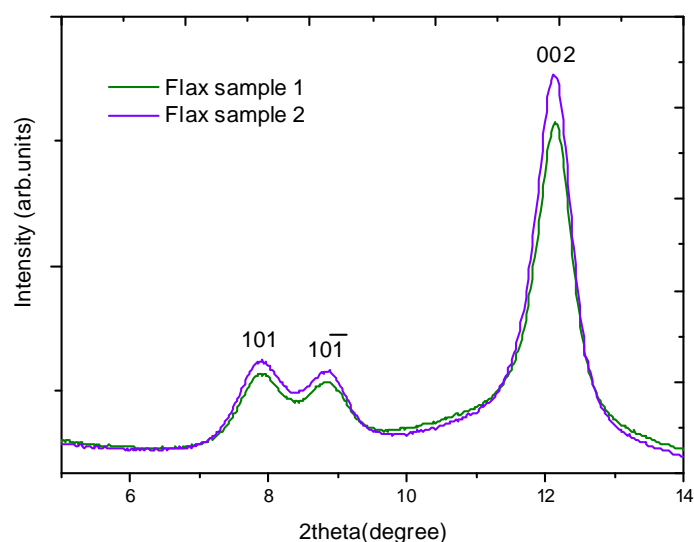


Fig. 11. SR- X-ray diffraction patterns of different flax samples

The CI value calculated using the Segal and Conrad method [27,28] for sample 1 was 72.92% and 71.44% for sample 2. However, flax cellulose has strong intermolecular

attraction between adjacent cellulose chains, which results from hydrogen bonding involving the hydroxyl groups [43]. This intermolecular association leads to a high degree of crystallinity (typically about 70% for flax [43, 44]); this value is in agreement with the values obtained for samples 1 and 2, which were used as a support for canvas. Since the crystallinity of these flax samples is suitable of cellulose as a structural material in plants and also lends it a high degree of chemical stability.

The X-ray diffractograms of both cotton fibres (samples 3 and 4) (Fig 12) revealed pronounced Bragg peaks at  $2\theta = 7.82^\circ$ ,  $8.95^\circ$  and  $12.11^\circ$ , indicating the presence of the cellulose crystalline phase in the fibres. Here, the crystalline index (CI) for sample 3 was 69.99%, and for sample 4 it was 69.34%, showing reduced crystallinity values in comparison with modern cotton fibres, which are in the range of 85.30% as reported by Parikh et al [45].

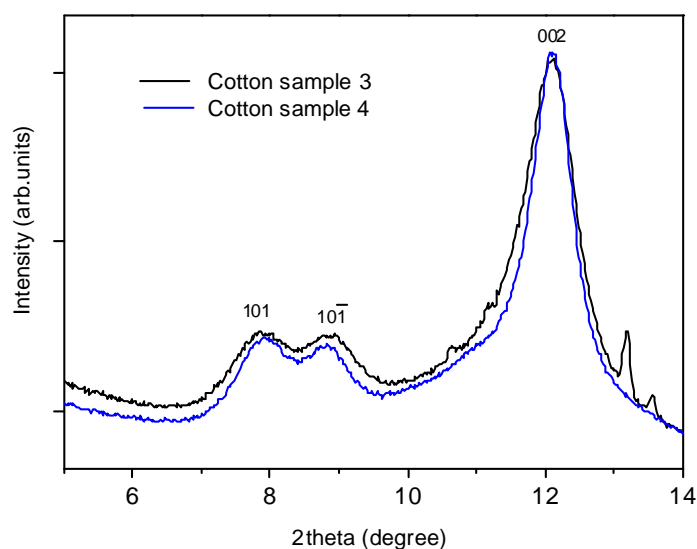


Fig. 12. SR- X-ray diffraction patterns of different cotton samples

The X-ray pattern of sample 5 (unprocessed plant material) shows only a very broad peak, probably corresponding to 002 diffraction attributed to a very low crystallinity (Fig.13). The 002 peak is also at a lower  $2\theta$  in comparison with the other samples studied. The cellulose of sample 5 is often classified as Cellulose IV according to some authors [46, 47, 48]. Cellulose I shows a higher crystallinity structure and is more abundant than Cellulose IV in natural fibres.

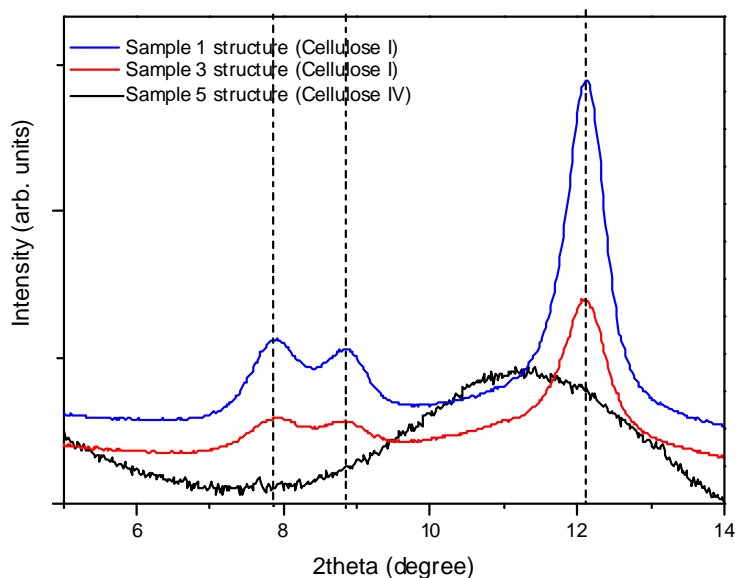


Fig. 13. SR-X-ray diffraction patterns of sample 5 as compared with the diffraction profiles of samples 1 and 3. Sample 5 showed major differences with respect to the diffraction peaks.

The value obtained for the CI of sample 5 was 18.70%, which is not in agreement with the typically values of CI reported for the Cellulose I structure. This result shows that the sample from the ceiling of the *Sala de Los Reyes* in the *Alhambra* has a different structure than those of the samples used as supports of Baroque canvases. These results have been confirmed by SEM studies that show the small bundles of this fibre that may be associated to the amorphitisation of the fibre cell of cellulose. The other important remark is that sample 5 presents greater degradation due to the exposure of this sample to microbiological attack, as reported in a previous study [49]. Cellulose is also susceptible to damage by a range of microorganisms, which break the polymer down to yield metabolites [50]; by-products of these reactions, such as hydrogen peroxide and organic acids, may cause additional damage to the polymer [50, 51].

The calculation of the crystallite size is based upon peak broadening, which requires us to estimate the peak width at half maximum amplitude or the integral breadth peak (FWHM). The values of apparent crystallite sizes of cotton, flax and unprocessed plant material studies were calculated from the 002 reflection using the Scherrer equation.

The results are given in Table III. The reduction of the 101 and  $10\bar{1}$  intensities relative to the 002 peak found in samples 2 and 4 have physical meaning involving the relative orientation of the crystals in the fibre bundle [30, 52, 53].

Table III. Crystallographic parameters: crystal size calculated from the (002) reflection

Sample	FWHM(°)	Average crystalline size(Å)
1	0.54	87
2	0.54	86
3	0.62	67
4	0.73	64
5	2.8	16

The 002 peak is slightly shifted towards lower angles, indicating an increase in d-spacing in sample 5. The crystallinity was also calculated from the diffractograms, and it is clear that the FWHM of the diffraction peak decreases depending of the type of fibres and their stage of degradation. The particle size is increased in the less degraded fibres. In X-ray crystallography, it is known that peak broadening can arise in a number of ways, including compositional inhomogeneity, the presence of defects in the crystal lattice, the presence of very fine particles, etc. In this work, a good correlation was found between the CI variation and the crystalline size of the flax and cotton samples.

With these results, it is possible to consider that sample 2 shows some characteristics of the ageing process, as demonstrated by the SEM image and the CI in comparison with sample 1. However, in general, the flax fibres of these two Baroque canvases are in an excellent state of conservation. The cotton fibres presenting similar CI and SEM images also show some kind of deterioration, but in general, the state of conservation is good, too. These results are very important for the restoration process of these canvases, which are performed by the restaurateurs involved in the Andalusian government project for the Baroque period.

#### IV.5. Conclusion

This work reports the results obtained by a combination of OM, SEM, FTIR, and SR-XRD; with these data, it was possible to explain the different characteristics of flax, cotton and unprocessed plant material.

With synchrotron radiation, it was possible to associate different cellulose structures with the samples studied. Flax and cotton presented the Cellulose I structure.

The different crystallographic parameters and CI extracted from the XRD patterns are in accordance with those reported for the Cellulose I structure.

The unprocessed plant material had a different cellulose structure than the structure of the flax and cotton samples. The CI values showed that this sample had a very low crystalline structure, and the unit cell was smaller than that of Cellulose I according to the crystalline size. These results show that not all native cellulose is identical in crystal structure. The SEM cross-section supports this result, showing that the bundle of unprocessed plant material was different than those from flax and cotton. The structure of Cellulose IV was associated with the unprocessed plant material, and it occurred in the primary plant cell wall, not in the dominant second wall, as is the case with fibres that are used for textiles [54]. There are two possible explanations: (i) only the plant fibre not used for textile making was used for filling the wooden ceiling, or (ii) due to the high microorganisms activity found in the microclimate around this sample, the fibre was highly degraded.

This study used SR-XRD to demonstrate that the fine structure of the natural fibres, represented by structural parameters such as crystallinity index and crystalline size, could play important role in the characterisation process of these fibres.

The evaluation of textiles should also provide information about the causes of deterioration, whether due to environmental factors or effects from other conditions.

### IV.6. References

- [1] R.W. Kessler, R. Kohler: *Chem. Tech*, 34, 42 (1996)
- [2] P. Cappelletto, F. Morgardini, M. Brizzil, J. Skinner, G. Sede, J. Hague, P. Pasini: *Molecular Crystals and liquid Crystals Science and Technology, Section A*, 354, 391 (2000)
- [3] T. Espejo Arias, A. López Montes, A. García Bueno, A. Durán Benito, R. Blanc García, R. Restaurator 29, 76 (2008)
- [4] A. Duran: PhD Thesis, Seville University, Spain (2006)
- [5] L.K. Herrera, S. Montalbani, G. Chiavari, M. Cotte, V.A. Solé, J. Bueno, A. Duran, A. Justo, J.L. Perez Rodriguez: *Talanta* (2009) Submitted
- [6] M. Müller, B. Murphy, M. Burghammer, I. Snigireva, C. Riekel, J. Gunneweg, E. Panos: *App. Phys A*, 3, 183 (2006)

- [7] C. Baley: Composites Part A, 33, 939 (2002)
- [8] C. Brett, K. Waldron: Physiological and biochemistry of plant cell walls. (Chapman and Hall, London, 1996)
- [9] R. Lakes, Nature, 361, 511 (1999)
- [10] D. Catling, J. Grayson: Identification of vegetable fibres. (Archetype Publishers, London UK 1998) p.89
- [11] A. Marshall. The Identification of Flax, Hemp, Jute and Ramie in Textile Artefacts (University of Alberta Publishers, USA 1992) p. 95
- [12] P. Garside and P. Wyeth: Postprints First Annual Conference of the AHRC Research Centre for Textile Conservation and Textile Studies London, UK, Archetype, 118 (2005)
- [13] J.W.S. Hearle, R.H. Peters: Fibre structure (Textile Institute Manchester, London Butterworths, 1963) p.667
- [14] M. Lewin, E.I, Pearce: Handbook of Fiber Chemistry Marcel Dekker, Inc, New York, USA1998)
- [15] Tímár-Balászy and Eastop: Chemical Principles of Textile Conservation. (Oxford: Butterworth-Heinemann. 1998)
- [16] V. Daniels: Studies in Conservation 44 73 (1992)
- [17] B. Dewilde: 20 eeuwen vlas in Vlaanderen, Lannoo, Tielt, Bussum (1983)
- [18] A. Leseigneur, Lin des Ville Line des Champs, Association pour la Valorisation du Patrimoine Normand, Elboeuf, France, 17
- [19] I. V. frampton, W.A. Pons, K. Thomas: Economy Botanic, 14, 197 (1958)
- [20] S. C. Naithani, R. N. Rama, Y. D. Singh: Physiol. Plant, 54, 225 (1982)
- [21] A. S. Basra, C. P. Malik, Znt. Rev. Cytol, 89,65 (1984).
- [22] M.Yatagai, S.H. Zeronian, Cellulose, 1, 205 (1994)
- [23] R.L. Feller, S.B. Lee, J. Bogaard: The kinetics of cellulose degradation, in Historic Textile and Paper Materials (Advances in Chemistry, 212), H. L. Needles and S. H. Zeronian (eds), 329–48. (Washington, DC: American Chemical Society 1986)
- [24] H.L. Bos, A.M. Donald: J. Mater Sci, 34, 3029 (1999)
- [25] J.D Guthrie: The chemistry of lint cotton in chemistry and chemical technology of cotton. (Ed. K. Warg, J.R, Interscience Publishers, New York, USA 1980)

- [26] K.H. Meyer, L.Misch: *Helv.Chim Acta*, 20, 232 (1937)
- [27] L. Segal, C.M. Conrad: *American Dyestuff Reporter*, 46, 637 (1957)
- [28] L. Segal, J.J. Creely, A. E. Martin, C.M. Conrad: *Textile Research Journal*, 29, 786 (1959)
- [29] Y.L. Hsieh, X.P. Hu, A. Nguyen: *Textile Research Journal*, 67, 216 (1997)
- [30] X.P. Hu, Y.L. Hsieh: *J. Polym Sci., Polym Phys. Ed* 34, 1451 (1996)
- [31] R.T Oconnor , E.F. Dupre, D. Mitchum: *Textile Research Journal*, 28, 382 (1958)
- [32] L. D’Orazio, E. Martuscelli, G. Orsello, F. Riva, G. Scala, A. Taglialatela: *J. Arch. Sci*, 27, 745 (2000)
- [33] H. Boss: *The potential of flax fibres as reinforcement for composite materials*. (Ed. Technische Universiteit, Eindhoven, Germany, 2004).
- [34] A. Gianolio: PhD Thesis, Bologna University, Italy (1987), p.250
- [35] C. Quaglierini: *Chimica della fibra tessili*. (Ed. Bologna University, Bologna, Italy, 1997).
- [36] P. Garside, P Wyeth: *Stud. Conserv.* 51, 205 (2006)
- [37] P. Garside, P. Wyeth: *Characterisation of plant fibres by infra-red spectroscopy*, *Polymer Preprints* 41, 1792, (2000)
- [38] C. Riekkel: *Rep. Prog. Phys.* 63, 223 (2000)
- [39] O. Paris, D. Loidl, H. Peterlik: *Carbon*, 40, 551 (2002)
- [40] M. Müller, B. Murphy, M. Burghammer, C. Riekkel, E. Pantos, J. Gunneweg: *Apply Phys A.* 89, 877 (2007)
- [41] K. Kölln, G. Ingo, M. Burghammer, S. V. Roth, S. S. Funari, M. Dommachc, M. Müller *J. Synchrotron Rad.* 12, 739 (2005)
- [42] A.C. Hermes, R.J Davies, S. Greiff, H. Hutzke, S. Lahlil, P. Wyeth, C. Riekkel. *Biomacromolecules*, 7, 77 (2006)
- [43] P. Garside, P Wyeth: *Characterisation of silk deterioration*, in *Preprints of the North American Textile Conservation Conference*, (Philadelphia: NATCC. 55–60, 2002)
- [44] P Wyeth: *Signatures of ageing: correlations with behaviour*, in *Preprints of Textile Conservation Conference*, (Archetype Publications, Malta 2005). 118-125.
- [45] D.V Parrikh, D.P. thibodeaux, B. Condon: *Textile Research Journal*, 77, 612 (2007)

- [46] C. Woodcock A. Sarko: *Macromolecules*, 18, 1183 (1980)
- [47] M. Müller, B. Murphy, M. Burghammer, C. Riekkel, M. Roberts, M.Papiz, S. Clarke, J. Gunneweg, E. Pantos: *Spectrochim. Act. B*, 59, 1669 (2004)
- [48] M. Müller, B. Murphy, M. Burghammer, I. Snigireva, C. Riekkel, J. Gunneweg, E. Pantos: *Apply Phys A*. 83, 183 (2006)
- [49] M.L Franquelo. Technical report. Materials Science Institute of Seville. p.50 (2007)
- [50] M. Lewin, E.M. Pearce, (eds): *Handbook of Fiber Chemistry*, 3rd edn. New York: Marcel Dekker Inc. (2002)
- [51] A. Tímár-Balászy, D. Eastop: *Chemical Principles of Textile Conservation*. (Oxford: Butterworth-Heinemann, England, 1998)
- [52] S.Y. OH, D.I. Yoo, Y. Shin, H.C. Kim, H.Y. Kim, Y. S.Chung, W.H.Park, J.H.Youk: *Carbohydrate Research*, 340, 2376 (2005)
- [53] S.J. Eichhorn, R.J Young, R.J. Davies, C. Riekkel: *Polymer*, 44, 5901 (2003)
- [54] M. Müller, C. Czihak, M. Burghammer, C. Riekkel: *J. Apply Crist*, 33, 817 (2000)

## V. Analysis of cultural heritage metallic artefacts from Andalusia

### V.1. Introduction

Several techniques have been used to characterize the materials and its products of alteration, but many of them only give chemical composition and frequently require the sampling and the destruction of the material (grinding, solution, heating, etc). Also, the material is altered during the analysis, being important to use techniques that give information of the phases present without any destruction (non-destructive techniques) or sampling.

Conventional techniques of X-rays diffraction requires sampling from artworks and grinding of the extracted samples, being, in this form, destructive analytical methods. Parafocusing Bragg-Brentano geometry leads to a  $2\theta$ -shift of the X-ray reflection, if the sample is not precisely positioned on the focusing circle. A sample displacement can occur if the sample has an uneven surface, as frequently happens in samples coming from archaeology or cultural heritage [1]

### V.2. Graded Multilayer Optics

Graded Multilayer Optics (“Göbel-Mirror”) have proved as very useful beam conditions for parallel-beam diffraction without sampling [2,3,4]. High-resolution XRD and XRD using capillary are used more frequently to study samples from cultural heritage but in these cases, sampling is necessary. The Göbel Mirror is a device, based on a layered crystal, which, mounted on a D5000 Siemens diffractometer, transforms the primary divergent X-ray beam into a highly brilliant, parallel beam (Fig.1).

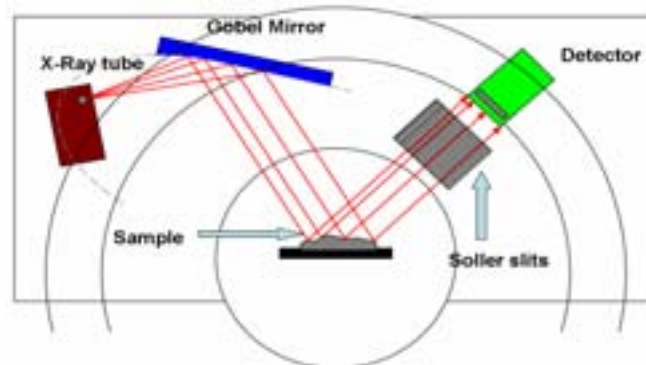


Fig. 1 Experimental procedure for non-destructive analysis by X-Ray Diffraction with Göbel mirrors of artefacts belonging to cultural heritage.

The crystalline phases on the surfaces of samples were characterized by X-ray diffraction (XRD) using a Siemens diffractometer model Kristalloflex D-5000 with and without Göbel mirror. Graded multilayer optics creates a highly parallel incident beam while suppressing  $K_{\beta}$ - radiation. By capturing a large solid angle, the mirror turns otherwise unusable radiation into a useful parallel beam. The Göbel mirror enables the investigation of irregularly shaped samples surfaces and reduces the requirement for the exact sample position. Also, low fixed incidence angles X-rays were used in complement with Göbel mirror. If dimensions of an object are adequate (up to 60 cm in bulk) it can be directly analyzed by XRD, without sampling. Even a rough, irregular surface, both on flat and bent objects, is suitable for the analysis. The XRD analysis using Göbel mirrors is therefore, totally non-destructive and very useful to study artefacts from Cultural Heritage [5,6,7]. It can be obviously very adaptable to study the surfaces of these artefacts, giving information of degradation and corrosion processes and information about pigments, ceramics, metals, patinas, crusts, etc., used to manufactured artworks. All the samples studied in this work belong to historic metals of Spanish Cultural Heritage.

### **V.3. Research aims**

The main objective of this work is the use of a totally non-destructive analytical method, X-ray diffraction with Göbel mirror, for the study of the superficial alteration of some metallic artefacts, so much bent as flat ones, proceeding from important artworks, since in most of the cases can not be taken samples for the study by conventional method of powder diffraction. The measures using Göbel mirrors and low fixed incidence angles were done to study superficial and underlying layers of metallic samples.

### **V.4. Materials**

Different metals were chosen for their inclusions in this chapter for showing general and exemplified degradation processes.

#### **V.4.1. Bronze samples**

Three different samples were taken from the Pardon Portico, located in the North façade of the Mosque-Cathedral of Cordoba (Fig.2)



Fig. 2 (a) rivet extracted from the gateway leaves (dated on March 1377) were made with pine wood covered with bronze plates. (b) a piece of bronze with a high degree of alteration in its surface (c) an altered piece containing nails used for knocking the bronzes to the wood.

All these pieces were extracted by experts and restorators using physical methods. Artefacts were not scraped to obtain powders, analysis were realized directly over the pieces. After adequate study and restoration, artefacts will be returned to its original places.

#### V.4.2. Iron samples

Several samples taking from iron artefacts have been studied. Three samples have been selected for this work:

Two iron artefact samples (A Roman arrow and a button from Roman clothing) found in the archaeological excavation located in Baena, Cordoba were selected for this work. (Fig.3)

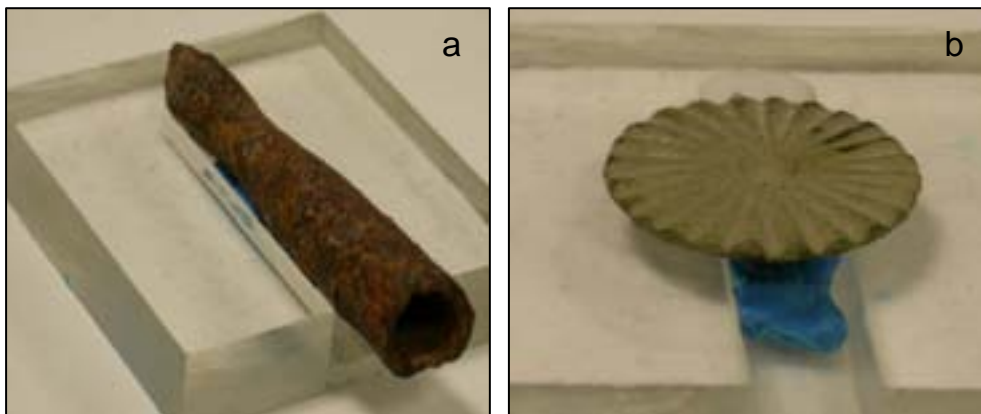


Fig. 3 Roman Samples (a) Roman arrow (b) Roman button

Other sample was a hammered nails of the windchest from baroque organ in San Lorenzo Church in Cadiz (Fig.4)

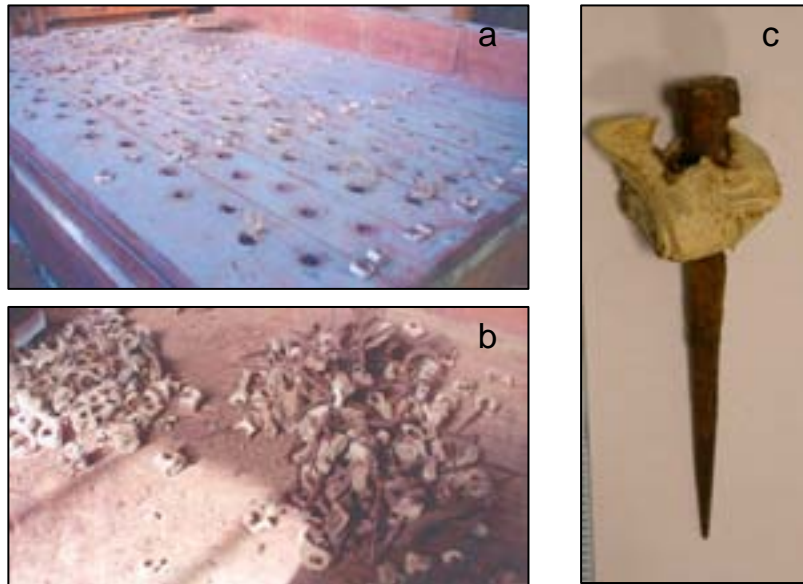


Fig. 4 (a) and (b) details of windchest from baroque organ in San Lorenzo Church in Cadiz (c) hammered nails

### V.4.3. Lead samples

#### V.4.3.1. Lead seals

Seville City Hall has an important lead seals collection. Part of the collection is stored in holes made in cardboard into the wood drawer that remain a long time closed without any adequate control of environmental conditions. Seals were manufactured with lead showing a “white rust” of lead due to alteration process (Fig.5). Samples of the seals powder, wood and cardboard were taken for the study.

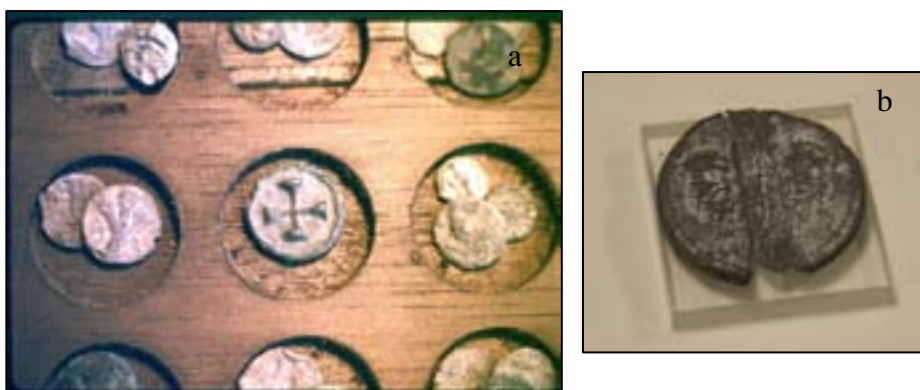


Fig. 5 (a) Lead seals collection of the Seville city Hall (b) lead seal detail

#### V.4.3.2. Lead-rich organ pipes

The atmospheric corrosion of lead-rich organ pipes in Spanish church has recently attracted the attention of organ builders. Organ pipe corrosion leads to the gradual development of cracks and holes which destroy the function of the pipes. One sample of lead air duct from an organ from the Zaragoza cathedral was studied (Fig.6)



Fig. 6 Wind duct of the baroque from the Zaragoza Cathedral

### V.5. Results and discussion

#### V.5.1. Bronze samples

Most frequently used copper alloys are brasses (Cu-Zn), and bronzes (Cu with Sn, Al or Si). Bronzes are used for the construction of different types of artworks, statues and monuments of cultural relevance, due to its high stability to environmental corrosion [8]. The corrosion of bronze monuments has been studied by several workers [9,10,11,12,13]. This interest is mainly due to the increasing awareness of air pollution damage to the cultural heritage. Some works have contributed to a better understanding on the reaction mechanisms of environmental deterioration [10].

The elemental analysis of the rivet (sample a) from the Pardon Portico shows that the original material is constituted by copper and tin (Fig.7).

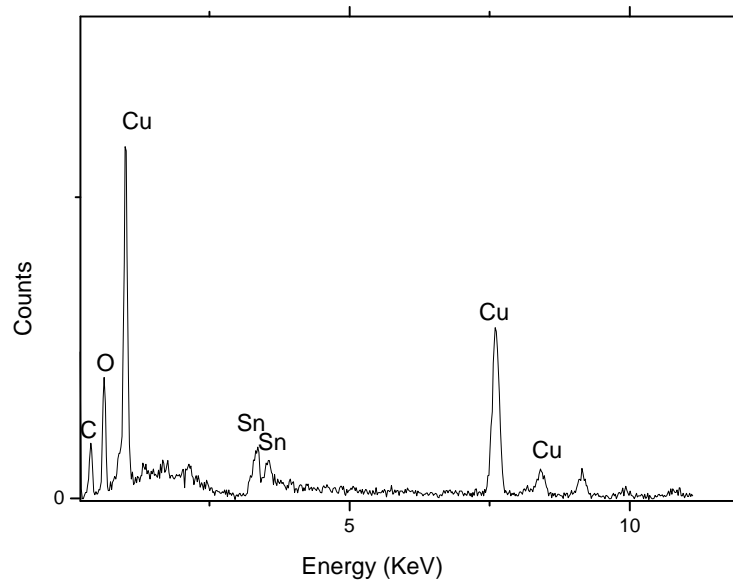


Fig. 7 EDX analysis of the rivet extracted from the Pardon Portico of the the Mosque-Cathedral

The x-ray diffraction pattern (obtained using Göbel mirrors) of this sample shows the presence of the diffractions at values  $42.8^\circ$  and  $49.7^\circ$  of angle  $2\theta$  (Fig.8), corresponding to alpha bronze (B), according with the file ASTM of JPCD. This piece was cleaned by restorators before studying and no degradation products are detected.

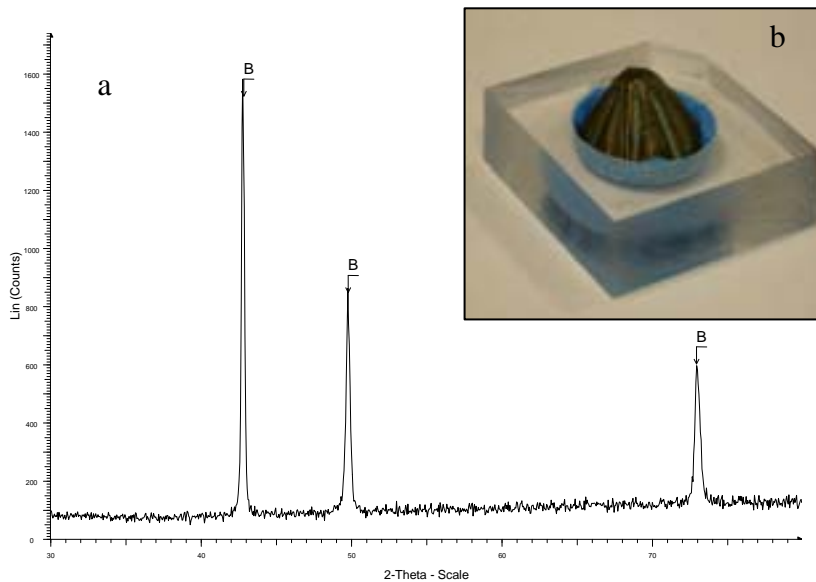


Fig. 8 X-ray diffraction pattern with Göbel mirrors of: (a) a rivet extracted from the Pardon Portico of the the Mosque-Cathedral, corresponding to alpha bronze (b) sample holder used for the measurement

The elemental analysis of the superficial products formed on the bronze (sample b) shows the presence of copper, chlorine, silicon, sulphur, calcium, iron, potassium and oxygen (Fig.9).

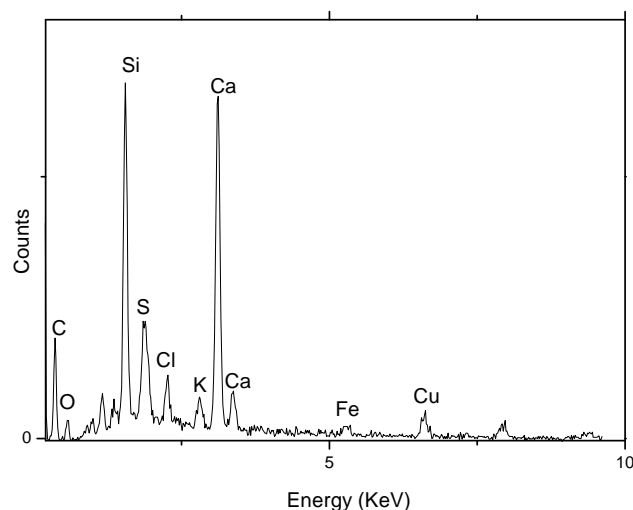


Fig. 9 EDX analysis of superficial products formed on the piece of bronze from Pardon Portico, showing the presence of Cu, Cl, Si, S, Ca, Fe, K and O

Frequently, the first reaction that takes place is the oxidation of the metallic base exposed to the atmosphere to produce cuprous ions. In a chloride polluted atmosphere, cuprous chloride is formed. This is an unstable compound that in the presence of oxygen and environmental humidity turns into basic copper chloride with simultaneous production of hydrochloric acid. The presence of this acid will induce a new cyclic reaction of copper until the total consumption of the metal. Only if the cuprous chloride is eliminated, these damaging cyclic processes (“bronze disease”) would be stopped [8,14,15].

The chemical examination of the corrosion of copper and bronze artifacts has been the subject of study for at least 150 years. Most probable cause concerning the origin of bronze disease is the slow action of gaseous pollutants in showcases constructed of unsuitable materials that evolve sulphurous contaminants [16]. The best-known early attempt to deal with the problem of bronze disease is that of Berthelot, in 1895 [17], who reported some of his proposals to account for the instability of certain bronzes. He recognized that there must be an important cyclical component to the reaction. He also realized that one of the important products of the reaction was the basic copper chloride, atacamite, which at that time was assigned the formula  $3\text{CuO}\cdot\text{CuCl}_2\cdot 4\text{H}_2\text{O}$ . Objects studied by Scott [18] show considerable variation in the extent to which surface disruption occurs with time. A number of bronze objects from Palestine are in the Petrie Collection, Department of Western Asia, University College, London. One of these objects, which had obviously suffered severe bronze disease and

had been stored in uncontrolled conditions for more than 20 years, was examined and analyzed. The light green corrosion was identified as a mixture of atacamite and paratacamite, the most commonly found mixture of isomers in many ancient bronzes regardless of the location in which they are found. Most of the small objects in this collection illustrate the effects of disintegration in poor storage conditions over many decades.

The XRD pattern measured with Göbel mirrors shows that the sample is constituted by atacamite [ $\text{Cu}_2\text{Cl}(\text{OH})_3$ ] (At), gypsum [ $\text{Ca}(\text{SO}_4)2\text{H}_2\text{O}$ ] (Gy), and weddellite [ $\text{Ca}(\text{C}_2\text{O}_4)2\text{H}_2\text{O}$ ] (We) (Fig.10). Atacamite has been detected previously in copper and copper alloys exposed outdoors due to environmental contamination [8,14]. This environmental contamination is also responsible of the presence of gypsum and other compounds. The weddellite, also present, may be formed by reaction between environmental gypsum and rests of calcite with oxalate ions from the dissolved acid. In urban areas oxalic acid is abundant in rain and mists [19] or it may be secreted by micro organisms, such as fungi and liquens [20].

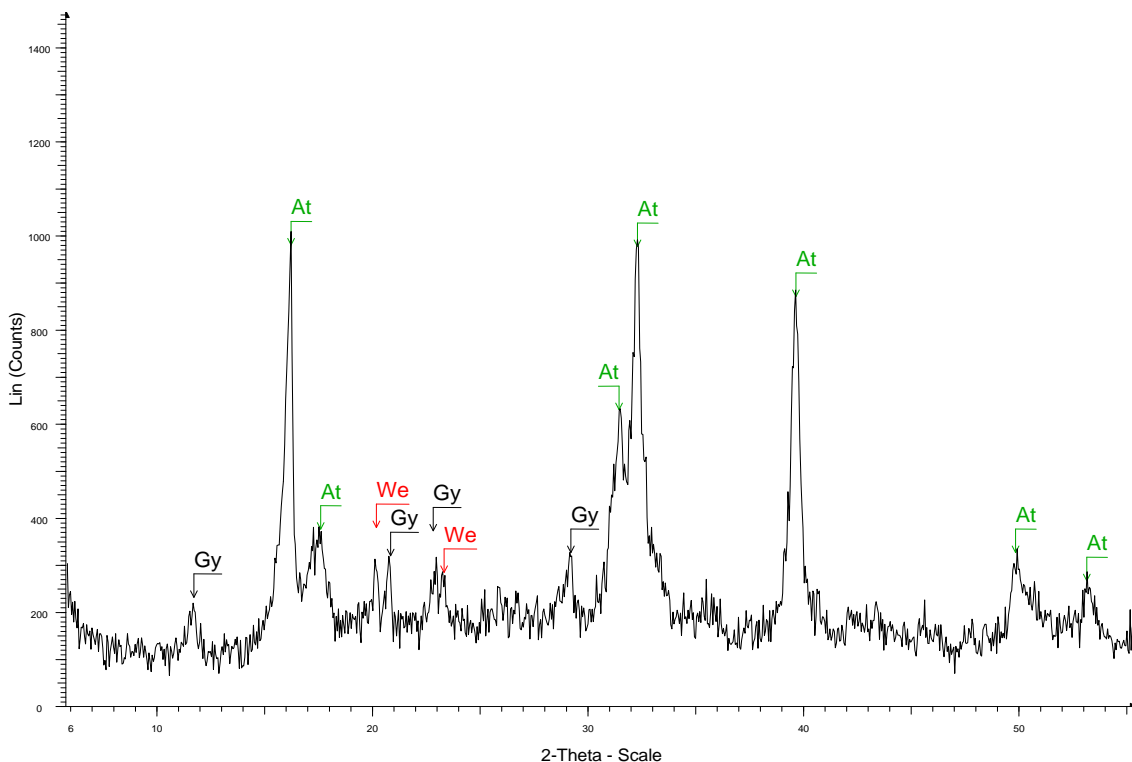


Fig. 10 X-ray diffraction pattern with Göbel mirrors of the superficial product on the altered bronze of the Portico, corresponding to atacamite (At), gypsum (Gy) and weddellite (We).

The punctual chemical analysis of the nail (sample c) shows the presence of iron and oxygen (Fig. 11).

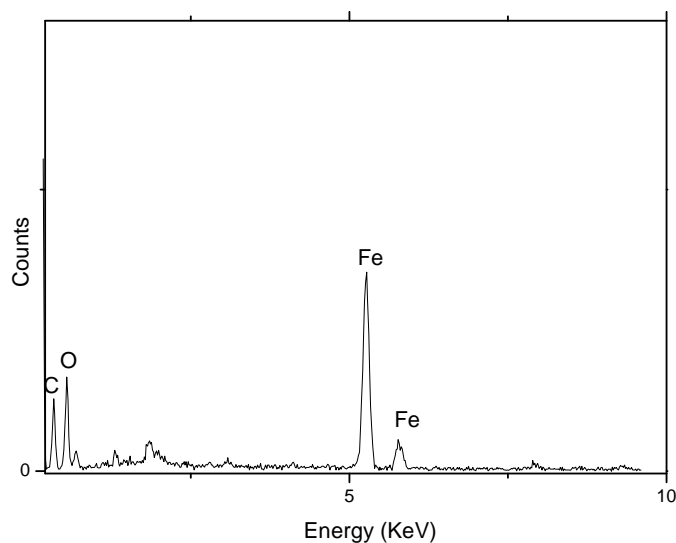


Fig. 11 EDX analysis of the powder taken from the nail that shows the presence of Fe and O

X-ray diffraction on the surface of the nail using Göbel mirrors confirms the presence of goethite [ $\alpha$ -Fe<sup>3+</sup>O(OH)] (Goe), lepidocrocite [ $\gamma$ -Fe<sup>3+</sup>O(OH)] (Lep) and [FeO(OH)] (Fig.12).

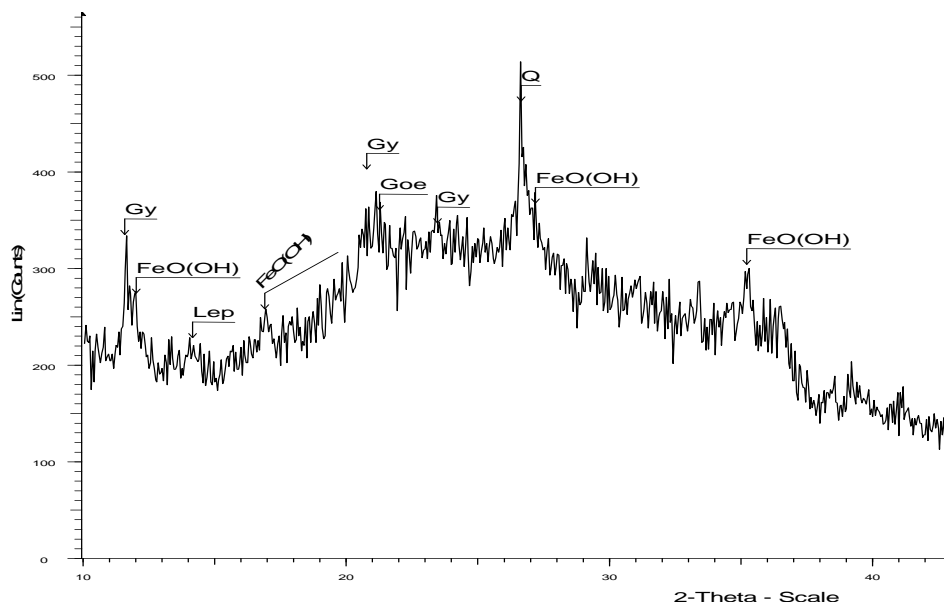


Fig. 12 X-ray diffraction pattern with Göbel mirrors of the altered iron nail of the Mosque-Cathedral of Cordoba, showing the presence of goethite (Goe), lepidocrocite (Lep), [FeO(OH)], gypsum (Gy)

Even when environmental conditions are adverse, oxyhydroxides or hydroxides compounds are formed in iron implements. The most common compounds formed are goethite (FeOOH), which gives the brown and dark reddish brown colours to

monuments. In poorly drained zones, lepidocrocite, an isomer of goethite, frequently has been reported [21], it gives a bright orange colour. The iron oxyhydroxides or hydroxides are frequently formed in the surface of iron artefacts due to environmental contamination. Also, gypsum (Gy) and quartz (Q) are present in the sample due to this factor.

## V.5.2. Iron samples

### V.5.2.1. Roman samples

Elemental analysis of a zone corresponding to a Roman arrow, where surface crust was removed, shows the presence of iron. Punctual chemical analysis carried out by EDX in the arrow is shown in Fig 13.

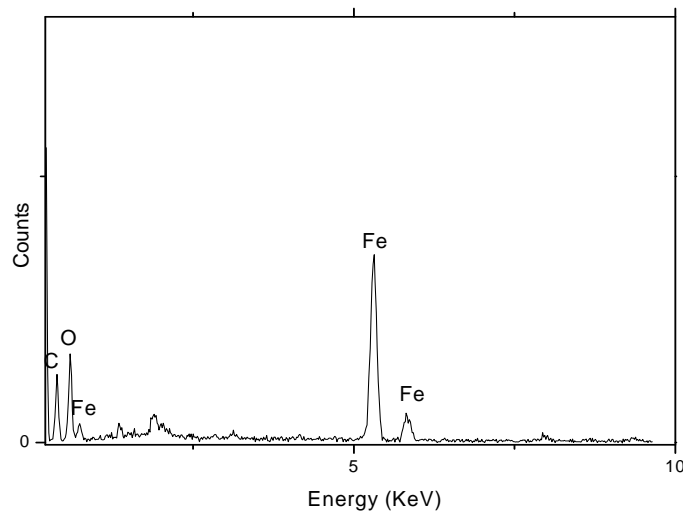


Fig. 13 EDX analysis of a Roman arrow from archaeological excavation in Baena after removing the surface crust, showed the presence of Fe.

X-ray diffraction analysis carried out with Göbel mirrors on the superficial covered area of crust shows the presence of calcite (Calc) and quartz (Q), deposited during the burial in the soil. Also vesuvianite (Ves) was found (Fig.14).

Vesuvianite, calcium magnesium iron aluminium silicate hydroxide ( $\text{Ca}_{10}(\text{Mg,Fe})_2\text{Al}_4(\text{SiO}_4)_5(\text{Si}_2\text{O}_7)_2(\text{OH,F})_4$ ), named after its discovery locality, Mount Vesuvius (Campania, Italy) is rarely found in iron artefacts that have been buried during long time. This mineral is produced by the reaction between iron from artefacts and silicates present in the soil.

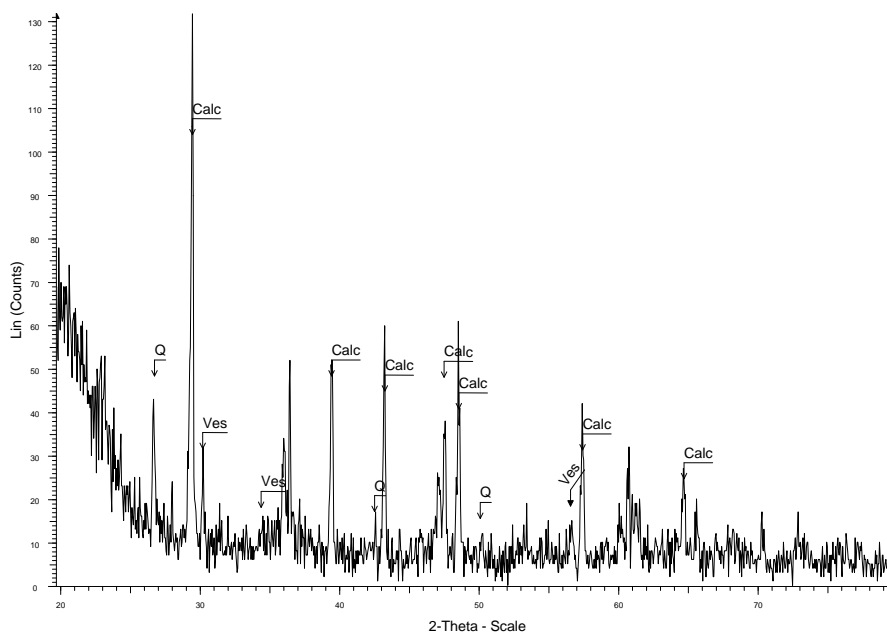


Fig. 14 X-ray diffraction pattern of the Roman arrow using Göbel mirrors, showing the presence of calcite (Calc), quartz (Q) and vesuvianite (Ves).

Vesuvianite, calcium magnesium iron aluminium silicate hydroxide, is rarely found in iron artefacts that have been buried during long time. This mineral is produced by the reaction between iron from artefacts and silicates present in the soil. Elemental analysis of the Roman button, where surface crust was removed similarly to the arrow sample cited before, shows the presence of copper and tin (Fig.15).

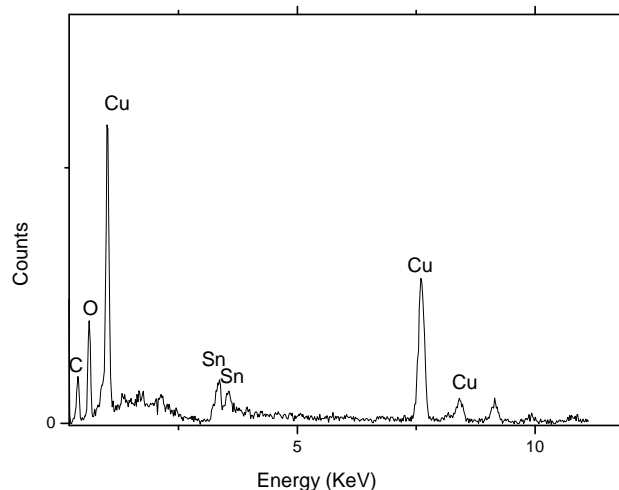


Fig. 15 EDX analysis of the Roman button

Studies realized on the surface of the sample by X-ray diffraction with Göbel mirrors only shows the presence of calcite, quartz (Fig 16) that were deposited from the soil. The crusts deposited on the surfaces of arrow and button are very thick and, except

in punctual areas cited before, do not permit the study of the underlying material (bronze) and its alteration products.

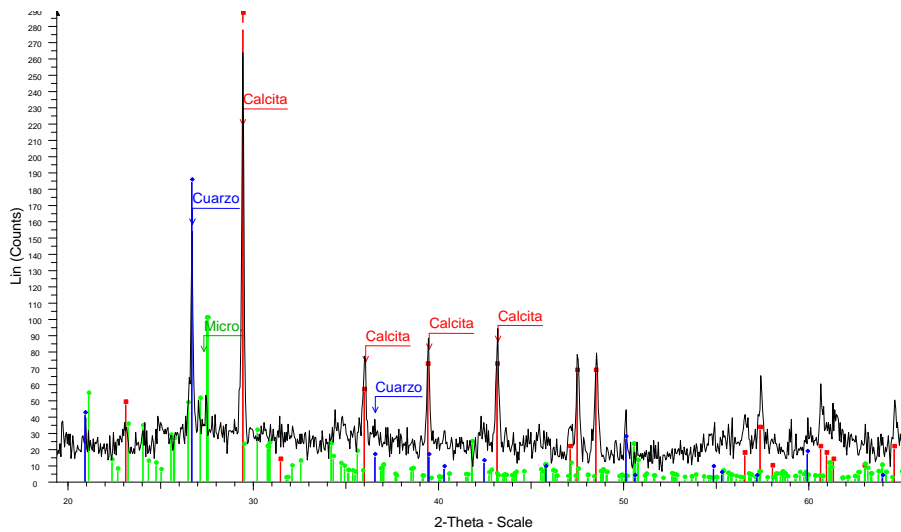


Fig. 16 X-ray diffraction pattern of the Roman button using Göbel mirrors, showing the presence of calcite (Calc), quartz (Q)

### V.5.2.2. Nails of the windchest from baroque organ

The study of the influence of atmospheric corrosion of iron artefacts expose on outdoor condition (coastal) is reported. Sulphur and chloride ions are the most common and important atmospheric corrosion agent. The XRD of the corroded surface of nails coming from the baroque organ in Cadiz (coastal indoor) shows akaganeite [ $\beta$ -FeOOH] phase, that is a common oxyhydroxide that forms in presence of chlorine [19] (Fig 17). Akaganeite frequently appear in the monuments located at the seaside and in archaeological site being chlorine present in the environment.

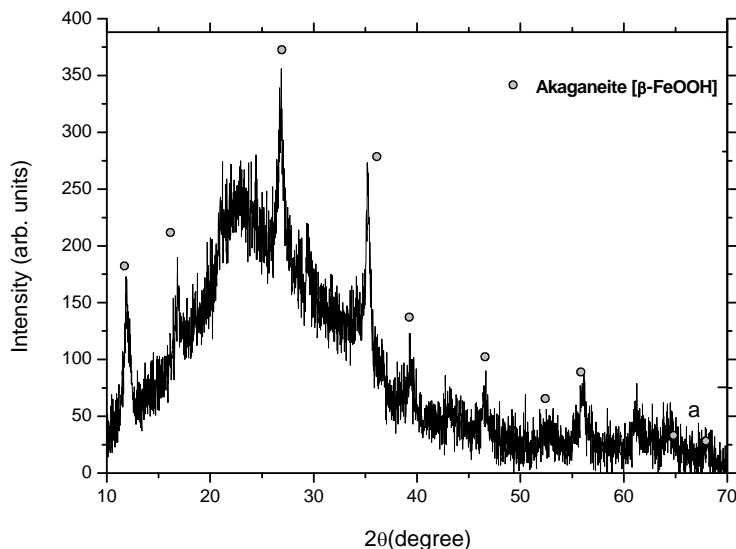


Fig. 17 X-ray diffraction pattern of the corroded surface of nails from the baroque organ in Cadiz

### V.5.3. Lead Samples

Lead alloys were widely used in antiquity, especially in organ pipes, coins and lead seals manufacturing. Depending on the characteristic of the environment to which it is exposed, lead is quite reactive, forming sulphates, carbonates or hydroxycarbonates compounds. The presence of lead carbonate compounds is responsible for the unsightly, white and powdery “white rust” of lead and can be localised on the surface in the form of pits [22]. The carboxylic acids formic, propanoic, tannic and acetic acids formed by cellulose hydrolysis from woods or paperboards used for store lead artifacts in museums can convert the lead surface of artifacts in voluminous corrosion compounds, and in some cases, the artworks may be corroded in bulk through a progressive peeling of the corrosion layer [23-25].

#### V.5.3.1. Lead seals

Fig. 18a shows the analysis by optical microscope of the cross section of the lead seals corresponding to Seville City Hall. EDX shows only the presence of lead (Fig 18b).

Lead seals were stored in wooden drawer inside of a hole made in paperboard, at variable temperatures values between 5° and 38° depending of the season, and relative humidity values normally higher than 85 %. The morphological studies of fibres and wood were realized using optical and scanning electron microscopes and comparison with standards.

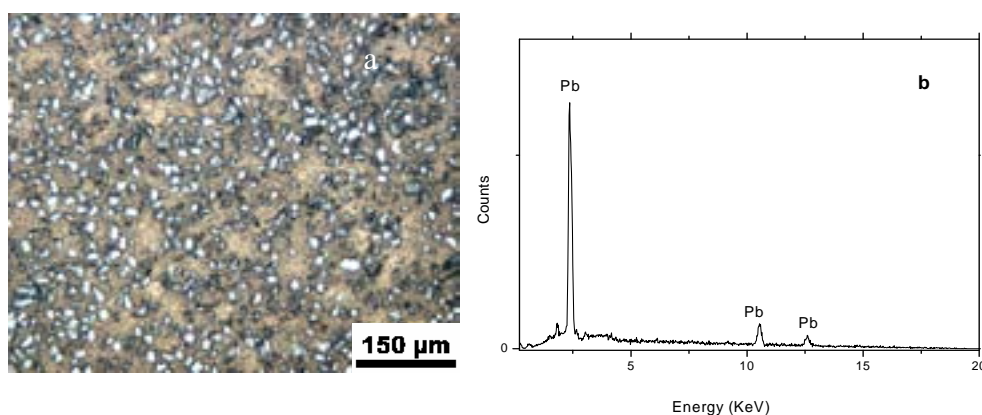


Fig. 18 (a) metallographic cross section (b) EDX analysis of the lead seals

The cross section of the wood shows the drawer was manufactured of pine wood (Figs 19a, 19b). The paperboard was composed of a mixture of fibres (vegetables and

synthetic) [26-27] (Figs 19c, 19d). These results suggest that the alteration might be due to the storage in enclosures in the museum for a long period. The hydrolysis of the cellulose from the wood drawer and the paperboard contributed to the formation of the carboxylic acid (mainly formic and acetic acids) that dissolves the PbO of surface forming lead carbonates [22-24, 28-30].

Lead seals belonging to Sevillian collection had suffered significant alteration processes, losing not only the external figurative prominence, but also some of them were corroded in bulk through a progressive peeling of the corrosion layer. This represents an alteration in the entire sample; showing powdery “white rust”; the study of this alteration process was carried out by X-ray diffraction with Göbel mirrors.

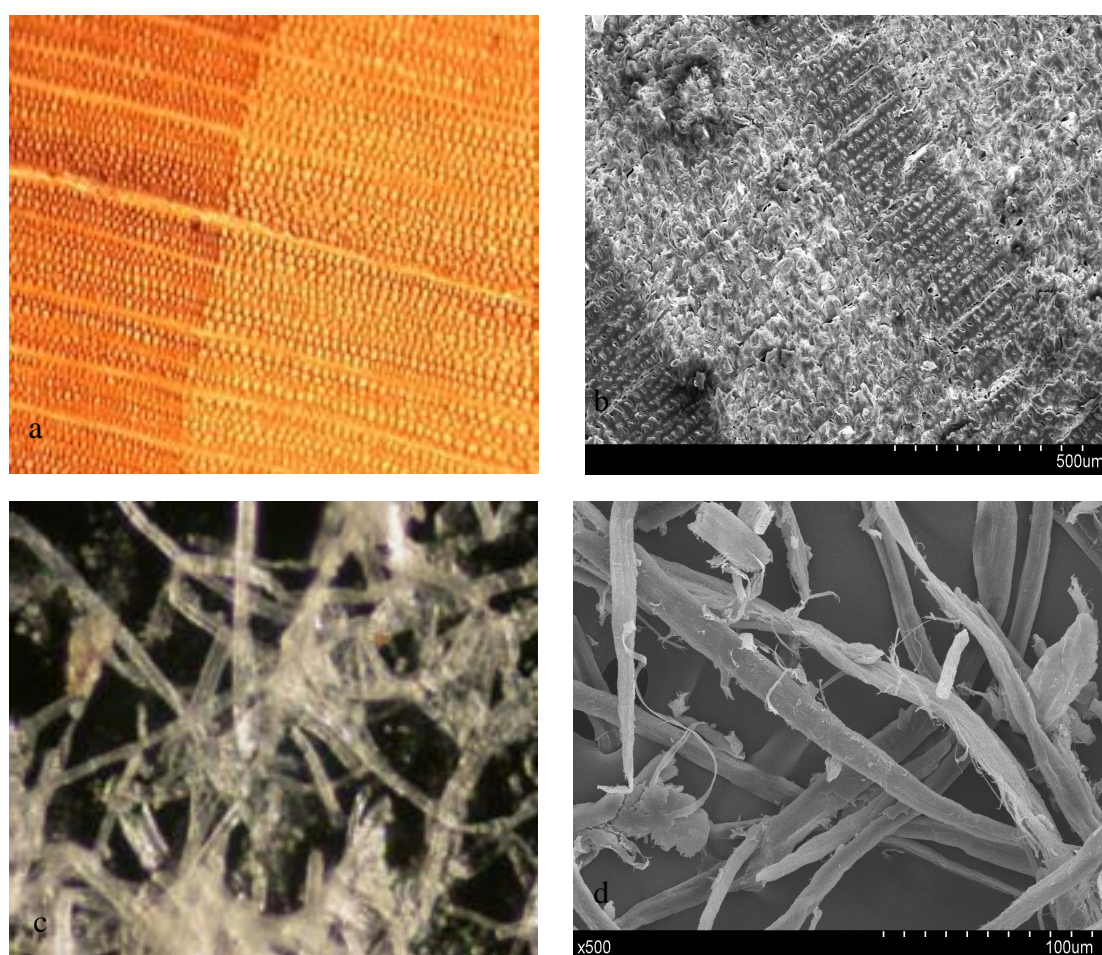


Fig 19 (a) Optical microscope image of the cross section of the drawer wood; (b) Scanning electron microscope image of the transversal cross section of the drawer wood; (c) Optical microscope image of the fibers from paperboard; (d) Scanning electron microscope image of the fibers from paperboard

The X-ray diffraction of the surface (Fig 20) shows that it is composed of hydrocerussite [ $\text{Pb}_3(\text{CO}_3)_2(\text{OH})_2$ ] and cerussite [ $\text{PbCO}_3$ ]. It suggests that this alteration

process can be due to the effect of the carboxylic acids produced by the hydrolysis of the paperboard and wood that are used for the seals store.

To check this suggestion, the following experiment was performed in the lab, at room temperature and relative humidity values close to 100 %. In a beaker was introduced a piece of paperboard together with another one of lead. The beaker also contains water and CO<sub>2</sub> separated of the paperboard and lead. After several months, the stored lead piece was covered with a white powder that the X-ray diffraction confirms as hydrocerussite and cerussite. The same experiment was repeated without using paperboard and in this case only lead oxide was formed on the surface. In this case, the experience in the lab shows undoubtedly the role of the paperboard in the corrosion process.

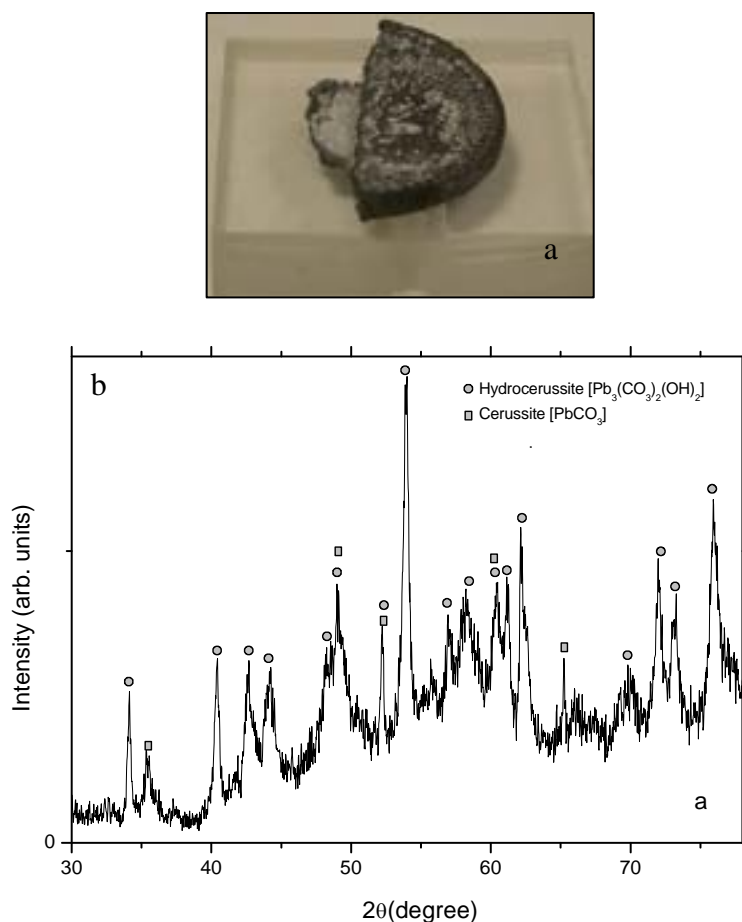


Fig.20 (a) Alteration of lead seal: “white rust” (b) X-ray diffraction pattern of the lead seal surface

This degradation process is ratified by the different studies by Bradey and Thicket [31] and Raychaudhuri and Brumblecombe [32]. The effect of compounds as acetic acid, formic acid and formaldehyde on lead was investigated at room temperature. At 100 % RH after 120 days, acetic acid had caused complete corrosion and formic acid

had caused extensive corrosion; formaldehyde had caused least corrosion. At 50 % RH acetic acid and formic acid were less corrosive than at 100 % RH, and formaldehyde did not cause corrosion. Although acetic acid was detected at 30 % RH, at all temperatures no corrosion of the lead coupons occurred. These experiments suggest that, as we thought, acetic and formic acids (in this case coming from paperboard), in conditions of high relative humidity, cause major processes of lead artefacts deterioration.

### **V.5.3.2. Lead-rich organ pipes**

The atmospheric corrosion of lead-rich organ pipes in Spanish church has recently attracted the attention of organ builders. Organ pipe corrosion leads to the gradual development of cracks and holes which destroy the function of the pipes. When this occurs, the historic lead organ pipes have to be replaced by new ones, and a part of the sounding cultural heritage is lost forever. It is not clear why this organ was corroded. However, the Zaragoza Cathedral environment to which this organ was exposed is characterized by relatively low temperature and high relative humidity. Another characteristic is the presence of large amounts of wood structures around organ.

The studied pipe organ is enclosed in wood furniture. The humidity in combination with alteration products of wood (organic vapors acid, such as acetic or formic, and aldehydes produced by the hydrolysis of the hemicellulose during aging) can react with lead forming corrosion products, mainly lead carbonates. In extreme cases, they can cause a complete destruction of the artefact. Crystalline corrosion products were analyzed; the diffractometer was equipped with Göbel mirrors and the measures were carried out in the mode of  $2\theta$  scans at low fixed incidence angles, which can be used to characterize as much the superficial layer as the underlying ones without any effect of the roughness and obtain information in the depth profile of the sample. The diffraction profiles of the sample was acquired under fixed incidence angles, at  $1^\circ(\theta)$  and  $5^\circ(\theta)$ , all the other parameters were kept constant. Fig. 21 shows the diffraction patterns at two incidence angles,  $1^\circ(\theta)$  and  $5^\circ(\theta)$ .

The XRD patterns of the  $1^\circ$  incident angle ( $\theta$ ) gives information about the more external layer. The crystalline phases detected can be attributed to tin (Sn), lead (Pb) and hydrocerussite (HC) (Fig. 21a). However, it is also evident that there is a certain evolution of the diffractogram from the surface to the depth of the sample. In particular,

the pattern taken at  $5^\circ$  ( $\theta$ ). (Fig. 21b) shows higher intensity of the peaks corresponding to tin (Sn). In the pipe organ surface is possible to detect the alteration process because the pattern at  $1^\circ$  ( $\theta$ ) shows some conversion of lead to hydrocerussite; peaks of lead decrease and peaks corresponding to hydrocerussite increases

In order to get the depth of the analyzed layer of the organ pipe, it is considered the global chemical composition (lead, tin and hydrocerussite), the density of these phases, the wavelength of X ray radiation ( $\lambda = 1.54 \text{ \AA}$ ), the diffraction angle for each compound (strongest peak, Pb  $2\theta = 31.28^\circ$ , Sn  $2\theta = 30.73^\circ$ , Pb<sub>3</sub> (CO<sub>3</sub>)<sub>2</sub>(OH)<sub>2</sub>  $2\theta = 34.15^\circ$ ), and finally the incidence angle.

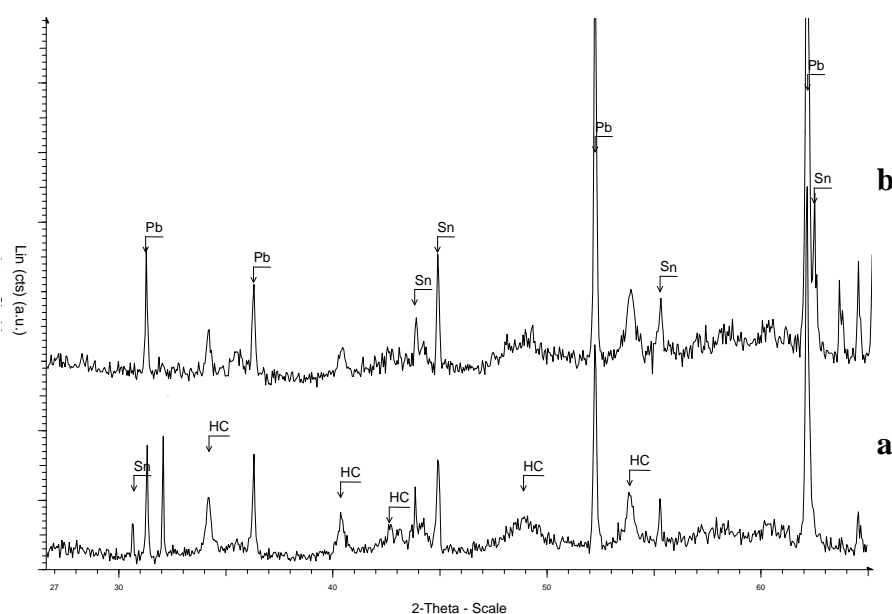


Fig.21 (a) XRD pattern at  $1^\circ$  incident angle of an organ pipe, tin (Sn), lead (Pb) and hydrocerussite (HC); (b) XRD pattern at  $5^\circ$  incident angle of the same pipe.

In order to get the depth of the analyzed layer of the organ pipe, it is considered the global chemical composition (lead, tin and hydrocerussite), the density of these phases, the wavelength of X ray radiation ( $\lambda = 1.54 \text{ \AA}$ ), the diffraction angle for each compound (strongest peak, Pb  $2\theta = 31.28^\circ$ , Sn  $2\theta = 30.73^\circ$ , Pb<sub>3</sub> (CO<sub>3</sub>)<sub>2</sub>(OH)<sub>2</sub>  $2\theta = 34.15^\circ$ ), and finally the incidence angle.

Due to the studied organ pipe has a curved and rough surface, obtained information cannot be comparable with that it would obtain in case of thin layers. With the use of fixed low incidence angles ( $\theta=1^\circ$  and  $\theta=5^\circ$ ), although it obtains major information about superficial layers, we cannot obviate that X-ray beam gets also in the

bulk of the sample. In another sonorous organ pieces, alloy composition is about 50% of lead and 50% of tin [33].

Table 1. The depth for 90 % contribution of the measured intensity for 1° and 5° in the study of organ pipes.

	Pb (µm)	Sn (µm)	Pb <sub>3</sub> (CO <sub>3</sub> ) <sub>2</sub> (OH) <sub>2</sub> (µm)
$\gamma = \theta = 1^\circ$	0.149	0.211	0.306
$\gamma = \theta = 5^\circ$	0.645	0.912	1.350
$\theta$ -2 $\theta$ couple	1.195	1.657	2.655

However, in the case of the samples studied in this work, the composition is about 90% of lead and 10% of tin, determined by X-ray diffraction semiquantitative analysis, what is corroborated by the presence of alteration products of lead (hydrocerussite) and no presence of alteration products of tin, such as cassiterite or romarchite [33,34]. In this form, the depth for 90% contribution of the measure intensity of the alloy layer would be, according with Table 1, approximately of  $x=0.155\mu\text{m}$  at  $\theta = 1^\circ$  and  $x = 0.671\mu\text{m}$  at  $\theta=5^\circ$ .

## V.6. Conclusions

The data obtained in this work show that X-ray diffraction with Göbel mirrors is a good method for the characterisation of the irregular surfaces from artefacts belonging to cultural heritage because allow non-destructive study (without sampling) of them.

Metals used in several chosen monuments of Andalusian Cultural Heritage have suffered varying degrees of alteration due to the different environmental conditions. This chapter shows example cases of the degradation of these metals. All the cases have been compared with similar processes found in the literature, showing almost comparable results.

The combination of Göbel mirrors attachment and measure at fixed low incidence angles allow to obtain information about the depth profile of sample, being a very important application in the artworks.

Bronze in the rivet from Pardon Portico of Mosque-Cathedral of Cordoba was detected using X-rays diffraction with Göbel mirrors, and on the surface of the bronze, wedellite, atacamite and gypsum were detected as alteration products.

Goethite, lepidocrocite and FeO(OH) appeared on an iron nail proceeding of this Portico too.

The study demonstrated that metallic point of a Roman arrow was composed of iron. On the surface, it was found calcite, quartz and vesuvianite. The Roman button was covered with a thick crust, formed by calcite and quartz. The surface of these materials is affected by environmental and soil in which they were buried.

Nails of the windchest from baroque organ are altered to akaganeite in seaside environmental

Cellulose hydrolysis from paperboard and wooden drawer has provided carboxylic acid that has dissolves the PbO formed on the surface of lead seals collection, forming lead carbonates.

organ pipes were altered to hydrocerussite by the method used for storing these materials in the Zaragoza Cathedral.

## V.7. References

- [1] M. Gross, S. Haaga, H. Fietzek, M. Herrmann, W. Engel, *Epdic* 5, Pts 1 and 2 *Materials Science Forum* (1998) 278-2, 242-247.
- [2] H. Göbel, 43<sup>rd</sup> Annual Denver X-Ray Conference (August 1-5, 1994), Paper D-63.
- [3] M. Schuster and H. Göbel, *J. Phys. D: Appl. Phys.* 28 (1995) A270-275.
- [4] M. Schuster and H. Göbel, *Adv. In X-Ray Analysis* 39 (1996) 57-71.
- [5] G. Chiari, A. Giordiano, G. Menges, *Science and Technology for Cultural Heritage*, 5 (1) (1996), 21-36.
- [6] G. Chiari, R. Compagnoni, R. Giustetto, M. Ricq-de-Bouard, *Le vie della pietra verde*, Omega Ed., (1996), 35-53.
- [7] G. Chiari, R. Compagnioni, M. Ricq-de-Bouard, XII Congress UISPP, Forli (1996).
- [8] L. Uller, H. Videla, and L.K. Herrera, *Patinas naturales y artificiales y su importancia en la preservación de piezas de cobre del patrimonio cultural*, Latincorr, 2006, Brasil.
- [9] E. Mattson, R. Holm, *Atmospheric Corrosion* (1982) 365-382.
- [10] P. Eriksson, L. Johansson, and J. Gullman, *Corrosion Science* 34 (1993) 1083-1097.
- [11] J.D. Meakin, D.L. Amest, D.A. Dolske, *Atmospheric environment* 26B (1992) 207-215.
- [12] G. Lanterna, *Thermichimica Acta* 269/270 (1995) 729-742.

- [13] L.S. Selwyn, N.E. Binnie, J. Poitras, M.E. Laver, and D.A. Dowham, *Studies in Conservation* 41 (1996) 205-228.
- [14] A.E. Cepero, *Principios científicos del deterioro de los objetos de arte metálicos y de sus tratamientos de conservación*, Cencrem, 2002, La Habana, Cuba.
- [15] M. Morcillo, and M. Almeida, *Corrosión y protección de metales en las atmósferas de Iberoamérica* (M. Morcillo et al., eds), 1998, 547-590.
- [16] W.A. Oddy, N.D. Meeks, *Unusual phenomena in the corrosion of ancient bronzes*, Bromelle and Thompson (eds), *International Institute for Conservation of Historic and Artistic Works*, London (1982), pp. 119-124.
- [17] M. P. E. Berthelot, *Etude sur les metaux qui composent les onjets de cuivre de bronze, d'etain, d'or et d'argent, decouverts dans les fouillees de Dahchour*, de Morgan, A. Holzhausen (eds), Vienna (1895) pp. 131-146.
- [18] D.A. Scott, *Bronze disease: a review of some chemical problems and the role of relative humidity*, *JAIC*, Vol 29, Number 2, Article 7, (1990), pp. 193-206.
- [19] S. Reguer, P. Dillmann, F. Mirambet, *Corrosion science* 49 (2007), pp. 2726-2744
- [20] A. Duran, J.L. Perez-Rodriguez, L.K. Herrera, M.C. Jiménez de Haro, M.D. Robador, A. Justo, *Rev. Metalurgia Madrid* 44 (1) (2008), pp. 85-91.
- [21] U. Schwertmann, J., *Neues Jb. Miner.* 93 (1959), pp. 67-86.
- [22] E. Rocca, C. Rapin, F. Mirambet, *Corros. Sci.* 46, (2004), pp. 653-665.
- [23] J. Tetrault, *IIC-CG17* (1992). pp. 152
- [24] N.H. Tennent, J. Tate, L. Cannon, *SSCR J.4*, 8 (1993).
- [25] C. Degriigny C., Le Fall, R. Geuilmoit, E. *Papers in: ICOM Committee for conservation 11th Triennial Meeting*, Edimburg, (1986), pp 865-870.
- [26] M. Lewin, E. Pearce, eds. *Handbook of fiber chemistry*, 2nd. Edition, Marcel Dekker, Inc. New York, (1998), p 1065.
- [27] C. Hall, M. Davies. *Identification of textile materials*, 3er Ed., Textile Institute, Manchester (1951), p.220
- [28] J. M. Cronyn, *The Elements of Archaeological Conservation*, London, Routledge, (1990), p. 352.
- [29] C. Turgoose, *Lead and tin: studies in conservation and technology*, in C.E. Miles (ed.), *UKIC Occasional Papers*, nº 3, London (1985), p. 15.

- [30] P.D. Donovan, J. Stringer, Proceedings of the 4th International Congress on Metallic Corrosion, N.E. Hammer (ed.), NACE, Houston (1972), p. 537.
- [31] S. Bradley, D. Thickett, IAP, The pollutant problem in perspective, Presentation 5 (1998).
- [32] M.R. Raychaudhuri, P. Brimblecombe, Studies in Conservation 45 (2000), pp. 226-232.
- [33] L.K. Herrera, A. Duran, M.C. Jiménez de Haro, J.L. Perez-Rodriguez, Á. Justo, "Study of baroque artworks by non-destructive techniques" in Coalition. CSIC Thematic Network on Cultural Heritage (Electronic Newsletter) 14 (2007) 10-14.
- [34] A. Justo, M.C. Jiménez, M.B. Sigüenza, A. Durán, J.L. Pérez-Rodríguez. Internal report "Estudio científico de muestras procedentes del Órgano de la Catedral de Zaragoza". CSIC, 2004, 40.

## CONCLUSIONS

### VI.1 Studies and research of paintings

**VI.1.1.** According to the analyses carried out on the Bocanegra painting of San Ignacio of Loyola, we conclude that this palette contained different pigments. Some colours were employed with great intensity. For example, the cinnabar used for the red dresses achieved contrast. At this time, his pictorial technique remains intoned. Because of this, a double current of the light and colour was applied in these pictures. In some works, he used a dark background that emphasized the figures. In others, the figures are outlined on a translucent background of ochre (iron oxides pigments) and blue (azurite pigment and smalt) tones. In the paintings of Bocanegra's second phase (1670-1676), typologies of the figures are set. Furthermore, the palette is limited and portrays a sense of harmony through the colours. The brushstrokes are looser and strong contrasts are not present. Bocanegra also melted the colours and smoothed out the transitions between light and shadow. Technical advances and greater intensity of colour can be appreciated in the three canvases of "la vida de S. Ignacio." This phase demonstrated the development of drama and expressiveness.

The results were obtained using different physical-chemical techniques and analytical methodologies. An evaluation of the relationships between them gave useful information about the employed materials and painting techniques in the cultural heritage field.

Scanning electron microscopy in combination with energy dispersive x-ray microanalysis is an indispensable tool. It contributed extensively to the identification of the elements that constituted the different inorganic pigments of the conventional cross-sections of the paintings. FTIR supplied information on the organic components that the painter used in the preparation layers. The advantage of Py-GC/MS as a tool for the rapid screening of the organic composition of art objects is apparent from the results of this study. This method permitted the identification of siccative oils like those used in the organic medium of these paintings. This technique is capable of providing information on the presence of inorganic compounds such as HgS.

The non-destructive technique of XRD was applied in the study of ancient textile fibres of Bocanegra paintings. Using a glass capillary, it was possible to complete the study with only one fibre of the material. The presence of crystalline parts in the cellulose means that the fibres are only partially degraded.

Synchrotron-based  $\mu$ -XRD and  $\mu$ -XRF are particularly useful for non-destructive studies as well as for the micro-characterisation of different materials present in multi-layered paintings. This study demonstrated that synchrotron radiation micro-imaging techniques can be used to analyse pictorial layers (including grains) at the micrometer scale.  $\mu$ -XRD is very useful for the identification of phases that are present in low proportions in multilayer paintings. It can be used to identify different inorganic pigments, such as cerussite and hydrocerussite. It can also identify compounds with a low powder reflection, such as azurite, cobalt blue, hematite, and goethite. Cinnabar has a high powder reflection and was identified by conventional XRD.

**VI.1.2.** Micro-infrared spectroscopy and energy dispersive x-ray elemental microanalysis are techniques that give important information about the chemical composition of the different components used in paints. It is impossible to characterise the different crystalline phases by conventional XRD because the pigments in the different layers are present at low concentrations relative to the bulk matrix components. Furthermore, the reflecting power of these iron containing pigments is weak relative to other components present in the sample. For the characterisation of iron oxide pigments by conventional XRD, raw fragments of the paintings were used. It was rather difficult to identify the phases of the thin paint layers (in the range of microns or less). However, SR  $\mu$ -XRD made it possible to identify the crystalline structure of iron oxide and lead pigments in the cross-section of the paint layers. The SR  $\mu$ -XRD technique is a valuable tool for the accurate identification of iron oxide and lead pigments.

Synchrotron radiation  $\mu$ -XRD and  $\mu$ -XRF techniques are particularly suited to non-destructive studies. They are useful in the micro-characterisation of the different materials present in multi-layered paintings.

**VI.1.3.** Synchrotron-based techniques are available for the study of cross-sections of painting layers. This is the first report of monazite (Mon) in the presence of iron oxide as an accompanying phase in the ochre of ancient pigments.

**VI.1.4.** Synchrotron-based  $\mu$ -XRD and  $\mu$ -XRF are useful in the study and micro-characterisation of the different materials present in multi-layered paintings. This study demonstrated that synchrotron radiation micro-imaging techniques have the ability to

analyse pictorial layers (including grains) at the micrometer scale. This data is difficult to obtain with other laboratory techniques.  $\mu$ -XRD is very useful for the identification of phases that are present in low proportions in multilayer paintings. It can identify inorganic pigments (cerussite and hydrocerussite) and those with low powder reflections (azurite, malachite, hematite, and goethite). A conversion of azurite to malachite was not observed. A mixture of both phases in the same grain was not detected. The identification of copper carboxylates by FTIR suggests an interaction between carboxylic acids and copper pigments. Micro-Raman spectroscopy was useful for the identification of copper pigments. Some difficulties were encountered with the Raman study. These difficulties were solved by synchrotron-based  $\mu$ -x-ray diffraction and  $\mu$  X-ray fluorescence. In Sample 5, the pigments were observed as small grains and mixtures with other pigments.

## VI.2. Studies on ancient mirrors

**VI.2.1.** The combined use of SEM/EDX, XPS, FTIR, Raman and XRD provided good insight into the surface chemical information and corrosion products of ancient mirrors. The combination of these techniques clearly determined the corrosion state of the mirror.

The combined use of GID and XPS provided good insight into the surface's chemical structure and the degradation of the different amalgam mirrors. GID enabled a notable increase in the volume of studied samples. GID allowed for a large irradiated area of the sample at small x-ray penetration depths. GID is a useful and non-destructive research tool for the study of cultural heritage artefacts.

The SRXRD experimental setup used on the amalgam surfaces allowed us to obtain a depth profile analysis of samples under identical conditions. This study allowed for correlation of information between the surface and bulk properties of the mirrors. XPS analysis reinforced the information obtained by GID. The use of a large beam with a high angle of resolution provided an accurate means for semi-quantitative analysis. The use of a sub-mm beam permitted us to separate the dark-corroded and uncorroded parts of the amalgam.

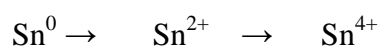
The tin amalgam mirror is composed of a binary alloy of tin and mercury. X-ray diffraction identified this structure as  $\text{Hg}_{0.1}\text{Sn}_{0.9}$ , with a primitive hexagonal structure and special group of P6/mmm.

Sample 1 presented with a very low degree of alteration. Sample 2 was largely degraded. In fact, the reflecting layers  $\text{Hg}_{0.1}\text{Sn}_{0.9}$  and the metallic  $\beta$ -Sn had disappeared. Mercury is

volatile and slowly evaporates. It ultimately leaves behind finely divided particles of tin that are easily oxidized to SnO (romarchite) and SnO<sub>2</sub> (cassiterite).

In Samples 2, 3 and 4, a unique chemical species, Sn<sup>4+</sup>, was found. In Sample 1, the XPS analysis was the only technique that confirmed the formation of Sn<sup>4+</sup> at the surface. SnO<sub>2</sub> is the most typical and stable corrosion product of tin.

The corroded mirrors studied in this work show a similar corrosion process. The oxidation of tin at the surface (~5 nm) occurs in the following way:



The semi-quantitative composition analysis of the different phases was accomplished using Rietveld refinement modelling. The findings contributed to the knowledge of the corrosion mechanisms on the amalgam surfaces of the ancient mirrors.

**VI.2.2.** The investigation of the corrosion processes of amalgam layers on a microscopic scale was completed using different techniques. Sn–Hg alloys, Hg and SnO<sub>2</sub> could be identified within the corrosion areas studied. Therefore, the corrosion process most likely starts with a segregation of mercury and tin. This segregation leads to the formation of Hg drops on the surface of the alloy layer. These nanoparticles are formed due to the oxidation process of the Sn polycrystalline layer. This layer remains behind and in contact with the Hg drops. SnO is likely formed first, followed by SnO<sub>2</sub>. The mercury drops eventually evaporate, leaving behind a “crater” surrounded by SnO<sub>2</sub> that is filled with a thin layer of SnO<sub>2</sub> nanoparticles. Eventually these fall out of the “crater.”

### **VI.3. Studies on baroque metallic organ pipes**

**VI.3.1** This study used μ-XRF to reveal the different trace elements and their localization in the two segregated areas. Organs built by organ builders are based on intuition and family tradition. It is possible that lead in the 17th century can be recreated by adding impurities that come naturally in old “pure” lead. These results are important for new organ builders because the lead in this time is totally pure. The addition of trace elements may allow for the recreation of antique technology.

**VI.3.2.** The composition and microstructure of historic tongues from reed pipes of baroque organs and modern organs was studied. The presence of lead and other trace elements in the two brass alloys was associated to different phases. These analyses show an excellent correlation between the XRD patterns of the old tongue and the quantification obtained with the PyMCA code. There was also correlation with the main elements using the synchrotron-based  $\mu$ XRF imaging. Information concerning the modern tongue obtained with these laboratory techniques was sufficient.

#### **VI.4. Studies of ancient fibres**

**VI.4.1.** This work reports the results obtained by a combination of OM, SEM, FTIR, and SR-XRD. With this data, it was possible to explain the different characteristics of flax, cotton and unprocessed plant material.

With synchrotron radiation, it was possible to associate different cellulose structures with the samples studied. Flax and cotton presented with a “Cellulose I” structure. The different crystallographic parameters and the CI extracted from the XRD patterns are in accordance with those reported for the Cellulose I structure.

The unprocessed plant material had a different cellulose structure than the flax and cotton samples. The CI values showed that this sample had a very low crystalline structure. The unit cell was smaller than that of Cellulose I according to the crystalline size. These results show that not all native cellulose is identical in crystal structure. The SEM cross-section supports this result. It showed that the bundle of unprocessed plant material was different than flax and cotton. The structure of Cellulose IV was associated with the unprocessed plant material. It occurred in the primary plant cell wall, not in the dominant second wall. This characteristic was unlike fibres that are used for textiles. There are two possible explanations: (i) plant fibre that was not used for textile making was used to fill the wooden ceiling, or (ii) due to the high microorganism activity found in the microclimate around this sample, the fibre was highly degraded.

This study used SR-XRD to demonstrate the fine structure of the natural fibres. Structural parameters such as crystallinity index and crystalline size were important in the characterisation of these fibres.

The evaluation of textiles provides information about the causes of deterioration. Deterioration may be due to environmental factors or other conditions.

## **VI.5. Studies of metallic artefacts**

**VI.5.1.** The data obtained in this work shows that x-ray diffraction with Göbel mirrors is a good method for the characterisation of the irregular surfaces from artefacts of cultural heritage. It allows for a non-destructive study (without sampling). The combination of Göbel mirrors and fixed low incidence angles allows for a depth profile of a sample. This is very important in artwork. Bronze in the rivet from Pardon Portico of Mosque-Cathedral of Cordoba was detected using x-ray diffraction with Göbel mirrors. On the surface of the bronze, weddellite, atacamite and gypsum were detected as alteration products. Goethite, lepidocrocite and  $\text{FeO}(\text{OH})$  appeared on an iron nail of Portico. This study demonstrated that the metallic point of a Roman arrow was composed of iron. On the surface, calcite, quartz and vesuvianite were found. The Roman button was covered with a thick crust formed by calcite and quartz. The surface of these materials was affected by the soil in which they were buried. Organ pipes were altered to hydrocerussite by storage of these materials in museums and churches.

Cellulose from paperboard and wooden drawers provided carboxylic acid. The acid dissolved the  $\text{PbO}$  formed on the surface of the lead seals of the Andalusia Government collection, forming lead carbonates.